High Permittivity Ceramics for Dielectrically Loaded Applications

By:

Simon John Nicholls

Thesis Supervisors:

Prof. Ian M. Reaney and Prof. Derek C. Sinclair

A thesis submitted in partial fulfilment of the requirements for the degree
of
Doctor of Philosophy

The University of Sheffield
Faculty of Engineering
Department of Materials Science and Engineering

January 2017

This thesis is dedicated to anyone diagnosed with dyslexia,
as proof that it is not always the handicap people think it is.

“Not everything that is faced can be changed,
but Nothing can be changed until it is faced.”
- James Baldwin

Acknowledgements

I wish to thank my supervisor: Prof. Ian M. Reaney for going out of his way to allow me the opportunity of undertaking this research project. Without this, and his continued support, guidance and, especially, patience with my writing, this thesis would not have been possible; for this, I am eternally grateful.

I would like to extend my gratitude to Dr. Iasmi Sterianou, who mentored me through the beginning of this project in the processes and techniques involved in the project, as well as initial interpretations of data. Iasmi was an invaluable source of help during the start of this project.

I would like to thank staff at the Department of Materials Science and Engineering for have assisted me and facilitated this research: Andrew Mould, Michael Bell, Bev Lane, Dr. Nik Reeves-McLaren, Dr. Peter Korgul, Dr. Le Ma, Dr. Peng Zeng, Dr. Cheryl Shaw and Prof. Derek C. Sinclair.

I would also like to extend my heartfelt gratitude towards the Disability and Dyslexia Support Service (DDSS) of the University of Sheffield, and to Jayne Woodward, who was my advisor throughout my entire time at the university. Without her guidance and advice, and arranging writing support with Christina Healey and Mr. Doud, I would have struggled to complete my undergraduate and postgraduate degrees.

I am grateful to my fellow colleagues in the Functional and Electronic Ceramics Research Group who have both helped me in less familiar territory and for providing enjoyable moments in my time within the group, including Leo’s Go-Karting bachelor party, going to the pub when things went wrong and introducing me to the best Chinese restaurants.

Last, but by no means least, I would like to thank my family and Rachel Bell, for providing endless support and encouragement through a rollercoaster of successes and frustrations which accompanied this project.

Thanks also to Dr. Oliver Leisten and the late Sarantel Ltd. for financially supporting this project. Without this support, the project never would have been available for me to undertake in the first place.

Publications:

S. J. Nicholls, I. M. Reaney, and O. P. Leisten, “Enhancing Properties in Microwave Ceramics Using a Designer Sintering Aid,” *J. Am. Ceram. Soc.*, vol. 98, no. 12, pp. 3891–3896, Dec. 2015.

A. L. Chinelatto, K. Boulahya, D. Pérez-Coll, U. Amador, C. Tabacaru, **S. Nicholls**, M. Hoelzel, D. C. Sinclair, and G. C. Mather, “Synthesis of a 12R-type hexagonal perovskite solid solution $Sr_3NdNb_{3-x}Ti_xO_{12-\delta}$ and the influence of acceptor doping on electrical properties,” *Dalt. Trans.*, vol. 44, no. 16, pp. 7643–7653, 2015.

R. Muhammad, A. Khesro, and **S. J. Nicholls**, “Layered perovskite structured $La_{5-x}Sr_xTi_{4+x}Sc_{1-x}O_{17}$ microwave ceramics for dielectrically loaded antennas,” *Ceram. Int.*, vol. 42, no. 5, pp. 6422–6427, 2016.

Conferences Attended:

Ferroelectrics UK 2013, Institute of Physics, University of Sheffield, 17th January 2013 at 10:00 - 18th January 2013 at 16:00 (GMT+00:00).

Abstract

A temperature-stable, ultra-high permittivity dielectric ceramic, based on CTLNT, has been successfully fabricated at significantly reduced sintering temperatures with no deterioration of microwave properties, through the addition of a $Bi_4B_2O_9$ (BBO) sintering aid. This work has been an extension of previous findings where it was shown that $0.2CaTiO_3$-$0.8(Li_{0.5}Nd_{0.5})TiO_3$ (CTLNT) with 4wt% BBO as a liquid-phase sintering aid gives rise to exceptional microwave (MW) dielectric properties, (relative permittivity, ε_r = 127, quality factor, Qf_0 = 2700 GHz, and temperature coefficient of the resonant frequency, τ_f = +4 ppm/°C) at reduced sintering temperatures (1200°C). Prior to this, it has been exceptionally difficult to produce a large ε_r dielectric material, with both a low sintering temperature and near-zero temperature stability, without dramatic deterioration of the dielectric properties of the material.

This contribution set out to investigate and understand the sintering mechanism between the CTLNT + $x$wt% BBO system, to aid in the development of designer sintering aids in the development of other microwave dielectric ceramic materials and devices. CTLNT + 1, 3, 4 and 5wt% BBO compositions were fabricated and a variety of analysis techniques were used, such as density, XRD, SEM, TEM, EDS and MW characterisation. Density increased with increasing BBO concentration and sintering temperature, and the MW results reflected the changes in density. The 1wt% BBO composition showed the greatest variation between the sintering temperatures, and 4wt% composition demonstrated optimum MW results of: $\varepsilon_r = 125$, $Qf_0 = 2518\,GHz$ and $\tau_f = 4\,ppm/°C$, at a sintering temperature of 1200°C. The variation of τ_f with changes in BBO concentration was non-linear, which suggested a chemical reaction was taking place. XRD results revealed no secondary phases, regardless of BBO concentration. SEM results showed increased crystal grain size as BBO concentration and sintering temperatures increased, as well as increased contrast variation on the polished surface and darker-contrast amorphous phase in the fracture surface. The contrast variation in the polished surfaces were also indicative of a chemical reaction.

Using a combination of XRD, TEM and SEM it was demonstrated that highly polarisable Bi^{3+} ions entered the CTLNT perovskite lattice and locally increasing ε_r. The accompanying ex-solution of TiO_2 precipitates, observed and analysed under SEM and TEM, as the BBO concentration increased implied the formation of Ti vacancies (V_{Ti}'''') in the perovskite matrix to compensate for the extra positive charge of the Bi^{3+}. The ex-solution of Ti indicates Bi^{3+} ions substitute onto the A-site of the perovskite crystal system for lower valence ionic elements, after the following generic defect equation:

$$4A_A^x + Ti_{Ti}^x \Rightarrow 4Bi_A^{\cdot} + V_{Ti}''''$$

The residual phase was found to be a boron-rich liquid-phase, which acted as the sintering aid, with a large negative τ_f which compensates for the positive τ_f of the CTLNT.

The CTLST + $x$wt% BBO system (S = Sm) was then investigated to determine if a similar mechanism would occur. CTLST + 1, 2, 3 and 4wt% BBO compositions were fabricated and underwent the same analysis techniques. Density increased with increasing BBO concentration up to 1250°C, after which density fell for all samples; the 4wt% BBO composition exhibited the largest density, at 1250°C. The MW results reflected this trend, which saw a general increase in ε_r as BBO concentration and sintering temperature increased, which fell universally at 1300°C. Qf_0 would generally increase with increased BBO concentration, across all sintering temperatures, while a dip was observed at 1250°C, and the 4wt% BBO composition demonstrated optimum properties of: ε_r = 105.7, Qf_0 = 3295 GHz and τ_f = -4 ppm/°C, sintered at 1200°C. Contrary to the CTLNT system, the variation of τ_f with BBO content and sintering temperature was linear.

SEM reflected density changes, where crystal grain increased with increasing BBO concentration, up to 1250°C. At 1300°C, samples suffered from dissolution into the liquid-phase, increasing pore sizes, decreasing density and, thus, impacting on the MW properties of the samples. Similar to the CTLNT system, contrast variation was observed, in addition to darker B-rich liquid phase in the fracture surface. EDS from both SEM and TEM revealed that Bi was present within the CTLST matrix, however no TiO_2 precipitates were observed. Large Zr contamination within CTLST is the likely cause of the difference in defect chemistry, as excess of Zr substitution onto the perovskite B-site compensates for Bi substitution onto the A-site, negating the need for TiO_2 precipitates to ex-solve.

Multi-layer ceramic capacitors (MLCCs) of the CTLNT + 4wt% BBO composition were fabricated to determine whether the temperature stabilities of the material in conjunction with a large ε_r would allow the material to be a suitable candidate as a Class 1 C0G/NP0 MLCC device. Fabrication of the devices followed the conventional method, but required modification due to delamination. These modifications included: longer firing times to allow for binders and plasticisers to burn-out fully; calcined alumina powder base to fire and sinter samples upon, to avoid sticking issues; and solvent wetting of individual layers to adequately fuse layers together pre-firing and sintering. Successful MLCC devices had case sizes of EIA ‘2928’ and IEC ‘7472’. SEM and EDS revealed no mixing or exchange of materials between the dielectric and the platinum internal electrode, and generally good adhesion between both materials. Electrical tests revealed that, despite the temperature stability observed at 1-3 GHz in the MW study, that the MLCC devices would be classed as EIA “M8J” and IEC “P1000”, however maximum available test frequency of 1 MHZ is much lower than the average operating frequencies of class 1 devices, which lie between 100 MHz – 30 GHz.

Contents

Chapter 1: Introduction

Since the turn of the millennium, the use of GPS (Global Positioning Systems) technology has become much more widespread, evolving from being used in cars to being used in small, hand-held devices and ‘smartphones’, figure 1. 1, driven by consumer demand for ever-smaller devices. Advances in materials and production processes has enabled the technology to be cheaper and more mobile. For an antenna to be both small and effective, the material core of the antenna should have a large relative permittivity, which will enable miniaturisation (ε_r > 20). Low dielectric losses improve frequency selectivity (Qf_0 > 2000, where $Q = \frac{1}{\tan\delta}$ and f_0 = resonant frequency) and near-zero temperature coefficient of resonant frequency (τ_f) prevents frequency drift in operation. The precise values ε_r, Qf_0 and τ_f vary based on the specific application and device but there is an inverse relationship between the relative permittivity (ε_r) and the quality factor ($\log_{10} Qf_0$) as illustrated in figure 1. 2 after Reaney and Iddles (2006) [1], and based on tabulated data from Zheng *et al.*, 2005 [2] (table 1. 1).

Figure 1. 1 A hand-held GPS device, with a suitably small antenna, produced by Garmin [3].

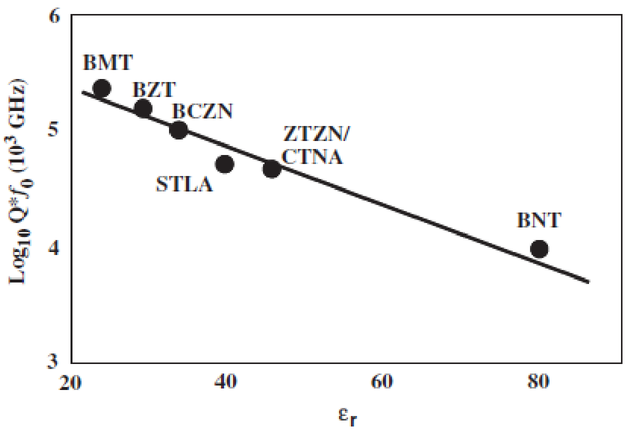

Figure 1. 2 Inverse relationship between ε_r and $\log_{10} Qf_0$ [1].

Table 1. 1 Common ceramics used as DLAs and filters, as featured in figure 1. 2, above, after Zheng *et al.*, 2005 [2].

Material	Abbreviation	ε_r	Qf_0 (GHz)	Crystal Structure
$Ba(Mg_{1/3}Ta_{2/3})O_3$	BMT	24	250,000	Complex Perovskites
$Ba(Zn_{1/3}Ta_{2/3})O_3$	BZT	29	150,000	
$Ba(CoZn)_{1/3}Nb_{2/3}O_3$	BCZN	34	90,000	
$SrTiO_3$-$LaAlO_3$	STLA	39	60,000	Simple Perovskites
$CaTiO_3$-$NdAlO_3$	CTNA	45	48,000	
$ZrTiO_3$-$ZnNb_2O_6$	ZTZS	44	48,000	α-PbO_2
$Ba_4Nd_{9.333}Ti_{18}O_{54}$	BNT	80	10,000	Perovskite/Tetragonal Tungsten Bronze

1.1 Dielectrically Loaded Antennas

Materials with the most promise for miniaturisation are normally based on TiO_2, $BaTiO_3$ and $CaTiO_3$ and are extensively used in devices known as dielectrically loaded antennas (DLAs), which uses the dielectric ceramics as the material core of the antennas. Metallisation is applied to the surface of the antenna cores, otherwise known as a ‘substrate’, to ‘sculpt’ the signal, based on the design of the metallisation, and relay information between the antenna and circuit.

As antennas and devices have become more compact and portable, one of the largest obstacles to overcome is that of a phenomenon known as ‘body loading’, which is the absorption, or obstruction, of the electric-field radiation within the ‘near-field’ of the antenna, such as the human body for portable devices [4]. DLAs, in addition to a large miniaturisation potential, are also particularly well suited against body loading, as they are able to concentrate the radiation within the dielectrically loaded ceramic substrate.

DLAs are at their most efficient when the devices are operated at, or close to, electrical resonance, known as their resonant frequency (f_0), which maximises the electromagnetic energy held in the surrounding space in and around the antenna, known as the ‘near-field’ [4], [5]. The near-field is responsible for the radiation of the signal to the ‘far-field’, by oscillating both the electric and magnetic field components of the signal wave, which takes the form of ‘traveling waves’ [5], [6]. The near-field contains the highest density of electromagnetic field lines, much more so than the far-field. As such, any physical presence capable of absorbing this electromagnetic energy, at the frequencies used, such as the human body of the user, is usually the most performance impairing factor of the devices [7], [8].

The use of DLAs increases the predictability of the antenna characteristics under body-loading. This is much more relevant to circularly polarised antennas, as the near-fields must now support a rotating dipole, since rotating fields are always more vulnerable to disruption by the surrounding environment [9]. There are two main competing DLA designs: the Microstrip Patch Antenna and the Dielectrically Loaded Multifilar-Helix (D-LMH) antenna (figure 1. 3). In industry, choosing one design over the other comes mainly from a balance of price, the aesthetic design of a product and which one is capable of the most miniaturisation, both physically and electrically.

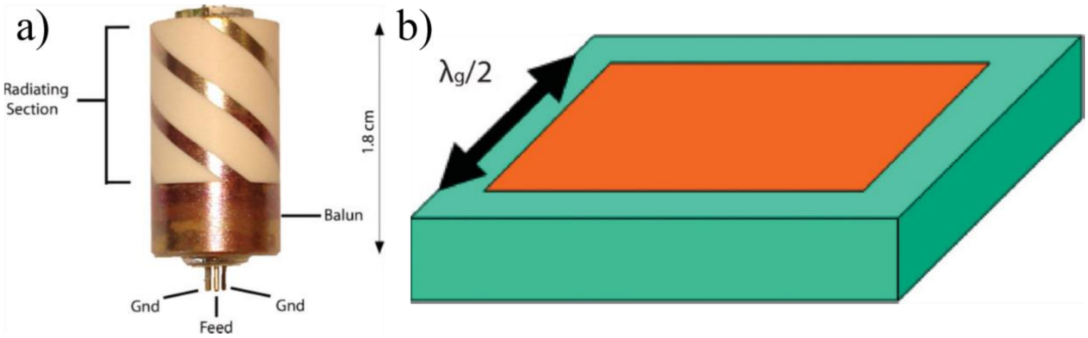

Figure 1. 3 The two main antenna designs, a) Dielectrically Loaded Quadrifilar-Helix (D-LQH) antenna and b) Microstrip Patch antenna [5].

1.1.1 Microstrip Patch Antennas

The Microstrip Patch antenna is a planar antenna which is printed on top of a dielectric slab underneath which is a large, extensive ‘ground plate’, and is generally rectangular in shape. The length of this square antenna is equal to $\frac{\lambda_g}{2}$, where λ_g is the guide wavelength dictated by the relative permittivity (ε_r) and the dimensions of the dielectric slab, as can be seen by equation 1.1 [5]. This equation works to give a prediction of a critical dimension for the antenna, which is important when designing a new antenna within ever increasing dimensional constraints:

$$\frac{\lambda_g}{2} = \frac{\lambda}{2} \times \frac{1}{\sqrt{\varepsilon_{eff}}}$$

(1.1)

where λ_g is the wavelength of the electromagnetic energy which is conducted in a waveguide (or 'the guide wavelength'), λ is the electromagnetic energy wavelength in free space and ε_{eff} is the effective permittivity of the waveguide. Finally, the length and breadth of the antenna is extended by approximately 1mm in order to constrain the area of fringing fields [5]. Although the width of the dielectric slab is normally no more than ~15mm, the electrical size of the antenna is controlled by the much wider ground plate, which in modern miniature devices becomes populated by other electronic components. The antenna works by combining two linear modes offset at 90° to each other, where both modes have the same amplitude, producing a circular polarisation mode [10].

1.1.2 Dielectrically Loaded Multifilar-Helix (D-LMH) Antennas

The D-LMH antenna is a cylindrical antenna, where the 'multifilar' part refers to the design of the antenna, which, in the case of the D-LMH, typically has two 'quadrature phased bifilar helical' loops [5], offset at 90° to each other. Each 'loop' is one full guide wavelength path, which accounts for two half-turn helix sections, the 'spirals' of which (figure 1. 3, a) are interconnected by currents flowing around the rim, or 'balun', at the bottom of the structure [11].

By offsetting the two loops to have slightly different resonant frequencies, 'quadrature' can be achieved. This is done by adjusting one element to slightly longer than resonance and the other element to slightly shorter than resonance, giving input impedance with +45° and -45° phase angle respectively. This is what produces the 90° shift between the two currents of loop 1 and 2 [11], [12].

The size of these helical antennas can be significantly reduced compared to its free space equivalent due to the dielectric loading given by the high permittivity of the core material used. The size of the antenna is equivalent to one half-turn of the helix, representing $\frac{\lambda_g}{2}$, rather than a planar dimension as seen in the Microstrip Patch antenna. Therefore, depending on the permittivity of the dielectric material core used, D-LMH antennas can be made to much lower dimensions than the microstrip patch antenna by almost a half, at the same values of permittivity [5], table 1. 2. However, they tend to be more expensive due to a more complex fabrication process.

Table 1. 2 Effective size comparisons with respect to their relative permittivity between two different antenna designs, in this case the microstrip patch antenna and a Dielectrically Loaded Quadri-Filar Helix antenna [5].

Width Dimension (mm)	Microstrip Patch Antenna ('width' is length and breadth of metallisation plus un-metallised border)	D-LQFH antenna ('width' is the diameter of dielectric cylinder)
15	$\varepsilon_r = 53$	
14		$\varepsilon_r = 21$
12	$\varepsilon_r = 82$	
10		$\varepsilon_r = 36$
7.5		$\varepsilon_r = 80$
6.5		$\varepsilon_r = 88$

1.2 Cost of Manufacture

From figure 1. 2, there are no wide-spread commercial DLA devices with larger ε_r values than 80-90, despite the fact that dielectric materials with ε_r values of 110-130 exist in the CTLRET family, based on $CaTiO_3$-$(Li.RE)TiO_3$ (RE = rare-earth) [13]–[15]. This is due to two main issues regarding these materials: firstly is the cost of the base materials due to the use of rare-earth elements [16]; secondly is the fact that these materials tend to have high sintering temperatures (> 1300-1400°C).

Since the year 2000, the main bulk of research has been focussed on fabricating these very large ε_r materials in such a way which results in a lowering of sintering temperature, which would make the fabrication costs feasible for mass-production, and modifying the τ_f values. This is normally achieved by adding and mixing sintering aids. However, invariably sintering aids are detrimental to some or all of the dielectric properties of the material, restricting the amount of sintering temperature reduction achievable. Until recently, it was difficult to develop a high enough ε_r material, which was also temperature stable, at relatively low sintering temperatures [17]. In 2012, Chen *et al.* reported a large reduction in sintering temperature, for a CTLNT system (where N = Nd lanthanide), with little or no deterioration of electrical properties, with only small additions of a $Bi_4B_2O_9$ (BBO) sintering aid [18].

While this is a significant advance in making ultra-high ε_r materials commercially feasible, there was no understanding as to why the sintering aid was not detrimental overall properties of the material and, thus, there was no application of these findings for other, high ε_r materials.

1.3 Key Aims of this Research

The main aim of this project is to investigate the relationship between the CTLNT and the BBO sintering aid, based on the initial findings by Chen *et al.* [18], to determine what role the BBO has on the sintering mechanism. Upon an understanding of this mechanism, the experiments will be repeated on a similar material within the CTLRET family to see whether any observed mechanism can be transferred and applied elsewhere. The hope is to be able to develop designer sintering aids to reduce the sintering temperature of other high ε_r materials. Finally, in addition to illustrating the potential of CTLNT – xBBO for use as a substrate in dielectrically loaded antennas, the possibility of using CTLNT – xBBO as the dielectric substrate in multilayer C0G devices is investigated.

1.4 References

[1] I. M. Reaney and D. Iddles, “Microwave Dielectric Ceramics for Resonators and Filters in Mobile Phone Networks,” *J. Am. Ceram. Soc.*, vol. 89, no. 7, pp. 2063–2072, Apr. 2006.

[2] H. Zheng, I. M. Reaney, D. Mum, T. Price, and D. M. Idoles, “Composite dielectric ceramics based on BaO-Ln2O3-TiO2 (Ln = Nd, La),” *Japanese J. Appl. Physics, Part 1 Regul. Pap. Short Notes Rev. Pap.*, vol. 44, no. 5 A, pp. 3087–3090, 2005.

[3] G. Ltd, “GPSMAP® 62,” 2016. [Online]. Available: https://buy.garmin.com/en-GB/GB/outdoor/handheld/gpsmap-62/prod63800.html. [Accessed: 08-Aug-2016].

[4] R. Hill, “Band switched patch radiators for telephone handsets,” in *Microwave Filters and Antennas for Personal Communication Systems, IEE Colloquium on*, 1994, pp. 2/1–2/6.

[5] M. Mirsaneh, O. P. Leisten, B. Zalinska, and I. M. Reaney, “Circularly Polarized Dielectric-Loaded Antennas: Current Technology and Future Challenges,” *Adv. Funct. Mater.*, vol. 18, no. 16, pp. 2293–2300, Aug. 2008.

[6] M. Zahn, *Electromagnetic Field Theory: a problem solving approach*. John Wiley & Sons, 1979.

[7] O. P. Leisten and B. Rosenberger, “Miniature Dielectric Loaded Antennas with Low SAR,” in *10th International Conference on Wireless Communications*, 1998, pp. 196–205.

[8] O. P. Leisten and A. P. Wingfield, “Commitment to Design for a Safety-Critical Function Reliable GPS Antenna Technology for E-911 in Handsets,” in *Proceedings of the 16th International Technical Meeting of the Satellite Division of The Institute of Navigation (ION GPS/GNSS 2003)*, 2003, pp. 1579 – 1584.

[9] J. S. Colburn and Y. Rahmat-Samii, “Human proximity effects on circular polarized handset antennas in personal satellite communications,” *IEEE Trans. Antennas Propag.*, vol. 46, no. 6, pp. 813–820, Jun. 1998.

[10] M. D. Deshpande and N. K. Das, “Rectangular Microstrip Antenna For Circular Polarization,” *IEEE Trans. Antennas Propag.*, vol. AP-34, no. 5, pp. 745–746, 1986.

[11] C. C. Kilgus, “Resonant Quadrifilar Helix Design,” *Microw. J.*, vol. 13, pp. 49–52, 1970.

[12] C. Kilgus, “Resonant quadrafilar helix,” *IEEE Trans. Antennas Propag.*, vol. 17, no. 3, pp. 349–351, May 1969.

[13] H. Takahashi, Y. Baba, K. Ezaki, Y. Okamoto, K. Shibata, K. Kuroki, and S. Nakano, “Dielectric Characteristics of (A 1/2 1+ ·A 1/2 3+)TiO 3 Ceramics at Microwave Frequencies,” *Jpn. J. Appl. Phys.*, vol. 30, no. Part 1, No. 9B, pp. 2339–2342, Sep. 1991.

[14] K. Ezaki, Y. Baba, H. Takahashi, K. Shibata, and S. Nakano, “Microwave Dielectric Properties of CaO-Li 2 O-Ln 2 O 3 -TiO 2 Ceramics,” *Jpn. J. Appl. Phys.*, vol. 32, no. Part 1, No. 9B, pp. 4319–4322, Sep. 1993.

[15] H. Takahashi, Y. Baba, K. Ezaki, and K. Shibata, “Microwave Dielectric Properties and Crystal Structure of CaO – Li 2 O –(1- x) Sm 2 O 3 – x Ln 2 O 3 – TiO 2 (Ln: lanthanide) Ceramics System,” *Jpn. J. Appl. Phys.*, vol. 35, no. Part 1, No. 9B, pp. 5069–5073, Sep. 1996.

[16] A. Walters, P. Lusty, and A. Hill, “Rare Earth Elements,” Nottingham, 2011.

[17] D. A. Abdel Aziz, I. Sterianou, and I. M. Reaney, “(1 − x)CaTiO3–x(Li0.5Nd0.5)TiO3 for ultra-small dielectrically loaded antennas,” *J. Mater. Sci.*, vol. 44, no. 23, pp. 6247–6250, 2009.

[18] X. Chen, W. Zhang, B. Zalinska, I. Sterianou, S. Bai, and I. M. Reaney, “Low Sintering Temperature Microwave Dielectric Ceramics and Composites Based on Bi 2 O 3 -B 2 O 3,” *J. Am. Ceram. Soc.*, vol. 95, no. 10, pp. 3207–3213, Oct. 2012.

Chapter 2: Literature Review

2.1 What is a Ceramic?

When most people think of the word ‘ceramic’, what normally comes to mind? Plates, cups or tiles, or perhaps anything fired in a kiln, maybe something with a glaze of some description. The overall opinion, then, is: something that is hard, resistant to heat and certainly, predominantly, brittle. If one were to consult the dictionary definition of the word ‘ceramic’, one may find: “Made of clay and permanently hardened by heat” [1]. This, however, is somewhat misleading and not broad enough to do the entire, modern ceramics industry justice. More specifically, then, a ceramic can be considered to be: a mixture of crystalline and glassy phases, in combination with porosity, in a wide variety of proportions and arrangements. Kingery *et al.* define the idea of ceramics thus: the art and science of making and using solid articles, which are largely made of inorganic, non-metallic materials [2].

This not only includes the traditional view of ceramics, such as: pottery, porcelains, refractories, abrasives and cements; but also non-metallic magnetic materials, ferroelectrics, manufactured single-crystals, glass ceramics and many other advanced, functional ceramics.

Certainly, over the last 80 years, the term ‘ceramic’ now includes some of the most rapidly evolving, exciting and important materials of the modern age. Ceramics are now used in areas such as: nuclear fuels, enamels for aluminium in the architecture industry, thermal resistant/protective coatings such as the ones used to protect jet turbine blades from melting during use, molecular sieves, high-temperature superconductors, electrical components for computing, and high-frequency microwave electronic applications.

2.1.1 Sintering Mechanisms

In most cases, the ceramics take the form of compact powders which are then fired at a sufficient temperature to develop enough density within the material in order to produce the required macroscopic properties

For complex oxides formed from two or more binary oxides, the powders are reacted to achieve the required crystal structure. When this reaction involves the decomposition of a carbonate, then it is termed ‘calcination’. Thereafter, any further changes come from three possible effects: increase in grain size (i.e. grain growth); changes in pore shape; and changes in pore size and distribution, usually resulting in a decrease in total porosity. Normally, grain growth (or recrystallization) occurs during heat treatment by the three distinct processes listed below:

1. *Primary Recrystallization*
    - The process by which nucleation and growth of new, strain-free, grains occurs within a plastically deformed matrix.
2. *Grain Growth*
    - The process by which the average size of these strain-free (or nearly strain-free) grains increases continuously throughout the heat treatment process without a change in grain-size distribution.
3. *Secondary Recrystallization*
    - The process by which a few large grains are nucleated and grow at the expense of a fine-grained, strain-free, matrix. This is also known as abnormal grain growth, or discontinuous grain growth.

All of the above concern the change in grain size during heat treatment but, generally, porosity decreases and density increases, a process commonly referred to as sintering.

The simplest, and most common mechanism of sintering is *solid state sintering* in which a compacted ceramic powder, composed of individual particle powder separated by 25-60 volume percent (vol%) porosity, is converted to a solid, dense and strong body with < 5 vol% porosity (figure 2.1). For any application requiring good thermal or electrical properties, it is desirable to eliminate as much porosity as possible.

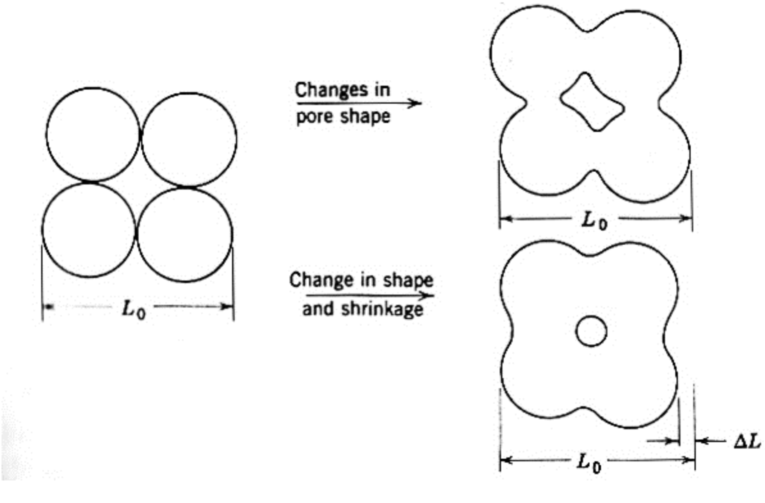

Figure 2. 1 The difference between changing pore shape and grain shape, with respect to shrinkage [2].

The Driving Force for Densification

The driving force for densification or sintering is usually considered to be the decrease in surface free energy. More precisely, this statement can be expressed as the decrease in surface area and lowering of the surface free energy (i.e. Gibbs free energy) by the elimination of solid-vapour interfaces, causing coincidental formation of new, lower energy, solid-solid interfaces [2].

On a microscopic level, material transfer is affected by pressure differentials and changes in free energy across a curved surface. If the particle size and radius of curvature is small, then material transfer effects increase. These effects are particularly high when the curvature is less than a few microns [2]. As a result, most ceramics are based on fine-particle materials, since this offers the best sintering (and densification).

The surface free energy driving force can be applied in almost all ceramic heat treatment densification systems. There are variations in results between different materials which may be attributed to different sintering mechanisms, such as: evaporation and condensation; viscous flow; surface diffusion; and grain boundary, or lattice, diffusion. Of these, evaporation and condensation, and viscous flow are the most common additional mechanisms attributed to any observed variation.

Evaporation-Condensation

During the sintering process, there is a tendency for material transfer to occur due to differences in surface curvature and, consequently, the differences in 'vapour pressure' surrounding the particles at various parts of the system. Initially, considering the case of just two particles of compact powder, as the sintering begins, there is a positive radius of curvature and, as such, the vapour pressure is larger than that for a flat surface. At the contact point, or junction, between the two particles there is a 'neck', at which there is a small, negative radius of curvature. As a result, at the neck, there is a vapour pressure an order of magnitude lower than that for the particles themselves which, as a result of the vapour pressure difference, tends to transfer material into the neck, illustrated by figure 2.2. This transfer also reduces surface free energy.

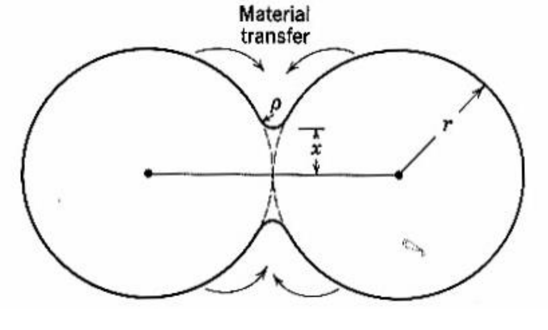

Figure 2. 2 The initial stages of sintering by the evaporation and condensation mechanism [2].

For vapour-phase material transfer to occur, it is required that the material be heated to a temperature sufficiently high enough for the vapour pressures to be appreciable. For particle sizes in the micron-range, vapour pressures in the order of 10^{-4} – 10^{-5} atmospheres (atm) are required [2].

The vapour-phase material transfer sintering mechanism is particularly important for changes happening in halide materials (such as sodium chloride), and in ice and snow technologies [2].

Other Solid State Processes

It is this difference in free energy, or chemical potential, between the neck area and the surface of the particles which provides the driving force of sintering and densification, causing material transfer by the fastest means available. In addition to the vapour transport mechanism discussed, material transport can happen from the particle surface, from the volume (or bulk) of the particles, or from the grain boundary between the particles, either by surface, lattice or grain boundary diffusion.

There is a big difference between the matter transfer paths and their potential results on the final densification of the overall material. For example, transfer of material from the surface of the particles to neck via surface or lattice diffusion, like vapour transport, does not change the distance between the particle centres and, therefore, results in no shrinkage. If shrinkage is desired, then only transfer of matter from the bulk of the particles, or from the grain boundaries between the particles, causes this. Table 2.1 and figure 2.3 lists and illustrates this.

Table 2. 1 List of alternate paths for material transport during the initial stages of sintering [2], illustrated in Figure 2.3.

Mechanism Number	Transport Path	Source of Matter	Sink of Matter
1	Surface diffusion	Surface	Neck
2	Lattice diffusion	Surface	Neck
3	Vapour transport	Surface	Neck
4	Boundary diffusion	Grain boundary	Neck
5	Lattice diffusion	Grain boundary	Neck
6	Lattice diffusion	Dislocations	Neck

It is noted by Kingery [2] that the sintering rate steadily decreases with time, such that just sintering over a long period of time becomes impracticable and, therefore, time is not a major, or critical, variable for process control. Instead, it is the control of the particle size which is critical; the sintering rate is approximately inversely proportional to the particle size. Additionally, during the early stages of sintering, it is the surface diffusion matter transfer mechanism which is most dominant. Thereafter, grain boundary and volume diffusion become more important and more dominant.

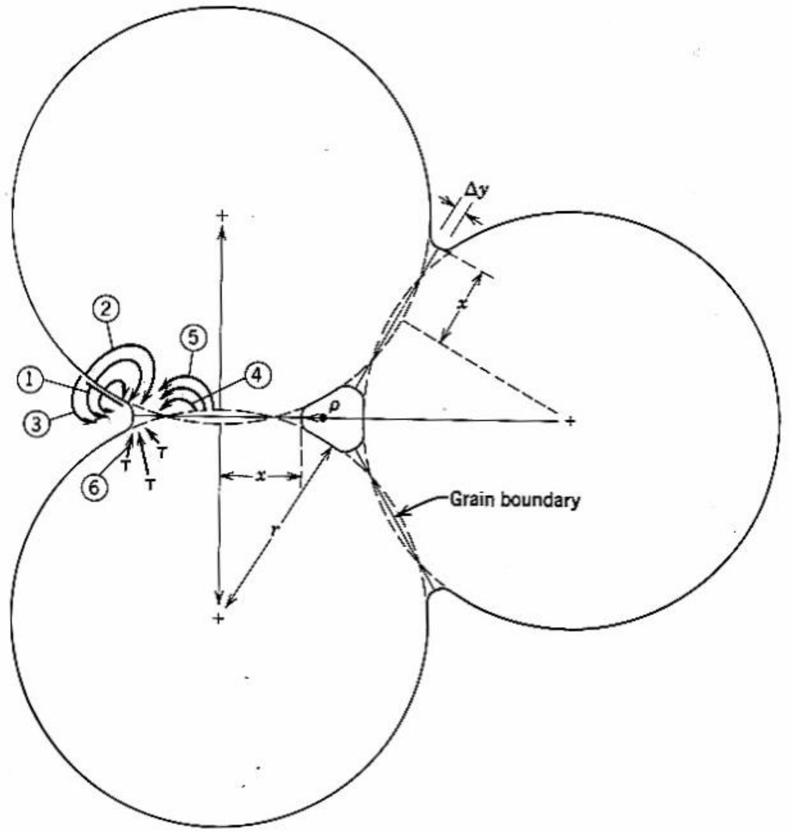

Figure 2. 3 Illustration of possible alternative paths for material transport during the initial states of sintering [2]. The circled numbers refer to different transport mechanism indicated in Table 2.1.

Liquid-Phase Sintering

Liquid-phase sintering, or sintering with a reactive liquid, is another process which causes densification, and is very important with respect to this project. Liquid-phase sintering occurs when the solid-phase has some limited solubility with the liquid at the sintering temperature. The driving force for sintering and densification, in this case, is derived from the 'capillary pressure', rather than the vapour pressure, of the liquid phase between the fine particles of the ceramic.

For rapid densification via liquid-phase sintering to take place, three criteria are essential [2]:

1. An appreciable amount of liquid phase;
2. An appreciable amount of solid-phase solubility in the liquid;
3. 'Wetting' of the solid particles by the liquid.

When the solid particles become 'wetted', the spaces between the particles becomes a capillary in which a substantial capillary pressure is developed. The range of pressures produced by these capillaries varies depending on the liquid-phase material, and the particles sizes of the solid-phase. For example, for sub-micron particle sizes, with capillary diameters in the range of 0.1 – 1 micron, the capillary pressure can range from 1.2-12 MPa (mega-pascals) for a silicate liquid-phase, or 6.7-67 MPa for a metallic liquid, such as liquid cobalt [2]. It is possible for both solid-state and liquid-phase sintering to occur simultaneously, if the first criterion is not fully met and there are regions of wetted and un-wetted particles.

Densification, as a result of this capillary pressure, is achieved via a different process than that of solid-state sintering, which occurs coincidentally. First, once the liquid phase has formed, the wetted particles begin to rearrange themselves, giving rise to a more effective packing order. This rearrangement can potentially lead to complete densification if there is enough liquid phase to fill-in all of the interstices completely. After this initial rearrangement, there are bridges at the contact points between particles with high local stresses. These stresses can lead to plastic deformation and creep, allowing for even further rearrangement of particles. Thereafter, during the sintering process itself, there is a solution of smaller particles in between the larger particles, and there is also growth of these larger particles through the transfer of material through the liquid phase. As a result of the constantly imposed capillary pressure, further particle rearrangement can occur during this grain growth, as well as grain-shape changes. All of this rearrangement gives rise to further densification of the ceramic.

In some cases, the liquid phase penetrates between particles, causing further increases in capillary pressure between the particles. This, in turn, leads to increased solubility of the solid-phase at the contact points, such that there is material transfer away from the contact areas. This instigates particle centres to approach one another, resulting in further shrinkage and densification. Finally, unless there is complete wetting by the liquid phase, recrystallization and grain growth may be sufficient enough to form a skeleton structure by particle coalescence through the ceramic system. The formation of this skeleton structure will eventually cause the densification process to be slowed and stopped [2].

For proper implementation of the liquid-phase sintering process, fine-particles are required to develop the necessary capillary pressures, which are themselves inversely proportional to the capillary diameter. An appropriate range of liquid concentration relative to the solid particle packing is also required.

2.2 Dielectric Ceramics

2.2.1 What is a Dielectric Material?

A dielectric material is an insulator which becomes polarised when subjected to an applied electric field. Polarisation occurs because electric charge does not flow through the material but shifts slightly away from the equilibrium position of charge regions/ions. This charge shift is very limited in movement and produces a phenomenon known as a dipole moment [2]. A good dielectric material is an insulator with high polarizability which gives rise to a large relative permittivity or dielectric constant, ε_r.

Dielectric Polarisation

The dielectric properties of a material are normally defined by how it behaves as a parallel plate capacitor, where the dielectric material occupies the space between two plates of known distance, d, and surface area, A. With a vacuum between the parallel, conducting plates, capacitance is defined by the following expression [3]:

$$C_0 = \frac{\varepsilon_0 A}{d}$$

(2. 1)

where:

C_0 = the capacitance of free space (farad, F);
ε_0 = the permittivity of free space (8.854×10^{-12} Fm^{-1});
A = surface area of the parallel plates (m^2), and;
d = distance between the parallel plates (m).

When a potential difference is applied across the plates, an amount of charge (Q_0) will be stored between the parallel plates. The amount of charge stored relates to the magnitude of the potential difference:

$$Q_0 = C_0 V$$

(2. 2)

where:

Q_0 = the charge stored in free space (coulomb, C);
C_0 = capacitance of free space (farad, F), and;
V = potential difference (volts, V).

Replacing the vacuum with any other material will change the amount of charge stored, and therefore the capacitance. If a dielectric material replaces the vacuum, then the amount of charge stored, and, thus, the capacitance, of the system increases. This increase is proportional to the relative permittivity of the material used, which is dependent on the degree of polarization, or charge displacement, of the material [2], [3].

In general, the relative permittivity (ε_r) of most ionic solids is $5 < \varepsilon_r < 20$ [4], compared with air ($\varepsilon_r = 1$) [5]. By comparison, the most commonly used dielectric material in capacitors, $BaTiO_3$, has a relative permittivity of $10^3 < \varepsilon_r < 10^4$ [6], [7].

Polarisation (α) can be induced within a material in four different ways, either individually or as a sum of all effects [2]:

$$\alpha = \alpha_e + \alpha_i + \alpha_d + \alpha_s$$

(2. 3)

where:

α_e = electronic polarizability, which occurs in all solids;
α_i = ionic polarizability, present in ionic solids;
α_d = dipolar polarizability, present in such things as H_2O and HCl, containing permanent dipoles;
α_s = space charge, which occurs in non-perfect dielectrics.

Of the four mechanisms, electronic polarisation (α_e) is common to all materials; and is the 'shift' of the electron orbital cloud, with respect to the central, positive nucleus, when under an applied electric field. Ionic polarisation (α_i) is the displacement, or repulsion, of positive and negative ions with respect to one another. Dipolar polarisation (α_d) is an uncommon occurrence in ceramic materials and is normally a permanent state, i.e. – an electric dipole which exists even in the absence of an electric field. An electric dipole is normally found in such molecules as water (H_2O) and hydrogen chloride (HCl). However, dipolar polarisation can be induced by an electric field, causing orientation polarisation of molecules and complex ions. Finally, space charge polarisation (α_s), which occurs in non-perfect dielectric materials, is caused by 'mobile charges', which are present due to either: interface impedances or charge trapping within the material [2]. Moulson and Herbert [3] have created a visual representation of each effect in figure 2.4.

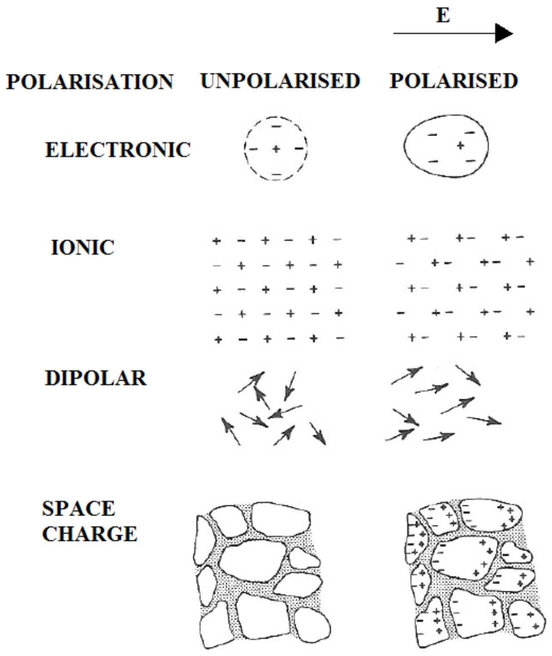

Figure 2. 4 Visual representations of each polarisation mechanism [2], [3].

It is important to note that not all polarisation mechanisms exist at all frequencies, and as the electromagnetic frequency increases, certain mechanisms will cease to apply due to various time-effect dependencies of each mechanism, figure 2.5. All polarisation mechanisms are able to participate at low frequencies ($< \sim 10^3$ Hz). At radio frequencies ($\sim 10^6$ Hz), space charge effects begin to 'relax out' and stop forming in most ionically conducting materials. At microwave frequencies ($\sim 10^{10}$ Hz), dipolar polarisation stops due to there not being enough time for the dipoles to fully re-orientate as the electric field changes direction. At the infra-red, or far infra-red, frequencies ($\sim 10^{13}$ Hz), ionic polarisation begins to lose effect. Finally, only the electronic polarisation mechanism continues to have an effect up to the X-ray frequencies ($\sim 10^{17}$ Hz) [2].

Additionally, space charge and dipolar polarisation effects are strongly temperature dependant mechanisms, whereas the electronic polarisation mechanism is temperature independent [2].

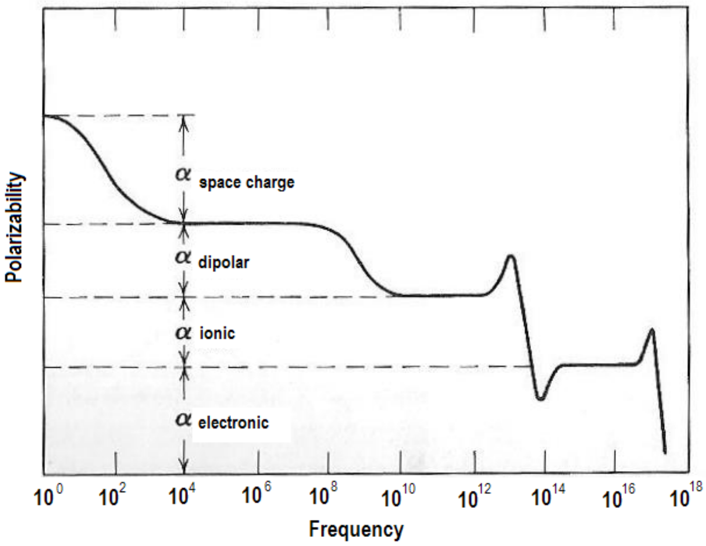

Figure 2. 5 Frequency dependency of different polarisation effects in dielectrics [2].

Dielectric Loss ($\tan\delta$)

Dielectrics are usually used in applications where an electric field polarises the material in a state of constant, often sinusoidal, change with time. As a result, there is a tendency to accrue energy losses because of delays in polarisation change with the actual change in electric field direction. In a 'perfect', or ideal, dielectric material, the current will lead the applied voltage by 90°. However, in real materials, the current will lead the voltage by an amount which is less than 90°; $90° - \delta$ [2]. This angle, δ, is known as the 'loss angle', and is directly comparable to the other, physical loss systems, such as mechanical strain. This loss angle is typically visualised by the current-voltage phase relation of a dielectric system, figure 2.6 [3].

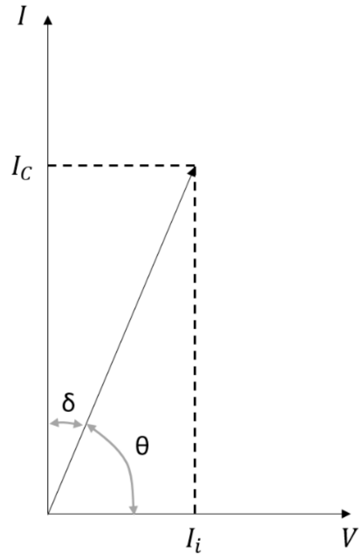

Figure 2. 6 Current-voltage phase relationship of a real dielectric capacitor [3].

θ is the dielectric phase angle and 90°-θ is the loss angle δ, which relates the capacitance of a given frequency to the combined losses from a series of internal resistance and dielectric leakage, such as overcoming the inertia of electric charge movement, required for polarisation. This loss angle is normally expressed as $\tan\delta$ (tangent of delta), or as its inverse, Q, the quality factor. Higher losses translate to a lower value of quality factor for a capacitor.

Additionally, as the operating frequency increases, the relative permittivity, ε_r, decreases because the charges are unable to keep-up with the increased rate of change of the electric field [2], [3] and decreased space available for distinct polarised charges, as seen in figure 2.7 [8].

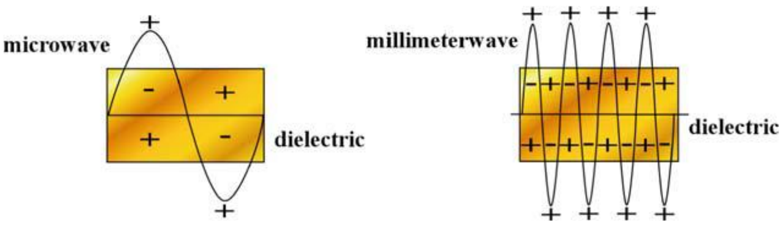

Figure 2. 7 Increased dielectric losses due to increased number of polarisations required over time and volume with increased frequency [8].

Analysis of the behaviour of a device in an alternating current (AC) circuit is usually carried out using complex quantities for the permittivity. As such, the complex relative permittivity is expressed as follows [2]:

$$\varepsilon_r^* = \varepsilon_r' + i\varepsilon_r''$$

(2. 4)

where:
ε_r^* = the complex expression of relative permittivity;
ε_r' = the real part of ε_r;
ε_r'' = the imaginary part of ε_r;
i = the square root of -1, $\left(\sqrt{-1}\right)$.

Where ε_r' and ε_r'' are derived as follows [2]:

$$\varepsilon_r' = \varepsilon_\infty + \frac{\varepsilon_s - \varepsilon_\infty}{1 + \omega^2\tau^2}$$

(2. 5)

$$\varepsilon_r'' = \frac{(\varepsilon_s - \varepsilon_\infty)\omega\tau}{1 + \omega^2\tau^2}$$

(2. 6)

where:
ε_∞ = the dielectric constant corresponding to instantaneous polarization;
ε_s = the static dielectric constant;
ω = $2\pi f$, where f is the frequency in cycles per second (Hz);
τ = a relaxation time and is a measure of the time lag of a system.

Finally, the ratio between the two complex quantities, ε_r' and ε_r'', is known as the dielectric loss [2]:

$$\tan\delta = \frac{\varepsilon_r''}{\varepsilon_r'} \qquad \left(= \frac{(\varepsilon_s - \varepsilon_\infty)\omega\tau}{\varepsilon_s + \varepsilon_\infty\omega^2\tau^2}\right)$$

(2. 7)

This loss factor is the figure of merit to consider when designing an insulating material. For capacitor applications, a device with high permittivity in combination with low losses is greatly sought after.

2.2.2 High-Frequency Microwave Dielectric Ceramics

Over the past two decades there has been an ever increasing need for smaller, more advanced and compact mobile telecommunications and GPS (Global Positioning System) devices, within the microwave frequency range. These frequencies vary depending on use. For example, mobile telephones operate between 900MHz-1.8GHz, GPS is at 12.6GHz and automotive devices operate at 77GHz [9]. Many of these applications require temperature stable ceramics which resonate at precise frequencies within the MW region of the EM spectrum [10]–[12].

The three most important material characteristics for microwave dielectric resonators are the relative permittivity (ε_r – also referred to as the 'dielectric constant'), the quality factor (Qf_0) and the thermal coefficient of resonant frequency (TCF or τ_f) [13]. A high permittivity drives the miniaturisation of the resonator [3], [14], a high quality factor gives high selectivity and a narrow resonance peak [10], [15], [16], and a stable TCF ('near-zero τ_f') ensures that there is no change to the resonant frequency if the temperature were to change during use [17]–[20]. The ideal properties for a material to miniaturise beyond current state of the art are: $\varepsilon_r > 110$, $Qf_0 > 2000$ GHz, and a τ_f tuned through $\pm 10 ppm/℃$ [10], [15], [21].

In the 1960's, TiO_2 ceramics ($\varepsilon_r = 104$, $Qf_0 = 14{,}000$ at 3GHz, $\tau_f = +427$ ppm/°C) were utilised in a limited way as dielectric resonators but these compositions had τ_f which were too high to drive widespread commercial exploitation [22]. As a result, in the 1980's and 1990's, research into potential solutions to this problem shifted to complex oxide compositions many of which have the perovskite structure. Notable early compounds include $BaTi_4O_9$ and $Ba_2Ti_9O_{20}$, which were found to be quite temperature stable with high Qf_0 and ε_r approximately 38 [23].

A significant body of work in the 1980's focused on complex perovskite structured compounds such as $Ba(Mg_{1/3}Ta_{2/3})O_3$ (BMT) and $Ba(Zn_{1/3}Ta_{2/3})O_3$ (BZT). Both of these are complex perovskites due to two different ions of different valence sharing the B-sites of the lattice. BMT has $\varepsilon_r = 24$ and $Qf_0 = 300{,}000$GHz, and BZT $\varepsilon_r = 29$ and $Qf_0 = 150{,}000$GHz [24]. Subsequently, in the 1990's, simple perovskite structures for microwave ceramics were developed based on $SrTiO_3$ and $CaTiO_3$ with $LnAlO_3$ (where Ln = Lanthanide) in solid solution. These materials are reported to have high ε_r values of 39-45 and very good Qf_0 values of $> 40{,}000$GHz [25]. For higher values of ε_r and high Qf_0, barium rare-earth titanate (BRET) compositions have been widely investigated, quoting $70 < \varepsilon_r < 80$ and $5000 < Qf_0 < 12{,}000$GHz [26].

Relative Permittivity/Dielectric Constant (ε_r)

The first important microwave dielectric parameter is the relative permittivity (or dielectric constant), which describes the ability of a material to concentrate electrostatic flux within the spatial volume that the material occupies. It also relates phenomena which occurs at the atomic scale, such as polarisation, with macroscopic properties such as capacitance [27].

In the case of microwave dielectric resonators, the electrostatic force takes the form of an electromagnetic standing wave, which resonates at a specific frequency within the device. This resonant frequency (f_O) is usually a high-frequency microwave, and is related to the permittivity and diameter of the resonator by the following set of equations [10], [3], [14]:

$$f_0 \approx \frac{c}{\lambda_d \sqrt{\varepsilon_r}} \approx \frac{c}{D\sqrt{\varepsilon_r}} \tag{2. 8}$$

where:
c = is the speed of light in a vacuum, and;
λ_d = is the wave-length of the standing wave along the diameter (D) of the resonator.

By manipulating the above formula, it can be seen that as ε_r increases, the diameter of the dielectric device decreases at a rate of $1/\sqrt{\varepsilon_r}$.

$$D \approx \frac{c}{f_0 \sqrt{\varepsilon_r}} \tag{2. 9}$$

Increasing ε_r is typically done by the substitution of the cations, either through the substitution of a cation with greater ionic polarizability or with one with a smaller ionic radius (more detail in section 2.4.3-2.4.4), or through a mixture of the two [3].

Thermal Coefficient of Resonant Frequency (TCF or τ_f)

The thermal coefficient of resonant frequency is a material property which represents the thermal stability of a resonator. This stability takes the form of the ‘drift’ of f_0 with changing temperature. If f_0 were to change with temperature, then it is not useful as an electric device which can operate within a range of changing temperatures. Therefore, it is important for the τ_f of a material to be as near to zero as possible [28].

τ_f itself is related to both the thermal coefficient of permittivity (τ_ε) and the thermal (or linear) expansion coefficient (α_L) of the material, by the following relationship [29]:

$$\tau_f = -\left(\frac{\tau_\varepsilon}{2} + \alpha_L\right)$$

(2. 10)

Which is a variation to the equation expressed by Takahashi *et al.* (1991) [30].

The τ_f is obtained experimentally, through recording the shift in the resonant frequency with the change of temperature. The term 'tuning' is used for the act of changing this parameter. A simplistic view of tuning the τ_f to zero, detailed by Wise [31], is to mix together both a positive and a negative τ_f material.

One good example of this it the $CaO:SrO:Li_2O:Sm_2O_3:Nd_2O_3:TiO_2$ system [32], where the Li_2O-Ln_2O_3-TiO_2 perovskite structure (large positive τ_f) was mixed together with CaO-TiO_2 system (large negative τ_f). Excellent microwave properties were recorded: $\varepsilon_r = 123$, $Qf_0 = 4150\ GHz$ and $\tau_f = 10.8\ ppm/℃$.

Influencing Factors

One factor influencing the τ_f is the relative permittivity (ε_r) which is proportional τ_f for a wide range of materials such that a large ε_r gives rise to large positive τ_f [33], [17], [34]. In 1969, Harrop [34] looked at the Classius-Mosotti (CM) equation, which relates ε with polarizability, α_j, and differentiated the equation to justify the following:

$$\tau_c = -\alpha_L \varepsilon_r$$

(2. 11)

which becomes:

$$\tau_\varepsilon \propto -\alpha \varepsilon_r$$

(2. 12)

Comparing this with equation 2.10, if there are small values of α_L, or large values of τ_ε, then τ_f is controlled by ε_r. In microwave dielectrics, ionic polarizability dominates the relative permittivity, and therefore τ_f [3].

In 1993 and 1994, it was shown that the onset of phase transitions, specifically octahedral tilting are a major controlling factor of τ_f [19], [35] in perovskites and related compounds. The mechanisms of octahedral tilting and its relation to *tolerance factor* are dealt with in greater detail in sections 2.4.2 and 2.4.3 but a brief summary of its influence on τ_f is discussed here. The tolerance factor, t, describes the stability of a perovskite crystal structure, where $t = 1$ represents a stable crystal in which the constituent ions fit together perfectly. However, compositions with t < 1 undergo octahedral tilt transitions above ambient temperature and, as a result, the magnitude and even the sign of τ_f can change [19].

Reaney *et al* [19], identified three distinct regimes of τ_ε with t (figure 2.8). The first region ($1.06 > t > 0.985$), τ_ε decreases from near-zero to a minimum of -300ppm/K, as a transition approaches, without exceeding, room temperature. In the second region ($0.985 > t > 0.965$), τ_ε rises steeply with decreased tolerance factor and is associated with the onset of a tilt transition above room temperature, where the octahedra rotate in anti-phase. In the third regime ($0.965 > t$), τ_ε increases further with decreased tolerance factor due to a second phase transition above room temperature, involving both in- and anti-phase tilting. The tolerance factor, therefore, not only controls the onset of a phase transition, but also the amplitude, or severity, of the rotations of the octahedra at room temperature [22]. For the purposes of this contribution, the expected tolerance factor of the material being investigated is expected to lie on the boundary between the second and third regimes.

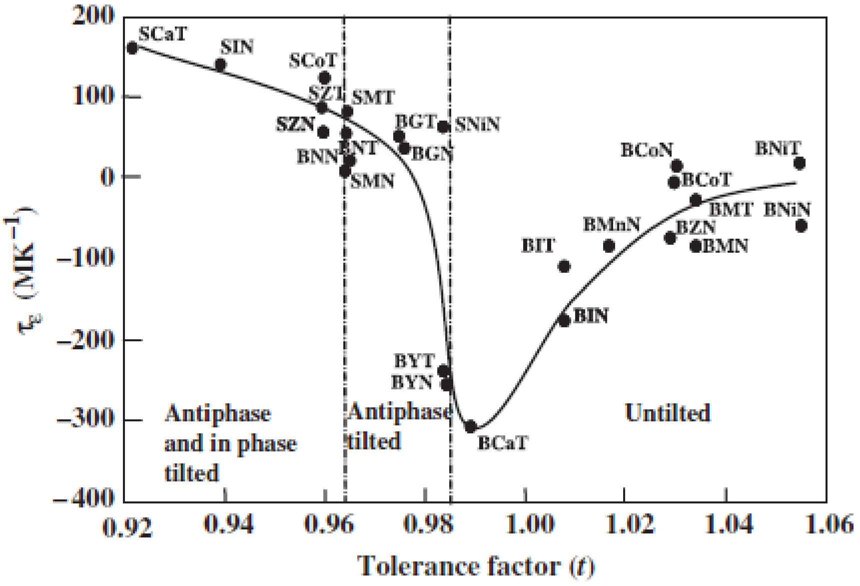

Figure 2. 8 The three regimes of tilting, and its effect on τ_ε, with changes in tolerance factor at room temperature of A(B'B'')O_3 1:1 and 1:2 complex ceramics (A= Sr and Ba, B'= In, Ca, Mn, Co, Ni, Zn, Mg, Nd, Gd, and B''= Ta and Nb) [19].

However, for some ceramic systems, such as the 1:2 ordered compounds in Ba-based complex perovskites, neither the relative permittivity nor the tolerance factor correlate well with τ_f [36]. In this case, for a narrow group of similar compositions, the degree of under-bonding for the B-site M^{2+} ions also plays a part in the value and sign of τ_f.

Quality Factor (Q)

The third important characteristic of a microwave dielectric ceramic is the quality factor (Q), which is normally written as a 'figure of merit' [27], of the form Qf_0, in relation to the performance of a resonator and it is approximately the inverse of dielectric loss ($\frac{1}{\tan\delta}$) [37]. Dielectric loss ($\tan\delta$) describes the ratio of between energy stored and energy dissipated within a material; the higher the dissipation, the lower the $\tan\delta$. However, simply stating that Q is the inverse of $\tan\delta$ is unhelpful if there is no appreciation for how that relates to the 'selectivity' of a resonator to a given frequency in the MW range.

More pertinently, Q is obtained from the shape of the resonance peak (f_0) and dividing that frequency by the width of the peak measured at 3 decibels (dB) below the peak maximum amplitude, figure 2.9. If the Q value is high, then f_0 is narrow, which means that it has high selectivity [10], [16]. High selectivity means that the operating frequency of a device is not wide enough to spill into other frequency channels and, therefore, means that a device with a high Q will not pick-up 'cross- talk'. By having a narrow resonant peak, it is possible to increase the density of channels (specific frequencies through which different devices communicate through) in a given band of frequencies [3].

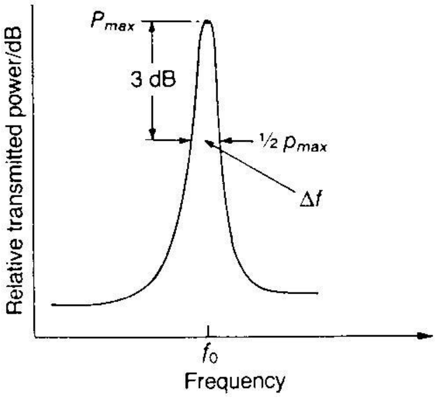

Figure 2. 9 The resonance peak on a frequency response graph of a microwave dielectric material, with peak width indicated at 3dB below peak maximum [10].

For a given material, the values of $Q \times f_0$ is considered constant and Qf_0 is a 'figure of merit' used to compare MW dielectric materials [3], [37].

The dielectric losses occur as a result of many different phenomena. At an intrinsic level, the microwaves interact with phonon modes of within the dielectric media, resulting in loss of energy. These losses typically increase with increasing frequency, figure 2.7 [8].

Dielectric losses can also depend upon whether the material in question is ferroelectric or paraelectric. Since ferroelectric materials exhibit spontaneous polarisation, they therefore have large dielectric losses and ε_r due to the exaggerated movement of cations, which relates to the paraelectric – ferroelectric transition. Paraelectric materials with centro-symmetric crystal structures are more suitable dielectric materials because they are dominated by ionic polarisation and exhibit lower losses [8].

Influencing Factors of the Quality Factor

Of the three MW parameters, Q is the least understood, however it is known that Qf_0 is composition, processing and structure dependant. Understanding what influences Q is important because its optimisation will maximise commercial exploitation of the available bandwidths in a given frequency range.

Overall, there are two types of losses: intrinsic and extrinsic. Intrinsic losses are dependent on the crystal structure and are controlled by anharmonicity and the dampening of the phonon modes of the fundamental lattice [38], which is possible to estimate with infra-red spectroscopy [39], and tend to be relatively lower in defect-free single crystals [38]–[40].

However, it is normally the extrinsic losses which dominate the value of Q, and optimisation thereof usually means attempting to minimise as many extrinsic losses as possible [38]. The extrinsic losses can be separated into three different categories: order/disorder behaviour [10], [41]–[44], processing effects [28], [45] and solid solution effects; all of which include crystal imperfections, porosity, grain size and cracks [40].

Order/Disorder Behaviour Effects

Increased long-range ordering has been shown to increase Q, such as the $BaZn_{1/3}Ta_{2/3}O_3$ (BZT) system, which showed an increase from Q=6500 to Q=14000, at 12GHz [41], [46], [47]. It was later shown that the sintering and crystallisation of the $Ba(Zn_{1/3}Ta_{2/3})O_3$ system was accelerated with the addition of $BaZrO_3$, which also improved the quality factor [48]. Additionally, within the BZT system, inducing a 1:2 trigonal, $P3m1$, ordering, by annealing the ceramic, can increase Q significantly [49]–[52].

Process Effects on Q

Raw (reagent) impurities of > 0.2wt% can reduce the value of Q by, for example, a factor of 2 for $BaTi_4O_9$ and $Ba_2Ti_9O_{20}$ ceramics [45]. Contamination from milling media and binders could also reduce Q by 15-20% [10]. Density and coring effects can also influence Q; using TiO_2 as an example, TiO_2 appears to have a maximum Q at approximately 5% porosity, which reduces upon increasing density [28]. The increase in density means the admittance of oxygen back into the grains becomes more difficult, and thus re-oxidation of Ti^{3+} to Ti^{4+} becomes slower. This results in the retention of oxygen vacancies and occasionally the onset of electronic conduction, which can further deteriorate the value of Q. The presence of oxygen vacancies causes an increase in the anharmonicity of vibrations and the dampening of phonon modes. Avoiding or eliminating coring, through acceptor doping [53], can increase Qf_0, for example from $Qf_0 < 6000$ GHz to $Qf_0 > 47000$ GHz for TiO_2 [28].

Solid Solution Effects on Q

Some materials, such as (1-x)$CaTiO_3$-(x)$Sr(Mg_{1/3}Nb_{2/3})TiO_3$ (CT-SMN) [54], (1-x)$CaTiO_3$-(x)$Sr(Zn_{1/3}Nb_{2/3})TiO_3$ (CT-SZN) [54] and (1-x)$CaTiO_3$-(x)$La(Mg_{0.5}Ti_{0.5})O_3$ (CT-LMT) [55], have low values of Q for unclear reasons, since there are no known reduction reactions or unwanted secondary phases. A possible explanation for the low Q values takes a different approach to the average tolerance factor (t) used to explain variations in τ_f in perovskites. Instead, a concept of a spread of tolerance factors (Δt) may be utilised, which relates to the spread of the ionic radii on the A- and B-sites within the perovskite structures [19], [56]. Δt is the difference in tolerance factors between the largest and smallest possible tolerance factor values for all of the unit-cell combinations within a solid solution.

A material containing a small Δt tends to have a larger Q value (figure 2.10 [10]). As such, a large range of bond lengths (i.e.: a large Δt) on the A- and B-sites results in greater anharmonicity and greater phonon mode dampening. Therefore, a large Δt increases the driving force for short-range ordering, resulting in nano-clustering of different bond-lengths, which perpetuates a cycle of further increases in anharmonicity and phonon-mode dampening and further deteriorations in Q [56], [57].

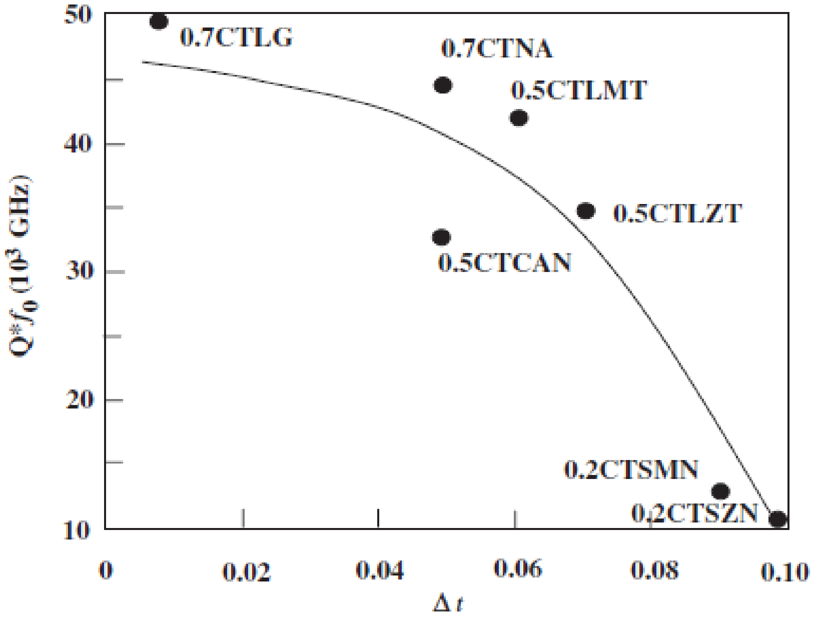

Figure 2. 10 Qf_0 versus the spread of tolerance factor, Δt, for a range of different CaTiO3-based perovskites [10].

To optimise Q, it is wise to minimize Δt for solid solutions [57] thus avoiding compositions where short-range ordering dominates, induce long-range ordering, where possible, for e.g. complex perovskites, use pure raw materials and attempt to minimise exposure to milling and aggressive processing.

2.3 Microwave Dielectric Applications

Dielectric materials have become one of the dominant core materials in the design of antenna for portable, wireless devices, such as handheld GPS (global positioning system) devices, mobile telephones and ‘smartphones’. The rise in the use of dielectrically loaded antennas may in part be attributed to a phenomenon known as ‘body loading’ [58], which dielectrically stabilised antennas can strongly reduce by concentrating the MW radiation within a high ε_r (loaded) substrate.

High radiation efficiency of a device is achieved when the antenna is operated at, or close to, electrical resonance. This maximises the electromagnetic energy held in the surrounding space in and around the antenna. This space is commonly referred to as the ‘near-field’, or sometimes the ‘reactance field’. The oscillation of the electric and the magnetic field components within the near-field is responsible for the transportation of a signal, and therefore information, to the ‘far-field’. The far-field is the region where the operation of an antenna is described purely by ‘travelling waves’ [59].

The near-field contains the highest density of electromagnetic field lines, much more so than the far-field. Therefore, any physical presence capable of absorbing this electromagnetic energy, at the frequencies used, such as the human body of the user, is usually the most performance impairing factor in the chain of information transfer [60], [61].

2.3.1 Dielectric Resonators and Filters

Within a mobile cellular network, there are base stations located and spread throughout the network, and cover, on average, a 35km or 18 km diameter at frequencies of 900 and 1800 MHz respectively. Housed within the base stations are microwave resonators used to carry signals at specific frequencies, while removing or filtering-out unwanted signals and ‘side-bands’, which could interfere with the quality of information communications.

High selectivity, a narrow bandwidth, is normally a very desirable parameter for a resonator or filter to possess. Where this is important, then low-loss, temperature-stable ceramics are preferred over cheaper, metal cavities [3].

The original design for a single-mode, microwave resonator was proposed in the late 1930’s [62], which was a cylindrical ceramic puck. These pucks were designed to hold, within the volume of the ceramic body, a standing electromagnetic wave of a specific resonant frequency. This resonant frequency allows the puck, or the device, to act as a filter or as a transmitting antenna. Figure 2.11 shows the interaction of the electric and magnetic field components of such a standing wave within a resonating puck.

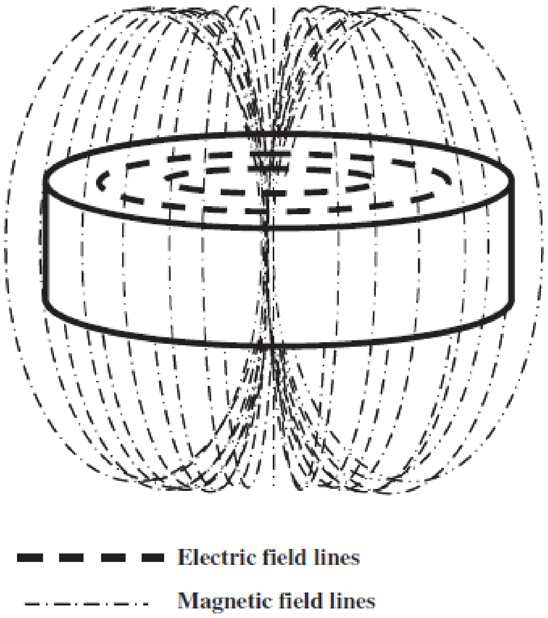

Figure 2. 11 The interaction of the electric and magnetic field components produced by a resonant electromagnetic standing wave [10]**, after Richtmyer, 1939 [62].**

These ceramic puck resonators are conceptually simple, however precisely controlling their physical dimensions and phase assemblage, during processing and sintering, is difficult. There can be any number of differences produced between batches, and even within the same batch, and these differences will have consequences regarding precise resonant frequencies, temperature stabilities and other microwave properties, as discussed in detail in section 2.2.2.

Resonators do have the potential to be multimodal, i.e.: have the ability to resonate multiple standing waves of different frequencies within their bodies, by utilising unusual geometries. This would allow a single device, for example, to be able to be selective over a wider set of frequencies.

In the infancy of mobile technology, ‘invar air cavities’ were used as resonators for both the base stations and for hand-sets. These were normally large and bulky, and was the main constraint in the design of hand-sets. In the 1980’s, invar air cavities were replaced by the first generations of *ceramic* resonators based on the $(Mg,Ca)TiO_3$, $ZrTiO_4$ and $BaTi_4O_9$ systems [43], [45], [63], [64].

In the 1990's, the ceramic technologies used for these two applications diverged. Base stations required much higher Q values, $40{,}000 < Qf_0 < 250{,}000$, and permittivities of $25 < \varepsilon_r < 50$, since the size of the base stations were not of paramount importance. Whereas the hand-set were dominated by a need for miniaturisation, thus a need for high ε_r was generated. The first wave of devices for the hand-held market was the development of the Negative-Positive Zero (NP0) chipsets, with $70 < \varepsilon_r < 130$, where Q was dominated by the metallisation on the antenna, rather than the ceramic. This was then succeeded by 'surface acoustic wave' and 'bulk acoustic wave' technologies. Reaney and Iddles [10], represented this movement of technologies into a roadmap, figure 2.12.

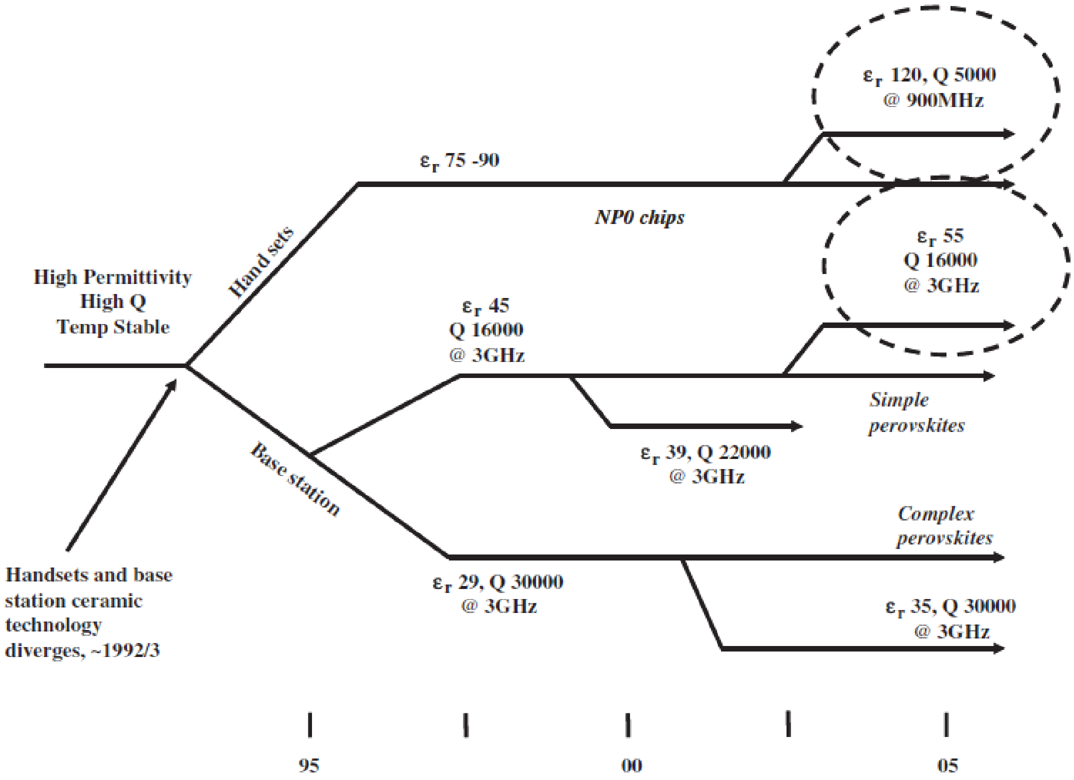

Figure 2. 12 A roadmap for the development of ceramic resonators during the 1990's and 2000's, where the ringed regions are specific properties of different NP0 chips [10].

2.3.2 Dielectrically Loaded Antennas

Practically, the design of an antenna for portable devices is strongly dictated by the aesthetics of the devices for the consumers. As such, there are two basic options for the designers:

1: Design the antenna such that it occupies the entire 'envelope volume' of the device using it;

2: Design the antenna such that is occupies a smaller portion of the device, where it will not be subject to a large amount of body loading.

Option 1 allows the device to achieve as much antenna gain and efficiency as possible, in order to try to overcome the accepted performance loss of body loading. This is mainly used in the mobile telephone market as this is relatively cheap and losses in efficiency can be absorbed by a dense network infrastructure instead [65]. Option 2 uses a dielectric material to load and constrain the electric field component of the near-field within the material itself. This produces antenna characteristic which are more predictable in the presence of body loading [65]. This is especially important with respect to ‘circularly polarised antennas’. Here, the near-field has to accommodate a rotating dipole in the same rotational direction as the electromagnetic wave. These rotating fields are especially vulnerable to disruption by any cluttering objects in the near-field [66].

As devices are becoming smaller, due to a consumer driven market for smaller devices, and global demand is calling for less energy intensive, more energy efficient solutions, it is becoming harder to justify design option 1 as a sustainable design. Any design using more energy than is necessary to actively overcome body loading will eventually be avoided, especially, for example, if the consumer wants longer-lasting batteries in their devices. Dielectric loading allow for an antenna which is both electrically and physically smaller, with more ‘predictable load impedance’ [15] and more frequency stable.

For dielectrically loaded antennas, there have traditionally been 2 main antenna designs which have been implemented for circularly polarised antennas: the microstrip patch antenna and the dielectrically loaded multifilar-helix antenna.

Microstrip Patch Antenna

The microstrip patch antenna is a planar antenna, printed onto a dielectric slab, with an extensive ground plate underneath. The ‘patch’ itself can have many different designs, depending on the performance and characteristic requirements of the device. Simply, it can be a square conductor where the lengths and breadths are simply equal to $\frac{\lambda_g}{2}$, where λ_g is the guide wavelength, which is set by the physical dimensions and relative permittivity of the dielectric slab [15], [67], figure 2.13.

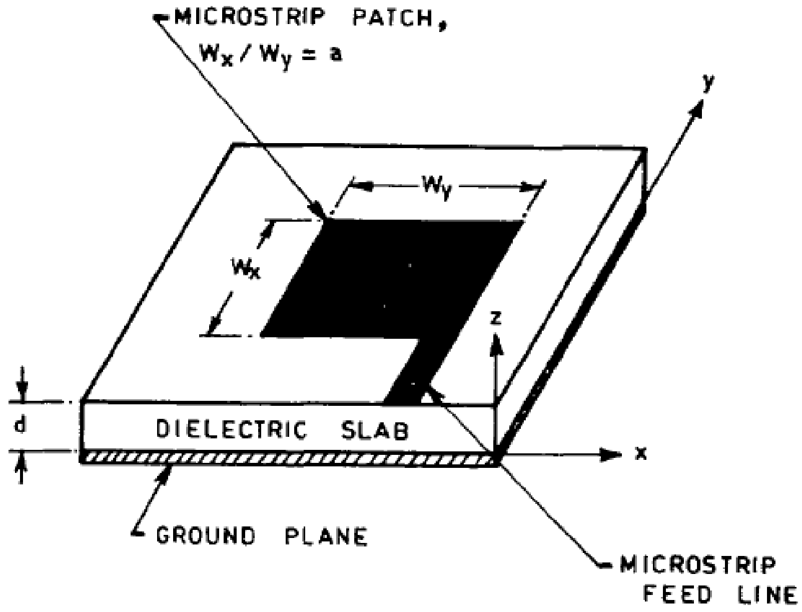

Figure 2. 13 A corner-fed, nearly square microstrip patch antenna [67].

On a square conductor profile, a circular polarisation mode can be produced by combining two linear modes, offset at 90°, of the same magnitude [67] (figure 2.14). The size of the metal patch is related to:

$$\frac{\lambda_g}{2} = \frac{\lambda}{2} \times \frac{1}{\sqrt{\varepsilon_{eff}}} \tag{2. 13}$$

where:

λ_g = the guide wavelength;
λ = the electromagnetic wavelength in free space;
ε_{eff} = the effective relative permittivity of the waveguide.

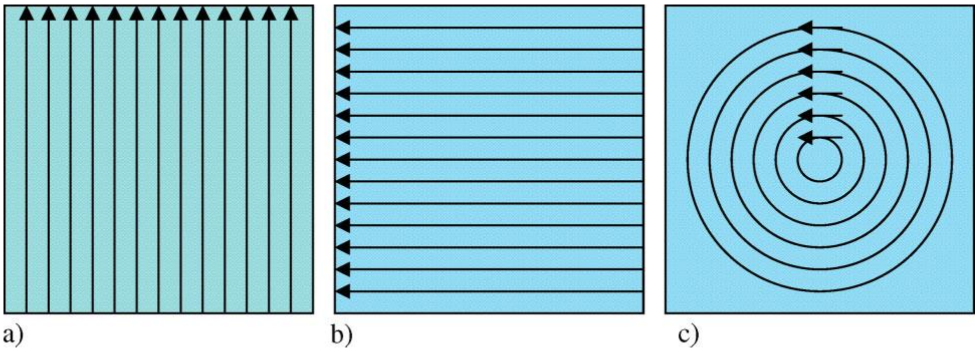

Figure 2. 14 Current on a microstrip patch antenna producing the phasing necessary for circular polarisation, where a) is a linear mode on the y-axis, b) is a linear mode on the x-axis and c) is the hybrid circular polarisation [15].

Commonly, it is possible to estimate the dimensions of the microstrip patch antenna, if the relative permittivity and thickness of dielectric substrate is known, as well as the desired resonant frequency, by using the following relationships [68]:

$$W = \frac{c}{2f_0\sqrt{\frac{(\varepsilon_r + 1)}{2}}}, \qquad L = L_{eff} - 2\Delta L$$

(2. 14)

Where

$$\varepsilon_{eff} = \frac{\varepsilon_r + 1}{2} + \frac{\varepsilon_r - 1}{2}\left[1 + 12\frac{h}{W}\right]^{-\frac{1}{2}}$$

(2. 15)

$$L_{eff} = \frac{c}{2f_0\sqrt{\varepsilon_{ff}}}$$

(2. 16)

$$\Delta L = 0.412h\frac{\left(\varepsilon_{ff} + 0.3\right)\left(\frac{W}{h} + 0.264\right)}{\left(\varepsilon_{eff} - 0.258\right)\left(\frac{W}{h} + 0.8\right)}$$

(2. 17)

where:
W = the width of the patch;
L = the length of the patch;
h = the height, or thickness, of the dielectric substrate;
L_{eff} = the effective length of the patch;
ΔL = the length extension;
f_0 = the resonant frequency;
ε_r = the relative permittivity of the dielectric substrate;
ε_{eff} = the effective permittivity;
c = the speed of the light in free space.

Length extensions are calculated and implemented into the design to constrain the extent of fringing fields, which is an ‘overspill’ effect of the electric field which can cause reduced efficiency and increased disturbances [15].

Multifilar-Helix antenna

In a similar vein to the microstrip patch antenna, there are many different designs of the multifilar-helix antenna, where the variation is usually in the number of 'filars' incorporated in the design. The most common design, however, is comprised of 2 quadrature phased bifilar helical loops, placed at right angles to one another [69], [70], otherwise known as a dielectrically-loaded 'quadrifilar-helix' antenna (DQHA). The loops, or filars, themselves are metal and printed onto the surface of a cylindrical dielectric substrate material. Each loop provides a full a full guide wavelength path, which are made of two half-turn helix sections, interconnected by currents flowing along the rim of a 'sleeve balun' at the base of the antenna (figure 2.15) [15].

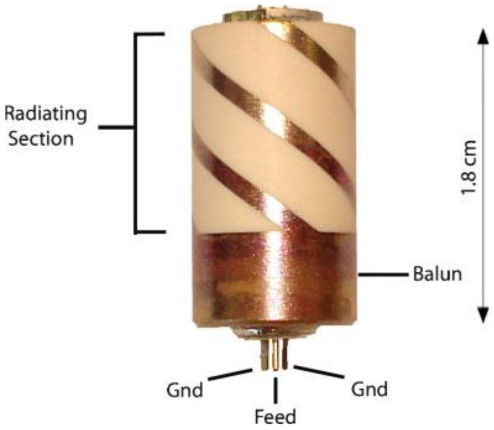

Figure 2. 15 A common quadrifilar-helix antenna design [15].

The antenna achieves quadrature phasing from the two bifilar loops by setting them at slightly offset resonant frequencies. This is done by setting one of the bifilar loops so that it is slightly longer than the resonant wavelength, producing an input impedance with a phase angle of 0°+45° and 180°+45°, and setting the second bifilar loop so that it is slightly shorter, producing an input impedance phase angle of 0°-45° and 180°-45°. This results in a 90° shift in phase between the currents in the two bifilar-helix loops, allowing for circular polarisation (figure 2.16) [71]. The sleeve balun in the base section of the antenna projects a balanced signal feed to the 'back-fire' tip of the antenna. This balanced feed is employed at the top, along with the differentially-phased helix loops, to organise orthogonal current phasing around the rim of the antenna [15], [71].

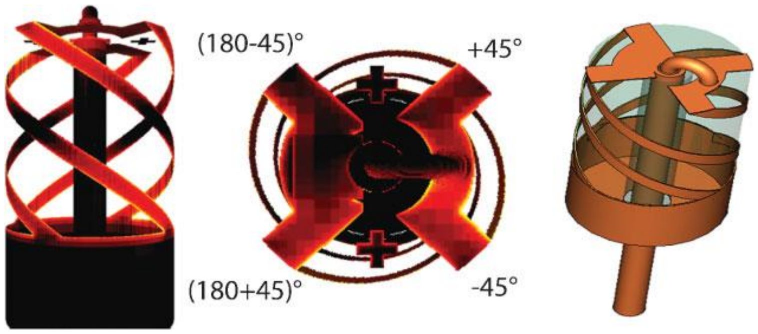

Figure 2. 16 The currents and phasing of dielectrically-loaded quadrifilar-helix antenna, producing circular polarisation [15].

The size of the antenna, when a dielectric is used in its core, is significantly smaller than its free-space, air-loaded counterpart, since the relative permittivity of the dielectric is much larger than that of the air. It has also been shown that the DQHA is not significantly affected by body loading and work in close proximity to other antennas without significant interaction, because the electromagnetic fields are contained with the dielectric core [71].

In 2008, Mirsaneh *et al* [15], concluded that the relationships between material properties, antenna size and performance was more favourable for the DQHA, over the microstrip patch antenna. The electrical length of the helix metallisation, the conductors, is basically $\frac{\gamma}{2}$ at the guide wavelength. This $\frac{\gamma}{2}$ dimension is curved around a half-turn helix, instead of planar for the microstrip patch antenna. It follows that the DQHA will occupy less space than the microstrip patch antenna, as it can be of lower thickness and diameter. Table 2.2 from a survey by Mirsaneh *et al* [15] highlights that, where the substrate relative permittivity is the approximate, the DHQA is smaller.

Table 2. 2 A list of thickness dimensions of DQHA and microstrip patch antennas, with their corresponding relative permittivities required [15].

Thickness Dimension (mm)	Microstrip Patch Antenna (metal patch length or breadth dimension plus un-metallised border)	DHQA (diameter of dielectric cylinder)
15	$\varepsilon_r = 53$	
14		$\varepsilon_r = 21$
12	$\varepsilon_r = 82$	
10		$\varepsilon_r = 36$
7.5		$\varepsilon_r = 80$
6.5		$\varepsilon_r = 88$

2.4 Perovskite Crystal Structure

The perovskite crystal structure has grown to become of great technological importance in the world of ceramics, especially with regards to physical properties such as: piezoelectricity, ferroelectricity, pyroelectricity, dielectric susceptibility, and linear and non-linear electro-optic effects. The actual properties and effects achieved varies from one material to another, without much apparent change to the crystal structure itself. Changes are particularly large when the ceramic is exposed to changes in external conditions, such as temperature or pressure. One of the most significant examples of this was the demonstration by Wul and Goldman, in 1945, showing a huge rise in the dielectric constant of $BaTiO_3$, by as much as 10^4 when heated [72].

The mineral with the crystal structure itself was first discovered in 1839 by Gustav Rose and named after the Russian mineralogist Lev Perovski. The idealised perovskite crystal structure is ${}^{XII}A^{2+}{}^{VI}B^{4+}X_3^{2-}$, or simply ABX_3, where A and B are cations and X is the anion, usually oxygen. Typical examples of materials with a perovskite crystal structure include $BaTiO_3$, $SrTiO_3$ and $CaTiO_3$. The overall structure is a framework of corner-shared octahedra, with the anions at the corners, B cations at the centres of the octahedra and A cations at the centre of the space between the octahedra, as demonstrated by figure 2.17 [73].

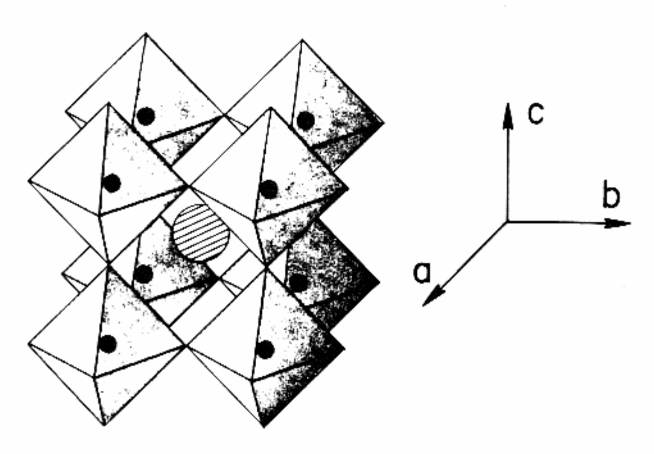

Figure 2. 17 The typical perovskite structure, as visualised by Burns and Glazer, 1978 [73].

From the indicated a, b and c axes in figure 2.17, above, using a B cation as a frame of origin, the A-site cations are found at $\left(\frac{1}{2},\frac{1}{2},\frac{1}{2}\right)$, the B-site cation is found at (0,0,0) and the X-site anions are found at $\left(\frac{1}{2},0,0\right)$, $\left(0,\frac{1}{2},0\right)$ and $\left(0,0,\frac{1}{2}\right)$, where $a = b = c$ and $\alpha = \beta = \gamma = 90°$. A perovskite can also be described using the A-site cation as the frame of origin; as such, the A-site cations occupy the (0,0,0) cube corner positions, the B-site cations the $\left(\frac{1}{2},\frac{1}{2},\frac{1}{2}\right)$ body-centre positions and the X-site anions occupy the face-centre positions $\left(\frac{1}{2},\frac{1}{2},0\right)$ [74].

The A- and B-type cations are normally very different in size, where the A-type cation is the larger of the two. The ratio between the two cation sizes is directly related to the stability of the perovskite crystal structure, and this stability has quite a strict range which is described by an idea known as the tolerance factor (t) (which is covered in detail in section 2.3.2).

2.4.1 Space Groups of Perovskites

The ideal, basic, perovskite structure occupies the space group number 221, $Pm\bar{3}m(O_h^1)$ [73]. The diagram from the International Tables for Crystallography [75] for this space group can be seen in figure 2.18 [76]. There are centres of inversion at the cations and mirror planes perpendicular to $\langle 100 \rangle$, i.e. – perpendicular to the b-axis and passing through (0,0,0) and $\left(0, \frac{1}{2}, 0\right)$. There are further mirror planes perpendicular to $\langle 110 \rangle$, passing through the face diagonals, and there are 3-fold axes along $\langle 111 \rangle$, perpendicular to the triangle faces of the octahedra and 2-fold axes parallel to the face diagonals of the cubic unit cell. All atoms lie on certain special positions of this space group, where the A cation is on 1 b site, the B cation is on 1 a site and the X anion is on 3 d sites [73].

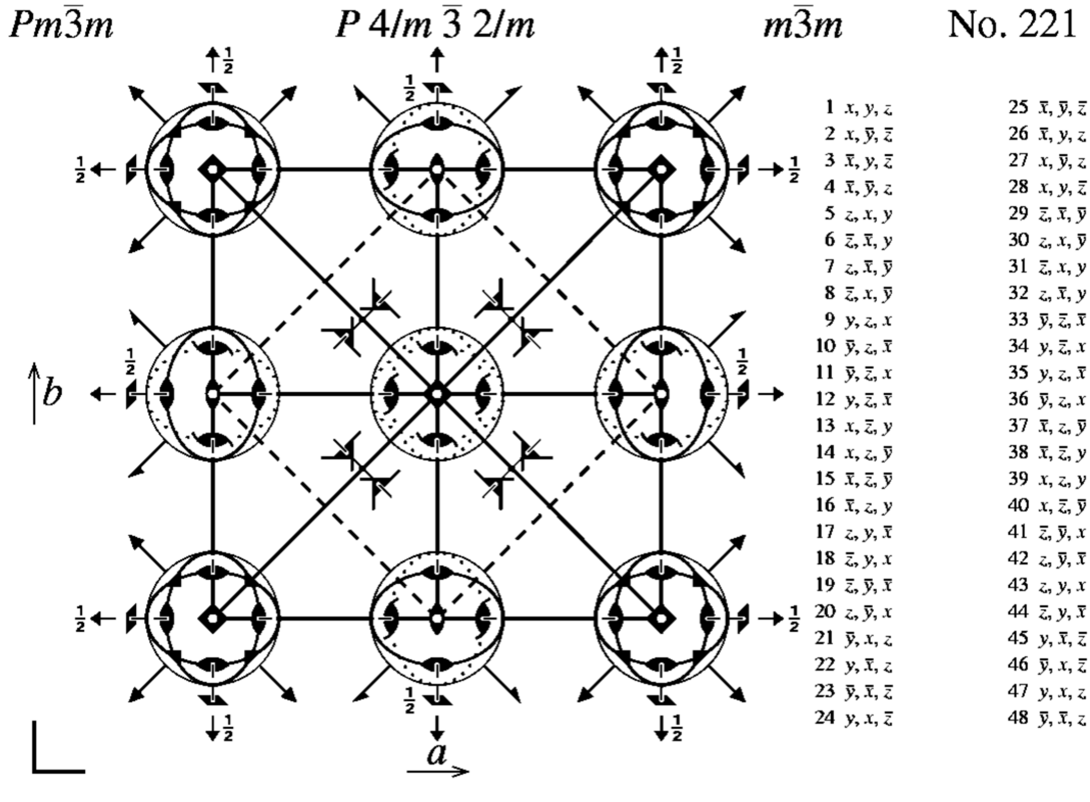

1	x, y, z	25	$\bar{x}, \bar{y}, \bar{z}$
2	$x, \bar{y}, \bar{z}$	26	$\bar{x}, y, z$
3	$\bar{x}, y, \bar{z}$	27	$x, \bar{y}, z$
4	$\bar{x}, \bar{y}, z$	28	$x, y, \bar{z}$
5	z, x, y	29	$\bar{z}, \bar{x}, \bar{y}$
6	$\bar{z}, \bar{x}, y$	30	$z, x, \bar{y}$
7	$z, \bar{x}, \bar{y}$	31	$\bar{z}, x, y$
8	$\bar{z}, x, \bar{y}$	32	$z, \bar{x}, y$
9	y, z, x	33	$\bar{y}, \bar{z}, \bar{x}$
10	$\bar{y}, z, \bar{x}$	34	$y, \bar{z}, x$
11	$\bar{y}, \bar{z}, x$	35	$y, z, \bar{x}$
12	$y, \bar{z}, \bar{x}$	36	$\bar{y}, z, x$
13	$x, \bar{z}, y$	37	$\bar{x}, z, \bar{y}$
14	$x, z, \bar{y}$	38	$\bar{x}, \bar{z}, y$
15	$\bar{x}, \bar{z}, \bar{y}$	39	x, z, y
16	$\bar{x}, z, y$	40	$x, \bar{z}, \bar{y}$
17	$z, y, \bar{x}$	41	$\bar{z}, \bar{y}, x$
18	$\bar{z}, y, x$	42	$z, \bar{y}, \bar{x}$
19	$\bar{z}, \bar{y}, \bar{x}$	43	z, y, x
20	$z, \bar{y}, x$	44	$\bar{z}, y, \bar{x}$
21	$\bar{y}, x, z$	45	$y, \bar{x}, \bar{z}$
22	$y, \bar{x}, z$	46	$\bar{y}, x, \bar{z}$
23	$\bar{y}, \bar{x}, \bar{z}$	47	y, x, z
24	$y, x, \bar{z}$	48	$\bar{y}, \bar{x}, z$

Figure 2. 18 Space group $Pm\bar{3}m$, from the International Tables for Crystallography [75], [76].

Although the basic arrangement of the ions in the perovskite cell is very simple, it is possible to have many different variations, due to phase transitions between different structures. These variations divide into three different types: 1 – where the cations are displaced from their centres, which is either parallel displacement or antiparallel displacement; 2 – where the anion octahedra tilt about 1, 2 or 3 axes; 3 – where effects 1 and 2 both occur.

2.4.2 Tolerance Factor

A comparison was made in 1969, by Harrop [34], between the ε_r and τ_c values of materials. The conclusion of this study came in the form of a relationship, dictating that materials with low τ_c also have low ε_r:

$$\tau_c = -\alpha_L \varepsilon_r$$

(2. 18)

where:
τ_c = the temperature coefficient of capacitance, and;
α_L = the thermal expansion coefficient.

Harrop's initial comparison did not take into account how the structural changes would affect τ_c, for example tilt transitions in the perovskite structures. Tilt transitions refers to the rotations of the corner-shared, oxygen-based octahedra about the major axis of the perovskite structure, and can either be in-phase or anti-phase [35], [77]–[79]. Figure 2.19, after Megaw [78], is an illustration of octahedral tilting.

In 1994, Reaney and co-workers speculated that the tolerance factor (t) controls the onset temperature of octahedral tilting and, therefore, magnitude and sign of τ_c [19]. However, the first description of the tolerance factor was made in 1926 by a Viktor M. Goldschmidt [80], and was used to describe the structural stability of perovskites in terms of its distortions. t is given by Megaw [78] as:

$$t = \frac{R_A + R_O}{\sqrt{2}(R_B + R_O)}$$

(2. 19)

where:
R_A = the ionic radius of the A-site element;
R_B = the ionic radius of the B-site element;
R_O = the ionic radius of oxygen, within an ABO_3 perovskite structure.

The above equation is Megaw's [78] interpretation of Goldschmidt's descriptions [80].

A perovskite forms when the tolerance factor (t) is close to 1. If the A-site cation reduces in size with respect to the B-site cation, then a reduction in the tolerance factor occurs. If this reduction reaches a certain point, the A-site cation becomes too small to occupy the volume of its interstice, and as a result the octahedra rotate in order to reduce the size of the cubo-octahedral site to accommodate this [19], [31], [77]–[79]. When tilting happens, it effectively reduces the volume of the interstices and improves structural stability. The amount of tilting varies depending on temperature and the value of t. It is this mechanism of tilting which reduces the symmetry with lowering of tolerance factor [78].

The idealised perovskite structure is normally represented by $SrTiO_3$, at room temperature. However, the structure at room temperature for different materials is slightly modified, due to a difference in their tolerance factors, by either cation displacement (e.g. $BaTiO_3$) or by tilting of the octahedra (e.g. $CaTiO_3$), or by a combination of both effects (e.g. $NaNbO_3$) [77].

Cation displacements are directly linked with ferroelectricity and anti-ferroelectricity, are relatively simple to deal with of the two modifications, and do not directly affect the lattice parameters aside from a relatively small octahedral distortion. Whereas octahedral tilting usually has a much greater effect on the lattice parameters of the crystal and is more difficult to describe.

2.4.3 Octahedral Tilting

The ideal perovskite, with no tilting or distortions, is usually the highest symmetry and temperature phase of any perovskite material, traditionally referred to as the ‘*aristotype*’. When displacements or tilting occurs, different types of structures, called ‘*hetotypes*’ are produced. These hetotypes are always of a lower order of symmetry than the aristotype.

In 1972 and 1975, Glazer made significant contributions into forming a notation for describing and classifying octahedral tilt systems, and how they affect the crystal symmetries; a notation which is widely used today [77], [79]. This contribution was strongly based on earlier work by Helen D. Megaw in the late 1960’s and early 1970’s [78]. Glazer set out to understand the origin of behavioural differences or changes to physical properties near phase transitions by achieving the best possible description of what is happening to the *atoms* within the crystal structure. Figure 2.19 illustrates octahedral tilting in perovskites.

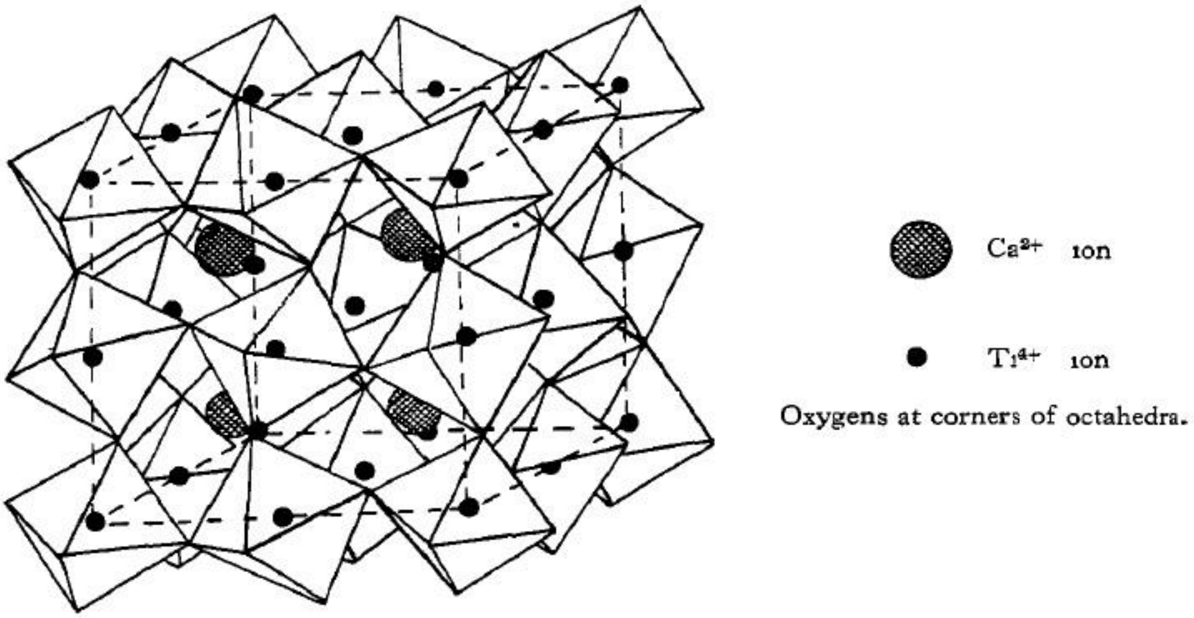

Figure 2. 19 Illustration of octahedral tilting of a simple $CaTiO_3$ perovskite crystal structure [78], with $a^0a^0c^-$ tilting.

Tilting of the octahedra affects the crystal structure through modifications in unit-cell length; unit-cell angle; and the introduction of superstructures.

Unit-Cell Length Changes

The most important consequence of tilting to the crystal structure is that it causes doubling of the repeat distance perpendicular to the tilt axis [79], due to the previously discussed opposite sense rotations of neighbouring octahedra (figure 2.20). As tilting occurs, and if the B cation bonds are to be maintained, then, as a result of the tilting, the B-cation – B-cation distances become shorter. As these distances become shorter, the overall axial lengths of the unit cells reduce as well.

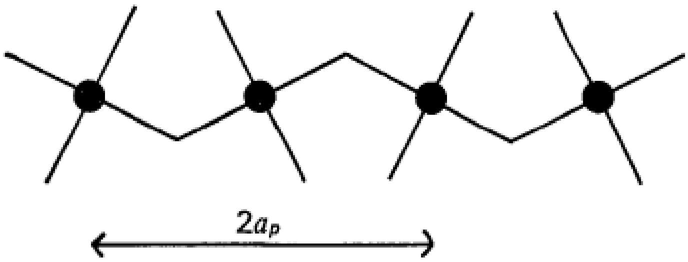

Figure 2. 20 A 2-dimensional representation of octahedra tilting about an axis normal to the plane of the page, showing doubling of the repeat distance [79].

In Glazer's work on octahedral tilting [77], [79], there are 3 simple relationships for calculating the new axial lengths resulting from tilting, using α, β and γ as the angles of tilt about the pseudocubic axes, [100], [010] and [001] respectively.

$$\begin{aligned} a_p &= a_o \cos\beta \cos\gamma \\ b_p &= b_o \cos\alpha \cos\gamma \\ c_p &= c_o \cos\alpha \cos\beta \end{aligned}$$

(2. 20)

where a_p, b_p and c_p are the new pseudocubic subcell lengths, and a_o, b_o and c_o are the aristotype cell edge lengths. However, because of the double of the repeat distances, the actual new subcell lengths are twice the lengths suggested by equations 2.20.

It is possible to have equality of tilting about more than one axis. In these cases, Glazer shows, by rearranging equations 2.20, that equality of any two tilt angles means equality of the cell axes *coincident* with the tilt axes:

$$\frac{a_p}{b_p} = \frac{\cos\beta}{\cos\alpha}, \qquad \frac{b_p}{c_p} = \frac{\cos\gamma}{\cos\beta}, \qquad \frac{c_p}{a_p} = \frac{\cos\alpha}{\cos\gamma}$$ [1]

(2. 21)

Therefore, if the tilts about [100] and [010] (α and β) are equal in magnitude, then a_p and b_p must also be equal. This gives rise to the notation form where equal tilts are represented by a repetition of the appropriate letters, such as '*abb*' or '*aac*', for equal tilting, and '*abc*' for unequal tilting about all three axes.

Unit-Cell Angle Changes

When an octahedra is tilted about one of the cubic $\langle 001 \rangle$ directions (e.g. clockwise), then the four neighbouring octahedra, in the plane normal to the axis of rotation, will rotate in the opposite sense (e.g. anticlockwise). This is due to the octahedra being constrained by the corner-sharing of the anions. However, octahedra above and below (parallel) are not constrained in the same way and can, therefore, tilt in one of two ways: if they rotate in the same sense (e.g. clockwise-clockwise), then this is referred to as in-phase tilting; if they rotate in the opposite sense (e.g. clockwise-anticlockwise), then this is called anti-phase tilting. In-phase tilting is denoted in Glazer notation with a superscript '$+$' sign, and anti-phase tilting is denoted by a superscript '$-$'

---

[1] This is assuming there are no distortions of the octahedra, such as cation displacements.

sign after the appropriate letter. If there is no tilting about an axis, then this is denoted by a superscript ‘0’. So, $a^0a^0c^-$ has anti-phase tilting about the pseudocubic c-axis only, figure 2.21.

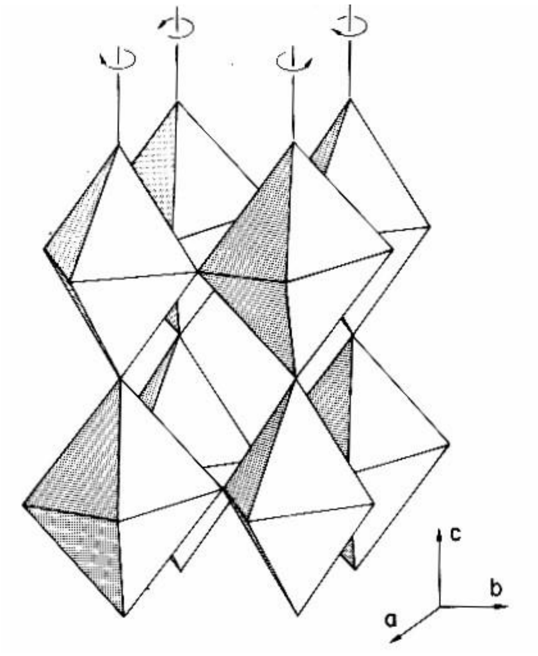

Figure 2. 21 Octahedral anti-phase tilting about the c-axis, from Burns and Glazer [73].

Whether there is in- or anti-phase tilting, knowing the signs associated with tilting is important for working out the lattice type and the unit-cell angles. Any two ‘$+$’ tilts, or one ‘$+$’ and one ‘$-$’, means that the relevant cell axes are normal to each other, whereas any two ‘$-$’ tilts indicates that the relevant cell axes are inclined to each other.

For example: the $a^-b^+c^+$ tilt system has 3 axes of unequal tilt and length normal to one another; the $a^-a^-c^+$ tilt system has 2 equal axes ($a_p = b_p$) inclined to each other and are both are normal to c_p; and the $a^-a^-a^-$ tilt system has 3 equal axes, all inclined to each other, with equal angles.

It was originally proposed that there are a total of 23 unique tilt systems, occupying a total of 15 distinct crystallographic space groups [77]. However, since there are only 15 distinct space groups occupied by the tilt systems, Howard and Stokes, in 1998 [81], [82], argued that there can only by 15 unique tilt systems, not 23. This came from their own work of doing group-theoretical analysis to determine the possible tilt systems. Their argument is summarised as such: if the different tilt systems result in the same space group, then ‘the system with the lowest symmetry must prevail’ [83]. The 15 possible tilts systems were diagrammatically represented by Howard and Stokes, figure 2.22.

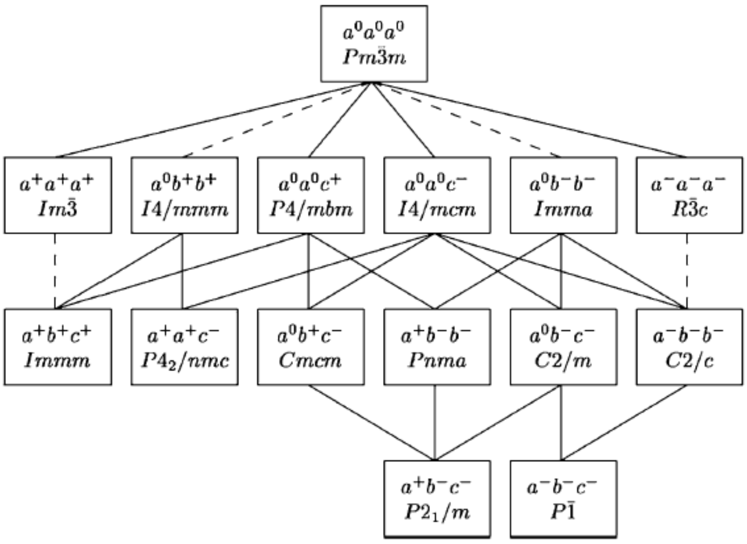

Figure 2. 22 The 15 distinct tilt systems and their corresponding group-subgroup relationships, as proposed by Howard and Stokes, 1998 and 2002 [81], [82].

NB: In 1997, Woodward made an argument, and demonstrated, that for two of the space groups ($P4_2/nmc$ and $Cmcm$) the octahedra could only remain connected if they distorted [84]. Howard and Stokes showed that these distortions are not necessary for $Cmcm$, however, along with Glazer, they treat the tilt systems with the assumption of perfectly rigid octahedra [77], [81], [82]. In reality, some distortion will always take place.

Superstructure Reflections

Since tilting causes doubling of the unit-cell axes, extra reflections are produced, lying on half-integral reciprocal-lattice planes. These reflections can be indexed with some indices 'odd', while the 'normal', main reflections have completely 'even' miller indices [79]. Fortunately, the two types of tilting (i.e. in- and anti-phase tilting) only results in 2 distinct classes of superstructure reflections: in-phase tilting produces odd-odd-even reflections, and anti-phase tilting produces odd-odd-odd reflections.

Glazer goes on to summarise these reflection relations into 6 simple rules and examples [79]:

a^+ : produces even-odd-odd, with $k \neq l$, e.g. miller indices 013, 031
b^+ : produces odd-even-odd, with $h \neq l$, e.g. miller indices 103, 301
c^+ : produces odd-odd-even, with $h \neq k$, e.g. miller indices 130, 310
a^- : produces odd-odd-odd, with $k \neq l$, e.g. miller indices 131, 113
b^- : produces odd-odd-odd, with $h \neq l$, e.g. miller indices 113, 311
c^- : produces odd-odd-odd, with $h \neq k$, e.g. miller indices 131, 311

Detecting Octahedral Tilting

There are a number of different techniques normally employed when detecting and identifying the structures and symmetries arising from tilted perovskites, and a large amount of research is concerned with this. The three more common techniques employed are X-Ray diffraction, neutron diffraction and electron diffraction.

X-Ray diffraction is readily available and is relatively cheap to operate, however it has a limitation in that scattering by the oxygen anions is much weaker than the scattering by the cations. This has the effect of masking any information which could have been garnered about the oxygen sub-lattice. In neutron diffraction, the diffraction from the oxygen sub-lattice is much stronger, compared to X-Ray diffraction, and has made the identification of distortions and rotations much more feasible. However, it is still difficult to resolve weak superstructure reflections from smaller structural distortions, if they occur over short coherence lengths [83].

Electron diffraction has the advantage over the other two techniques listed in that single-crystal or domain diffraction data may be obtained, from relatively small regions of samples. Electron diffraction is also sensitive to superstructure reflections from weak, short range effects [83].

In 2005, Woodward and Reaney [83] reported how the different perovskite tilt systems relate to electron diffraction patterns by simulating the tilt systems listed by Howard and Stokes [81], [82] and compared the simulated profiles with real results. Effectively, these authors created a simple mechanism by which tilt systems can be identified using the appropriate superstructure reflections along the three major zone axes of the perovskite structure, <001>, <110> and <111> [83].

2.4.4 Cation Displacement

Where half-integral superstructure reflections do not conform to the previously established tilt reflections, they likely arise from cation displacement. Superstructure reflections occur due to cation displacement when they are in anti-parallel. When they are parallel, no superstructure reflections are produced [79]. Normally, the most reliable method of predicting whether a material will demonstrate displacements is to have previous knowledge of the space group of the material, particularly whether the space group is centrosymmetric or not.

According to Glazer and Burns [73], [79], if the displacements are anti-parallel, then the structure is said to be centrosymmetric, and the space group is normally the same as that of the tilt system. If the displacements are parallel, then the structure is non-centrosymmetric and the space group is a subgroup of the tilt system. If there are no tilts present, from the lack of reflections observed for the material, then the displacements are obtained from the unit-cell geometries.

The following is an example of determining the space group changes as a result of cation displacement with changes of temperatures, after Burns and Glazer, 1978 [73].

In the case of $BaTiO_3$, its aristotype has a cubic $Pm\bar{3}m$ (space group number 221) at high temperatures, however as the temperature is reduced, the Ti and Ba ions are displaced along $[001]$, with respect to the oxygen octahedra (Figure 2.23 (b)). As a result, there is now a non-centrosymmetric structure where the **c**-axis is different from the **a**- and **b**-axes. This displacement is confined along the 4-fold axes of the original cubic structure, which also retains that particular 4-fold axis while those that are perpendicular are lost.

This displacement causes the structure to become tetragonal and now occupies space group number 99, $P4mm(C_{4V}^{1})$ [73], [75]. This tetragonal structure still has a primitive cell and still has two types of mirror planes, however it does not have the mirror planes perpendicular to $[001]$. In this space group, Ba is on a 1a site, Ti on a 1b site, O_I is on a 1b site, and O_{II} and O_{III} are on 2c sites. All symmetry operators of this new tetragonal space group are all contained within the original cubic space group [73].

Lowering the temperature further, the displacements in the $BaTiO_3$ switch from $[001]$ to the $[110]$ direction (figure 2.23 (c)). This new structure is now orthorhombic and occupies space group number 35, $Cmm2(C_{2V}^{14})$ [73], [75]. This C-centred orthorhombic structure now has a 2-fold axis along $[110]$ and mirror planes perpendicular to $[001]$ and parallel to $[110]$.

Finally, the lowest temperature phase has displacements along $[111]$ (figure 2.23 (d)), with a Rhombohedral point group of $R3m$ [73].

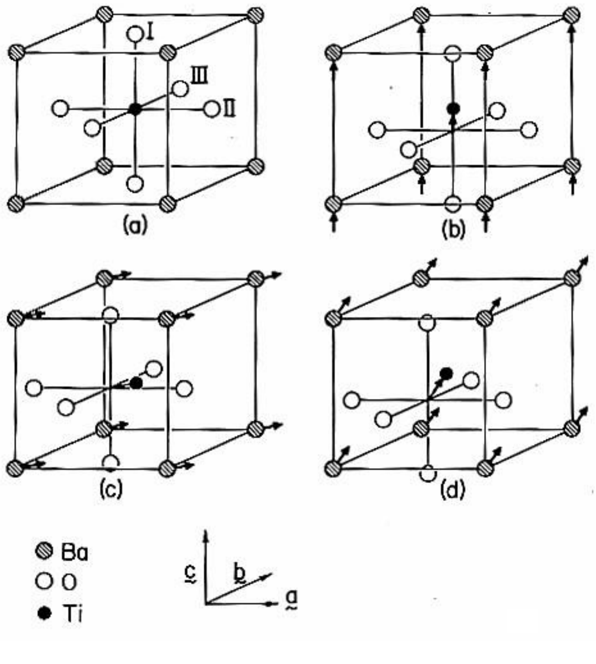

Figure 2. 23 Cation displacement in the perovskite structure, from Burns and Glazer [73].

2.5 $CaTiO_3$-based MW Dielectric Ceramics

The development of MW dielectric materials over the past 10-20 years has moved from TiO_2-based materials to $CaTiO_3$-based materials, as a result of the ever-present drive for miniaturisation, pushing for ever-higher ε_r values to facilitate this. The metallisation used on the surface of dielectrics means that Qf_0 is less critical to the performance of the antenna and, as a result, the exact minimum acceptable level of Qf_0 is still debated. Since the metallisation also decreases Qf_0, which broadens the resonant peak. This relaxes the strict requirements of the τ_f from ±1 ppm/°C to ±10 ppm/°C [15].

Generally, the material development for MW resonators used in filters and base-stations, and those used as antenna cores, have gone in two different directions, as mentioned in section 2.3. Dielectrics used for filters tend not to be mass-produced, and so tend to be made from more expensive materials, and a zero τ_f and high Qf_0 are of a higher priority than a large ε_r. Whereas materials used for antenna cores do tend to be mass-produced, so cheaper materials, whilst maintaining high ε_r values, are the higher priority. Figure 2. 24 shows the different temperature stable ceramics which are currently used for antenna cores and resonator applications. The straight line represents the average highest overall Qf_0 values attainable for a given value of ε_r.

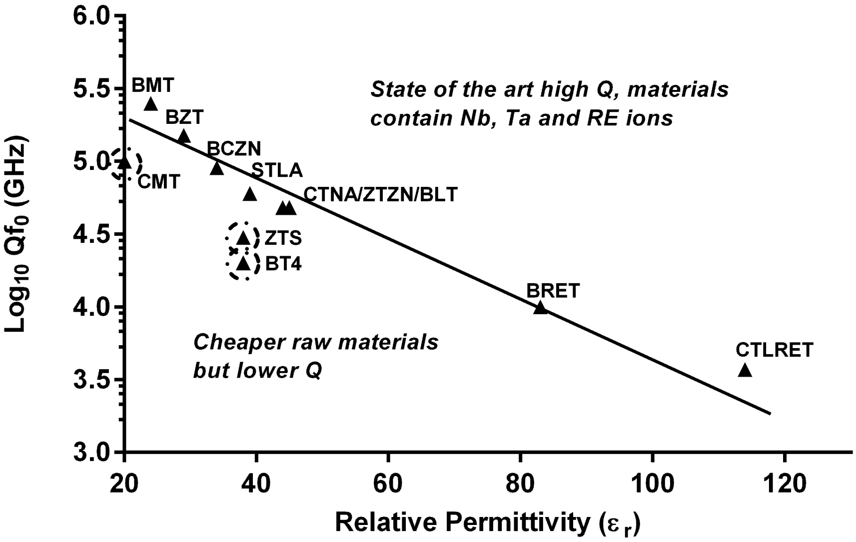

Figure 2. 24 Temperature stable ceramics which are currently used for antenna and resonator applications: $BaMg_{1/3}Ta_{2/3}O_3$ (BMT) [10], $BaZn_{1/3}Ta_{2/3}O_3$ (BZT) [10], $Ba(Co,Zn)_{1/3}Nb_{2/3}O_3$ (BCZN) [10], $CaTiO_3$-$NdAlO_3$ (CTNA) [10], $SrTiO_3$-$LaAlO_3$ (STLA) [10], $ZrTiO_4$-$ZnNb_2O_6$ (ZTZN) [10], $BaLa_4Ti_4O_{15}$ (BLT) [10], $BaRE_2Ti_4O_{12}$ (BRET) [15], $CaTiO_3$-$(Li1/2RE1/2)TiO_3$ (CTLRET) [85], $Zr(Ti,Sn)O_4$ (ZTS) [15], $CaTiO_3$-$MgTiO_3$ (CMT) [86] and $BaTi_4O_9$ (BT4) [15]. Ringed compositions are used mainly as substrates for dielectrically loaded antennas [87].

Barium RE titanate (BRET) based compositions have been the most popular compositions used for physically and electrically small dielectrically loaded antennas, however, where size is not as important and a greater efficiency or bandwidth is required, then (Ca,Mg)TiO_3 (CMT) [86], $BaTi_4O_9$ (BT4) [15] and Zr(Ti,Sn)O_4 (ZTS) [15] based materials tend to be used. CMT, BT4 and ZTS have the advantage in that they have cheaper raw materials, compared to the other compositions, which are made up of more expensive materials which lie on, or above, the optimal line.

Over the years, many different dielectric materials have been developed, which have been based on TiO_2 and Ba, such as Ba(Zn,Ta)O_3 - Ba(Zn,Nb)O_3 [41], (Zr,Sn)TiO_4 [63] and BaO-PbO-TiO_2-Nd_2O_3 [11], each of which had their advantages and disadvantages. The first two have large Qf_0 values, but low ε_r, and the third one had a large ε_r, but a low Qf_0 value. There was also another issue to overcome, that of τ_f, which tends to have a larger positive value as ε_r increases [17]. While the method of combining two different materials with positive and negative τ_f to produce a zero τ_f material was known for some time, there were not many materials available which had both a large ε_r and a large *negative* τ_f value. In the late 1980's and early 1990's, the only material of this kind, which would mix with $SrTiO_3$ and $CaTiO_3$ (both of which have large positive τ_f values), was $PbZrO_3$ + RE_2O_3 (where the RE = lanthanide group). However, mixing of these materials proved largely fruitless, due to a large difference in sintering temperatures and the appearance of secondary phases, resulting in insufficient MW dielectric properties [30], [88].

Then, in the early 1990's, research moved to finding and developing other high ε_r, large negative τ_f, which could be mixed with existing $CaTiO_3$-based MW dielectric materials. This was initially conducted by Ezaki *et al.* [30], [33], [32], which was based on some initial findings reported by Sakata *et al.* [89]. Ezaki *et al.* focussed on the $CaTiO_3$-($Li_{0.5}RE_{0.5}$)TiO_3 (CTLRET) system, over a range of different compositions, using different lanthanide rare-earth elements and studied how the different compositions altered the material MW properties of the system.

From 1991 – 1996, Ezaki *et al.* reported properties of ε_r = 81, Qf_0 = 6150 GHz and τ_f = +17 ppm/°C in a composition of $(1-0.4)\left(Li^{1+}_{1/2}Sm^{3+}_{1/2}\right)TiO_3 - 0.4\left(Na^{1+}_{1/2}Sm^{3+}_{1/2}\right)TiO_3$, in addition to other potential candidates showing large negative τ_f values with high ε_r in the $\left(Li^{1+}_{1/2}A^{3+}_{1/2}\right)TiO_3$ system, where A was substituted for large ionic radius lanthanides, such as La^{3+}, Pr^{3+}, Nd^{3+} and Sm^{3+} [30]. Further improvement of properties were reported in 1993 with 15CaO : SrO : 9Li_2O : 12Sm_2O_3 : 63TiO_2 (molar ratio), showing properties of ε_r = 110, Qf_0 = 4500 GHz and τ_f = +7 ppm/°C [33]. In 1996, a material composed of 15CaO : SrO : 9Li_2O : 6Sm_2O_3 : 6Nd_2O_3 : 63TiO_2 was presented and reported to have MW properties of ε_r = 123, Qf_0 = 4150 GHz and τ_f = +10 ppm/°C [32]. Later, in 1999, Kim *et al.* further optimised the composition of the CTLST system, with properties of ε_r = 114, Qf_0 = 3700 GHz and τ_f = +11.5 ppm/°C for a composition of $0.3CaTiO_3 - 0.7(Li_{0.5}Sm_{0.5})TiO_3$ [85].

In addition to developing dielectric materials with excellent MW properties and near-zero τ_f, Ezaki *et al.* also contributed to the understanding that the ionic radius of the lanthanide element had a strong influence on the dielectric properties of the materials. It was found that the ε_r of the material would increase as the unit cell of the crystal increased, due to increasing ionic radius. It was also reported that the Qf_0 of the material is affected by variations in the crystal structure and whether any secondary phases appeared.

The next main issue for these excellent MW materials were their high sintering temperatures, which raised an issue, along with the price of the rare-earth elements, with the cost of mass-production of these materials for regular use as antenna cores. In 2009, Aziz *et al.* showed that similar properties to the Kim *et al.* material could be produced in the $0.2CaTiO_3 - 0.8(Li_{0.5}Nd_{0.5})TiO_3$ composition, at lower sintering temperatures with the addition of a $Li_2O - B_2O_3$ sintering aid. Unfortunately, they were unable to reduce the sintering temperature any lower than 1300°C without strong deterioration of the MW properties [90].

In 2012, a breakthrough occurred where Chen *et al.* were able to fabricate a CTLRET dielectric material, with excellent MW properties, at a sintering temperature of 1200°C, using $Bi_4B_2O_9$ (BBO) as a sintering aid, and maintaining a >95% theoretical density. The properties reported were ε_r = 127, Qf_0 = 2700 GHz and τ_f = +4 ppm/°C for a composition of $0.2CaTiO_3 - 0.8(Li_{0.5}Nd_{0.5})TiO_3$ with only up to 4wt% additions of BBO [91]. The authors also investigated the use of BBO as a sintering aid for BRET-based ceramics and found a similar reduction in sintering temperature while maintaining MW properties of ε_r = 86 and Qf_0 = 6000 GHz at the reduced sintering temperatures.

While this is a significant contribution in the fabrication of ultra-high performance dielectric materials at lower costs, due to the potential reduction of sintering temperature, there was, at that point, no understanding as to the mechanism between the CTLNT and the BBO. At least in terms of what interaction the two materials had upon another which would result in maintained, or even improved, MW properties at lower sintering temperatures.

The scope of this contribution is determining the precise role of the BBO in its interaction with the CTLRET system, both for the CTLNT and the CTLST, and whether this understanding will have further developmental value for combining different dielectric materials with ‘made for purpose’, designer sintering aids.

2.6 References

[1] OxfordDictionaries.com, “Definition of Ceramic,” 2015. [Online]. Available: http://www.oxforddictionaries.com/definition/learner/ceramic.

[2] W. D. Kingery, H. K. Bowen, and D. R. Uhlmann, *Introduction to ceramics*, 2d ed. New York: Wiley, 1976.

[3] A. J. Moulson and J. M. Herbert, *Electroceramics: Materials, Properties, Applications*. New York: Chapman & Hall, 1990.

[4] R. D. Shannon, “Dielectric polarizabilities of ions in oxides and fluorides,” *J. Appl. Phys.*, vol. 73, no. 1, pp. 348–366, 1993.

[5] L. G. Hector and H. L. Schultz, “The Dielectric Constant of Air at Radiofrequencies,” *J. Appl. Phys.*, vol. 7, no. 4, pp. 133–136, 1936.

[6] K. Kinoshita and A. Yamaji, “Grain-size effects on dielectric properties in barium titanate ceramics,” *J. Appl. Phys.*, vol. 47, no. 1, pp. 371–373, 1976.

[7] G. Arlt, D. Hennings, and G. de With, “Dielectric properties of fine-grained barium titanate ceramics,” *J. Appl. Phys.*, vol. 58, no. 4, pp. 1619–1625, 1985.

[8] H. Ohsato, T. Tsunooka, T. Sugiyama, K. Kakimoto, and H. Ogawa, “Forsterite ceramics for millimeterwave dielectrics,” *J. Electroceramics*, vol. 17, no. 2–4, pp. 445–450, Dec. 2006.

[9] J. Laskar, S. Chakraborty, A.-V. Pham, and M. M. Tantzeris, *Advanced integrated communication microsystems*, vol. 174. John Wiley & Sons, 2009.

[10] I. M. Reaney and D. Iddles, “Microwave Dielectric Ceramics for Resonators and Filters in Mobile Phone Networks,” *J. Am. Ceram. Soc.*, vol. 89, no. 7, pp. 2063–2072, Apr. 2006.

[11] K. Wakino, K. Minai, and H. Tamura, “Microwave Characteristics of (Zr, Sn)TiO4 and BaO-PbO-Nd2O3-TiO2 Dielectric Resonators,” *J. Am. Ceram. Soc.*, vol. 67, no. 4, pp. 278–281, 1984.

[12] I. C. Hunter, L. Billonet, B. Jarry, and P. Guillon, “Microwave filters-applications and technology,” *IEEE Trans. Microw. Theory Tech.*, vol. 50, no. 3, pp. 794–805, Mar. 2002.

[13] R. J. Cava, “Dielectric materials for applications in microwave communications,” *J. Mater. Chem.*, vol. 11, no. 1, pp. 54–62, 2001.

[14] H. Sreemoolanadhan, M. T. Sebastian, and P. Mohanan, “High permittivity and low loss ceramics in the BaO-SrO-Nb2O5 system,” *Mater. Res. Bull.*, vol. 30, no. 6, pp. 653–658, 1995.

[15] M. Mirsaneh, O. P. Leisten, B. Zalinska, and I. M. Reaney, “Circularly Polarized Dielectric-Loaded Antennas: Current Technology and Future Challenges,” *Adv. Funct. Mater.*, vol. 18, no. 16, pp. 2293–2300, Aug. 2008.

[16] H. Ohsato, “Research and Development of Microwave Dielectric Ceramics for Wireless Communications,” *J. Ceram. Soc. Japan*, vol. 113, no. 1323, pp. 703–711, 2005.

[17] A. G. Cockbain and P. J. Harrop, “Temperature Coefficient of Capacitance,” *J. Phys. D-Applied Phys.*, vol. 1, no. 9, p. 1109–&, 1968.

[18] E. L. Colla, I. M. Reaney, and N. Setter, “The Temperature-Coefficient of the Relative Permittivity of Complex Perovskites and Its Relation to Structural Transformations,” *Ferroelectrics*, vol. 133, no. 1–4, pp. 217–222, 1992.

[19] I. M. Reaney, E. L. Colla, and N. Setter, “Dielectric and Structural Characteristics of Ba- and Sr-based Complex Perovskites as a Function of Tolerance Factor,” *Jpn. J. Appl. Phys.*, vol. 33, no. Part 1, No. 7A, pp. 3984–3990, Jul. 1994.

[20] M. T. Sebastian, *Dielectric materials for wireless communication*. Elsevier, 2010.

[21] H. Hughes, D. M. Iddles, and I. M. Reaney, “Niobate-based microwave dielectrics suitable for third generation mobile phone base stations,” *Appl. Phys. Lett.*, vol. 79, no. 18, pp. 2952–2954, 2001.

[22] I. M. Reaney, P. Wise, R. Ubic, J. Breeze, N. M. Alford, D. Iddles, D. Cannell, and T. Price, “On the temperature coefficient of resonant frequency in microwave dielectrics,” *Philos. Mag. A*, vol. 81, no. 2, pp. 501–510, Feb. 2001.

[23] D. M. Iddles, A. J. Bell, and A. J. Moulson, “Relationships between Dopants, Microstructure and the Microwave Dielectric-Properties of ZrO_2-TiO_2-SnO_2 Ceramics,” *J. Mater. Sci.*, vol. 27, no. 23, pp. 6303–6310, 1992.

[24] I. M. Reaney, I. Qazi, and W. E. Lee, “Order-disorder behavior in Ba(Zn1/3Ta2/3)O3,” *J. Appl. Phys.*, vol. 88, no. 11, pp. 6708–6714, 2000.

[25] F. N. Hirahara; Seiichiro Enami; Shinichi, Nishi; Toyomi, “Dielectric ceramic composition and dielectric resonator,” Patent, 08/082,024, 1994.

[26] I. M. Reaney and R. Ubic, “Dielectric and structural characteristics of perovskites and related materials as a function of tolerance factor,” *Ferroelectrics*, vol. 228, no. 1–4, pp. 23–28, 1999.

[27] P. L. Wise, “Structure-Microwave Dielectric Property Relations in Sr and Ca Titanates,” PhD Thesis, The University of Sheffield, Sheffield, 2002.

[28] A. Templeton, X. Wang, S. J. Penn, S. J. Webb, L. F. Cohen, and N. M. Alford, “Microwave Dielectric Loss of Titanium Oxide,” *J. Am. Ceram. Soc.*, vol. 83, no. 1, pp. 95–100, Jan. 2000.

[29] B. C. Steele, *Electronic Ceramics*. Springer, 1991.

[30] H. Takahashi, Y. Baba, K. Ezaki, Y. Okamoto, K. Shibata, K. Kuroki, and S. Nakano, “Dielectric Characteristics of (A 1/2 1+ ·A 1/2 3+)TiO 3 Ceramics at Microwave Frequencies,” *Jpn. J. Appl. Phys.*, vol. 30, no. Part 1, No. 9B, pp. 2339–2342, Sep. 1991.

[31] P. L. Wise, I. M. Reaney, W. E. Lee, D. M. Iddles, D. S. Cannell, and T. J. Price, “Tunability of tau(f) in perovskites and related compounds,” *J. Mater. Res.*, vol. 17, no. 8, pp. 2033–2040, 2002.

[32] H. Takahashi, Y. Baba, K. Ezaki, and K. Shibata, “Microwave Dielectric Properties and Crystal Structure of C a O – L i 2 O –(1- x) S m 2 O 3 – x L n 2 O 3 – T i O 2 (Ln: lanthanide) Ceramics System,” *Jpn. J. Appl. Phys.*, vol. 35, no. Part 1, No. 9B, pp. 5069–5073, Sep. 1996.

[33] K. Ezaki, Y. Baba, H. Takahashi, K. Shibata, and S. Nakano, “Microwave Dielectric Properties of CaO-Li 2 O-Ln 2 O 3 -TiO 2 Ceramics,” *Jpn. J. Appl. Phys.*, vol. 32, no. Part 1, No. 9B, pp. 4319–4322, Sep. 1993.

[34] P. J. Harrop, “Temperature coefficients of capacitance of solids,” *J. Mater. Sci.*, vol. 4, no. 4, pp. 370–374, 1969.

[35] E. L. Colla, I. M. Reaney, and N. Setter, “Effect of structural changes in complex perovskites on the temperature coefficient of the relative permittivity,” *J. Appl. Phys.*, vol. 74, no. 5, p. 3414, 1993.

[36] M. W. Lufaso, “Crystal Structures, Modeling, and Dielectric Property Relationships of 2:1 Ordered Ba 3 MM‘ 2 O 9 (M = Mg, Ni, Zn; M‘ = Nb, Ta) Perovskites,” *Chem. Mater.*, vol. 16, no. 11, pp. 2148–2156, Jun. 2004.

[37] B. Żalińska and P. I. M. Reaney, “Bismuth-based Glasses, Glass-Ceramics and Composites for Microwave Applications,” PhD Thesis, The University of Sheffield, Sheffield, 2010.

[38] V. L. Gurevich and A. K. Tagantsev, “Intrinsic dielectric loss in crystals,” *Adv. Phys.*, vol. 40, no. 6, pp. 719–767, Dec. 1991.

[39] V. M. Ferreira, J. L. Baptista, S. Kamba, and J. Petzelt, “Dielectric spectroscopy of MgTiO3-based ceramics in the 10^9-10^{14}Hz region,” *J. Mater. Sci.*, vol. 28, no. 21, pp. 5894–5900, 1993.

[40] R. Muhammad, Y. Iqbal, C. Rambo, and H. Khan, “Research trends in microwave dielectrics and factors affecting their properties: A review,” *Int. J. Mater. Res.*, vol. 105, no. 5, pp. 431–439, 2014.

[41] S. Kawashima, M. Nishida, I. Ueda, and H. Ouchi, “$Ba(Zn_{1/3}Ta_{2/3})O_3$ Ceramics with Low Dielectric Loss at Microwave Frequencies,” *J. Am. Ceram. Soc.*, vol. 66, no. 6, pp. 421–423, Jun. 1983.

[42] D. J. Barber, K. M. Moulding, J. Zhou, and M. Li, “Structural order in $Ba(Zn_{1/3}Ta_{2/3})O_3$, $Ba(Zn_{1/3}Nb_{2/3})O_3$ and $Ba(Mg_{1/3}Ta_{2/3})O_3$ microwave dielectric ceramics,” *J. Mater. Sci.*, vol. 32, no. 6, pp. 1531–1544, 1997.

[43] M. Onoda, J. Kuwata, K. Kaneta, K. Toyama, and S. Nomura, “$Ba(Zn_{1/3}Nb_{2/3})O_3$ – $Sr(Zn_{1/3}Nb_{2/3})O_3$ Solid Solution Ceramics with Temperature-Stable High Dielectric Constant and Low Microwave Loss,” *Japanese J. Appl. Physics, Part 1 Regul. Pap. Short Notes*, vol. 21, no. 12 Pt 1, pp. 1707–1710, 1982.

[44] D. A. Sagala and S. Nambu, “Microscopic Calculation of Dielectric Loss at Microwave Frequencies for Complex Perovskite $Ba(Zn_{1/3}Ta_{2/3})O_3$,” *J. Am. Ceram. Soc.*, vol. 75, no. 9, pp. 2573–2575, Sep. 1992.

[45] T. Negas, G. Yaeger, S. Bell, N. Coats, and J. Minis, “$BaTi_4O_9$/$Ba_2Ti_9O_{20}$-based ceramics. Resurrected for modern microwave applications,” *Am. Ceram. Soc. Bull.*, vol. 72, no. 1, pp. 80–89, 1993.

[46] F. Galasso and J. Pyle, “Ordering in Compounds of the $A(B'_{0.33}Ta_{0.67})O_3$ Type,” *Inorg. Chem.*, vol. 2, no. 3, pp. 482–484, Jun. 1963.

[47] S. B. Desu and H. M. O’Bryan, “Microwave Loss Quality of $BaZn_{13}Ta_{2/3}O_3$ Ceramics,” *J. Am. Ceram. Soc.*, vol. 68, no. 10, pp. 546–551, Oct. 1985.

[48] H. Tamura, T. Konoike, Y. Sakabe, and K. Wakino, “Improved High-Q Dielectric Resonator with Complex Perovskite Structure,” *J. Am. Ceram. Soc.*, vol. 67, no. 4, pp. c59–c61, Oct. 2006.

[49] P. K. Davies, J. Tong, and T. Negas, “Effect of Ordering-Induced Domain Boundaries on Low-Loss $Ba(Zn_{1/3}Ta_{2/3})O_3$-$BaZrO_3$ Perovskite Microwave Dielectrics,” *J. Am. Ceram. Soc.*, vol. 80, no. 7, pp. 1727–1740, Jan. 1997.

[50] K. Kageyama, “Crystal Structure and Microwave dielectric Properties of $Ba(Zn_{1/3}Ta_{2/3})O_3$-$(Sr,Ba)(Ga_{1/2}Ta_{1/2})O_3$ Ceramics,” *J. Am. Ceram. Soc.*, vol. 75, no. 7, pp. 1767–1771, Jul. 1992.

[51] I. M. Reaney, P. L. Wise, I. Qazi, C. A. Miller, T. J. Price, D. S. Cannell, D. M. Iddles, M. J. Rosseinsky, S. M. Moussa, M. Bieringer, L. D. Noailles, and R. M. Ibberson, “Ordering and quality factor in $0.95BaZn_{1/3}Ta_{2/3}O_3$–$0.05SrGa_{1/2}Ta_{1/2}O_3$ production resonators,” *J. Eur. Ceram. Soc.*, vol. 23, no. 16, pp. 3021–3034, Dec. 2003.

[52] I. M. Reaney, I. Qazi, and W. E. Lee, “Order–disorder behavior in $Ba(Zn_{1/3}Ta_{2/3})O_3$,” *J. Appl. Phys.*, vol. 88, no. 11, p. 6708, 2000.

[53] J. M. Herbert, *Ceramic dielectrics and capacitors*, vol. 6. CRC Press, 1985.

[54] A. Pashkin, S. Kamba, M. Berta, J. Petzelt, G. D. C. C. de Györgyfalva, H. Zheng, H. Bagshaw, and I. M. Reaney, “High frequency dielectric properties of $CaTiO_3$ -based microwave ceramics,” *J. Phys. D. Appl. Phys.*, vol. 38, no. 5, pp. 741–748, Mar. 2005.

[55] M. . Seabra, M. Avdeev, V. . Ferreira, R. . Pullar, and N. M. Alford, “Structure and microwave dielectric properties of $La(Mg_{0.5}Ti_{0.5})O_3$–$CaTiO_3$ system,” *J. Eur. Ceram. Soc.*, vol. 23, no. 14, pp. 2403–2408, Jan. 2003.

[56] L. M. Rodriguez-Martinez and J. P. Attfield, “Cation disorder and size effects in magnetoresistive manganese oxide perovskites,” *Phys. Rev. B*, vol. 54, no. 22, pp. R15622–R15625, Dec. 1996.

[57] M. P. Seabra, V. M. Ferreira, H. Zheng, and I. M. Reaney, “Structure property relations in $La(Mg_{1/2}Ti_{1/2})O_3$-based solid solutions,” *J. Appl. Phys.*, vol. 97, no. 3, p. 033525, 2005.

[58] R. Hill, “Band switched patch radiators for telephone handsets,” in *Microwave Filters and Antennas for Personal Communication Systems, IEE Colloquium on*, 1994, pp. 2/1–2/6.

[59] M. Zahn, *Electromagnetic Field Theory: a problem solving approach*. John Wiley & Sons, 1979.

[60] O. P. Leisten and B. Rosenberger, “Miniature Dielectric Loaded Antennas with Low SAR,” in *10th International Conference on Wireless Communications*, 1998, pp. 196–205.

[61] O. P. Leisten and A. P. Wingfield, “Commitment to Design for a Safety-Critical Function Reliable GPS Antenna Technology for E-911 in Handsets,” in *Proceedings of the 16th International Technical Meeting of the Satellite Division of The Institute of Navigation (ION GPS/GNSS 2003)*, 2003, pp. 1579 – 1584.

[62] R. D. Richtmyer, “Dielectric Resonators,” *J. Appl. Phys.*, vol. 10, no. 6, p. 391, 1939.

[63] K. Wakino, “Recent development of dielectric resonator materials and filters in Japan,” *Ferroelectrics*, vol. 91, no. 1, pp. 69–86, Mar. 1989.

[64] G. Wolfram and H. E. Göbel, “Existence range, structural and dielectric properties of ZrxTiySnzO4 ceramics (x+y+z=2),” *Mater. Res. Bull.*, vol. 16, no. 11, pp. 1455–1463, Nov. 1981.

[65] O. P. Leisten, “The Case for Isolating the Antenna from the Box,” in *IEE Conference on Antenna Measurement and SAR, Vol. 7*, 2002, pp. 1–7.

[66] J. S. Colburn and Y. Rahmat-Samii, “Human proximity effects on circular polarized handset antennas in personal satellite communications,” *IEEE Trans. Antennas Propag.*, vol. 46, no. 6, pp. 813–820, Jun. 1998.

[67] M. D. Deshpande and N. K. Das, “Rectangular Microstrip Antenna For Circular Polarization,” *IEEE Trans. Antennas Propag.*, vol. AP-34, no. 5, pp. 745–746, 1986.

[68] R. Kapur, “Microstrip Patch Antenna Calculator,” *Everything RF*, 2016. [Online]. Available: http://www.everythingrf.com/rf-calculators/microstrip-patch-antenna-calculator. [Accessed: 21-Mar-2016].

[69] C. C. Kilgus, “Resonant Quadrifilar Helix Design,” *Microw. J.*, vol. 13, pp. 49–52, 1970.

[70] C. Kilgus, “Resonant quadrafilar helix,” *IEEE Trans. Antennas Propag.*, vol. 17, no. 3, pp. 349–351, May 1969.

[71] O. Leisten, J. C. Vardaxoglou, P. McEvoy, R. Seager, and A. Wingfield, “Miniaturised dielectrically-loaded quadrifilar antenna for Global Positioning System (GPS),” *Electron. Lett.*, vol. 37, no. 22, p. 1321, 2001.

[72] B. M. Wul and I. M. Goldman, “Dielectric constants of titanates of metals of the second group,” *Compt. rend. Acad. sci. URSS*, vol. 46, pp. 139–142, 1945.

[73] G. Burns and A. M. Glazer, *Space Groups for Solid State Scientists*, First Edit. New York, San Francisco, London: Academic Press, 1978.

[74] H.-R. Wenk and A. Bulakh, *Minerals: their constitution and origin*. Cambridge University Press, 2004.

[75] E. Prince, A. J. C. Wilson, T. Hahn, and U. Shmueli, *International tables for crystallography*. International Union of Crystallography, 1999.

[76] University of London, Birkbeck College, “Pm-3m,” 2016. [Online]. Available: http://img.chem.ucl.ac.uk/sgp/large/221az1.htm.

[77] A. Glazer, “The classification of tilted octahedra in perovskites,” *Acta Crystallogr. Sect. B*, vol. 28, no. 11, pp. 3384–3392, 1972.

[78] H. D. Megaw, *Crystal Structures: A Working Approach*, vol. Volume 10 . W. B. Saunders, 1973.

[79] A. Glazer, “Simple ways of determining perovskite structures,” *Acta Crystallogr. Sect. A*, vol. 31, no. 6, pp. 756–762, Nov. 1975.

[80] V. M. Goldschmidt, “Die Gesetze der Krystallochemie,” *Naturwissenschaften*, vol. 14, no. 21, pp. 477–485, 1926.

[81] C. J. Howard and H. T. Stokes, “Group-Theoretical Analysis of Octahedral Tilting in Perovskites,” *Acta Crystallogr. Sect. B Struct. Sci.*, vol. 54, no. 6, pp. 782–789, 1998.

[82] C. J. Howard and H. T. Stokes, “Group-Theoretical Analysis of Octahedral Tilting in Perovskites. Erratum,” *Acta Crystallogr. Sect. B*, vol. 58, no. 3 Part 2, p. 565, 2002.

[83] D. I. Woodward and I. M. Reaney, “Electron diffraction of tilted perovskites,” *Acta Crystallogr. Sect. B*, vol. 61, no. 4, pp. 387–399, 2005.

[84] P. M. Woodward, “Octahedral Tilting in Perovskites. II. Structure Stabilizing Forces,” *Acta Crystallogr. Sect. B Struct. Sci.*, vol. 53, no. 1, pp. 44–66, 1997.

[85] W. S. Kim, K. H. Yoon, and E. S. Kim, “Far-Infrared Reflectivity Spectra of CaTiO3-Li1/2Sm1/2TiO3 Microwave Dielectrics,” *Mater. Res. Bull.*, vol. 34, no. 14/15, pp. 2309–2317, 1999.

[86] V. M. Ferreira, F. Azough, R. Freer, and J. L. Baptista, “The effect of Cr and La on $MgTiO_3$ and $MgTiO_3$-$CaTiO_3$ microwave dielectric ceramics,” *J. Mater. Res.*, vol. 12, no. 12, pp. 3293–3299, 1997.

[87] S. J. Nicholls, I. M. Reaney, and O. P. Leisten, “Enhancing Properties in Microwave Ceramics Using a Designer Sintering Aid,” *J. Am. Ceram. Soc.*, vol. 98, no. 12, pp. 3891–3896, Dec. 2015.

[88] K. Tatsuki, K. Murano, T. Kawamura, H. Kato, S. Yano, and S. Nishigaki, “Dielectric properties of PbO-ZrO-REOX ceramics at microwave frequency,” in *Proceedings of the 6th Meeting of the Ferroelectric Materials & Their Applications*, 1987, vol. 26, no. SUPPL. 26–2, pp. 80–82.

[89] K. Sakata, Y. Masuda, and G. Ohara, “No Title,” *Chitabari Jitsuyouka Kenkyuukai Shiryo*, vol. 71, p. 452.

[90] D. A. Abdel Aziz, I. Sterianou, and I. M. Reaney, “(1 − x)$CaTiO_3$–x$(Li_{0.5}Nd_{0.5})TiO_3$ for ultra-small dielectrically loaded antennas,” *J. Mater. Sci.*, vol. 44, no. 23, pp. 6247–6250, 2009.

[91] X. Chen, W. Zhang, B. Zalinska, I. Sterianou, S. Bai, and I. M. Reaney, “Low Sintering Temperature Microwave Dielectric Ceramics and Composites Based on Bi_2O_3-B_2O_3,” *J. Am. Ceram. Soc.*, vol. 95, no. 10, pp. 3207–3213, Oct. 2012.

Chapter 3: Experimental Methods

The following sections describe the techniques used in the fabrications and characterisation of the ceramics discussed in subsequent chapters.

3.1 Fabrication of Materials

3.1.1 Fabrication of $0.2CaTiO_3$ – $0.8(Li_{0.5}Nd_{0.5})TiO_3$ (CTLNT) and $0.2CaTiO_3$ – $0.8(Li_{0.5}Sm_{0.5})TiO_3$ (CTLST)

Both the $0.2CaTiO_3$ – $0.8(Li_{0.5}Nd_{0.5})TiO_3$ (CTLNT) and $0.2CaTiO_3$ – $0.8(Li_{0.5}Sm_{0.5})TiO_3$ (CTLST) were prepared via the conventional mixed-oxide, solid-state reaction route. The starting reagent materials were $CaCO_3$, TiO_2, $LiCO_3$, Nd_2O_3 and Sm_2O_3. Reagent details are listed in table 3. 1. These compounds were chosen for their reported properties and, specifically for the CTLNT, for the observations made prior to this contribution by Chen *et al* [1], as well as allowing any observed results to be directly comparable to the field.

Table 3. 1 List of raw materials used in the fabrication of all ceramics.

Reagent Name	Chemical Formula	Molar Mass (g/mol)	Purity	Manufacturer	Batch Number
Calcium Carbonate	$CaCO_3$	100.0869	+99%	Sigma-Aldrich	MKBB6040, A.C.S. reagent
Titanium Oxide	TiO_2	79.866	≥99.9%	Aldrich Chemistry	BCBF4537V
Lithium Carbonate	Li_2CO_3	73.891	+99%	Sigma-Aldrich	10318PD, A.C.S. reagent
Neodymium Oxide	Nd_2O_3	336.48	99.9%	Stanford Materials Corporation	CST0911250
Samarium Oxide	Sm_2O_3	348.72	99.9%	Stanford Materials Corporation	CST091016
Bismuth Oxide	Bi_2O_3	465.96	99.9%	Acros Organics	A0301187
Boric Acid	H_3BO_3	61.83	≥99.5%	Sigma Life Science	080M0136V

Both the Nd_2O_3 and Sm_2O_3 were pre-milled in propan-2-ol in an attrition mill (Szegravi Attritor Systems, Union Process™, Ohio, 44213) for 1 hour, using 2-3mm diameter yttria-stabilised zirconia milling media. The slurry was separated from the milling media through a 250µm aperture stainless steel sieve (Fisherbrand Test Sieve, ISO3310-1:2000, BS410-1:2000, Ser. No: 0144136) and dried in an oven set to ~80°C overnight. The dried powders were once again sieved using the same sieve and collected into sealed glass containers.

The TiO_2, Nd_2O_3 and Sm_2O_3 powders were dried at 800°C for 6 hours and held at 200°C overnight, in mullite crucibles. The carbonates, $CaCO_3$ and $LiCO_3$, were dried at 180°C overnight in mullite crucibles to avoid premature decomposition prior to mixing and calcination. For a 60g batch, the following were measured (Precisa: 925M-202A high-precision scale) and loosely mixed: 6.60070g, 4.87308g; 22.19062g; 26.33561g of CaCO3, Li2CO3, Nd2O3 and TiO2 respectively for CTLNT; and 6.5131g, 4.8084g, 22.6925g and 25.9860g of CaCO3, Li2CO3, Sm2O3 and TiO2 respectively for CTLST.

All reagents and mixtures were stored in a desiccator prior to and post batching, within unique sealed glass containers. Reactions and heating temperatures over 180°C were all conducted in an electric furnace in air.

The two compositions were then mixed in an attrition mill for 1h, separated from the yttria-stabilised zirconia (YSZ) milling media and dried using the same process described previously. Test reactions were conducted in closed calcined alumina crucibles in air at 1100°C, 1150°C and 1175°C for 4 hours with a heating/cooling rate of 2°C/min. X-Ray Diffraction (XRD) was performed on CTLNT calcined at 1150°C and for CTLST at 1175°C to determine the phase assemblage (see section 3.2.4). The final batches underwent calcination at these two temperatures, and the calcined powder milled and dried as before.

3.1.2 Fabrication of Bismuth Borate - $Bi_4B_2O_9$ (BBO)

A batch of 50g of bismuth borate was prepared using a similar conventional mixed-oxide, solid-state reaction route using Bi_2O_3 and H_3BO_3 reagents (Table 3.1). The Bi_2O_3 was dried in a furnace at 500°C for 3 hours, with a heating and cooling rate of 10°C/min and held at 200°C overnight, in a mullite crucible, in air, using an electric furnace. Bi_2O_3 and H_3BO_3 were measured (Precisa: 925M-202A high precision scale) and mixed in correct stoichiometric proportions of 6.183g and 46.494g, respectively, in acetone, rather than propan-2-ol, in an attrition mill, with 2-3mm diameter YSZ milling media, for 1 hour. The slurry was then separated from the milling media using a 250μm aperture stainless steel sieve and dried at room temperature for up to two weeks. Once dried, the powder was sieved as before.

Two test reactions were conducted, one at 660°C and one at 650°C, to find the optimal phase assemblage. Calcination temperature (650°C) was chosen based on previous work [1]. The calcined powder was then re-milled in an attrition mill in acetone, dried at room temperature for two weeks and stored in a sealed glass container.

3.1.3 Fabrication of Composite Ceramics $(1\text{-}x)$CTLNT+xBBO and $(1\text{-}x)$CTLST+xBBO

Composite CTLNT and CTLST ceramic samples were fabricated with BBO additions from 1 to 5 weight (wt) %, with each a batch of 10g. CTLNT and BBO were mixed together and ball-milled overnight in polyethylene containers, with acetone as the lubricant and YSZ milling media followed by drying at room temperature. The dried, mixed powders were sieved through a 250µm aperture stainless steel sieve, and stored in sealed glass jars.

3.1.4 Pressing Pellets and Sintering

9 pellets were pressed for each composition of CTLNT and CTLST, 3 pellets were sintered at 3 different sintering temperatures: 1150°C, 1200°C and 1250°C for the CTLNT compositions; and 1200°C, 1250°C and 1300°C for the CTLST. Powder for the pellets were weighed (Precisa: 925M-202A high precision scale) so that each sample was ~1g and then pressed in a 10mm die with a loading of ~600 kg for approximately 1 minute. All pellets were sintered in a tube furnace, on a bed of calcined alumina powder, at their respective sintering temperatures for 4 hours, with heating and cooling rates of 5°C/min, in air. Two refractory stoppers were attached to both ends of the tube furnace to prevent heat within the tube escaping through convection, and to keep volatile elements from escaping.

3.1.5 Fabrication of CTLNT + 4wt% BBO Multilayer Ceramic Capacitor (MLCC)

A 40g batch of CTLNT + 4wt% BBO was pre-synthesised, using the solid-state reaction method previously outlined. The fabrication of multilayers followed a similar path to that outlined by Ming-Jen and Randal [2] which is summarised in the schematic shown in figure 3.1.

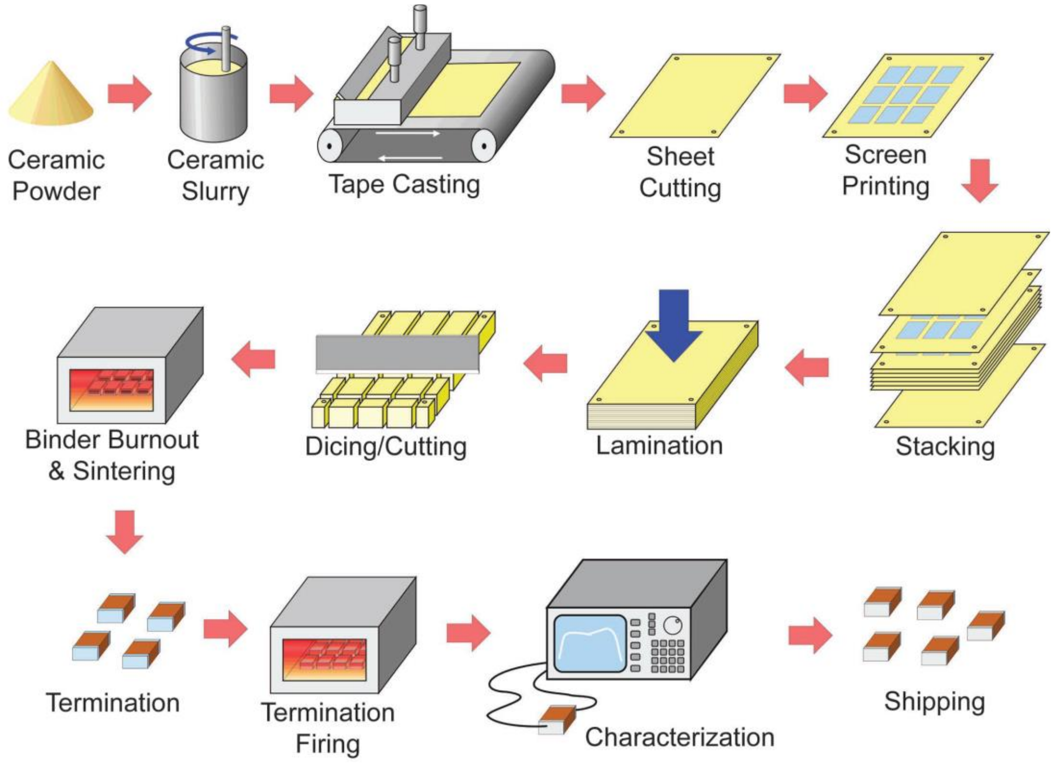

Figure 3. 1 A schematic of the MLCC fabrication process, as shown by Ming-Jen and Randal [2].

The powder was first mixed into a solvent slurry, or paste, for tape casting using the following recipe of solvents, dispersants and binders, in table 3. 2:

Table 3. 2 Recipe used in the fabrication of the ceramic solvent slurry for tape casting.

Ingredient	Details	Weight (g)	Wt %
CTLNT + 4wt% BBO	Pre-fabricated ceramic compound	40	57.65 %
Solvent 1	MEK : EtOH (50:50)	16	23.09 %
Dispersant	Hypermer KD-1	0.59	0.85 %
Plasticiser 1	Butyl benzyl phthalate	2.67	3.85 %
Plasticiser 2	PEG 400 (Poly(ethylene glycol))	3.2	4.61 %
Binder	Butvar® B-98	4.8	6.92 %
Solvent 2	MEK : EtOH (50:50)	2.13	3.07 %

Each material was added to the mixture within a plastic mixing pot, in order of appearance in the above table, using either sterilised pipettes for any liquids or a spatula, cleaned with acetone, for any solids. Details of the chemicals and solvents used are listed in table 3.3. Once the powders and solvents had been added together in the plastic mixing pot, the pot was placed into a spinning mixer (model: "SpeedMixer^{TM}", DAC 800 FVZ, 8003021, Hauschild Engineering, Germany) for approximately 10 minutes, at 2100 revolutions per minute (rpm), until the mixture resembles a homogenous, honey-like consistency, with no visible bubbles.

Table 3. 3 List of materials used in the production of MLCC's.

Chemical Name	Also Known As (a.k.a.)	Manufacturer	Batch Number
2-Butanone, ACS reagent, ≥99.0%	**MEK**, Methyl ethyl ketone, Ethyl methyl ketone	Sigma-Aldrich	Lot# SHBF2462V
Ethanol	EtOH, AnalaR NORMAPUR	VWR® PROLABO®	Product: 20821.330 Batch: 11K250512
Butvar® B-98	n/a	Sigma Life Science	Lot# SLBH2178V
Benzyl butyl phthalate	n/a	Aldrich Chemistry	Lot# MKBL5086V
Kollisolv® PEG E 400	**PEG**, Lutrol® E 400, Macrogol 400, Poly(ethylene glycol), Polyethylene glycol 400	Sigma Life Science	Lot# BCBL6294V
Hypermer KD-1	n/a	Croda Europe Ltd.	GH0904
Platinum electrode paste	Platinum Internal Electrode	Heraeus	Lot No. 127147307

The slurry was then poured into the stainless steel tape casting hopper, in such a way that the slurry had an even spread across the width of the stainless steel blades as the slurry was drawn out onto the moving sheet of acetate. The blades and acetate were set at a height and speed such that the tape being cast was approximately 350µm thick, and then left to dry in a well-ventilated area overnight.

The tape was then collected and cut into square sections, using conventional scissors, and further cut into a grid of 4x4 smaller squares, using the University of Sheffield's own sheet cutting jig (figure 3.2), made for purpose by Medway Cutters (Whitstable, Kent, UK), and a uniaxial press (Model: Kennedy® HBP030, Hydraulic Ram, 30 tonne capacity).

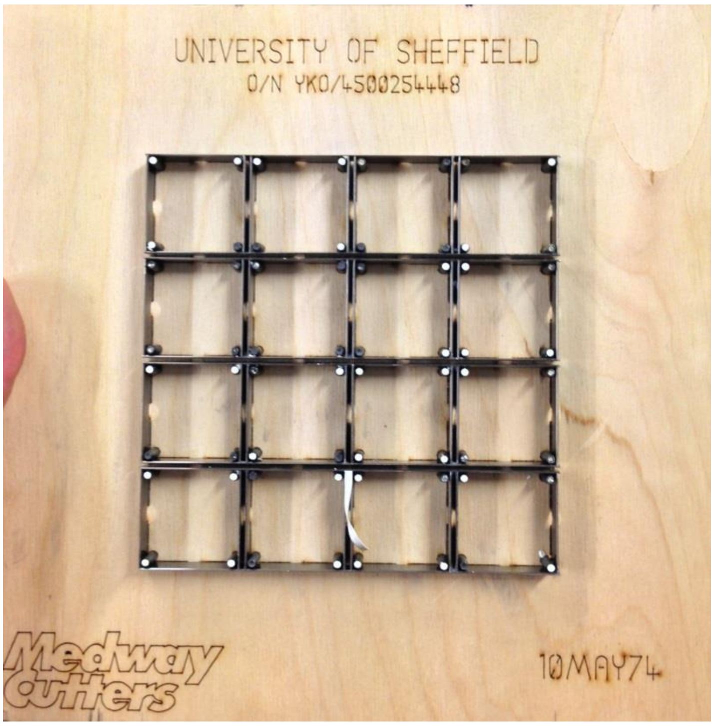

Figure 3. 2 Sheet cutting jig for multilayers, made by Medway Cutters for the University of Sheffield.

Platinum electrodes were screen printed onto the 4x4 grid using a screen printer (model: DEK 247, DEK printing machines, serial no. 64286-01, batch no. 59410, Weymouth, England) and platinum electrode paste (Heraeus, Electronic Materials, Item: M637C, Lot No. 127147307, Hanau, Germany), ensuring the cut sheets were aligned with the shape of the screen printer. The screen-printed sheets were left in a drying oven at 50°C, overnight, to dry the platinum ink. The layers were then stacked using a purpose-made, steel jig (figure 3.3), with blank sheets used as the first and last layer, to align the layers correctly, ensuring that alternate electrode layers were placed at 180° to each other.

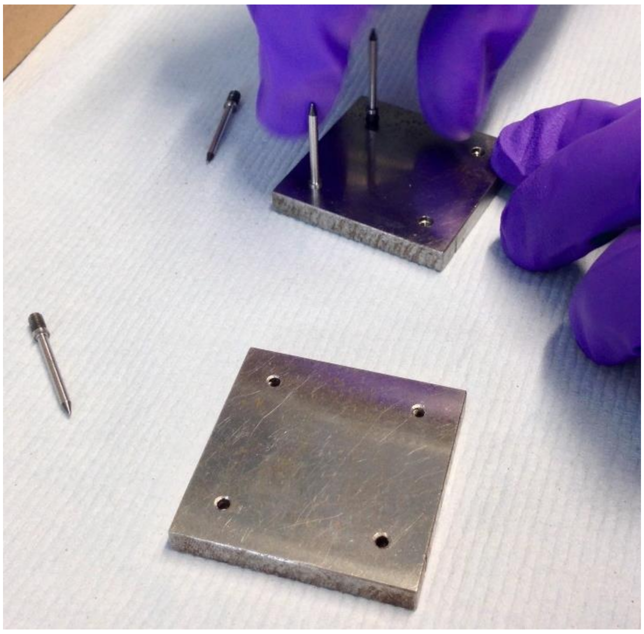

Figure 3. 3 Steel stacking jig used for stacking layers with accurate alignment.

Once the required number of layers have been stacked, the stack was pressed between two plates for approximately 10 minutes with an approximate loading of 200 kg. The stack was then diced into four individual green capacitors, and vacuum-sealed within an electrostatic shielding bag (Statshield®, Anti-Static Heat Seal ESD-Safe Bag, RS Components Ltd., Stock No. 287-7773) using a heated vacuum packing device (Model V.100, La.Va Premium Linie, Manfred Landig, Valentinstraße 35-1, Germany) for further pressing within a cold isostatic press (CIP; Autoclave Engineers, Serial Number: 06-03550005, Notified body #0871, Erie, PA, USA) for 5 minutes, under a pressure of ~200 MPa.

The MLCC's underwent a lengthy sintering process of approximately 57 hours; in order to carefully burn away the binder and plasticiser without causing delamination between the layers of the capacitor. The sintering steps were as follows (figure 3.4):

1. Heating at 1°C/min to 350°C, hold for 16 hours;
2. heating at 1°C/min to 550°C, hold for 4 hours;
3. heating at 3°C/min to 1200°C, hold for 4 hours;
4. cooling at 1°C/min to room temperature.

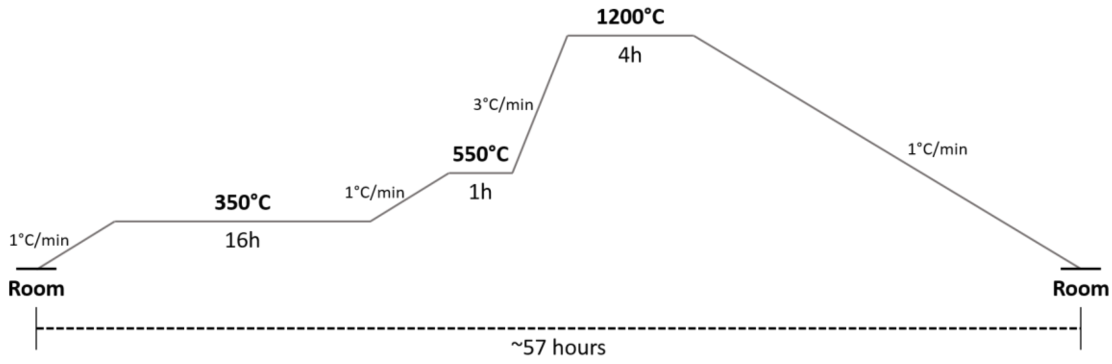

Figure 3. 4 Outline of the MLCC sintering process, beginning and ending at ambient, room temperature.

When completed, samples were collected, labelled and prepared for electrical testing.

3.2 Characterisation

3.2.1 Pellet Dimensions and Densities

The thickness and diameter of each pellet was measured using a pair of digital callipers (Mitutoyo Absolute, Code No. 500-196-20, Model No. CD-6" CSX, Serial No. 09085232, Mitutoyo Corp., Kawasaki, Japan) across 5 points on each dimension and averaged.

The density of each pellet was determined using Archimedes' Principle, using a Mettler Toledo (Type: NewClassic MF, Model: MS104S /01, Max = 120g, d = 0.1mg, made in Switzerland) density kit. The Archimedes' principle establishes that the apparent weight of an object decreases in a liquid equal to the weight of the volume that is displaced.

The pellets were first weighed in air, followed by being weighed in distilled water. The temperature of the water at the time of measuring each pellet was noted each time, so that density would be correctly calculated with respect to the density of the water. The following equation was used by the density kit to calculate the density of each sample:

$$\rho = \frac{A}{A-B}(\rho_O + \rho_L) + \rho_L$$

(3.1)

Where ρ, A, B, ρ_O and ρ_L are density, weight of sample in air, weight of sample in liquid, density of air (0.0012g/cm^3) and density of liquid, respectively.

An approximate bulk density of each pellet was calculated from the volume of each pellet and their mass, and compared with the volume obtained by Archimedes' Principle.

3.2.2 Relative Density

Relative density was calculated through comparison with the density of the pure sample, which is represented as a percentage of the pure sample density, through the following method:

$$\%_{\rho} = \left(\frac{\rho_n}{\rho_0}\right) \times 100$$

(3.2)

where
$\%_{\rho}$ = the relative density of the sample;
ρ_n = the density of the composite sample;
ρ_0 = the density of the pure sample.

3.2.3 Microwave Dielectric Analysis

The microwave dielectric properties of each sample were determined using a network analyser (Advantest R3767CH Network Analyser, 40Mhz – 8GHz, Tokyo, Japan), connected via coaxial cables to a brass cavity of known dimensions (25mm diameter and 20mm in height) with a low-loss fused silica spacer within the cavity with a known height (4.77mm). Each ceramic puck sample was placed on top of the spacer within the centre of the cavity.

The permittivity of each sample was determined using the Kajfez-Guillion method [3] with the aid of a program called DRRECALC, which was provided by the manufacturer of the network analyser. The program required the following to be known in order to calculate ε_r and unloaded quality factor (Q_U): the thickness and diameter of each pellet, the height of the cavity and the spacer within, the resonant frequency (f_0), the insertion loss (s_{21} in dB) and the loaded quality factor (Q_L) of the samples. Q_L was calculated by dividing f_0 by $f_{\Delta 3dB}$.

$$Q_L = \frac{f_0}{f_{\Delta 3dB}}$$

(3.3)

f_0, s_{21} and $f_{\Delta 3dB}$ were all obtained directly from the network analyser, where $f_{\Delta 3dB}$ was obtained from measuring the width of the resonant peak 3 decibels (dB) below the maximum amplitude of the peak. The Q_U was multiplied with the resonant frequency to give the quality factor Qf_0, measured in GHz.

$$Qf_0 = Q_U \times f_0$$

(3.4)

The TCF was obtained by tracking the drift of f_0 with increasing temperature, using a Peltier device to heat the cavity through 5 set points, between 20°C and 80°C, allowing 30 minutes between each point for the temperature to equilibrate within the cavity and pellet. Accurate measurements of temperature were acquired using a T-type thermocouple (-185°C$< x <$ 300°C) and a thermocouple reader. The TCF was then calculated using equation 3.5 [4], where the terms were modified to account for fluctuations in ambient temperature:

$$TCF = \left(\frac{(f_T - f_{T_o})}{f_{T_O}(T - T_o)}\right) \times 10^6$$

(3.5)

where:

f_T = the resonant frequency at maximum temperature °C;
f_{T_O} = the resonant frequency at the original ambient temperature °C;
T = the maximum temperature °C;
T_O = the original ambient temperature °C.

In order to gauge the accuracy of the TCF value, the TCF was obtained from the slope of a linear equation of the form of $y = mx + c$, where m gives the value of TCF in parts per million per °C (ppm/°C). The frequency change with temperature was recorded onto a table (e.g. table 3.4), and was plotted as a series of points, with values of temperature on the horizontal axis and values of [f_0 x10^6]/f on the vertical axis. A line of best fit was then taken from the series. From here, the coefficient of determination (R^2) was used to measure how well the line of best fit represented the data, and therefore how well the TCF value from equation 3.5 represented the true TCF of the material.

Table 3. 4 An empty table for recording information needed to calculate the TCF of a material.

Set	Temperature (°C)	Time	S_{21}	Frequency (GHz)	(f_0 x10^6)/f
Off					
1					
2					
3					
4					

3.2.4 X-Ray Diffraction (XRD)

XRD was used to determine and confirm the crystalline phases present in all fabricated compositions. All samples were in powder form, therefore any bulk sample used was crushed and ground using a quartz mortar and pestle in acetone. Samples were placed in a plastic sample holder, using a glass slide to ensure a flattened surface.

Two pieces of XRD equipment were used: a Siemens D500 (Kristallo-Flex 710H X-ray generator) and Siemens D5000 (Kristallo-Flex 710D X-ray generator). Both machines used Cu radiation source at the following operating conditions: 40kV, 30mA, operating in reflection geometry, maximum 2θ range of 3 to 140°2θ. Both instruments were each operated at ambient temperature, at 2θ angles between 10° - 80°, with a step size of 0.050° 2θ, in reflection mode.

Processing of the raw data was conducted using WinX^{Pow} software (version 2.10, Germany) and the analysis of the diffraction patterns was conducted using PDF 4+ software. Table 3.5 lists the standard XRD ICDD card numbers used in this project.

Table 3. 5 A list of the standard XRD ICCD cards used in this project.

Chemical Compositions	ICDD Card Numbers
$CaTiO_3$	01-077-8908 [5]
$CaTiO_3$	01-077-8909 [5]
$Li_{0.5}Nd_{0.5}TiO_3$	04-005-6196 [6]
$(Li_{0.3125}Nd_{0.5625})TiO_3$	00-046-0461 [7]
$(Li_{0.3125}Nd_{0.5625})TiO_3$	00-046-0462 [7]
$(Li_{0.5}Sm_{0.5})TiO_3$	04-006-1962 [8]
Nd Pyrochlore – $Nd_2Ti_2O_7$	04-005-7194 [9]
Sm Pyrochlore – $Sm_2Ti_2O_7$	04-008-6356 [10]
Sm Pyrochlore – $Sm_2Ti_2O_7$	00-047-0283 [11]
$Bi_4B_2O_9$	00-025-1089 [12]

3.2.5 Scanning Electron Microscopy (SEM)

A JEOL, JSM-6400 scanning electron microscope (Tokyo, Japan) was used at an accelerating voltage of 20kV at a working distance of 15-25mm. Polished and fracture surfaces of each sample were analysed, with no thermal or chemical etching. The polished surfaces were imaged in both the secondary electron imaging (SEI) and backscatter electron (BE) imaging modes. The fracture surfaces were only imaged under the SEI mode. Energy dispersive spectroscopy (EDS) was used on both polished and fracture surfaces to obtain a semi-quantitative analysis of the elements present in each sample. SEI was used to see any microstructural features on the samples and BE imaging was used alongside SEI to distinguish areas of differing elemental composition.

Polished samples were prepared by grinding the surface through successively finer grades of silicon carbide (SiC) paper, from 280, 400, 800 and 1600 grit grades, and then polished using diamond paste, from 6μm, 3μm and 1μm diamond paste, on polishing cloths with a water based lubricant. For even distribution of pressure during grinding and polishing, samples were temporarily mounted onto single-sample stubs with thermoplastic wax, and a figure of eight motion was employed. Special care was taken during the polishing stage in order to obtain a high quality polished surface.

Both polished and fracture surface samples were mounted onto aluminium stubs using silver electrodag (Agar Scientific Ltd., Electrodag 1415, 50g, G364, Batch No.: 136656066) and carbon coated using a coating unit ("SpeediVac" ™, Coating Unit, Model: 12E6/1598, Edwards High Vacuum Ltd., Crawley, England) to avoid charging.

Multilayer ceramic capacitor (MLCC) samples were mounted in 5:1 epoxy resin (5 parts EpoColor^{TM} Epoxy Resin, 20-8143-032, 1 part EpoColor^{TM} Epoxy Hardener, 20-8144-008; Buehler, USA), held upright with small, steel coils such that the cross-section would be visible across the face of the resin puck. The resin was left to harden overnight, and the sample, held in the resin, was then polished and carbon coated as previously described. MLCC samples were imaged using a Philips XL-30S FEG scanning electron microscope, fitted with an EDS (EDAX) system, with an accelerating voltage of 20kV.

3.2.6 Transmission Electron Microscopy (TEM)

A Philips, EM 420 transmission electron microscope (Eindhoven, Holland) was used at an accelerating voltage of 120kV, using single-tilt and dual-tilt sample holders for bright-field imaging, electron diffraction and EDS analysis on all samples in order to obtain qualitative data on microstructure and chemical distribution in the samples. The EDS detector used was a Link Analytical EDS detector, which was attached to the Philips EM 420.

Samples were prepared by polishing sintered samples and gluing the polished side onto a stub using thermoplastic wax (Agar Scientific). The unpolished side was then ground on 1200 grit SiC paper to an approximate thickness of >50μm. Once thin enough, the samples were mounted onto a copper ring (Agar Scientific, product: G2600C, 3mm external diameter, 1mm internal diameter hole) with a 2-part araldite glue. The samples were then further thinned such that it would be electron-transparent using a Duo Ion Mill (Model 600, Gatan, USA), operating at 4.5kV with a total current of 0.8mA. The samples were ion beam milled at an incident angle of 15° for 2-6 hours, at 1-2 hour intervals, until a hole could be seen under a standard optical microscope, upon which they were further milled at an incident angle of 12° for a further 30 minutes, to ensure the edges of the hole would be as thin as possible.

Samples were handled with exceptional care and were stored in plastic capsules to avoid damage and contamination.

Once a diffraction pattern had been resolved, bright-field (BF) images were obtained using an aperture to eliminate all ‘light’ apart from a spot which formed the image. The contrast in the BF images is called diffraction contrast.

CrystalMaker® for Windows [13] and SingleCrystal^{TM} for Windows [14] software was used to perform kinematic simulations of electron diffraction patterns. The atomic positions, lattice parameter and space group of each structure were inputted into the CrystalMaker® software which then calculated a structure model and associated reciprocal lattice, and imported into SingleCrystal^{TM}. The kinematic simulation of the electron diffraction pattern was taken as the plane of the reciprocal lattice normal to the chosen zone axis.

3.2.7 LCR Measurements of MLCC’s

A Hewlett Packard (HP), Precision LCR Meter (model: 4284A, 20Hz – 1MHz, serial number: 2940J03342, made in Japan) was used to take the LCR measurements. Readings were taken at 1kHz, 10kHz, 100kHz, 250kHz and 1MHz, every minute over a temperature sweep from room temperature to ~100°C, at 1°C/min, with an applied voltage of 100mV.

Samples were prepared by first polishing the two end-terminals of the MLCC’s to fully reveal the internal electrodes, which were then subsequently coated with a gold electrode paste ensuring that the paste on either side does not overlap, causing a short-circuit. The samples were placed in a furnace set to 200°C between coatings such that the gold paste was dry enough to coat the opposite side. Once coated, the samples were placed in a furnace at 650°C, for 3 hours and 30 minutes to sinter the gold external electrodes onto the samples. The prepared samples were then attached to the LCR meter via platinum wires housed within an in-house created jig, which would be seated within a small, conventional tube furnace.

3.2.8 Impedance Measurements of MLCC’s

An Agilent Precision LCR Meter (model: E4980A, 20Hz – 2MHz) was used to take impedance measurements of all samples. Readings were taken at set temperatures over a frequency sweep between 20 Hz and 1 MHz, with an applied voltage of 100mV. The temperature range for all readings were between room temperature and ~200°C, with emphasis on temperatures between room temperature and ~100°C.

The samples were prepared in precisely the same manner used for LCR measurements, above. For the purpose of comparison, the same samples were used for both LCR and Impedance measurements.

3.2.9 Evaluation of Errors

Every measurement taken is usually accompanied with some degree of uncertainty. These errors were considered at each stage of sample preparation and characterisation. There were multiple repeats of measurements to give a mean value and a corresponding standard deviation.

By and large, measurements can only be as accurate as the instruments used to measure the parameters. In general, the highest precision instrument was used at each stage. For example, the weighing scales used were capable of measuring to a precision of 0.0001g, also known as ‘four significant figures’. Therefore, when manipulating multiple parameters with each other, the end value cannot be more accurate than the lowest precision parameter used.

Additionally, within every measurement, random errors may still be introduced, which are usually out of the control of the user, introducing a level of uncertainty. These errors may arise from small, unnoticed variations in the techniques employed, small environmental changes, such as temperature or the movement of air on the plate of a weighing scale, slightly affecting the value on the readout at the time of measurement. In the end, however, these random fluctuations will average-out of the results if a large enough number of repeats are undertaken. As a result, there will be a standard deviation of results to consider for each data point, which provides the error bars within figures, and an evaluation can be made as to the accuracy the data, usually written as “$\pm x$”.

The ± values were calculated using a common percentage error equation (eq. 3.6), which was then multiplied against the original values.

$$\%\ error = \left|\frac{n_E - n_A}{n_E}\right| \times 100$$

(3.6)

where
n_E = the exact number;
n_A = the average/approximate number.

3.3 References

[1] X. Chen, W. Zhang, B. Zalinska, I. Sterianou, S. Bai, and I. M. Reaney, “Low Sintering Temperature Microwave Dielectric Ceramics and Composites Based on Bi_2O_3-B_2O_3,” *J. Am. Ceram. Soc.*, vol. 95, no. 10, pp. 3207–3213, Oct. 2012.

[2] M.-J. Pan and C. A. Randall, “A brief introduction to ceramic capacitors,” *IEEE Electr. Insul. Mag.*, vol. 26, no. 3, pp. 44–50, May 2010.

[3] D. Kajfez and P. Guillon, *Dielectric Resonators*. Artech House, Dedham, MA, 1986.

[4] I. M. Reaney and D. Iddles, “Microwave Dielectric Ceramics for Resonators and Filters in Mobile Phone Networks,” *J. Am. Ceram. Soc.*, vol. 89, no. 7, pp. 2063–2072, Apr. 2006.

[5] M. Yashima and R. Ali, “Structural phase transition and octahedral tilting in the calcium titanate perovskite CaTiO3,” *Solid State Ionics*, vol. 180, no. 2–3, pp. 120–126, 2009.

[6] A. G. Belous, G. N. Novitskaya, S. V Polyanetskaya, and Y. I. Gornikov, “The crystal-chemical and electrophysical characteristics of the complex oxides $Ln_{2/3-x}M_{3x}TiO_3$,” *Russ. J. Inorg. Chem*, vol. 32, pp. 156–157, 1987.

[7] A. D. Robertson, S. G. Martin, A. Coats, and A. R. West, “Phase diagrams and crystal chemistry in the Li^+ ion conducting perovskites, $Li_{0.5-3x}RE_{0.5+x}TiO_3$: Re = La, Nd,” *J. Mater. Chem.*, vol. 5, no. 9, pp. 1405–1412, 1995.

[8] S. M. Emel’yanov and G. Geguzina, “Preparation and investigation of new oxides $A'_{0.5}A''_{0.5}BO_3$ with perovskite-type structure,” *Izv. Akad. Nauk SSSR, Neorg. Mater.*, vol. 20, no. 12, pp. 2005–2008, 1984.

[9] V. N. Agafonov, V. A. Davydov, N. V. Porotnikov, and K. I. Petrov, “Vibrational Spectroscopic Study of the Structure of the Compounds $Ln_2Ti_2O_7$ (Ln = La, Pr, and Nd) and the High-pressure Phase of Sm2Ti2O7,” *Russ. J. Inorg. Chem*, vol. 28, p. 817, 1979.

[10] Y. Tabira, R. L. Withers, L. Minervini, and R. W. Grimes, “Systematic Structural Change in Selected Rare Earth Oxide Pyrochlores as Determined by Wide-Angle CBED and a Comparison with the Results of Atomistic Computer Simulation,” *J. Solid State Chem.*, vol. 153, no. 1, pp. 16–25, 2000.

[11] V. G. Zubkov, “X-ray Powder Diffraction Pattern and Digitized Diffractograms (.PD3) of New Inorganic Compounds,” *ICDD Grant-in-Aid*. Institute of Solid State Chemistry of Sciences, Ural Branch of the Russian Academy, Russia, 1997.

[12] E. M. Levin and C. L. McDaniel, “The System Bi_2O-B_2O_3,” *J. Am. Ceram. Soc.*, vol. 45, no. 8, pp. 355–360, Aug. 1962.

[13] C. S. Ltd., “CrystalMaker® for Windows.” CrystalMaker Software Ltd., http://www.crystalmaker.com/, 2016.

[14] C. S. Ltd., “SingleCrystalTM for Windows.” CrystalMaker Software Ltd., http://www.crystalmaker.com/, 2016.

Results and Discussion

Chapter 4: Investigations into $0.2CaTiO_3$ – $0.8(Li_{0.5}Nd_{0.5})TiO_3$ (CTLNT) with $Bi_4B_2O_9$ (BBO) sintering aid.

4.1 Introduction

Over the past 30 years within portable, handheld satellite communications, growth has been driven by the need for physically and electrically smaller devices. In microwave (MW) dielectrics, this has resulted in research and development of higher-permittivity (ε_r) ceramics, since the size of the product decreases by a factor of $\sqrt{\varepsilon_r}$ for a given frequency [1]. However, the increase in ε_r must not be to the detriment of both the MW quality factor (Qf_0) and the temperature coefficient of resonant frequency (τ_f) which, along with ε_r, are the three most important parameters in MW dielectrics.

For a ceramic to be used as an antenna substrate $20 < \varepsilon_r < 130$, Qf_0 must be large enough so that the ceramic does not dominate the dielectric over the metallisation losses, and $\tau_f \approx \pm 10$ ppm/°C. However, for small substrates (higher ε_r) the bandwidth becomes increasingly narrow and data transmission rates may decrease. These parameters and responses are conflict against each other in the design of substrates for radio frequency (RF) applications.

There are many temperature stable ceramics currently used for antenna and resonator applications. For physically and electrically small dielectrically loaded antennas (DLAs), barium RE titanate (BRET) based compositions are often used but where size is not as critical and a greater efficiency/bandwidth are required (Ca,Mg)TiO_3 (CMT), $BaTi_4O_9$ (BT4) and (Zr,Sn)TiO_4 (ZTS) based compositions dominate. The latter 3 compositions have the advantage of lower raw material costs in comparison with many other commercial MW ceramics, which contain either Nb, Ta or RE ions. As a result of the above factors, the development of materials for DLA applications is essentially split in two directions: high permittivity for miniaturisation for high value products and lower processing and raw material costs for mass market applications.

For physically and electrically ultra-small antennas, high permittivities are required and there is much interest in the ceramic system $CaTiO_3$-$(Li_{0.5}RE_{0.5})TiO_3$ (CTLRET) which was first reported in the 1990s [2], [3], and later optimized by Kim *et al*. with $0.3CaTiO_3$-$0.7(Li_{0.5}Sm_{0.5})TiO_3$ having ε_r=114, Qf_0=3700 GHz and τ_f of 11.5 ppm/°C [4].

In an increased attempt to make these high-end materials more accessible, research into using sintering aids to reduce the high sintering temperatures and, therefore, cost has been explored.

However, the use of sintering aids, which usually facilitates a liquid-phase sintering route, often has a detrimental effect on one, or more, of the MW dielectric properties of the material.

A case in point is the work by Aziz *et al.* [5], who showed that $0.2CaTiO_3$-$0.8(Li_{0.5}Nd_{0.5})TiO_3$ (CTLNT) could be reduced in sintering temperature to <1300°C but not without deteriorating ε_r and Qf_0. However, in 2012, Chen and co-workers [6] fabricated a CTLRET material using $Bi_4B_2O_9$ (BBO) as a sintering aid and reduced the sintering temperature to 1200°C, whist maintaining >95% theoretical density and very good MW dielectric properties of ε_r=127, Qf_0=2700 GHz and τ_f of 4 ppm/°C. In addition, these authors reported a similar lowering of sintering temperature whilst improving properties (Qf_0 = 6000 GHz, ε_r = 86) for BRET based ceramics, thereby demonstrating that the right choice of sintering aid is critical to controlling the properties of MW ceramics. Despite what is a significant contribution in the fabrication of lower cost, low loss MW dielectric ceramics, the lack of understanding of how BBO simultaneously aided densification and improved performance limits our ability to design further bespoke sintering aids for other ceramic systems.

This chapter is, therefore, a detailed examination of the role of BBO in the densification and enhancement of the material properties of the Sheffield flagship composite material $(1\text{-}x)$CTLNT-xBBO. With this understanding, comes the hope of guiding the synthesis of designer or bespoke sintering aids for other MW ceramics.

4.2 Phase Assemblage

Initial fabrication routes followed that of previous work [6], with test reactions conducted to confirm and adjust calcination temperatures as necessary. Powder X-Ray diffraction (XRD) was conducted on test samples of pure $0.2CaTiO_3$-$0.8(Li_{0.5}Nd_{0.5})TiO_3$ (CTLNT) and that of $Bi_4B_2O_9$ (BBO). Figure 4. 1-figure 4. 2 shows the presence of a secondary phase in the 1100°C sample, which was identified as an $A_2B_2O_7$ pyrochlore-structured compound (ICDD: 04-005-7194, figure 4. 2 [7]) but which was absent in samples calcined at 1150°C. There were no ICDD cards in the database for CTLNT solid solution and therefore, XRD traces for CTLNT were compared with ICDD cards for $CaTiO_3$ (ICDD: 01-077-8908 [8]), $(Li_{0.5}Nd_{0.5})TiO_3$ (ICDD: 04-005-6196 [9]) and $(Li_{0.3125}Nd_{0.5625})TiO_3$ (ICDD: 00-046-0461 [10]), figure 4. 3.

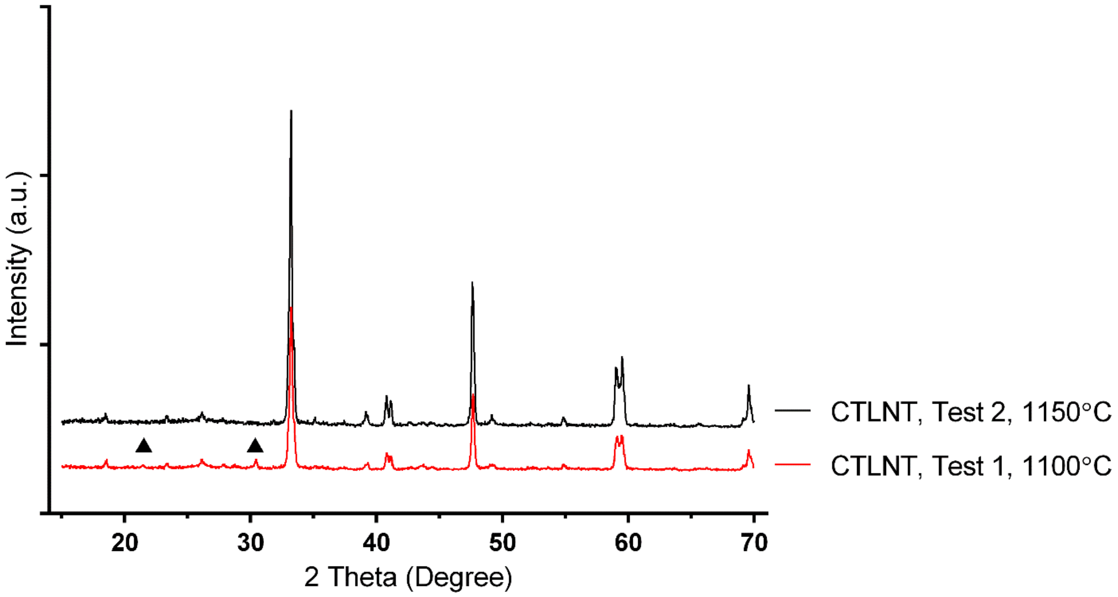

Figure 4. 1 XRD of two CTLNT test reactions at 1100°C and 1150°C, showing the presence of a secondary, pyrochlore phase.

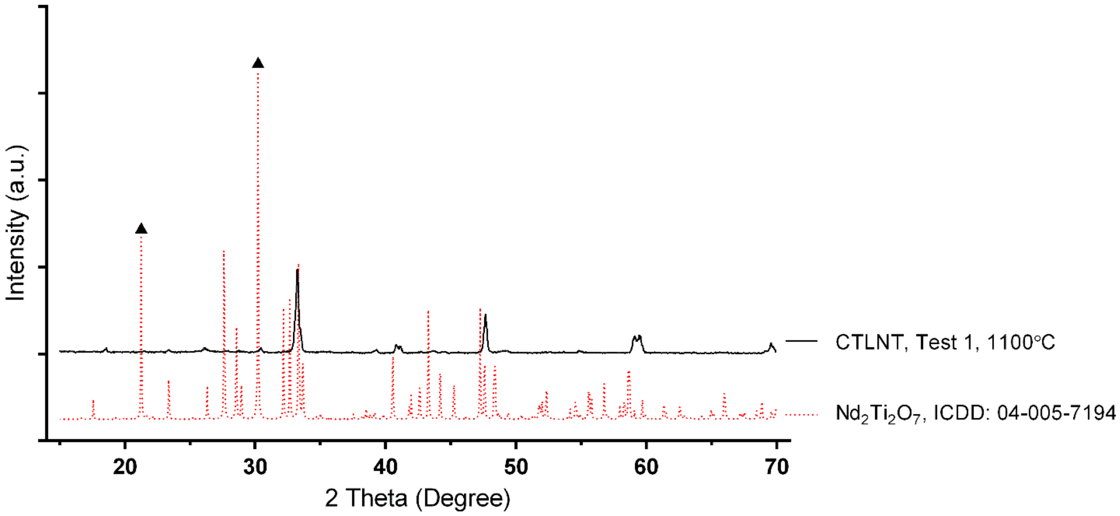

Figure 4. 2 XRD Comparison between CTLNT Test 1 with the ICCD card for $Nd_2Ti_2O_7$ pyrochlore structure, where the two main peaks of the ICDD card matches the main peaks of secondary phase of the test sample, labelled with solid triangles.

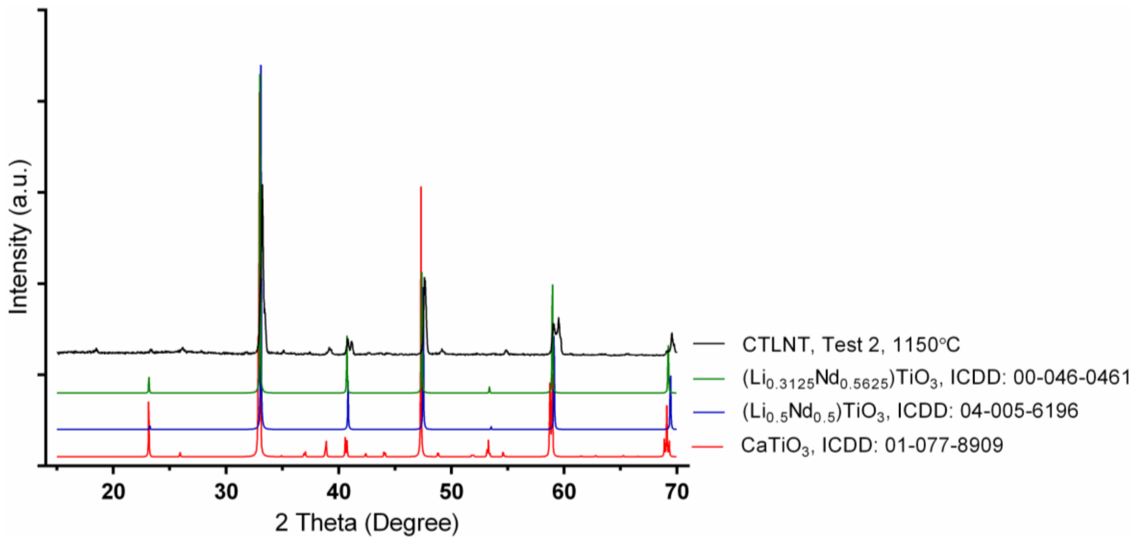

Figure 4. 3 XRD of CTLNT test 2, compared with 3 other ICDD cards in order to resolve all peaks.

Based on previous work by Chen *et al*. [6], BBO was calcined at 650°C and 660°C, and analysed against existing ICDD: 00-025-1089, figure 4. 4. The optimal calcination temperature for single-phase $Bi_4B_2O_9$ was 660°C at which temperature no secondary phases (arrowed) were observed.

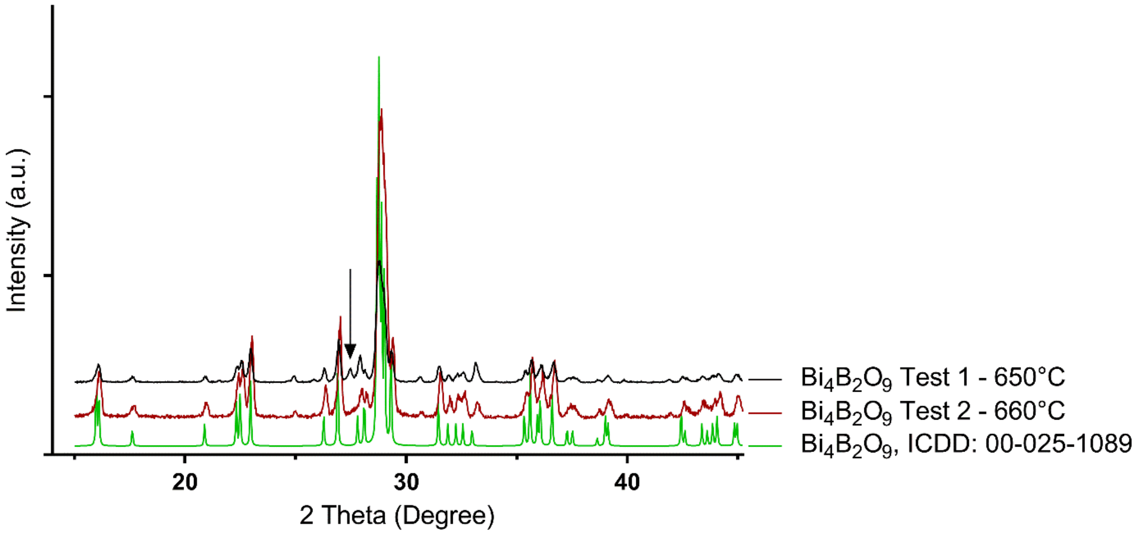

Figure 4. 4 XRD confirmation of single-phase $Bi_4B_2O_9$ compared with the database ICDD card data for $Bi_4B_2O_9$. Arrowed is an indication of secondary phase at 650°C, no longer present at 660°C.

XRD patterns of crushed CTLNT+ xBBO composite samples over a range of sintering temperatures are shown in figure 4. 5. Both figure 4.5 a) and b) show no discrepancy in phase assemblage up to 5wt% BBO, irrespective of sintering temperature. All composite compositions were indexed according to a perovskite phase with a similar symmetry and structure to room temperature $CaTiO_3$ (ICDD card no. 01-077-8909), $(Li_{0.5}Nd_{0.5})TiO_3$ (ICDD card no. 04-005-6196) and $(Li_{0.3125}Nd_{0.5625})TiO_3$ (ICDD card no. 00-046-0462). However, previous work by Chen *et al*. has shown the appearance of unidentified secondary phases at $x \geq 7.5$wt% BBO [6].

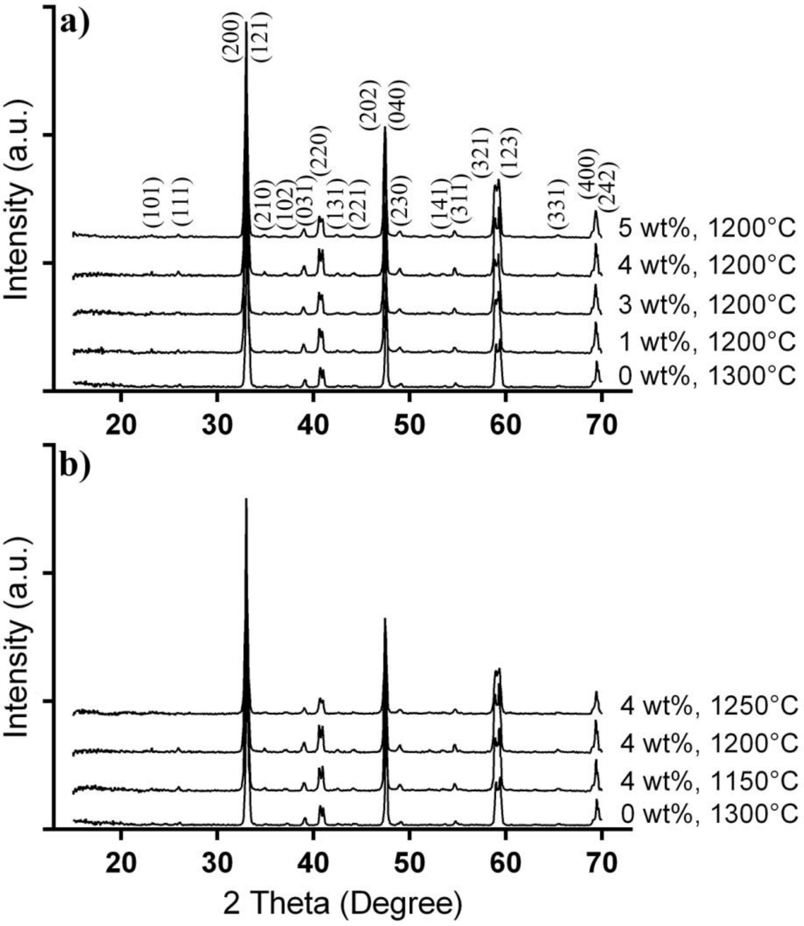

Figure 4. 5 X-Ray diffraction patterns of a) CTLNT + $x$wt% BBO compositions, sintered at 1200°C, and b) CTLNT + 4wt% BBO at different sintering temperatures, compared with pure CTLNT sintered at 1300°C.

4.3 Shrinkage and Density

Ceramics are micro-crystalline solid materials produced by sintering, at high temperatures such that the particles fuse together to reduce surface free energy, thereby shrinking the material. This process produces a material which is tightly packed, very hard and in principle dense but pores and pockets of air can often remain within the structure [11].

The densities of all (1-x)CTLNT-xBBO compositions were measured using the Archimedes' principle which takes into account the presence of pores by weighing the samples both in the air and within the liquid. The measured densities are then compared with the theoretical density, which was calculated from the XRD data to give a % theoretical density.

Table 4. 1 lists the densities and linear shrinkages of all (1-*x*)CTLNT-*x*BBO compositions, and figure 4. 6 compares both the average densities and linear shrinkage of each composition over three sintering temperatures. The % theoretical density of the composite samples were calculated based on the 'rule of mixtures' densities from the theoretical densities of the CTLNT and BBO.

Table 4. 1 List of densities and linear shrinkages of the (1-*x*)CTLNT-*x*BBO compositions, including the pure CTLNT and BBO for comparison.

Sample Type	Sintering Temperature (°C)	Density (g/cm^3) (±0.02)	% Theoretical Density (±0.3)	Shrinkage (%) (±0.1)
CTLNT	1300	4.83	99.3	17.8
$Bi_4B_2O_9$	650	7.49	91.5	16.0
1wt%	1150	4.43	90.7	15.2
	1200	4.70	96.1	17.2
	1250	4.79	98.1	17.5
3wt%	1150	4.51	91.7	16.5
	1200	4.68	96.1	17.5
	1250	4.74	96.4	17.9
4wt%	1150	4.65	94.0	16.2
	1200	4.76	96.2	17.1
	1250	4.72	95.4	17.7
5wt%	1150	4.54	92.9	13.8
	1200	4.72	94.1	15.7
	1250	4.78	95.7	16.2

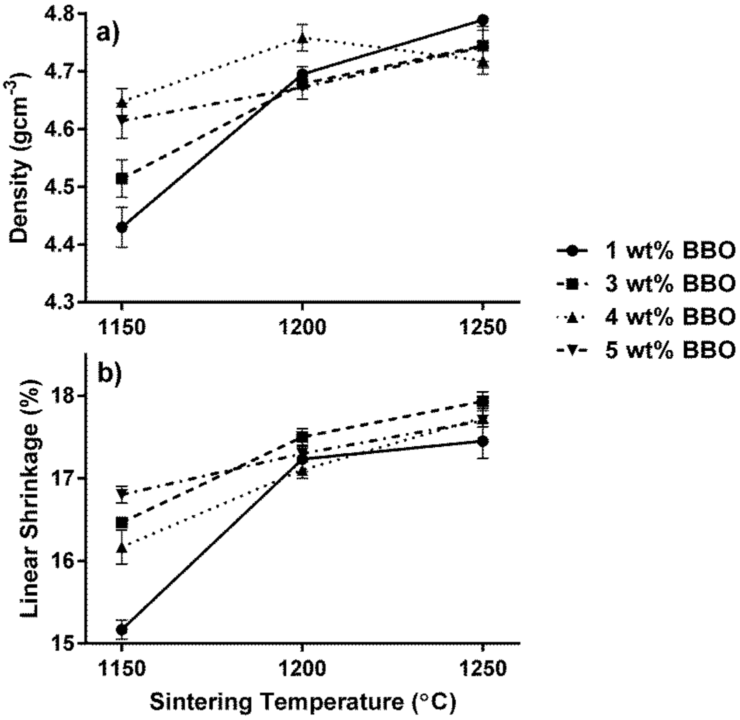

Figure 4. 6 Average relationships of sintering temperature and composition with that of a) density and b) linear shrinkage.

There is a positive trend between increased sintering temperatures with increased densities and linear shrinkages. Generally, increasing the BBO concentration also increases the density and shrinkage, with a stronger effect at lower sintering temperatures. The 1wt% BBO composition appears to have the largest variation in density and linear shrinkage between 1150°C and 1250°C. Samples with 4wt% BBO have the highest peak density at 1200°C, although this peak density does not appear to relate to a maximum peak in linear shrinkage. Additionally, samples with 3wt% BBO appear to have the largest linear shrinkage above 1200°C. Table 4. 1 indicates that no composite achieves a greater density than that of the pure CTLNT. However, it should be noted that, for a pure CTLNT sample, optimum densities are achieved at sintering temperatures of ≥1350°C [5], [6], [12]. The density of pure CTLNT, sintered at 1200°C, was reported to be ≈4.61 gcm^{-3} by Chen *et al* [6]. Therefore, at 1200°C, densities are improved even with BBO additions as low as 1wt%.

The increase in density with increased BBO concentration, at lower sintering temperatures, suggests that it promotes sintering, most likely due to liquid phase formation since BBO melts at ~700°C [6]. It should be noted that BBO has a higher density (7.49 gcm^{-3}) than that of CTLNT and therefore an increase in density with increasing addition of sintering aid is anticipated. However, the actual increase in density is far greater than anticipated from a simple rule of mixtures. For example, from the simple rule of mixtures, the anticipated density for 1wt% and 5wt% is 4.84 and 4.91 gcm^{-3}, respectively, using the pure CTLNT and BBO densities of 4.83 gcm^{-3} and 7.49 gcm^{-3}, respectively. The difference between these two densities is only 0.07 gcm^{-3}, while the difference between the 1 and 5wt% compositions, sintered at 1200°C, is 0.18 gcm^{-3}. All Values of density are reported with an error of ± 0.02 gcm^{-3}.

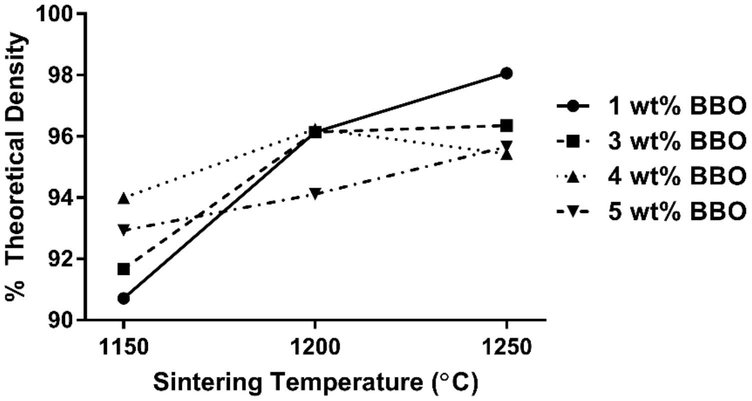

Figure 4. 7 % Theoretical densities of the composite samples, where the theoretical density is taken from the rule of mixtures between the theoretical densities of the CTLNT and BBO materials.

4.4 Microstructure Observations from Scanning Electron Microscopy (SEM)

The microstructure is important in that it often dictates MW dielectric properties, in particular the quality factor. Pores are the most obvious microstructural feature and can be considered as a phase in their own right, with their own MW properties which will influence the overall properties. Secondary phases, particularly at grain boundaries, can also lead to a reduction in the MW properties depending on the nature of the phase. Scanning electron microscopy (SEM) was therefore carried out on all composite samples to establish a link between microstructure and the MW properties.

For each sample, secondary electron imaging (SEI) was conducted on the fracture surface and SEI and backscatter electron (BE) imaging on the polished surface. The polished surfaces were neither thermally nor chemically etched but studied as polished to discern the distribution of porosity and regions of differing atomic number.

Energy-dispersive X-Ray spectroscopy (EDS) analysis was conducted to investigate the differences between the observed microstructures and regional contrast differences in the previous SEM images for the CTLNT composite ceramics. Note that all EDS data recorded and presented here are semi-quantitative, not fully quantitative, while lithium is not able to be detected under EDS and boron is difficult to distinguish from carbon, which is used as the conductive coating on the samples. The lighter elements, such as boron, have low photon energies, which can lead to complications such as having large re-absorptions in the sample [13]. Theoretical weight and atomic percentages for pure CTLNT have been calculated and included with the EDS results of the CTLNT compounds for comparison, with Li removed as it would not be included in the raw data from the detector.

CTLNT + 1wt% BBO Compositions

The following figures (figure 4. 8 to figure 4. 12) highlight the differences in morphology between sintering temperatures for CTLNT + 1wt% BBO compositions. At 1150°C, figure 4. 8, both the SEI and BE image of the polished surface reveal a highly porous sample. The BE image, figure 4. 8 b), indicates that, despite additions of BBO, the sample appears is homogenous and predominantly single phase. The fracture surface, figure 4. 8 c), is irregular, with an average grain size of 1-3µm.

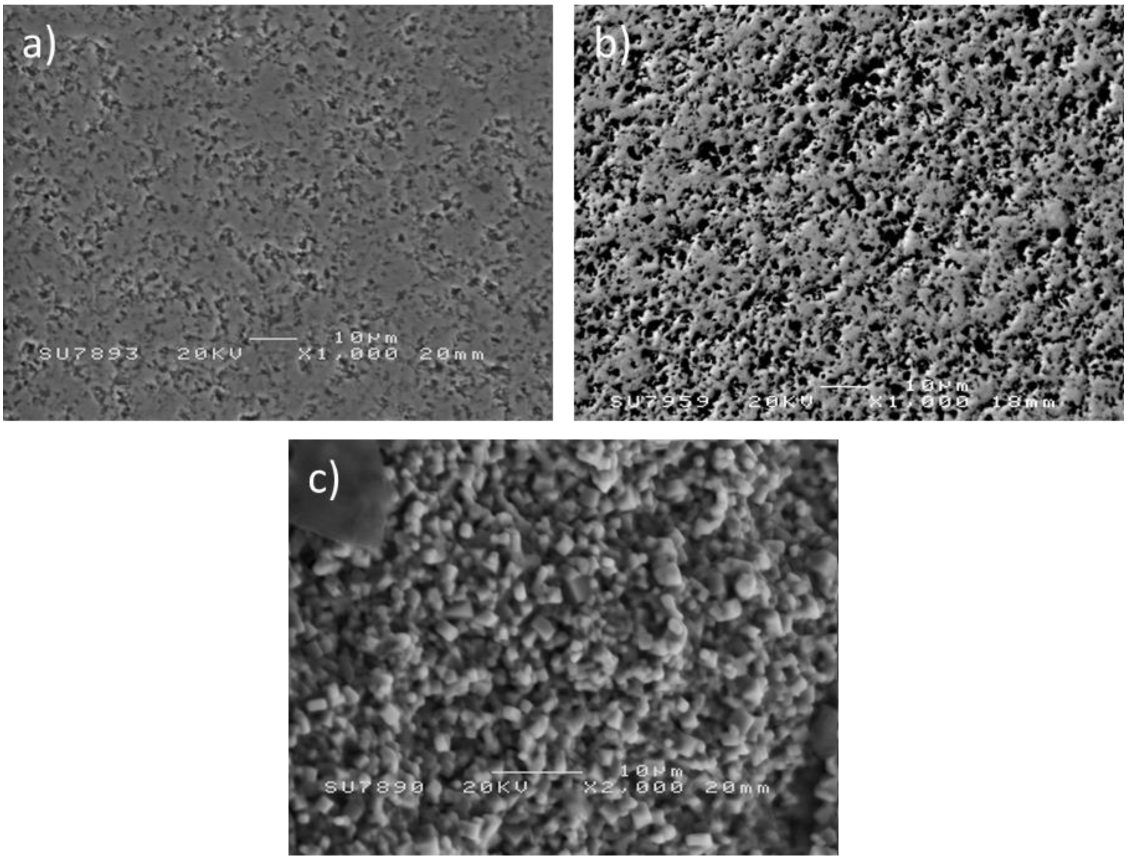

Figure 4. 8 SEM images of the 1wt% BBO composition, sintered at 1150°C for 4 hours, showing the a) SEI of the polished surface, b) BE image of the polished surface and c) SEI of the fracture surface.

At 1200°C, figure 4. 9, the polished surface reveals a reduction in porosity and the sample remains homogenous, as evidenced by the lack of large contrast variation in the BE image, figure 4. 9 b). The fracture surface, additionally, reveals regular cuboid grain structure, with an average grain size between 2-4μm.

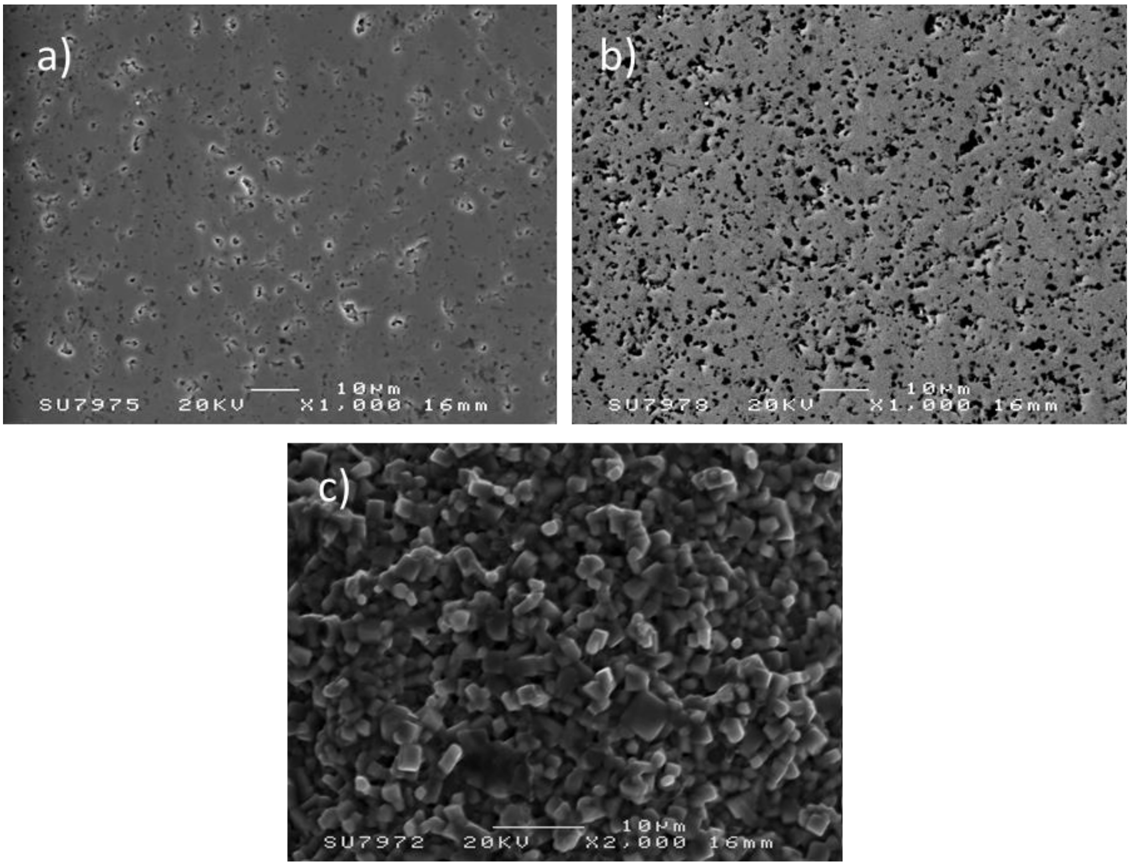

Figure 4. 9 SEM images of the 1wt% BBO composition, sintered at 1200°C for 4 hours, showing the a) SEI of the polished surface, the b) BE image of the polished surface and the c) SEI of the fracture surface.

At 1250°C, Figure 4. 10, CTLNT + 1wt% BBO compositions exhibit a decrease in porosity when compared with samples sintered at 1150°C and 1200°C, which can more easily be seen from the BE image of the polished surface, figure 4. 10 b). As with all previous BE images, regions which are completely black are where there is no returned signal to the equipment (pore). Apart from the pores, figure 4. 10 b) reveals no other gradation of contrast, and thus it is assumed that the CTLNT + 1wt% BBO remains a homogenous, essentially single phase material at 1250°C.

In addition to the change in porosity, the fracture surface, figure 4. 10c), further reveals a cuboid grain morphology as well as a slightly larger average grain sizes of 3-5μm.

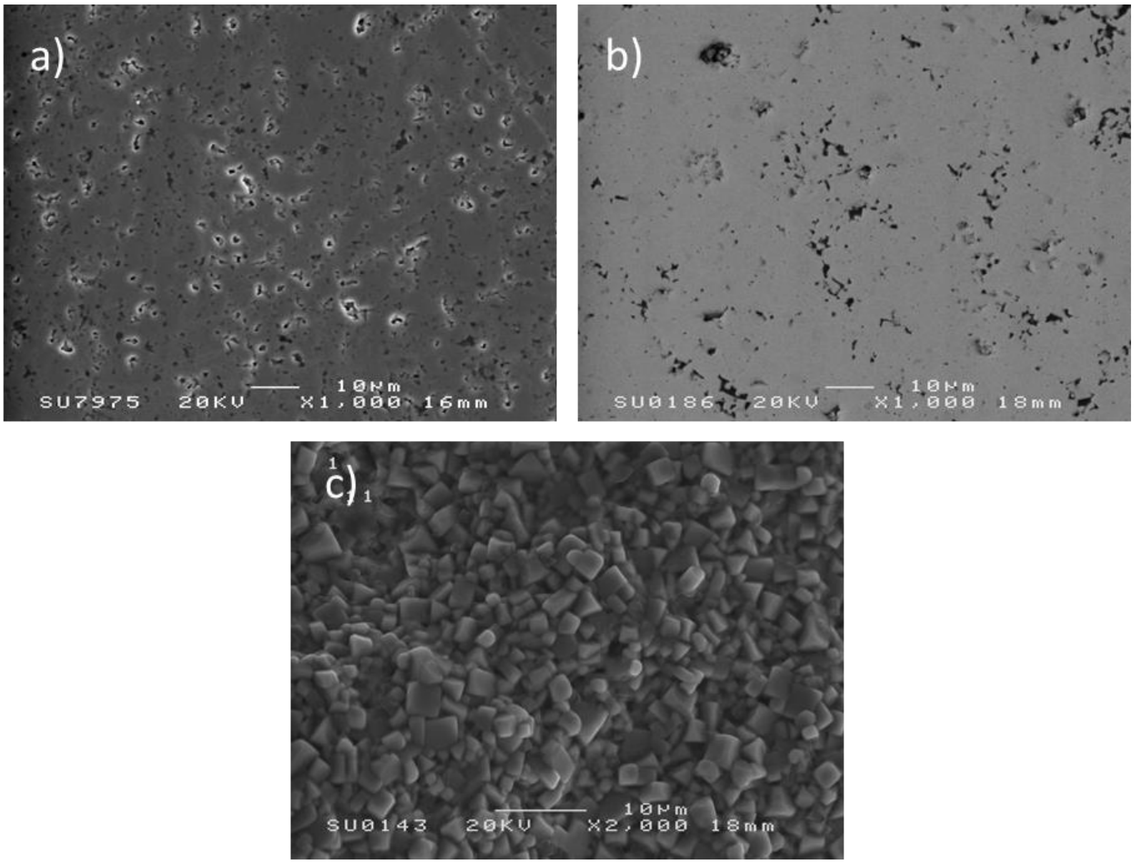

Figure 4. 10 SEM images of the 1wt% BBO composition, sintered at 1250°C for 4 hours, showing the a) SEI of the polished surface, b) BE image of the polished surface and c) SEI of the fracture surface.

Figure 4. 11 is a more direct comparison of the fracture surfaces of the CTLNT + 1wt% BBO composition at three different sintering temperatures, highlighting the regular cuboid grains and the change in average grain size with sintering temperature.

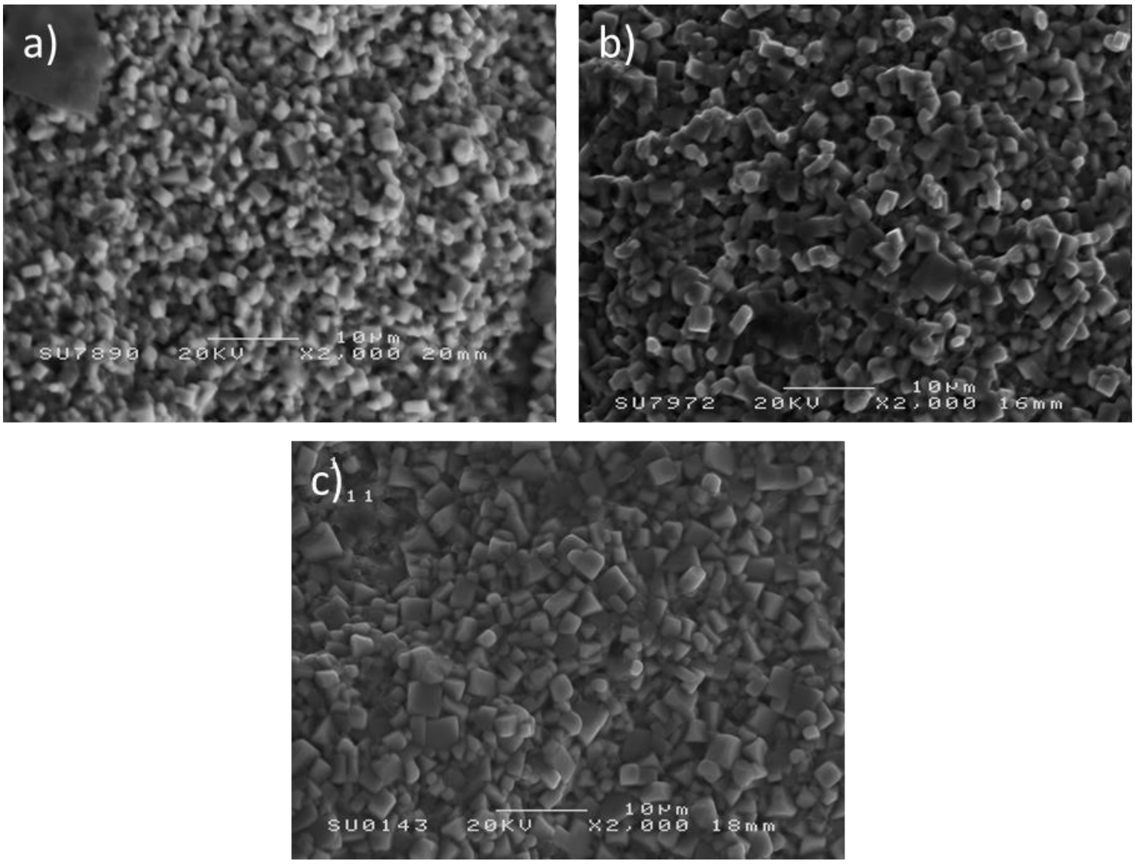

Figure 4. 11 SEM SEI images of the 1wt% BBO system, highlighting the change in the size of the grains over increased sintering temperatures, where a) is 1150°C, b) is 1200°C and c) is 1250°C.

Figure 4. 12 is a direct comparison of the polished surface images, illustrating the effect that sintering temperature has on porosity. The ceramic is significantly less porous at the higher sintering temperature of 1250°C, compared with at 1150°C. This matches well with the increase in density and linear shrinkages, figure 4. 6, as fewer pores correlate with higher density.

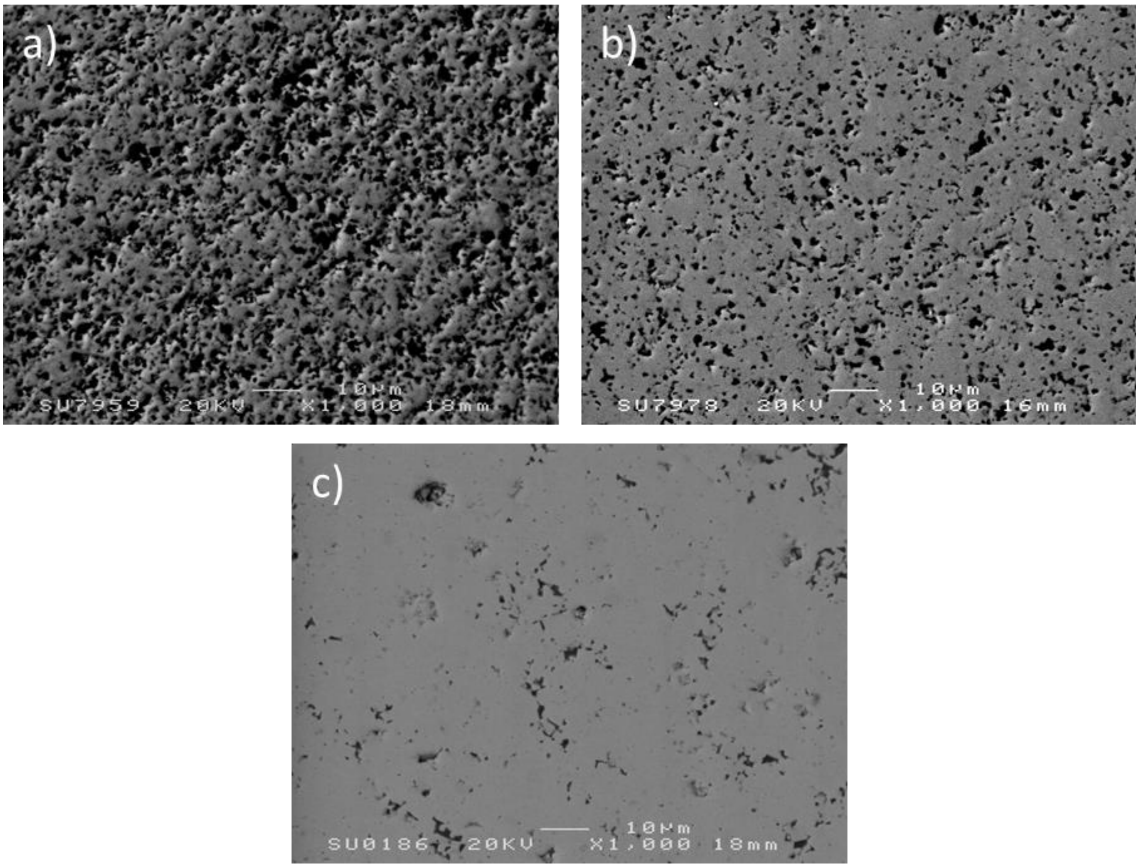

Figure 4. 12 SEM BE images of the 1wt% BBO system, showing decreased porosity with increased sintering temperature, where a) is 1150°C, b) is 1200°C and c) is 1250°C.

The fracture surface of a 1wt% BBO composite CTLNT sample, sintered at 1200°C, is shown in figure 4. 13. Spectra were taken from the grains (spectrum 1) and amorphous phase (spectrum 2) which was found after careful inspection. Peaks were automatically labelled within the EDS scanning software, and weight and atomic percentages are displayed in table 4. 2. Carbon is present and expected in all spectra since all samples have been carbon coated. Spectrum 1 indicates that the grains contain all of the elements expected for pure CTLNT. While the proportions for spectrum 1 in figure 4. 13 are not particularly close to the calculated proportions for a pure sample; this may simply be due to the fact that the data was collected on an uneven surface. The amorphous phase has reduced levels of all elements, with exception to oxygen, and indicates the presence of sulphur. The sulphur peak is likely a mislabelled Bi peak, since the Kα peak of sulphur and the M peak of Bi are very similar.

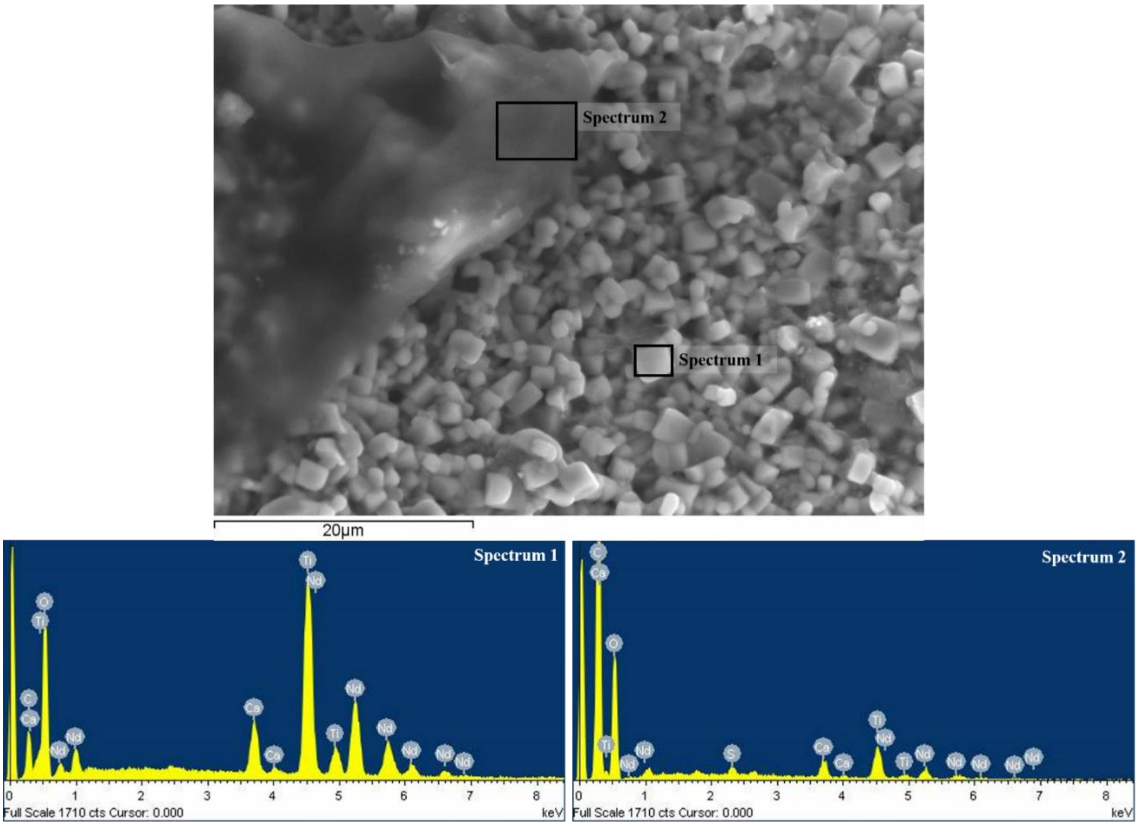

Figure 4. 13 EDS of CTLNT + 1wt% BBO composite fracture surface. Spectrum 1 is a typical representation of the grains, and spectrum 2 is of an amorphous material. The image depicting the locations of the EDS is a SEI.

Table 4. 2 List of elements detected by the EDS equipment used for each of the spectra in figure 4. 13, above. Results for the spectra are semi-quantitative and automatically calculated. Theoretical calculations, in weight and atomic %, for pure CTLNT is included for comparison. The sulphur in Spectrum 2 is likely mislabelled bismuth.

Pure CTLNT (Calculated)			**Spectrum 1**			**Spectrum 2**		
Element	Weight %	Atomic %	Element	Weight%	Atomic%	Element	Weight%	Atomic%
O	36.16	68.18	O Kα	47.61	80.43	O Kα	85.95	95.80
Ca	6.04	4.55	Ca Kα	3.58	2.42	S Kα	0.75	0.42
Ti	36.06	22.73	Ti Kα	21.22	11.98	Ca Kα	2.25	0.99
Nd	21.73	4.55	Nd Lα	27.59	5.17	Ti Kα	5.71	2.14
						Nd Lα	5.34	0.65
Totals	100	100	Totals	100	100	Totals	100	100

Figure 4. 14 is the polished sample of the 1wt% BBO composition, sintered at 1200°C, where spectrum 1 is of the average matrix surface and spectrum 2 is of a darker contrast region along a fault on the surface of the sample.

Table 4. 3 lists the various elements detected in figure 4. 14 for both spectra in weight and atomic %. Elemental quantities from the polished surface are more accurate representations and more comparable with the theoretical calculation for pure CTLNT, due to there being very little topological variation. From table 4. 3, spectrum 1 has roughly the same proportions of CTLNT elements, compared with the theoretical quantities, with slightly elevated quantities of oxygen and Nd, and reduced levels of Ca and Ti. There is also the presence of small quantities of Bi. The numbers are only qualitative, however, so some error margins should be considered. Having said that, the matrix phase appears to be very similar to that of the calculated proportion of pure CTLNT. Spectrum 2 appears to be predominantly composed of oxygen with much reduced levels of Ca, Ti and Nd. The darker contrast region in spectrum 2 suggests a region of lower atomic density, which would indicate a region which is rich in B, which is difficult to detect. This may relate to the elevated levels of oxygen as BBO is rich in oxygen. The appearance of Ca, Ti and Nd within this B-rich region would suggest that this region is relatively thin at the location of spectrum 2, allowing for more elements from the matrix to be detected through the darker phase.

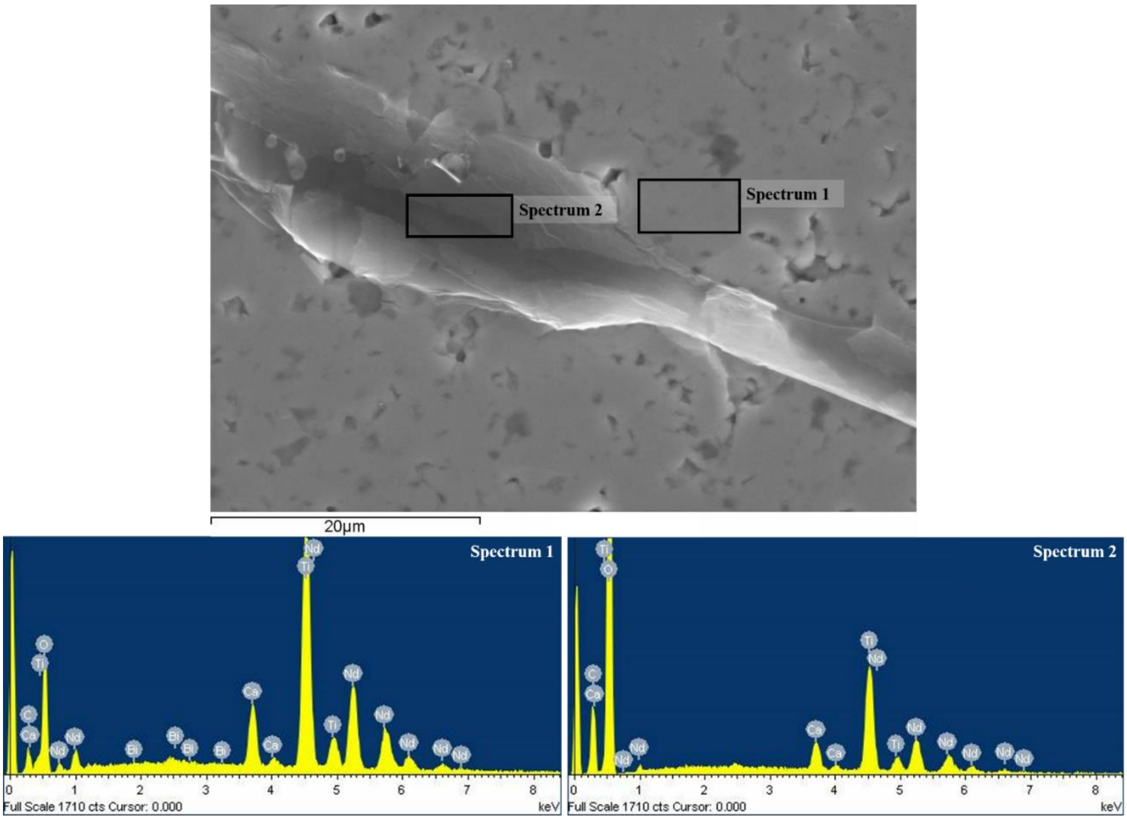

Figure 4. 14 EDS of CTLNT + 1wt% BBO composite polished surface. Spectrum 1 is of the polished matrix surface and spectrum 2 is of an amorphous phase. The image depicting the locations of the EDS is a SEI.

Table 4. 3 List of elements detected by the EDS equipment used for each of the spectra in figure 4. 14, above. Results for the spectra are qualitative and automatically calculated. Theoretical calculations, in weight and atomic %, for pure CTLNT is included for comparison.

Pure CTLNT (Calculated)			**Spectrum 1**			**Spectrum 2**		
Element	Weight %	Atomic %	Element	Weight%	Atomic%	Element	Weight%	Atomic%
O	36.16	68.18	O Kα	37.66	73.08	O Kα	77.43	93.67
Ca	6.04	4.55	Ca Kα	4.45	3.45	Ca Kα	1.82	0.88
Ti	36.06	22.73	Ti Kα	25.53	16.55	Ti Kα	9.89	4.00
Nd	21.73	4.55	Nd Lα	31.48	6.78	Nd Lα	10.86	1.46
			Bi M	0.89	0.13			
Totals	100	100	Totals	100	100	Totals	100	100

CTLNT + 3wt% BBO Compositions

Compositions with 3wt% BBO differ to that of the 1wt% BBO system, as illustrated by the following figures (figure 4. 15 to figure 4. 18). The polished surface of the 3wt% BBO system, sintered at 1150°C, figure 4. 15 a) and b), is less porous, compared with the 1wt% BBO system, at lower sintering temperatures. Additionally, the BE image in figure 4. 15 b) reveals a homogeneous contrast characteristic of a single-phase material. The fracture surface, at 1150°C, reveals a greater abundance of cuboid grains compared with the 1wt% BBO system, figure 4. 15 c), with grain sizes ranging from ~1-4µm. The increase in grain size suggests that sintering is occurring at lower temperatures with greater wt% BBO.

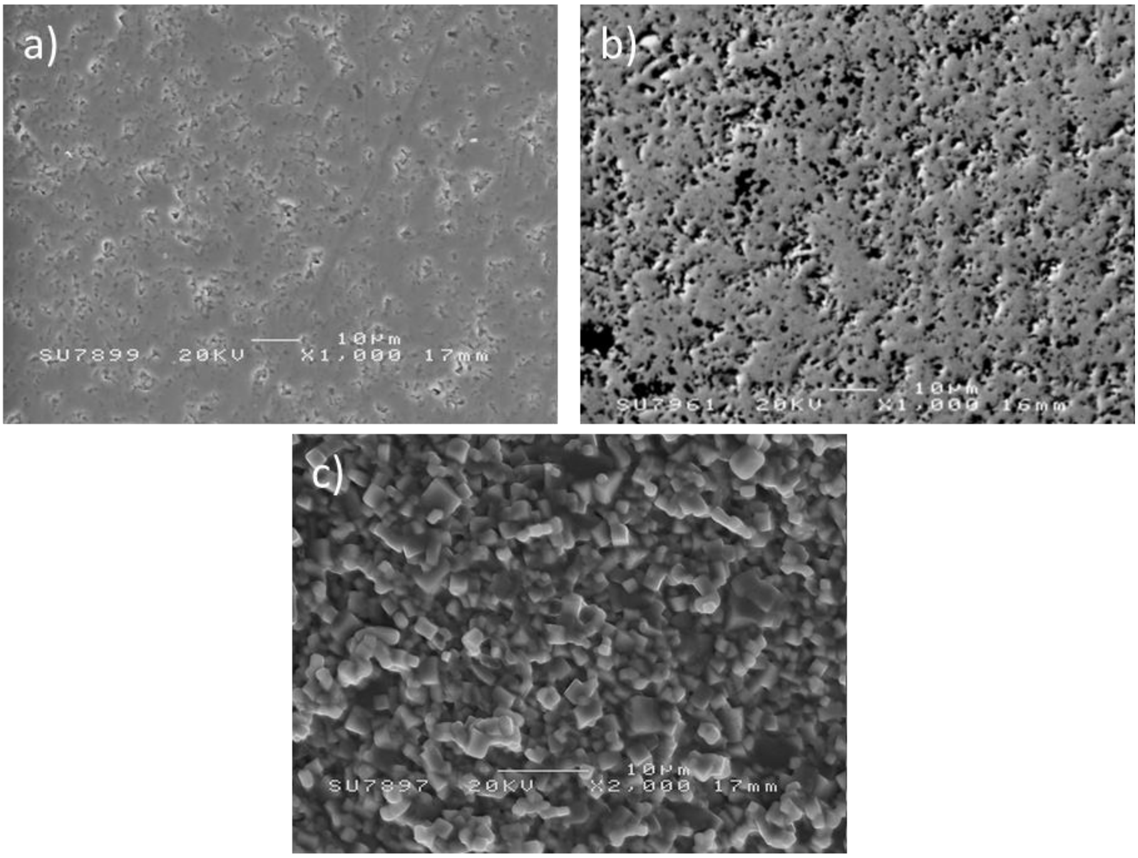

Figure 4. 15 SEM images of the 3wt% BBO composition, sintered at 1150°C for 4 hours, showing a) SEI of the polished surface, b) BE image of the polished surface and c) SEI of the fracture surface.

At a sintering temperature of 1200°C, the polished surface, figure 4. 16 a) and b), of the 3wt% BBO system follows similar trends to samples with 1 wt % BBO system, i.e. there are fewer pores with increasing sintering temperature. The BE image in figure 4. 16 b) continues to indicate an essentially homogeneous microstructure characteristic of a single-phase material but weak contrast variations are apparent in the SEI, figure 4. 16 a). The fracture surface, figure 4. 16 c), however, clearly reveals the largest difference between the 1 and 3wt% BBO systems in that the latter compositions show clear evidence of atomic number (effectively density) contrast (darker regions) on the polished surface and a ‘glue-like’ phase with no evidence of a grain structure. The presence of regions with darker contrast than the matrix suggests a material with lower electron density (which would emit fewer electrons). Since BBO has a higher density than CTLNT, the regions are most likely B-rich compared with that of the matrix and given the propensity of B_2O_3 to form low melting point glasses, amorphous at room temperature but liquid at the sintering temperature. This assumption is consistent with the absence of an apparent grain structure for these regions in the fracture surface. Conversely, there are also regions of brighter contrast (higher electron dense phase), which may be residual BBO or more likely Bi rich regions in the matrix. The presence of B_2O_3 rich regions in addition to Bi rich regions of the matrix would suggest that the BBO reacts with the matrix and decomposes into a B-rich liquid phase, losing Bi to the matrix. However, without further TEM studies this mechanism, however plausible, is speculative. Aside from the liquid phase, the grain size of the matrix has increased with increasing sintering temperature to 3-5µm, in addition to being more defined and regular in shape.

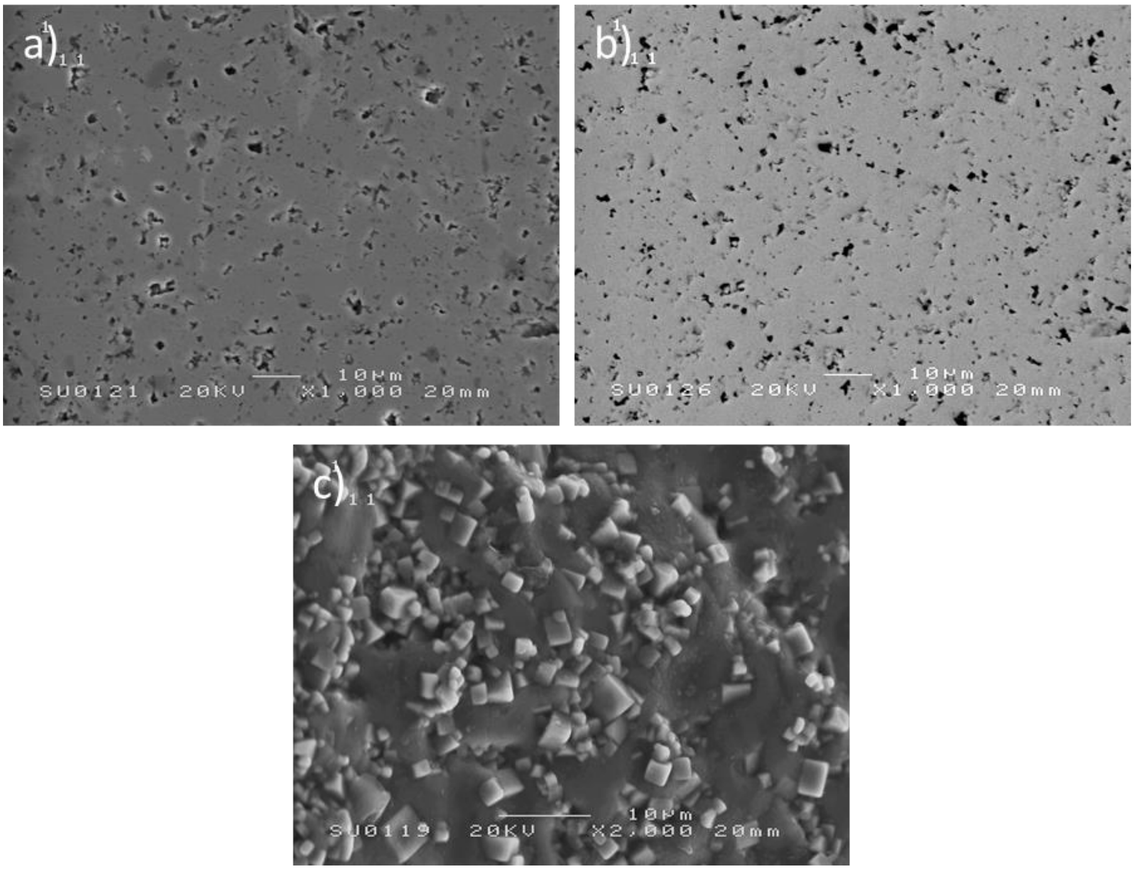

Figure 4. 16 SEM images of the 3wt% BBO composition, sintered at 1200°C for 4 hours, showing the a) SEI of the polished surface, the b) BE image of the polished surface and the c) SEI of the fracture surface.

In the 3wt% BBO sample sintered at 1250°C, there is little change in the porosity of the material, figure 4. 17 a) and b), compared with lower sintering temperatures but in the BE image of the polished surface, figure 4. 17 b), which was taken in the same location as the SEI image, figure 4. 17 a), there is now slight evidence of variations in contrast in the SEI image. These regions are likely to be similar to the proposed liquid phase discussed above and thus B-rich liquid. However, in this sample there are no brighter regions, such as those found at 1200°C. Once again, the fracture surface, figure 4. 17 c), exposes the presence of liquid phase and illustrate a larger average grain size (4-6μm) associated with a higher sintering temperature. The anomalously larger amount of apparent glassy phase in the fracture surfaces compared with the area of darker regions in polished samples may be explained by considering that the glassy regions are likely sites which initiate fracture and thus are inevitably more abundant in samples prepared in this manner.

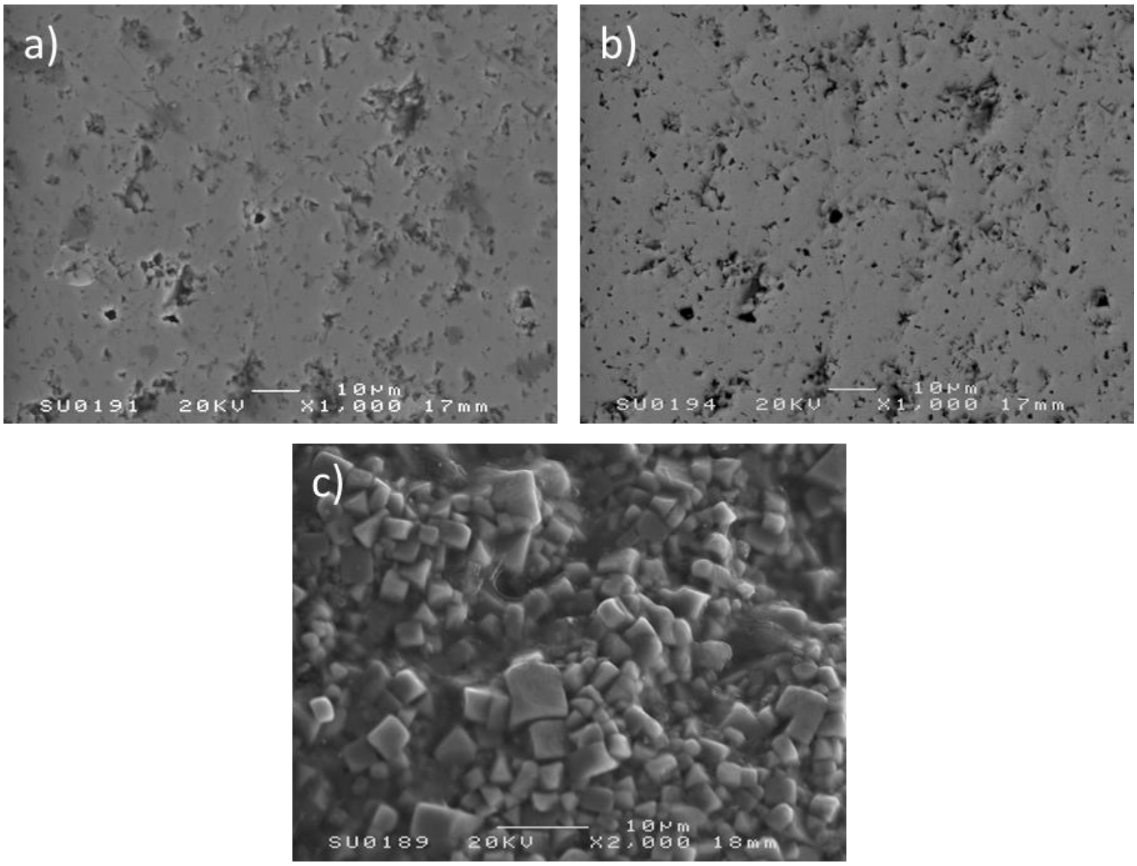

Figure 4. 17 SEM images of the 3wt% BBO composition, sintered at 1250°C for 4 hours, showing the a) SEI of the polished surface, the b) BE image of the polished surface and the c) SEI of the fracture surface.

The differences between the 3wt% BBO samples, with respect to the change in sintering temperature, is more clearly illustrated in comparing figure 4. 18 and figure 4. 19. The fracture surface, figure 4. 18, underlines the general trend of increasing grain size and regularity with increasing sintering temperature. Perhaps most importantly is the presence of the assumed B-rich glassy phase surrounding the matrix. This is also observed in the polished surfaces, figure 4. 19, where the BE images suggest the presence of 'darker' secondary phases, with lower electron density. The overall reduction in apparent porosity as the sintering temperature is increased from 1150-1250°C fits well with the density and shrinkage data in figure 4. 6 and table 4. 1.

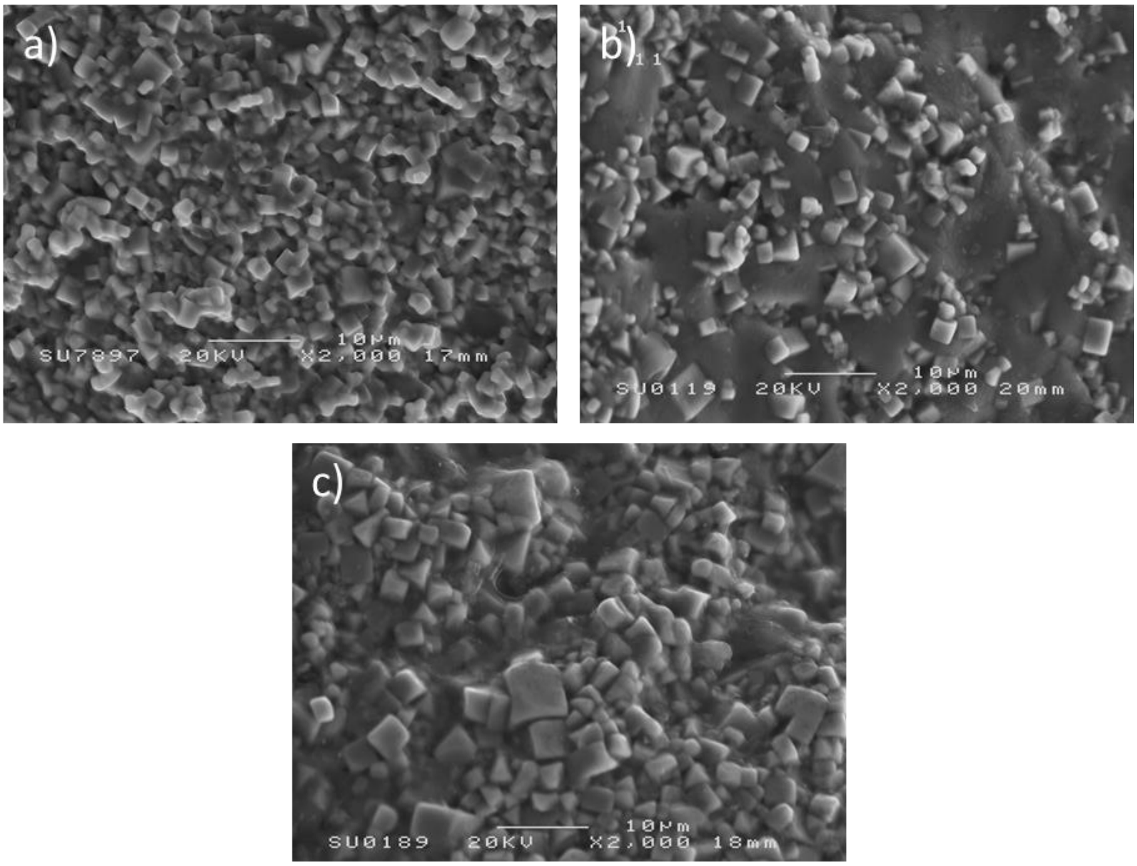

Figure 4. 18 SEM SEI, fracture surface images, of the 3wt% BBO system, illustrating the change in the size of the grains, and the introduction of liquid phase, over increased sintering temperatures, where a) is 1150°C, b) is 1200°C and c) is 1250°C.

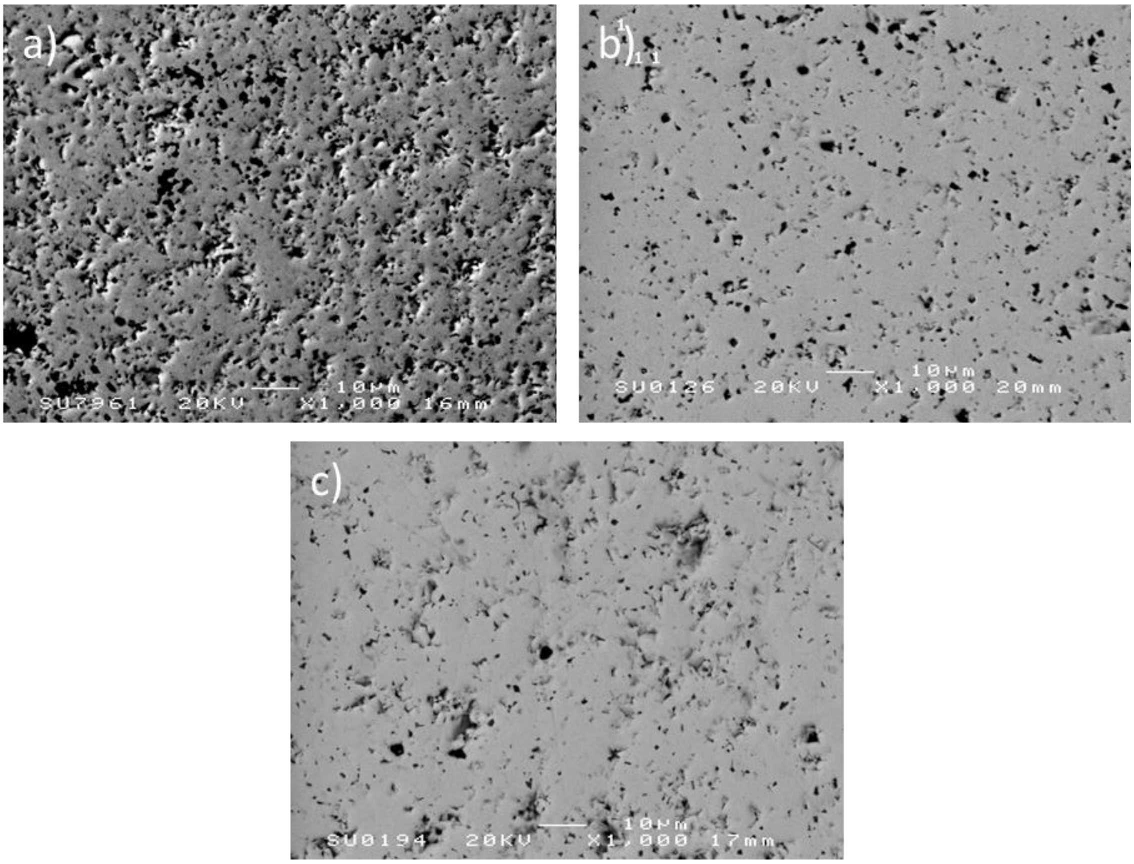

Figure 4. 19 SEM BE, polished surface images, of the 3wt% BBO system, showing decreased porosity, and the presence of possible secondary-phase, over increased sintering temperatures, where a) is 1150°C, b) is 1200°C and c) is 1250°C.

The fracture surface of a 3wt% BBO composite sample, sintered at 1200°C, is shown in figure 4. 20, where spectrum 1 is an area across the face of a grain and spectrum 2 is an area of the 'glue-like' phase. Table 4. 4 lists the proportions of elements, in both weight and atomic percent, for both spectra, and compared to the theoretical proportions of elements in a pure CTLNT sample.

Spectrum 1, of the grain, contains approximately comparable proportions of O, Ca, Ti and Nd, when compared to the pure CTLNT, with slightly elevated proportions of O and Nd, and slightly reduced proportions of Ca and Ti. There also appears to be silver (Ag) and Bi present, although Ag is likely mislabelled Bi, since the Kα of Ag and the M of Bi are similar. The 'glue-like' phase in spectrum 2 appears to have much lower quantities of Ca, and Nd, and elevated levels of O and Ti, in addition to a convincing zirconium (Zr) presence. Zr is likely present due to contamination from the milling media used during the fabrication of the ceramic compounds, where yttria-stabilised zirconia (YSZ) milling media was used. Bi appears to solely be present within the grains of the material, according to data from figure 4. 20 and table 4. 4.

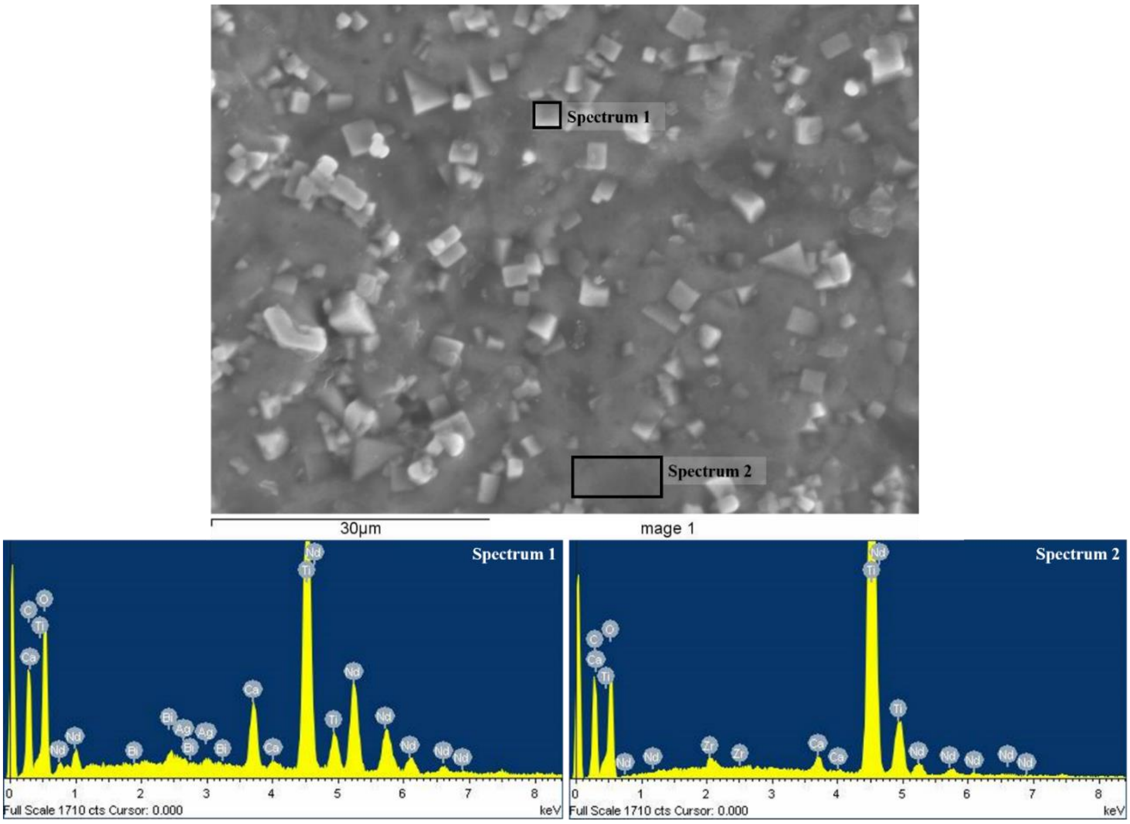

Figure 4. 20 EDS of CTLNT + 3wt% BBO composite fracture surface. Spectrum 1 is taken over the flat surface of a single grain, spectrum 2 is an area of the glue-like phase. The image depicting the locations of the EDS is a SEI.

Table 4. 4 List of elements detected by the EDS equipment used for each of the spectra in figure 4. 20, above. Results for the spectra are qualitative and automatically calculated. Theoretical calculations, in weight and atomic %, for pure CTLNT is included for comparison.

Pure CTLNT (Calculated)			**Spectrum 1**			**Spectrum 2**		
Element	Weight %	Atomic %	Element	Weight%	Atomic%	Element	Weight%	Atomic%
O	36.16	68.18	O Kα	43.46	77.49	O Kα	49.78	76.15
Ca	6.04	4.55	Ca Kα	3.83	2.73	Ca Kα	0.93	0.57
Ti	36.06	22.73	Ti Kα	23.59	14.05	Ti Kα	43.38	22.16
Nd	21.73	4.55	Ag Lα	0.89	0.24	Zr Lα	1.25	0.33
			Nd Lα	26.79	5.29	Nd Lα	4.68	0.79
			Bi M	1.44	0.20			
Totals	100	100	Totals	100	100	Totals	100	100

CTLNT + 4wt% BBO Compositions

The vol% porosity of the 4wt% BBO sample sintered at 1150°C decreases further, compared with the previous 1 and 3wt% samples, figure 4. 21 a) and b). The SEI also reveals darker regions, figure 4. 21 a), which may be interpreted as further evidence of residual B-rich glassy phase, but this is not reflected in the BE images of the same location, figure 4. 21 b). This may be due to the glassy phase being relatively ‘thin’ in comparison to the volume of material which contributes to the BE data. In contrast, secondary electrons come from thin, near the surface regions of the sample whose precise depth depends on the accelerating voltage.

Figure 4. 21 includes two different fracture surface images, one, c), displaying a region with less liquid phase to assess the grain morphology, and the other, d), displaying the ever-present glassy phase in the samples. In the 4wt% BBO system, the glassy phase can even be seen at 1150°C, where it was only observed at 1200°C in the 3wt% BBO composition. Both fracture surfaces reveal slightly larger grain size than observed in previous samples (3-6μm) with well-defined grain shape (cuboid), even at 1150°C.

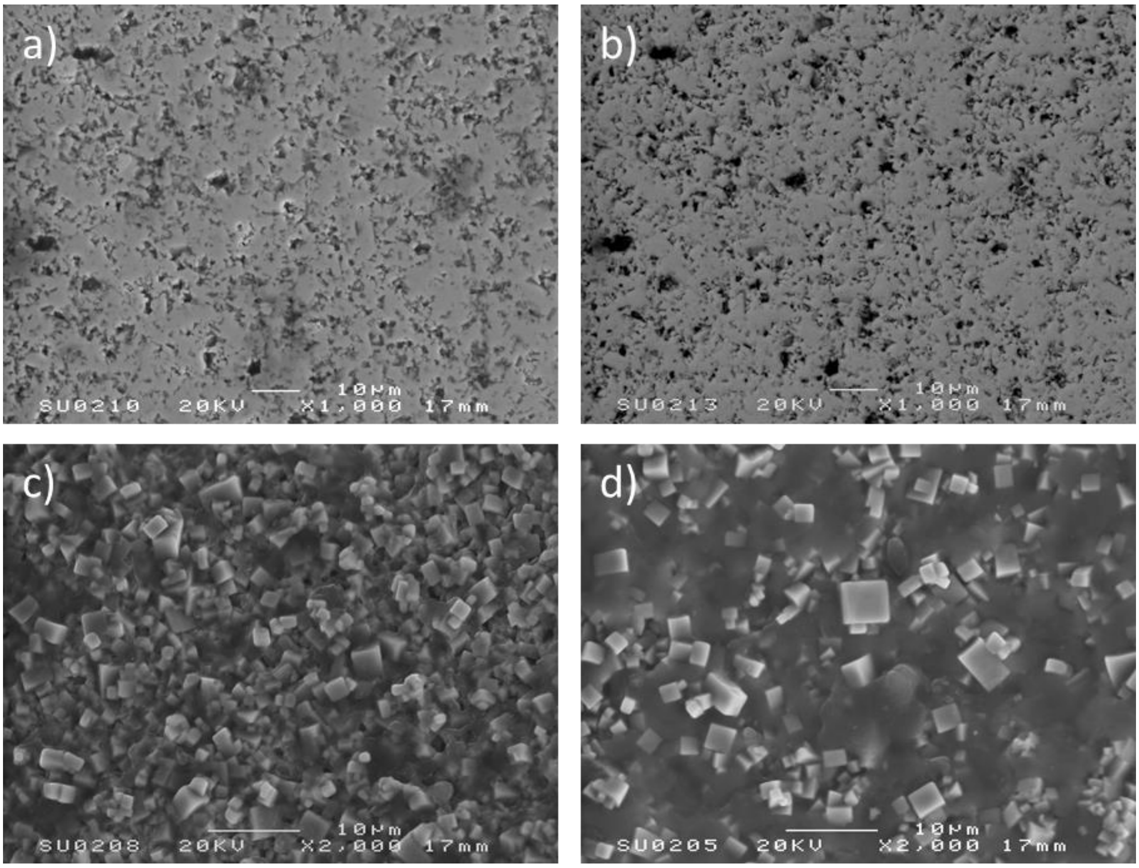

Figure 4. 21 SEM images of the 4wt% BBO composition, sintered at 1150°C for 4 hours, showing the a) SEI, the b) BE image of the un-etched polished surface, the c) SEI of the fracture surface and the d) SEI of the fracture surface at a different location.

Both the polished surface images of the 4wt% BBO composition, sintered at 1200°C, reveal regions of differing contrast, figure 4. 22 a) and b). The SEI image in figure 4. 22 a) reveals both lighter and darker regions which is not wholly reflected by the BE image in b). Although, there are darker regions in the BE image. These darker regions could perhaps be areas where the liquid phase is thick enough to backscatter enough electrons to be detected as a secondary phase. The brighter regions in the SEI does not appear to be a different phase in the BE image.

The fracture surface of the 4wt% sample sintered at 1200ºC is displayed in two images. Figure 4. 22 c) shows the crystal grain morphologies of the sample, with evidence of glassy phase in contact with the grains, and figure 4. 22 d) in which a large quantity of liquid phase, gathering as a large 'pool' is observed. The grain sizes are larger and more consistent at the higher sintering temperature of 1200°C, with an average grain size of between 5-8μm.

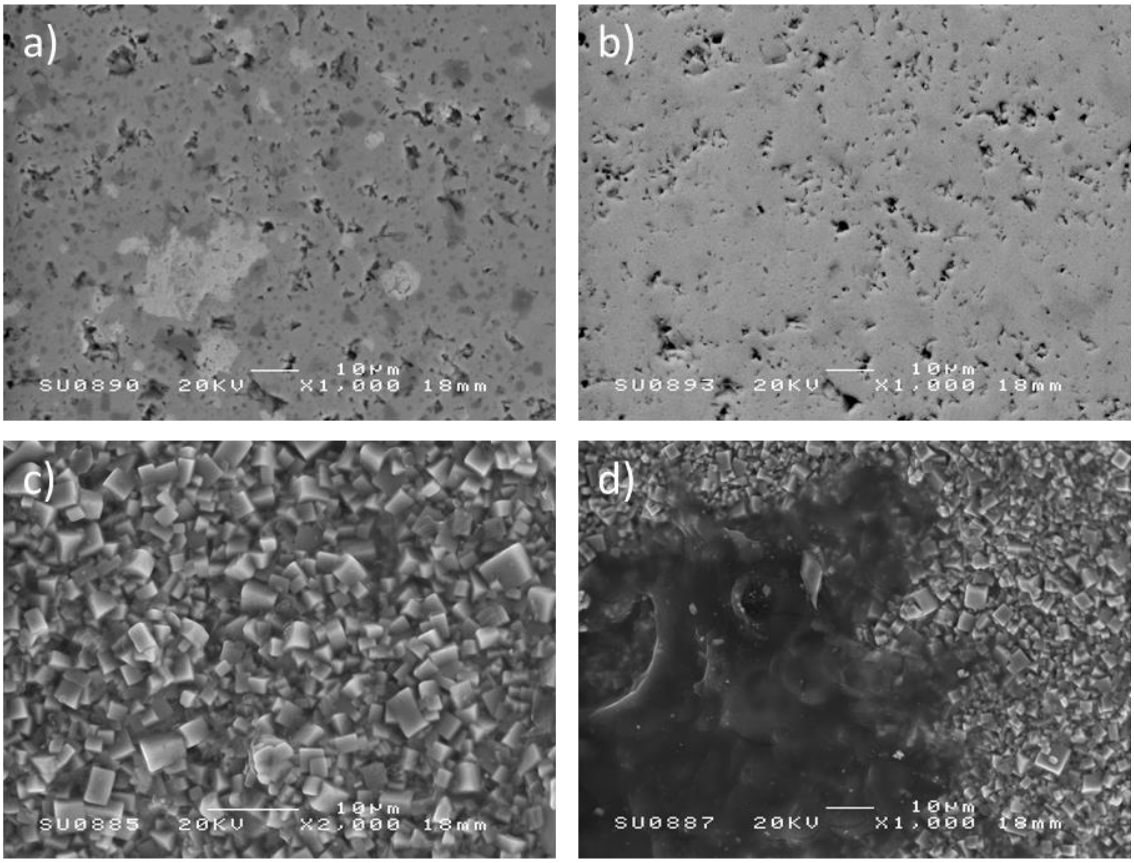

Figure 4. 22 SEM images of the 4wt% BBO composition, sintered at 1200°C for 4 hours, showing a) the SEI of the polished surface, b) the BE image of the polished surface, c) the SEI of the fracture surface and d) the SEI of the fracture surface at a different location.

Figure 4. 23 a) and b) are images of 4wt% samples sintered at 1250°C where the porosity is marginally less than that at 1200°C, although there are examples of single, much larger pores. There are also no lighter regions visible in the SEI image of the polished surface, figure 4. 23 a), compared with the same sample sintered at 1200°C, figure 4. 22 a). However, there are larger darker regions visible in both the SEI and the BE images, figure 4. 23 a) and b), with the visible darker regions in the BE image appearing in the same locations. This suggests that the darker regions in the secondary electron images are a different phase than that of the matrix with a lower weight average atomic number. It is assumed that this darker region is likely the B-rich liquid phase and, therefore the same as the amorphous phase observed in fracture surfaces, figure 4. 23 c), which surrounds the matrix grains (7-8μm).

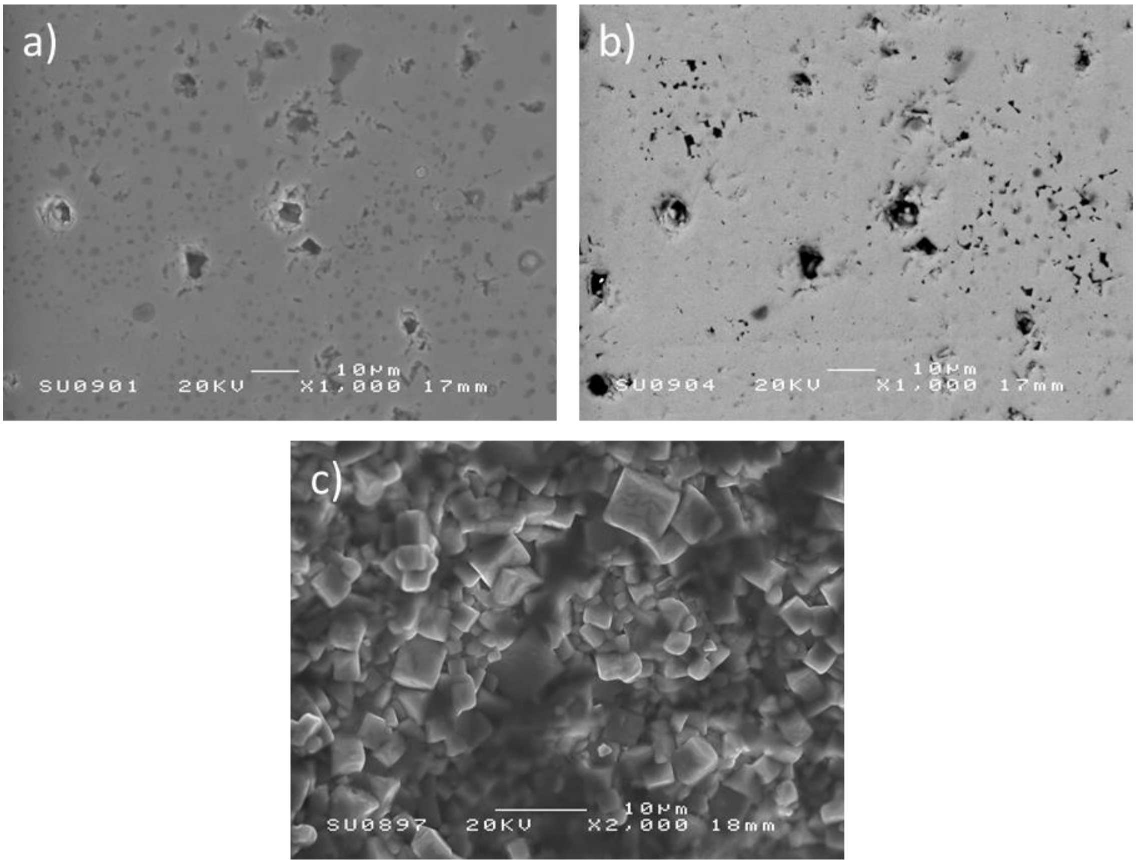

Figure 4. 23 SEM images of the 4wt% BBO composition, sintered at 1250°C for 4 hours, showing a) the SEI of the polished surface, b) the BE image of the polished surface and c) the SEI of the fracture surface.

Generally, with increasing sintering temperature, the fracture surface of the 4wt% BBO composition increases from 3-6μm up to 7-8μm. The liquid phase was prevalent throughout, even at the lower sintering temperature of 1150°C. For the polished surfaces, porosity appears reduced with increasing sintering temperature but with larger single pores sometimes present 1250°C. Finally, the volume fraction of darker regions (presumably glassy phase) increases with sintering temperature. The lowering of porosity with increased sintering temperature fits well with the density and shrinkage data in figure 4. 6 and table 4. 1. The slight reduction in density in figure 4.6 at 1250°C might be reflected in the presence of larger pores. Figure 4. 24 and figure 4. 25 summarise the development of the fracture surfaces and polished surfaces of the 4wt% BBO system over the different sintering temperatures.

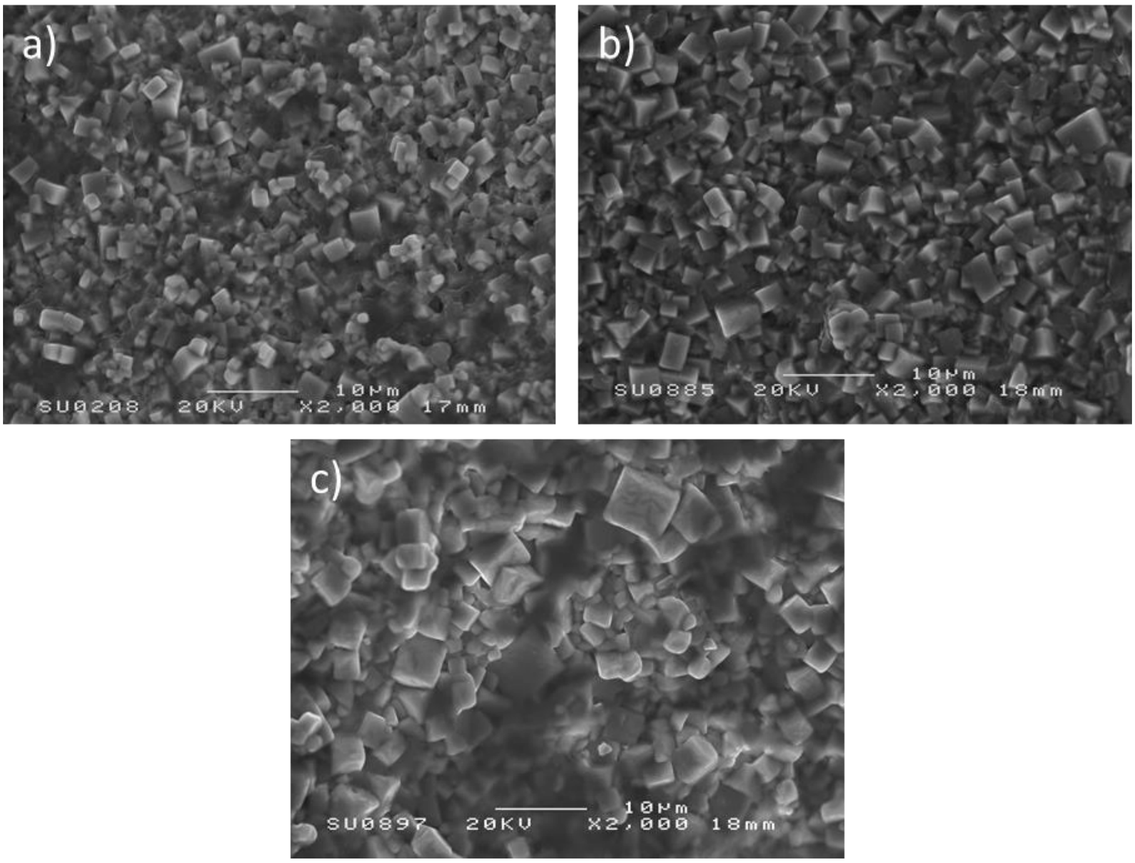

Figure 4. 24 SEM SEI images of the 4wt% BBO system, highlighting the change in the size of the grains and the presence of visible liquid phase over increased sintering temperatures, where a) is from a sample sintered at 1150°C, b) 1200°C and c) 1250°C.

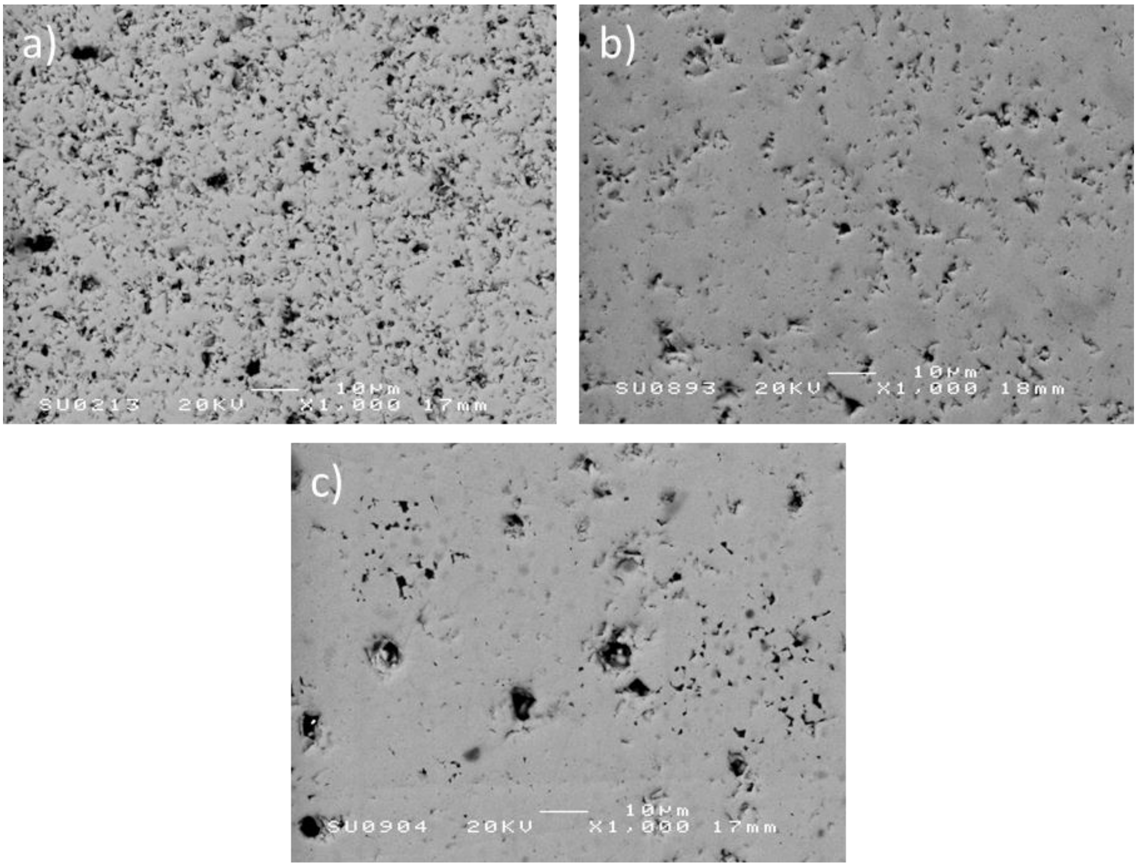

Figure 4. 25 SEM BE, polished surface images, of the 4wt% BBO system, displaying decreased porosity, and the presence of possible secondary-phase, over increased sintering temperatures, where a) is from a sample sintered at 1150°C, b) 1200°C and c) 1250°C.

The EDS of both the fracture and polished surface of a 4wt% BBO composition, sintered at 1200°C for 4 hours, are displayed in figure 4. 26 and figure 4. 27, respectively. Table 4. 5 and table 4. 6 list the proportions of elements present, in both weight and atomic percent, for all spectra displayed within the figures, respectively, including calculated proportions for pure CTLNT for comparison.

Spectrum 1 of the fracture surface is of a cluster of grains, and spectrum 2 is from an area of the amorphous, darker contrast phase. Spectrum 1 shows an abundance of the CTLNT elements Ca, Ti, and Nd in approximately similar proportions to the pure CTLNT material, and also contains strong Bi M peaks and some weak Bi Lα peaks. Spectrum 2, by comparison, has a much weaker peak response across the spectrum, apart from a strong carbon peak. There appears to be a Bi peak in the spectrum 2 for the liquid phase, however this appears to be too low to be adequately recognised by the EDS software. The fact that there is signal return for the other elements suggests that the liquid-phase in figure 4. 26 is relatively thin.

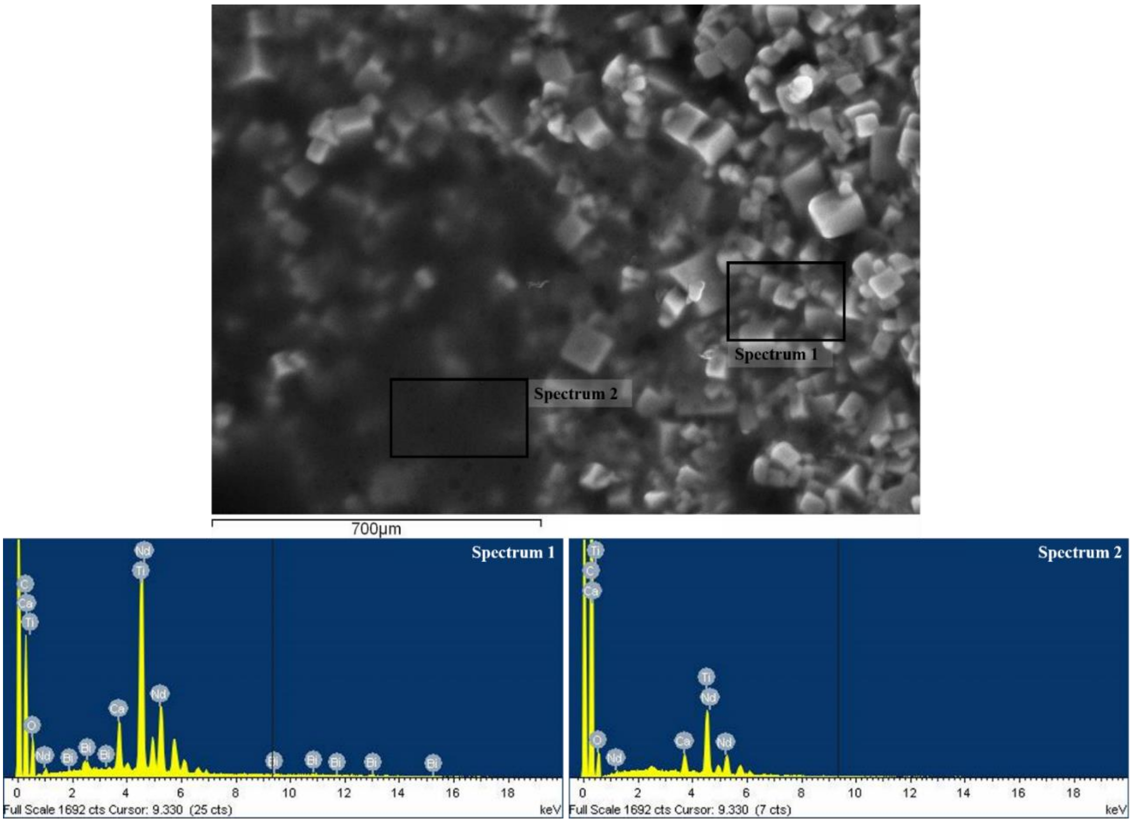

Figure 4. 26 EDS of CTLNT + 4wt% BBO composite fracture surface. Spectrum 1 is that of an area of predominantly grains, spectrum 2 is that of an area of amorphous phase. The image depicting the locations of the EDS is a SEI.

Table 4. 5 List of elements detected by the EDS equipment used for each of the spectra in figure 4. 26, above. Results for the spectra are qualitative and automatically calculated. Theoretical calculations, in weight and atomic %, for pure CTLNT is included for comparison.

Pure CTLNT (Calculated)			**Spectrum 1**			**Spectrum 2**		
Element	Weight%	Atomic%	Element	Weight%	Atomic%	Element	Weight%	Atomic%
O	36.16	68.18	O Kα	25.48	60.69	O Kα	51.45	81.82
Ca	6.04	4.55	Ca Kα	4.76	4.54	Ca Kα	4.11	2.63
Ti	36.06	22.73	Ti Kα	31.08	24.74	Ti Kα	21.83	11.57
Nd	21.73	4.55	Nd Lα	36.29	9.60	Nd Lα	22.62	3.97
			Bi M	2.38	0.43			
Totals	100	100	Totals	100	100	Totals	100	100

Spectrum 1 for the polished surface, in figure 4. 27, is of a darker contrast region of the surface, spectrum 2 is of a brighter region of contrast of the surface. There is very little difference, visibly, in the spectra between the two regions on the secondary electron image.

From table 4. 6, both spectra have roughly similar proportions to the pure CTLNT, with slightly increased proportions of O and Nd, and slightly decreased proportions of Ca and Ti. When comparing the two spectra, spectrum 1, the darker region, has a slightly larger proportion of O and Bi, and slightly reduced proportions of Ca, Ti and Nd. Apart from these slight variations, and given the nature that the data quality is only semi-quantitative, the two regions offer little insight into the difference between lighter and darker contrast regions, in this particular case.

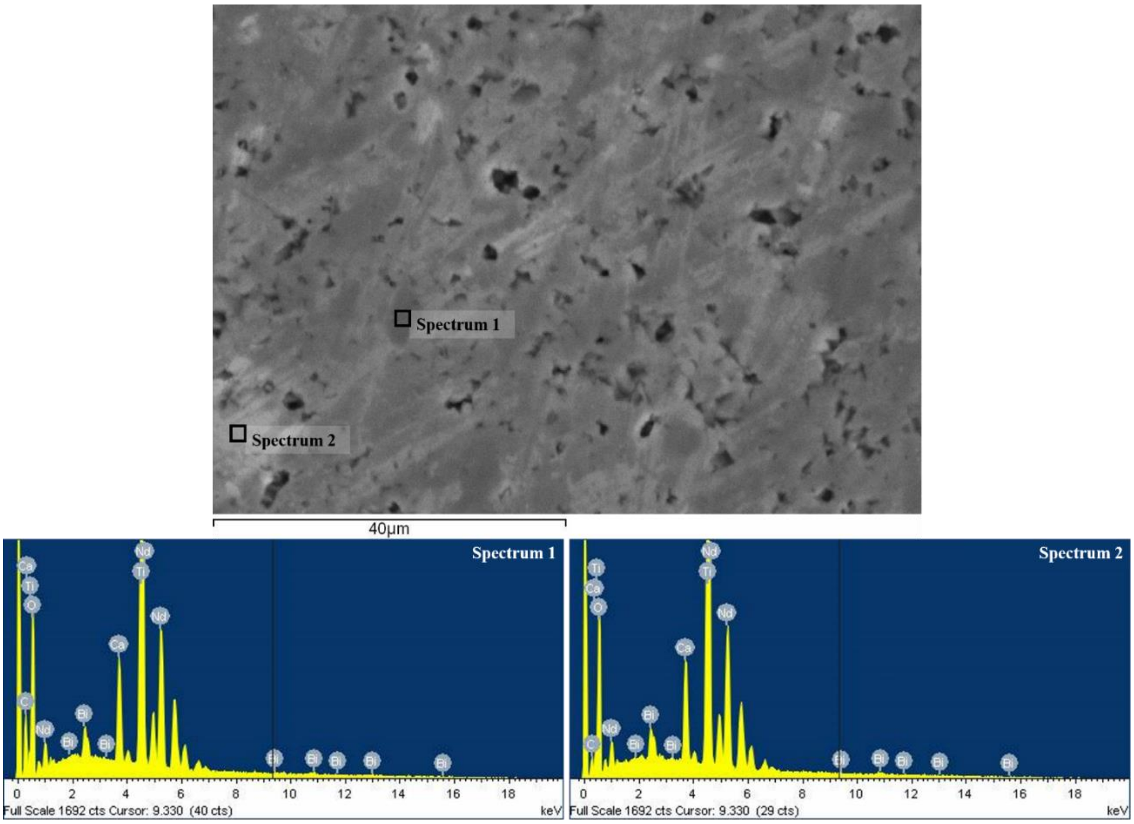

Figure 4. 27 EDS of CTLNT + 4wt% BBO composite polished surface. Spectrum 1 is that of a darker region and spectrum 2 is that of a lighter region. The image depicting the locations of the EDS is a SEI.

Table 4. 6 List of elements detected by the EDS equipment used for each of the spectra in figure 4. 27, above. Results for the spectra are qualitative and automatically calculated. Theoretical calculations, in weight and atomic %, for pure CTLNT is included for comparison.

Pure CTLNT (Calculated)			Spectrum 1			Spectrum 2		
Element	Weight%	Atomic%	Element	Weight%	Atomic%	Element	Weight%	Atomic%
O	36.16	68.18	O Kα	35.66	71.87	O Kα	34.75	71.06
Ca	6.04	4.55	Ca Kα	4.45	3.58	Ca Kα	4.56	3.72
Ti	36.06	22.73	Ti Kα	25.38	17.08	Ti Kα	25.64	17.51
Nd	21.73	4.55	Nd Lα	30.99	6.93	Nd Lα	31.66	7.18
			Bi M	3.52	0.54	Bi M	3.39	0.53
Totals	100	100	Totals	100	100	Totals	100	100

CTLNT + 5wt% BBO Compositions

The 5wt% BBO composition follows the trend set by the other compositions: a relatively high porosity from the polished surface images, reducing with increased sintering temperature, and grains which increase in size with sintering temperature. Compared with the 1wt% BBO composition, the porosity in figure 4. 28 a) and b) is lower and the fracture surface, in figure 4. 28 c), yields larger and more defined grains (3-5μm), at the lower sintering temperature. The fracture surface shows occasional examples of larger grains up to ~6μm. The BE image, figure 4. 28 b), of the polished surface appears to be largely homogenous, with the exception to the ringed areas, which indicates possible secondary phase.

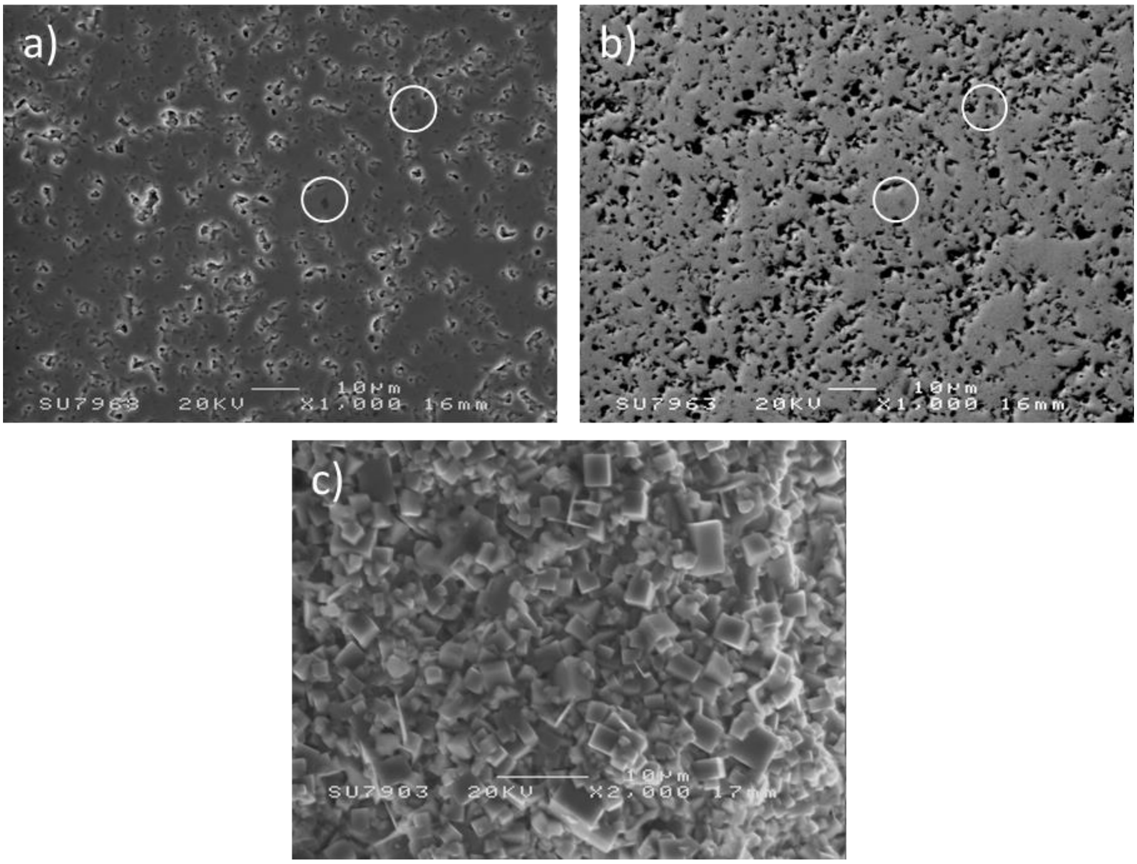

Figure 4. 28 SEM images of the 5wt% BBO composition, sintered at 1150°C for 4 hours, showing a) the SEI of the polished surface, b) the BE image of the polished surface and c) the SEI of the fracture surface. Ringed areas are possible secondary phase.

At 1200°C, the polished surface of the 5wt% BBO sample contains darker regions in the SEI, figure 4. 29 a), although this is scarcely reflected by the BE image, figure 4. 29 b), in the ringed locations. The dark regions may be too thin to be detected by the BE detector, or the contrast may not be optimised. The two ringed locations may simply show liquid phase within a pore, providing a thick enough region to be detected by the backscattered electrons. Overall, the porosity of the ceramic reduced with increased sintering temperature. The fracture surface, figure 4. 29 c), revealed more liquid phase in contact with marginally larger grains (4-6μm) than those in the sample sintered at 1150°C. The grains, though, appear more rounded, perhaps indicating dissolution of the matrix into the liquid phase at the sintering temperature.

Figure 4. 29 SEM images of the 5wt% BBO composition, sintered at 1200°C for 4 hours, showing the a) SEI of the polished surface, the b) BE image of the polished surface and the c) SEI of the fracture surface. Ringed area is possible secondary phase.

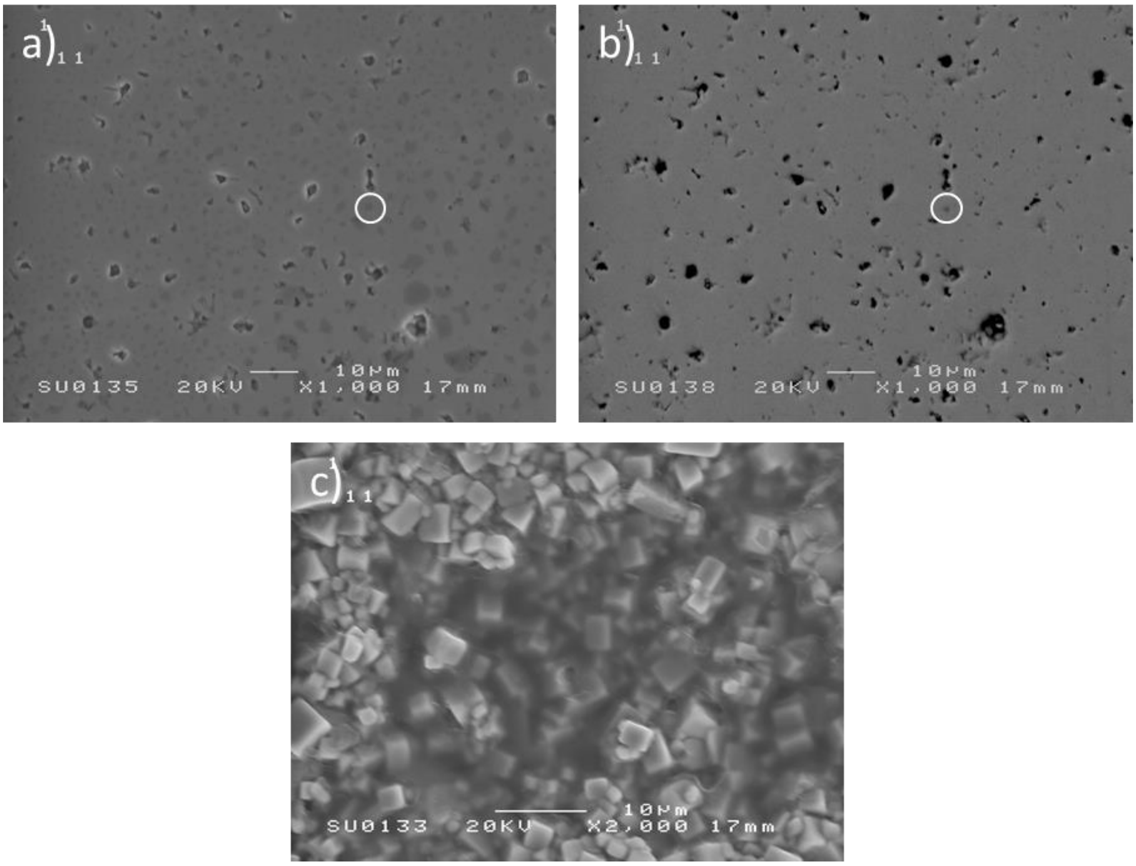

Figure 4. 29 SEM images of the 5wt% BBO composition, sintered at 1200°C for 4 hours, showing the a) SEI of the polished surface, the b) BE image of the polished surface and the c) SEI of the fracture surface. Ringed area is possible secondary phase.

At a sintering temperature of 1250°C, the polished surface revealed further darker regions, figure 4. 30 a), again not reflected by the BE image, figure 4. 30 b); possibly due to the regions being too thin to get a strong enough signal to the back scattered detector. The polished surface reveal that the volume fraction of small pores decreases but there are also a larger number of large single pores when compared to samples sintered at 1200°C. The initial porosity of the polished surface is in agreement with density and shrinkage data in figure 4. 6 and table 4. 1, compared to the 1wt% BBO composition sintering at 1150 °C. The overall slow rise in density, for the 5wt% BBO system, with sintering temperature, also agrees well with the density and shrinkage data, supporting the premise that the porosity levels at 1200°C and 1250°C are similar. The fracture surface of the 5wt% BBO composition, sintered at 1250°C, reveals larger grains (6-10 μm) with rounding at the edges, figure 4. 30 c).

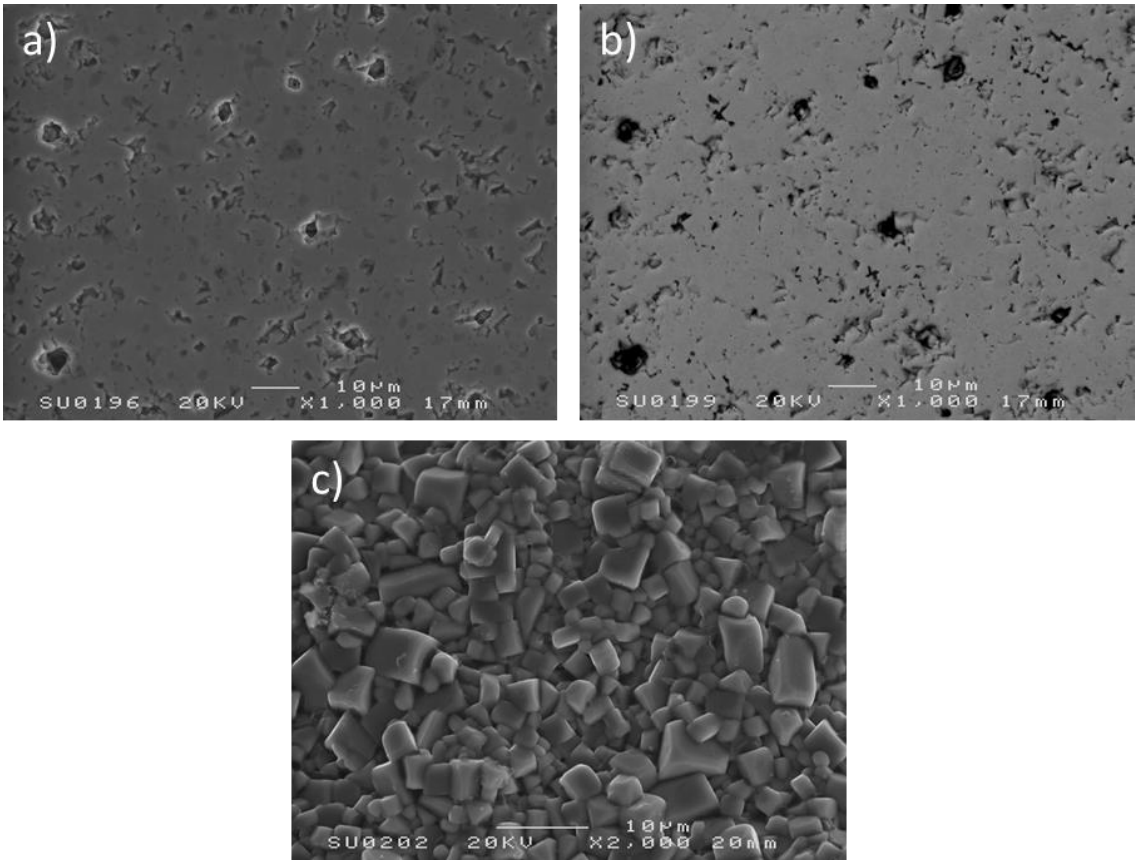

Figure 4. 30 SEM images of the 5wt% BBO composition, sintered at 1250°C for 4 hours, showing a) the SEI of the polished surface, b) the BE image of the polished surface and c) the SEI of the fracture surface.

In summary, for the 5wt% BBO composition, the porosity appears to be lower than the 1wt% BBO composition at a sintering temperature of 1150°C, and decreases at a lower rate with increasing sintering temperature, compared with the other compositions. The difference in porosity between the polished surface at 1200°C and 1250°C is marginal, with a possible increase at 1250°C through the presence of large single pores. Fracture surfaces revealed that the grain size increased as a function of sintering temperature, much like the other compositions, from 3-5μm up to 6-10μm, with some evidence of rounding, figure 4. 31 and figure 4. 32.

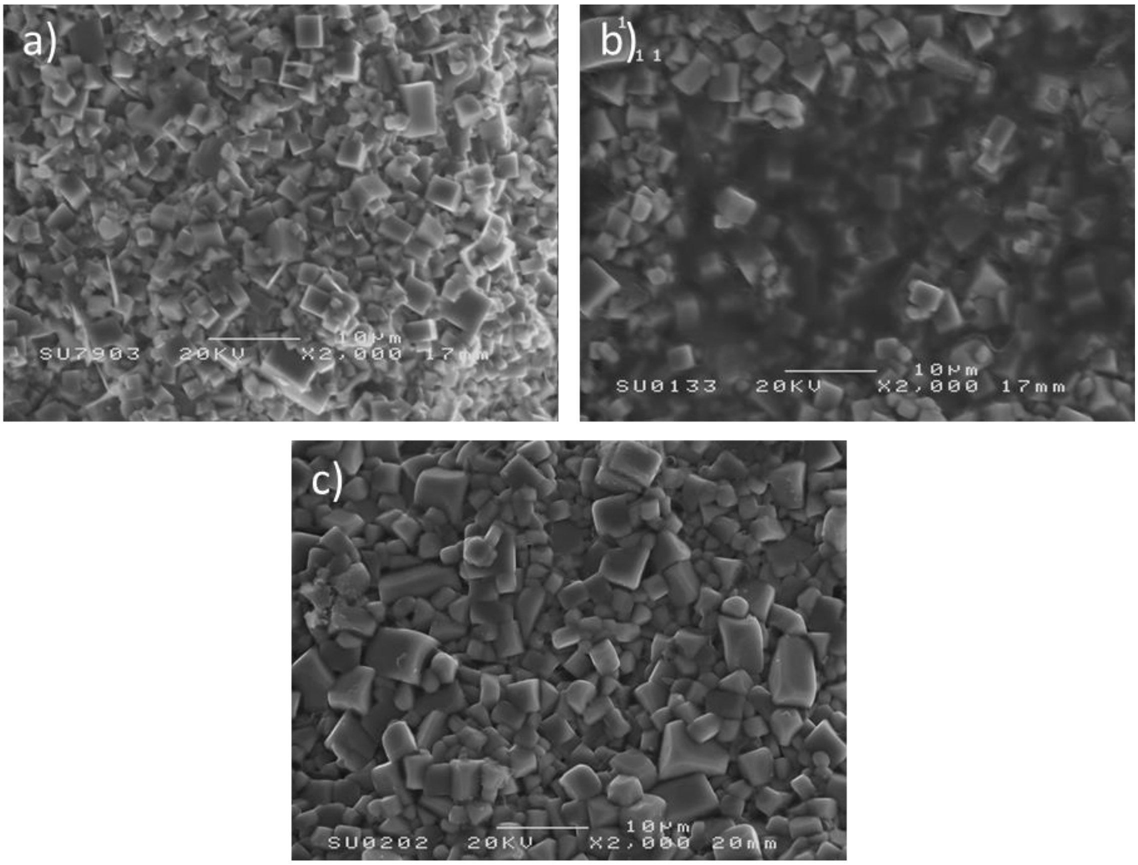

Figure 4. 31 SEM SEI of the 5wt% BBO system, highlighting the change in the size of the grains over increased sintering temperatures, where a) was obtained from a sample sintered at 1150°C, b) at 1200°C and c) at 1250°C.

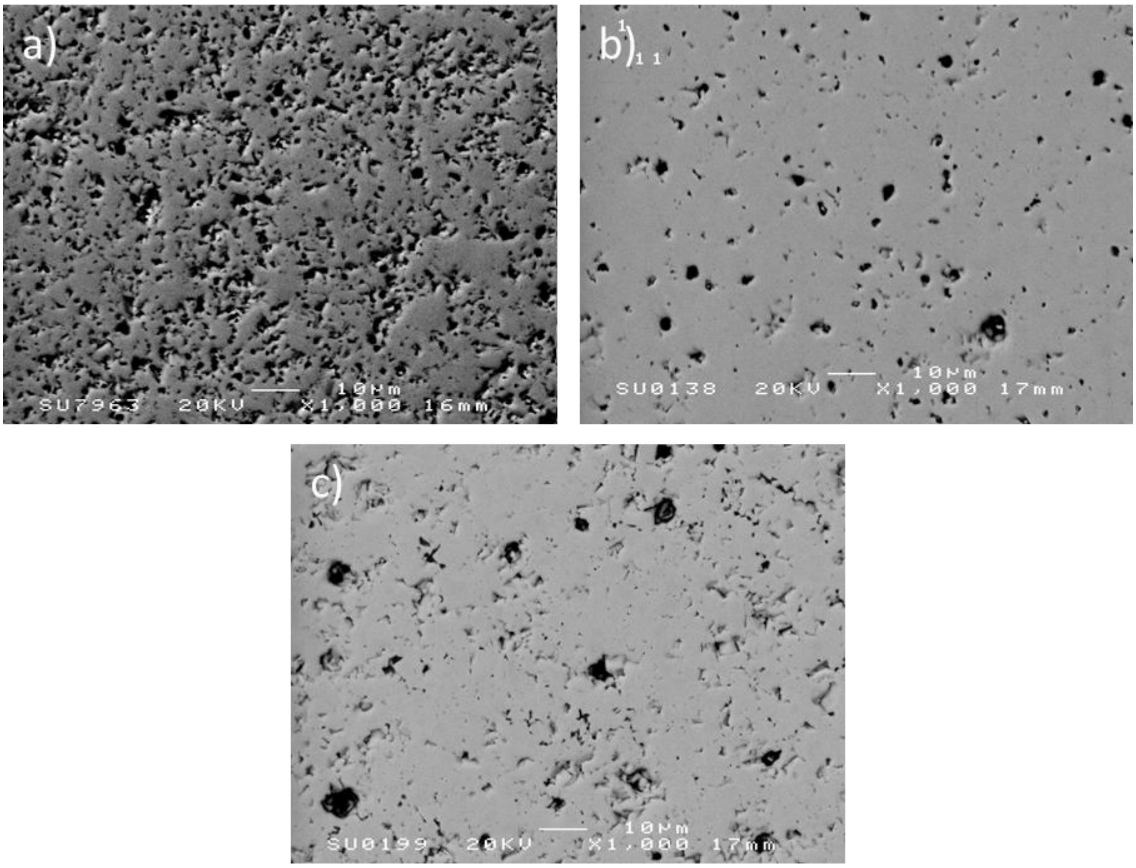

Figure 4. 32 SEM BE images of the polished surface images of the 5wt% BBO system, displaying generally decreased porosity over increased sintering temperatures, where a) is 1150°C, b) is 1200°C and c) is 1250°C.

The EDS spectra of the fractured and polished surface of a 5wt% BBO composition are displayed in figure 4. 33 and figure 4. 34 respectively, with the values from each spectrum displayed in table 4. 7 and table 4. 8 respectively.

Spectrum 1 of the fracture surface (figure 4. 33) is located across two grains, and spectrum 2 is of an area of amorphous phase. Due to the uneven nature of the fracture surface, elemental proportions for both spectra do not match well with the theoretical proportion of pure CTLNT. Spectrum 1 has larger proportions of O, and spectrum 2 has larger proportion of Ca, Ti, Nd and Bi. This does not correlate well with apparent contrast of the regions, where the brighter contrast regions are expected to contain a higher density of electrons (i.e. heavier atoms). As noted previously, these spectra are of an uneven surface of varying thicknesses and, as such, the data can only be used to confirm whether certain elements are present.

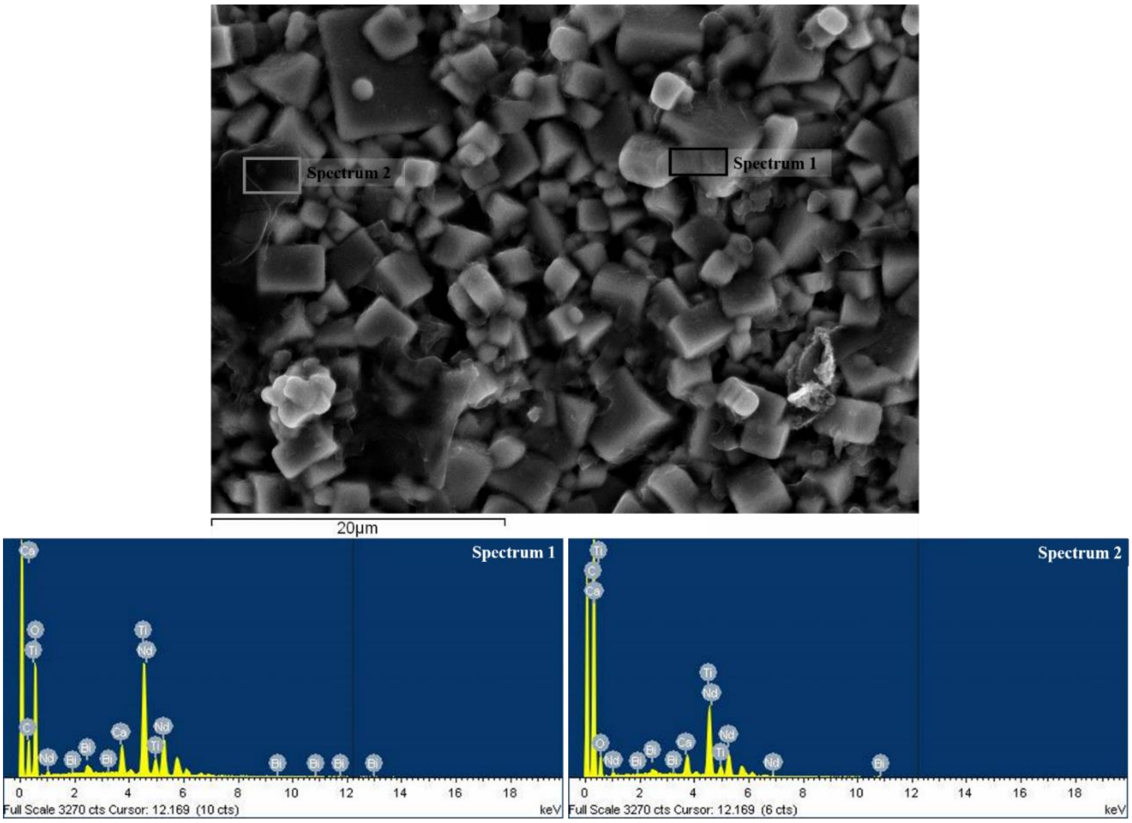

Figure 4. 33 EDS of CTLNT + 5wt% BBO composite fracture surface. Spectrum 1 was taken of the grains and spectrum 2 was taken of the liquid phase. The image depicting the locations of the EDS is a SEI.

Table 4. 7 List of elements detected by the EDS equipment used for each of the spectra in figure 4. 33, above. Results for the spectra are semi-quantitative and automatically calculated. Theoretical calculations, in weight and atomic %, for pure CTLNT is included for comparison.

Pure CTLNT (Calculated)			**Spectrum 1**			**Spectrum 2**		
Element	Weight%	Atomic%	Element	Weight%	Atomic%	Element	Weight%	Atomic%
O	36.16	68.18	O Kα	54.34	84.34	O Kα	40.64	75.22
Ca	6.04	4.55	Ca Kα	3.19	1.98	Ca Kα	4.60	3.39
Ti	36.06	22.73	Ti Kα	18.71	9.71	Ti Kα	24.92	15.40
Nd	21.73	4.55	Nd Lα	21.56	3.72	Nd Lα	27.59	5.68
			Bi M	2.20	0.25	Bi M	2.25	0.30
Totals	100	100	Totals	100	100	Totals	100	100

The polished surface of the 5wt% BBO composite sample is shown in figure 4. 34, showing regions of differing contrast across the surface area. Spectrum 1 is of an area of the average, brighter, contrast and spectrum 2 is of an area of darker contrast, and the black regions in the image are pores. The spectra themselves are difficult to differentiate between the three areas, apart from a rise in the levels of carbon in the darker contrast region. Despite this, differences in the EDS data is expected since there are physical differences in contrast. From table 4. 8, the brighter regions of spectrum 1 contain larger proportions of heaver elements, such as Bi and Nd consistent with the atomic number contrast.

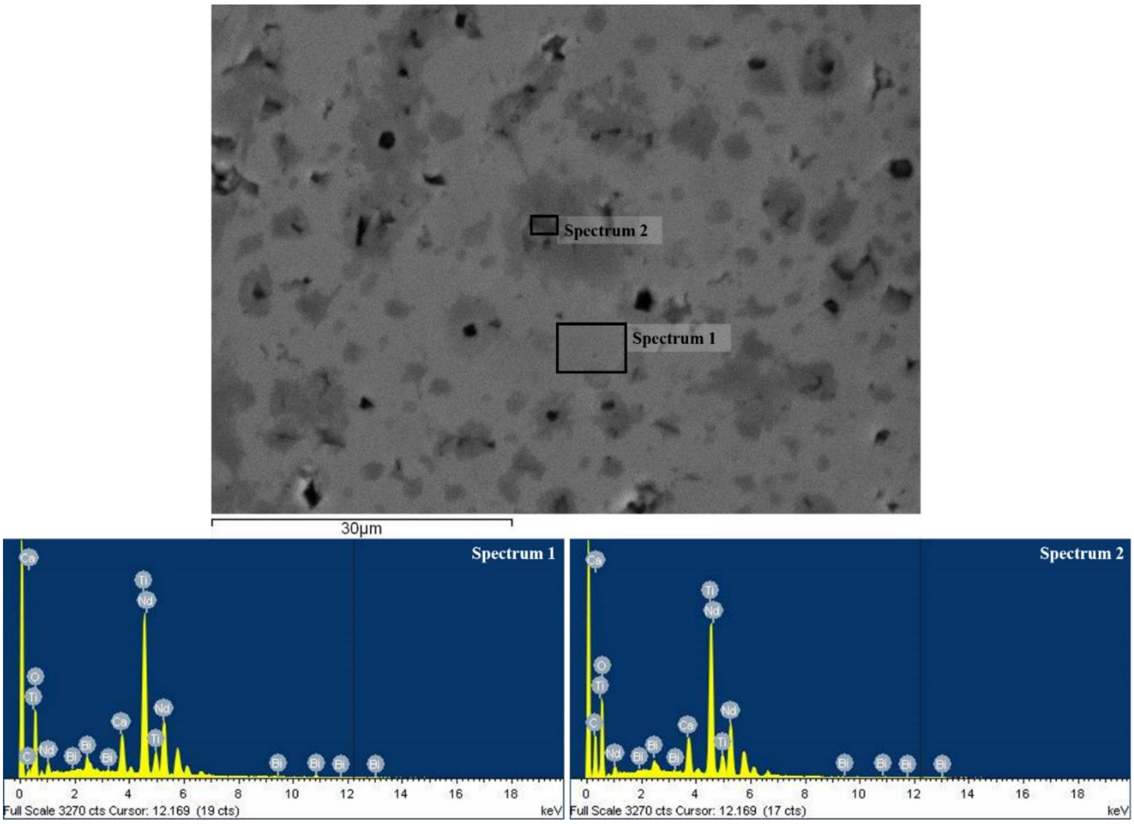

Figure 4. 34 EDS of CTLNT + 5wt% BBO composite polished surface. Spectrum 1 is that of the average matrix and spectrum 2 is that of a darker region of the polished surface. Locations of the EDS are shown in the SEI.

Table 4. 8 List of elements detected by the EDS equipment used for each of the spectra in figure 4. 34, above. Results for the spectra are qualitative and automatically calculated. Theoretical calculations, in weight and atomic %, for pure CTLNT is included for comparison.

Pure CTLNT (Calculated)			**Spectrum 1**			**Spectrum 2**		
Element	Weight%	Atomic%	Element	Weight%	Atomic%	Element	Weight%	Atomic%
O	36.16	68.18	O Kα	34.19	70.64	O Kα	41.21	76.19
Ca	6.04	4.55	Ca Kα	4.32	3.57	Ca Kα	3.97	2.93
Ti	36.06	22.73	Ti Kα	25.98	17.93	Ti Kα	23.80	14.70
Nd	21.73	4.55	Nd Lα	31.60	7.24	Nd Lα	28.35	5.81
			Bi M	3.90	0.62	Bi M	2.66	0.38
Totals	100	100	Totals	100	100	Totals	100	100

To summarise, due to the nature of the fracture surfaces, elemental proportions in weight and atomic percent are not reliable to ascertain accurate elemental proportions. Rather, the spectra are used more to confirm the presence of different elements. Additionally, SEI of the fracture surface can be used in conjunction with SEI and EDS of polished surfaces in order to determine what the different contrast regions are likely to be. Polished surfaces tend to be more reliable sources of information, with observed elemental proportions similar to the calculated proportions for pure CTLNT.

There is an observable trend of increased liquid-phase with increased BBO content, in addition to increased levels of Bi in both weight and atomic percent, within the grains and bulk material, from the EDS data. This is reflected within the increased tendency of seeing different contrast regions as the content of BBO is increased, where there is an observable trend to see larger proportions of heavier elements, such as Bi and Nd within the brighter regions, while the darker regions are more abundant in lighter elements, such as Ca, and Ti.

From the fracture surface spectra, there does not appear to be an abundant supply of Bi within the observed liquid-phases. Boron was expected to be observed within the dark contrast regions of the observed liquid-phases, however, likely due to X-ray absorption complications [13], particularly within a glassy amorphous phase, were not detected. It is therefore assumed that the Bi from the BBO sintering aid is reacting with the CTLNT in some way during sintering. EDS alone is not sufficient enough to make concrete conclusions as to the specific sintering mechanisms between the BBO sintering aid and the CTLNT, and for this, further observations under TEM were required.

4.5 Microwave Dielectric Properties

Table 4. 9 and figure 4. 35 show the relative permittivity (ε_r), quality factor (Qf_0) and the temperature coefficient of resonant frequency (τ_f) for CTLNT + $x$wt% BBO compositions, sintered at 1150, 1200 and 1250°C for four hours. Table 4. 9 also shows the MW dielectric properties for a pure CTLNT and BBO sample for comparison, sintered at 1300 and 650°C for four hours, respectively.

In general, ε_r of every CTLNT composition increased with increased sintering temperature. The largest increase in relative permittivity, from 106 (at 1150°C) to 129 (at 1250°C), was associated with 1wt% BBO compositions, the 4wt% BBO composites showed the most consistent ε_r as a function of sintering temperature and all compositions, with the exception of those with 5wt% BBO, showed an increased in ε_r with sintering particularly in the range 1150 – 1200°C.

Table 4. 9 Microwave dielectric results for the CTLNT + $x$wt%BBO at each sintering temperature, including pure CTLNT and BBO.

Sample Type	Sintering Temperature (°C)	Relative Permittivity (ε_r) (±1)	Quality Factor (Qf_0) (±30)	Temperature Coefficient of Resonant Frequency (τ_f) (±0.5)
Pure	1300	132	2231	50
$Bi_4B_2O_9$	650	40	2328	-178
1wt%	1150	106	2388	45
	1200	123	2023	38
	1250	129	1967	39
3wt%	1150	117	2482	42
	1200	126	2136	42
	1250	127	1870	21
4wt%	1150	119	2572	6
	1200	125	2518	4
	1250	128	2107	22
5wt%	1150	115	2581	-18
	1200	120	2486	-1
	1250	123	2052	7

Qf_0 of all CTLNT compositions decreased with increased sintering temperatures and increase in ε_r. The data also shows that Qf_0 increases with increased BBO content, although the 4 and 5wt% BBO compositions show very similar values. The 4 and 5wt% BBO compositions maintain a high level of Qf_0 until 1250°C compared with the 1 and 3wt% BBO composites.

τ_f decreased with increase in BBO concentration, presumably due to the addition of a large negative (-ve) τ_f (BBO = -178 ppm/°C) sintering aid to the positive (+ve) τ_f CTLNT (50 ppm/°C) matrix, table 4. 9. 1wt% BBO reduced τ_f of the CTLNT at 1150°C but remained at approximately the same value at higher sintering temperatures. A similar evolution of τ_f was observed for 3wt% BBO composition except that τ_f decreased at 1250°C.

Compositions with 4 and 5wt% BBO have the largest changes in τ_f. The increased BBO concentration tunes τ_f to ‘near-zero’, or less, at 1150°C and 1200°C but surprisingly increases τ_f at 1250°C. In contrast, the 5wt% BBO concentration exhibits a constant rise in τ_f with increased sintering temperature. ‘Near-zero’ τ_f tuning was achieved for both 4 (4 ppm/°C) and 5wt% BBO (-1 ppm/°C) composites at a sintering temperature of 1200°C.

The behaviour of τ_f with sintering temperature is less predictable and erratic in comparison with ε_r and Qf_0 which have largely similar linear trends. This perhaps suggests that there is a reaction occurring between the CTLNT and BBO, which becomes more prominent with increased BBO content and at a higher sintering temperatures. The reaction products presumably have different values of τ_f and thus their relative volume fractions strongly influence temperature stability.

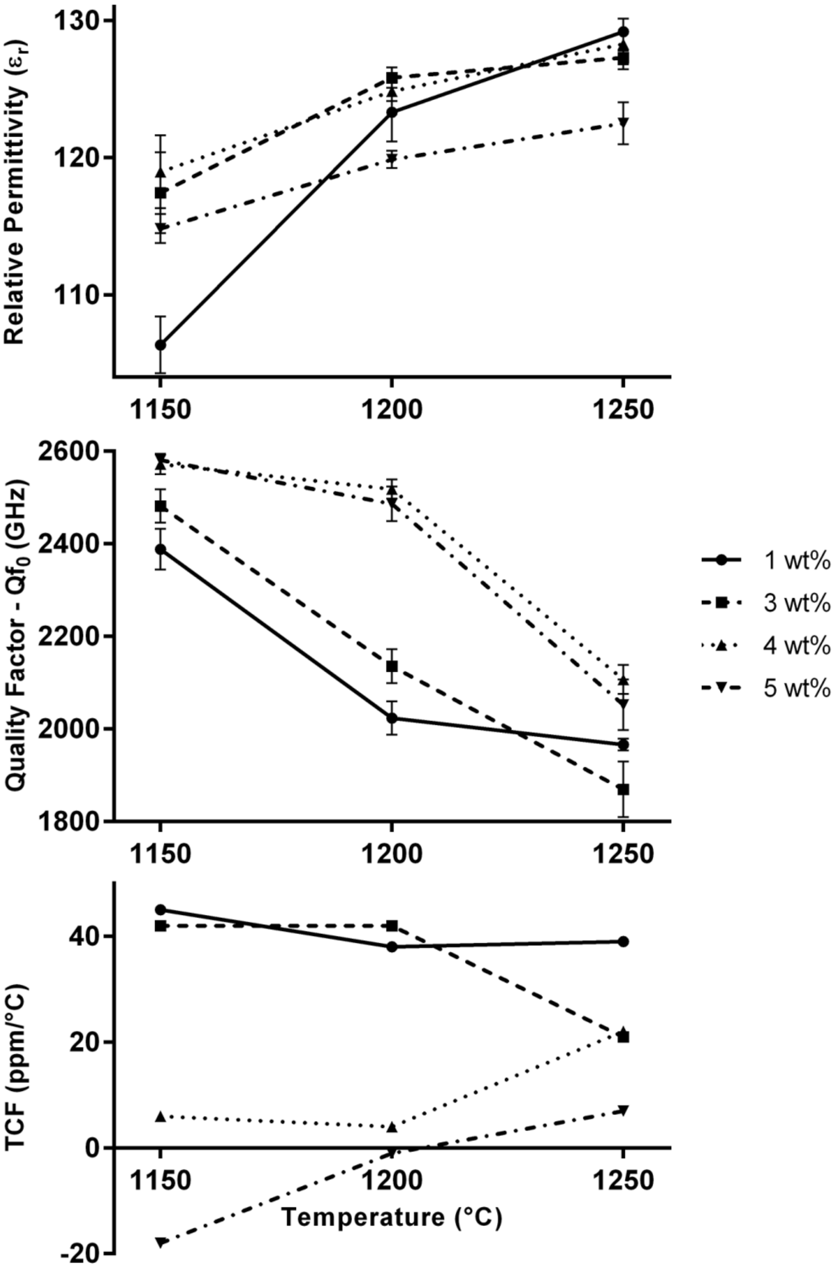

Figure 4. 35 Microwave dielectric results of each CTLNT + $x$wt% BBO with increasing sintering temperature.

Overall, the best properties, in combination with density, is that of the CTLNT+ 4wt% BBO composition sintered for 4h at 1200°C for with ε_r = 125, Qf_0 = 2500 GHz and τ_f = 4ppm/°C. All MW properties compare well with previous work [6].

4.6 Transmission Electron Microscopy (TEM) Observations

CTLNT End-Members: $CaTiO_3$ and $(Li_{0.5}Nd_{0.5})TiO_3$

A brief study on the CTLNT end-members was conducted to acquire preliminary results to compare with those of $0.2CaTiO_3$-$0.8(Li_{0.5}Nd_{0.5})TiO_3$ (CTLNT), especially whether or not changes in crystal structure are induced by the addition of the BBO. Transmission electron microscopy (TEM) diffraction patterns of the two end members are shown in figure 4. 36, where a) and b) are the $CaTiO_3$ (CT) end-member, and c) and d) are the $(Li_{0.5}Nd_{0.5})TiO_3$ (LNT) end-member. All fundamental spots for both end-members are indexed according to pseudocubic perovskite setting, and both diffraction patterns have superstructure reflections consistent with $a^-a^-c^+$ Glazer tilt system [14].

The CT has been indexed along the a) <100> and b) <110> zone axes respectively. There is evidence of strong $\frac{1}{2}\{eeo\}$, where e = even and o = odd, superstructure reflections as a result of in-phase tilting around the [100] axis and strong $\frac{1}{2}\{ooo\}$ reflections from anti-phase tilting around the [011] axis. In the <110> zone axis (figure 4. 36 b) there are also weak reflections at $\frac{1}{2}\{eeo\}$, as a result of anti-parallel A-site cation displacements associated with the presence of both in phase and antiphase in a single tilt system [15], [16].

The LNT end-member shows similar $\frac{1}{2}\{ooo\}$ reflections, from anti-phase tilting to CT in the <110> zone axes (figure 4. 36 d) but there are also diffuse weak reflections, especially surrounding the fundamental spots. In the <111> zone axes (figure 4. 36 c)), $\frac{1}{2}\{ooe\}$ and $\frac{1}{2}\{oeo\}$ reflections are observed, characteristic of in-phase rotations of the O-octahedra. The diffuse scatter in the LNT compound may relate to the "chessboard structure" described by Davies and co-workers [17], [18] and discussed in detail in later sections.

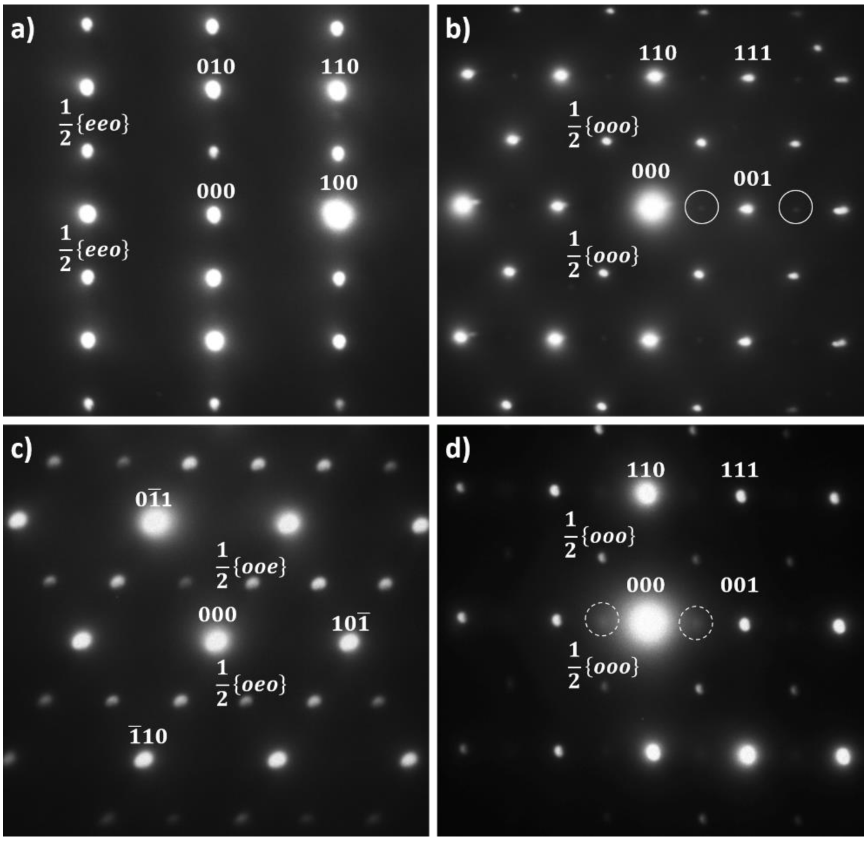

Figure 4. 36 TEM diffraction patterns of the two CTLNT end-members, $CaTiO_3$ a) and b), and $(Li_{0.5}Nd_{0.5})TiO_3$ c) and d). A) and b) have been arbitrarily indexed along the [001] and [110] zone axes respectively, and c) and d) have been arbitrarily indexed along the [111] and [110] zone axes respectively. The circled regions in b) denote the presence of weak $\frac{1}{2}\{eeo\}$ tilt reflections, and the broken circle regions in d) show the presence of diffuse scatter.

CTLNT + BBO

Transmission electron microscopy (TEM) was carried out to elucidate further structure-microstructure property relations in the CTLNT-BBO system. Bright field (BF) images and electron diffraction patterns of a CTLNT + 4wt% BBO sample are shown in figure 4. 37. The fundamental reflections <100>, <110> and [111] zone axes are indexed according to a pseudocubic perovskite cell with superstructure reflections at half-integer positions. From Woodward and Reaney [14], the superstructure reflections are best explained by comparison with the $CaTiO_3$ end member which has an $a^-a^-c^+$ Glazer tilt system [14] with $\frac{1}{2}\{ooo\}$, $\frac{1}{2}\{ooe\}$ and arising from anti-phase tilting and in-phase tilting and $\frac{1}{2}\{eeo\}$ from the so called concert effect. These three main superstructure reflections are denoted by ‘a’, ‘i’ and ‘c’, respectively.

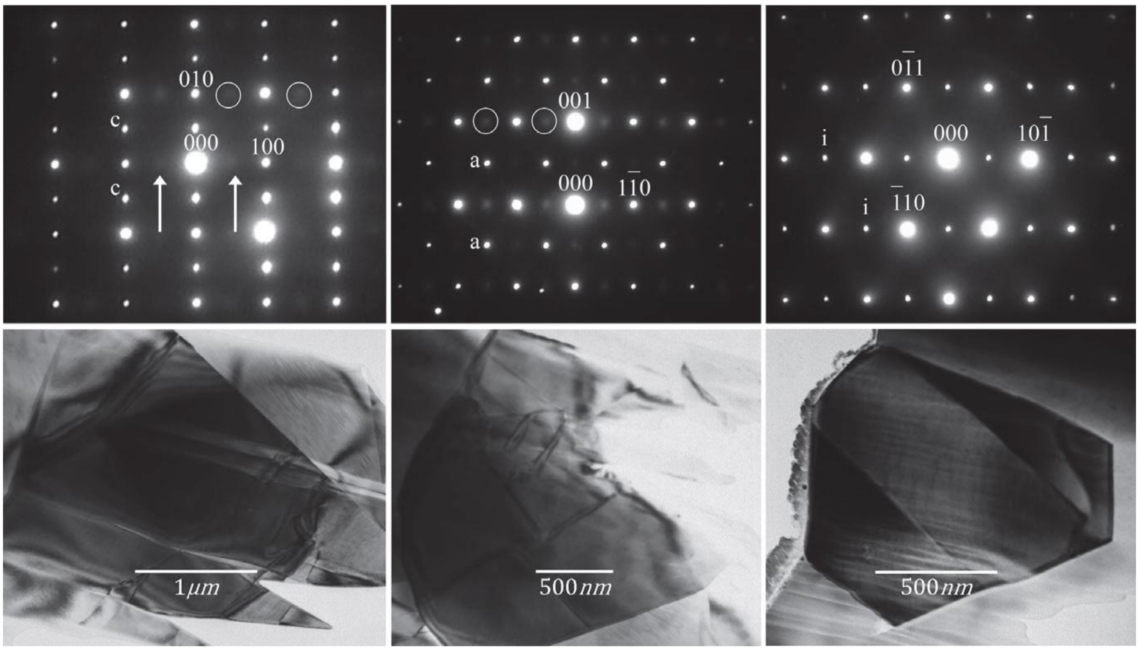

Figure 4. 37 Electron-diffraction patterns obtained from a typical sample of CTLNT + $x$wt% BBO, sintered at 1200°C for 4h. These are arbitrarily indexed with zone axes (a) $[100]$, b) $[110]$, and c) $[111]$, with respective diffraction pattern locations (d), (e) and (f) below. Superstructure reflexions are labelled with: a = antiphase tilting, i = in-phase tilting, and c = concert tilting. The ringed and arrowed regions show evidence of diffuse scatter relating to the end member checkerboard structure [17], [19], [20].

There is also evidence of weak diffuse reflections, indicated by ringed and arrowed regions in figure 4. 37, which cannot be considered to arise solely from octahedral tilting. While a full analysis into the diffuse scatter is beyond the remit of this study, previous research suggest that this is likely due to a “nano-checkerboard”, or “nano-chessboard” structure, which has frequently been reported for the end-member compound, $Li_{1/2}RE_{1/2}TiO_3$ (LRT) [18], [20], [21], figure 4. 38. In LRT compounds, diffuse or weak multiple satellite reflections have been reported at $\frac{1}{2}\{eeo\}$ positions [17].

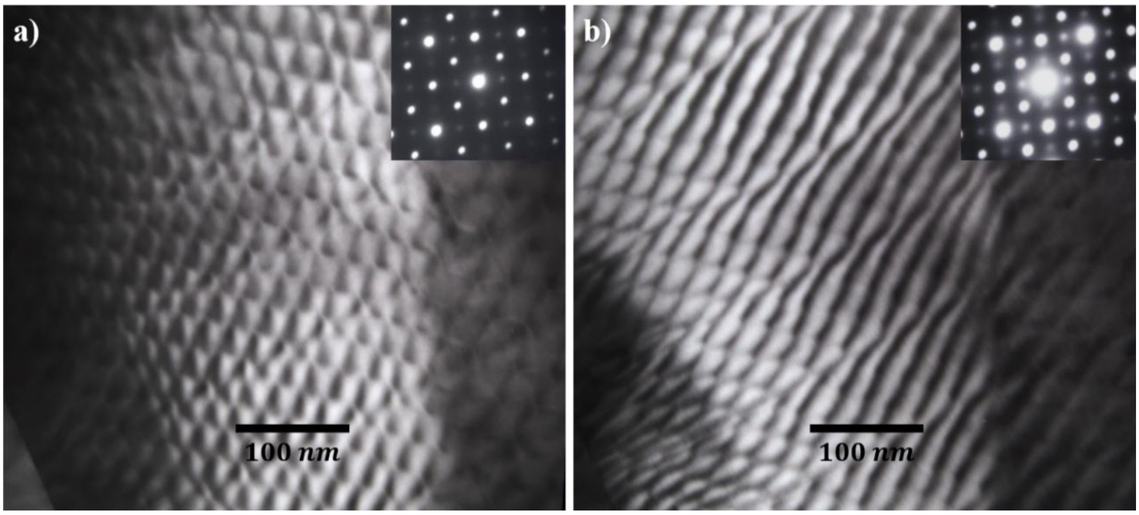

Figure 4. 38 TEM bright field image of a CTLNT + 5wt% BBO sample, sintered at 1200°C for 4 hours, demonstrating the presence of a diamond-type nano-chessboard structure. Both a) and b) are taken along the [100] zone axis, of the same region, with a very minor tilt difference between the images.

The nano-chessboard structure forms spontaneously into nano-patterned structures with a periodic arrangement of phases with compositional and functional contrast [22], [23]. This structure occurs in the solid solution of a Li-ion conducting perovskite of $(Nd_{2/3-x}Li_{3x})TiO_3$, in which there is phase separation into a super-lattice of nano-domains (composed of $(Nd_{1/2}Li_{1/2})TiO_3$), separated by a zigzagging boundary region (composed of $Nd_{2/3}TiO_3$). This leads to extremely periodic, diamond-like nanostructures, figure 4. 40 (from Guiton, 2008 [20]).

Figure 4. 39 shows the EDS of the nano-chessboard structure as well as the average matrix. The arrowed peaks point to a higher Nd concentration within the nano-chessboard structure compared with the average matrix. This appears to be consistent with the necessary quantities required for the production of a nano-chessboard structure, as indicated by the literature [20], [22], [23]. Although, not a common occurrence in the CTLNT-BBO composition, the regions are thought to arise due to local variations in the Ca:Li:Nd ratio through inhomogeneous mixing of the raw materials.

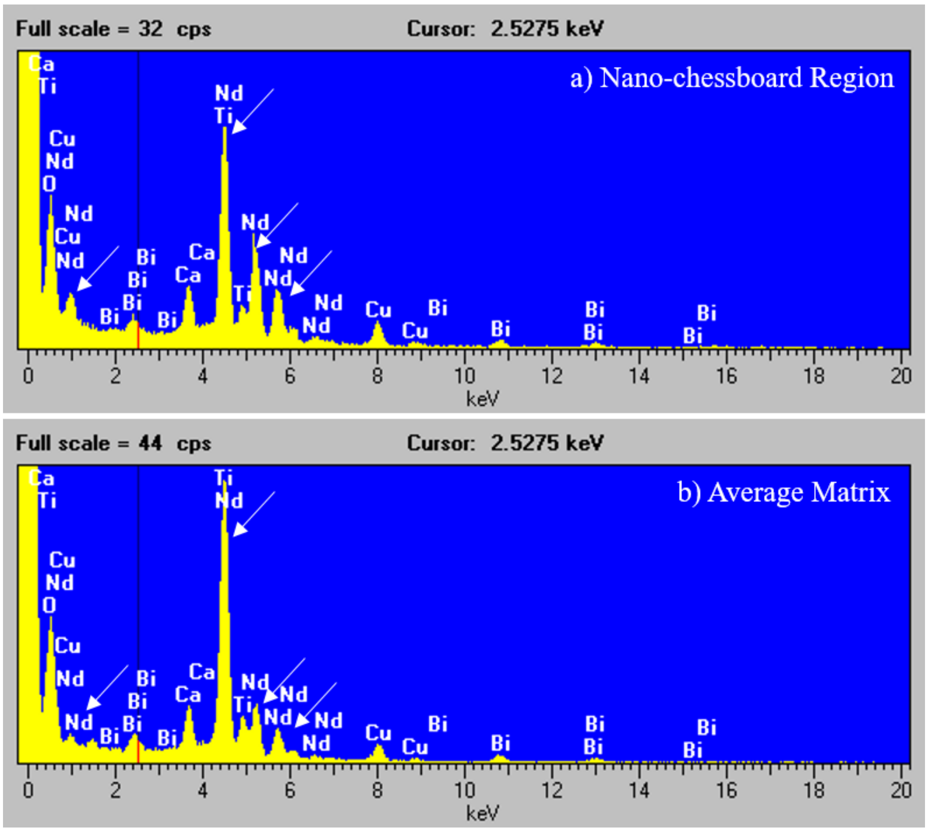

Figure 4. 39 TEM EDS of the a) nano-chessboard region and b) a general matrix region. Arrows point to the important peak differences between the two spectra, with larger proportions of Nd in the nano-chessboard structure compared with the average matrix.

In the nano-chessboard structure, the cation ordering responsible for phase separation occurs on many different levels. First, a prerequisite of 1:1 primary ordering is required to give alternating perovskite A-site (001) layering, one fully occupied by Nd^{+3} cations and another occupied by Li^{+} cations, vacancies and residual Nd^{+3} [24]–[27]. Second ordering then occurs, in the nanometre scale, as phase separation, with mixed layers, to give the periodically arranged superlattice of nano-domains [21]. The driving force for this phase separation is hypothesised to derive from small, under-bonded Li cations, which displace in the [100] and [010] directions, away from the A-site and towards 4-fold “square-window” sites [28]–[31]. This displacement is inhibited by adjacent Nd cations in the mixed layer [20], [21].

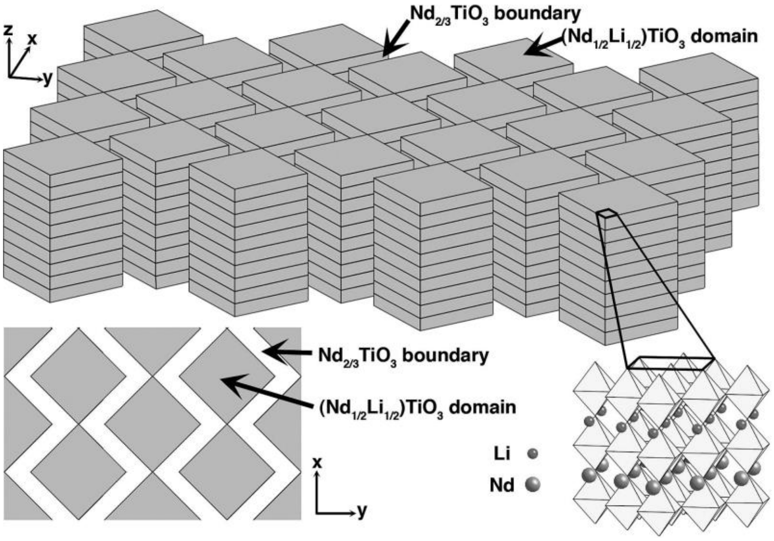

Figure 4. 40 Figure from Guiton and Davies, 2008, illustrating the periodic phase separation of $(Nd_{2/3-x}Li_{3x})TiO_3$. The top image is a three-dimensional representation of the stacking of square nano-domains along the z-direction. The bottom left image is a cross-sectional view, looking down the z-direction, showing a diamond-like structure. The bottom right image is a polyhedral model of the TiO_6 octahedra and the (001) A-site layering of the Li and Nd in the domains [20].

The presence of diffuse weak reflections at $\frac{1}{2}\{eeo\}$ in the CTLNT matrix may therefore relate to the checkerboard structure. The substitution of Ca onto the A-site destroys the long-range Li and RE ordering, which resulting in diffuse short range ordered intensities with weak discrete satellite reflections characteristic of the checkerboard configuration. Although SRO is detrimental for ultra-high Qf_0 materials such as $BaZn_{1/3}Ta_{1/2}O_3$, due to anharmonicity of the phonon modes, the relatively modest Qf_0 values of the CTLNT system are broadly insensitive. Moreover, without significantly altering the composition, it is difficult to eliminate SRO to further explore the ordering relationship of this particular system. Significantly altering the compositions would also result in an increase in the magnitude of τ_f, and a likely decrease in ε_r.

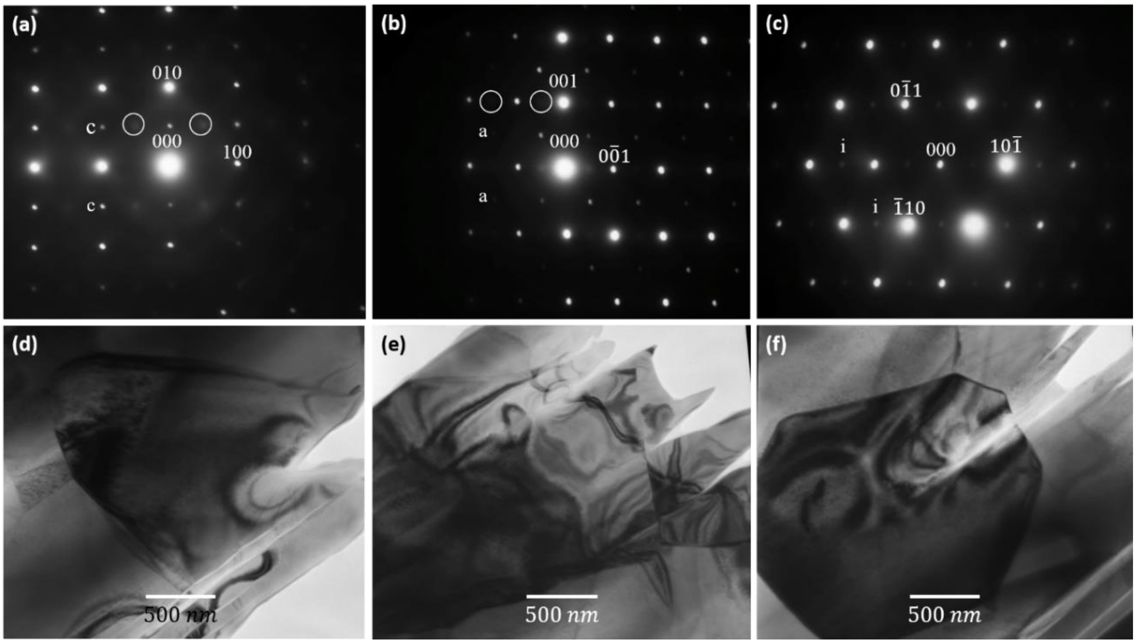

Figure 4. 41 Electron-diffraction patterns obtained from a sample of the end-member LNT, sintered at 1150°C for 4h. These are arbitrarily indexed with zone axes (a) [100], b) [110], and c) [111], with respective diffraction pattern locations (d), (e) and (f) below. Superstructure reflexions are labelled with: a = antiphase tilting, i = in-phase tilting, and c = concert tilting. The ringed regions show evidence of diffuse scatter relating to the end member checkerboard structure [17], [19], [20].

From the literature on the checkerboard structure, it can be concluded that the diffuse scatter and superstructure reflections are not caused by the addition of BBO to the CTLNT system but rather an intrinsic function of the matrix phase. Figure 4. 42 shows the grain size and typical microstructure of the CTLNT matrix in CTLNT + 5wt% BBO. Note that no ferroelastic domains are observed or at least very few. Ferroelastic domains are typical in the orthorhombically distorted $CaTiO_3$ end member due to the appearance of spontaneous strain simultaneously with the onset of octahedral tilting [32]. However, domains are common only in ceramics with large grain size, >1 μm [33]–[36]. For smaller grain size materials, much of the spontaneous strain is accommodated at the grain boundary and fewer domain walls are observed. The largest grain sizes (5-8 μm) were typically observed in this study for compositions with 5wt% BBO. Nonetheless, no domain walls are visible which suggest that the spontaneous strain may be lower in CTLNT ceramics compared with the end member, $CaTiO_3$. Peak splitting in XRD patterns of CT versus CTLNT (figure 4. 3, p.74) suggest that the distortion away from pseudocubic is indeed greater for CT than CTLNT and thus the driving force for domain formation due to ‘grain clamping’ is reduced and spontaneous strain is more easily accommodated at the grain boundary.

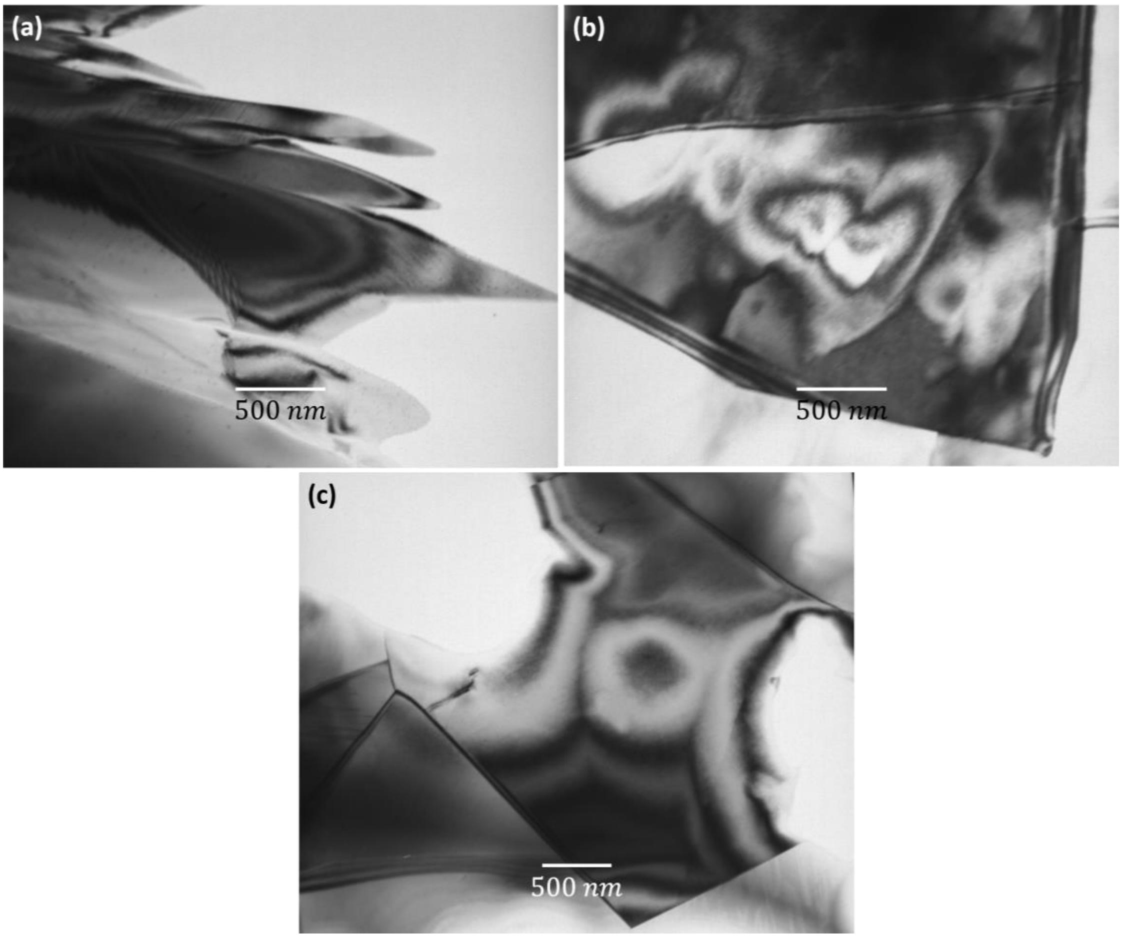

Figure 4. 42 TEM bright-field images of (a) the 1wt% BBO, (b) the 4.5wt% BBO and (c) the 5wt% BBO systems, sintered at 1200°C for 4 hours.

4.7 Mechanisms of Densification and Enhancement of Properties

Up to this point, BBO has been shown empirically to be a highly successful sintering aid for CTLNT compositions, resulting in the highest permittivity (125), temperature stable (4 ppm/°C) MW ceramic to date at 150°C lower sintering temperature than the matrix phase. The SEM images in section 4.4 reveal the presence of darker contrast glassy phases (possibly B-rich) in the fracture surfaces as well as light contrast Bi-rich regions. From the SEM data, it is clear that there is evidence of reaction between the BBO and CTLNT which is responsible for the non-linear (with BBO and sintering temperature) in some of the MW data in reported in section 4.5.

Direct evidence of the reaction is difficult to observe even by TEM but some CTLNT grains in compositions with the highest concentration of BBO exhibit small cuboid precipitates, figure 4. 43 ranging from $50 \leq x \leq 500nm$ in size. These precipitates exist only within the grain interiors, and are never been observed at the grain boundaries. Moreover, they are absent for 0 % BBO and have not to date been observed in 1% BBO samples, although this may be because of the small available specimen volume in TEM for analysis.

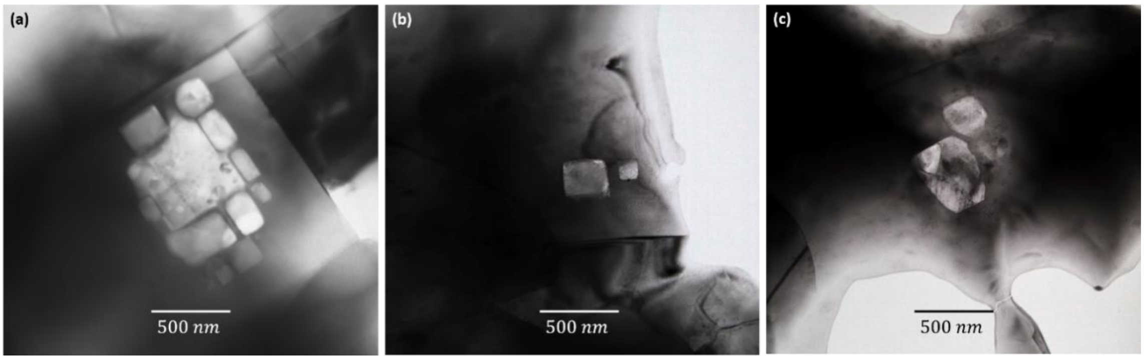

Figure 4. 43 TEM bright field images of the CTLNT + 5wt% BBO system, sintered at 1200°C for 4 hours, with observed precipitate microstructures.

Their cuboid shape, their absence or scarcity in low BBO concentration samples and their presence in the grain interiors rather than boundaries unambiguously defines the precipitates as reaction product rather than unreacted materials or common second phases for the CTLNT system. Figure 4. 44 shows the TEM bright-field image (a) of a CTLNT + 5wt% BBO sample matrix along with the EDS traces from the observed precipitate (b) and the adjacent matrix (c). The precipitate appears to be rich in titanium and therefore either anatase or rutile.

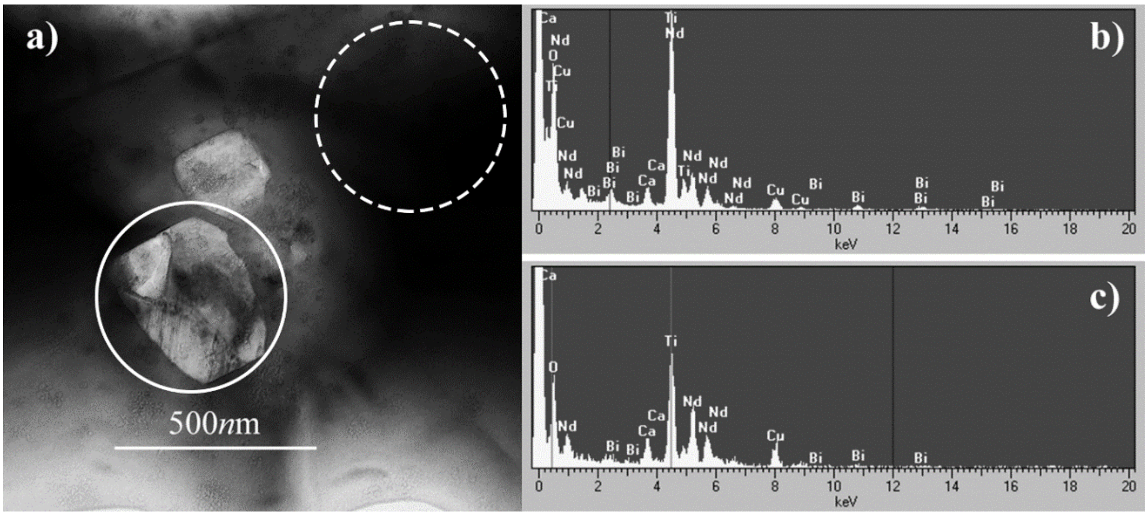

Figure 4. 44 TEM bright field image a) of a CTLNT + 5wt% BBO sample with corresponding EDS, where b) indicates a larger concentration of titanium within the precipitate, and c) indicates a lower concentration of titanium within the matrix in general. The full circle is the EDS data of collection area for spectra b) and the broken circle is that for spectra c). [19]

In addition, the EDS trace of the matrix contains not only calcium, titanium and neodymium as anticipated (lithium cannot be detected), but also a marked presence of bismuth within the CTLNT matrix. This suggests that Bi^{3+} has entered the CTLNT lattice during sintering as part of the reaction The presence of some matrix grains rich in Bi is consistent with the SEM data in section 4.4, especially at the higher BBO concentrations.

From the data obtained, it appears that Bi^{3+} enters the CTLNT lattice, however, the formation of the TiO_2 precipitates suggests that substitution of Bi^{3+} onto the A-site is not isovalent for Nd^{3+}, as would be expected. Instead, Ti^{4+} is ex-solved from the perovskite matrix, which implies the formation of titanium vacancies (V_{Ti}'''') within the CTLNT. The Bi therefore substitutes for either Ca or the combined Li/Nd, according to the following, proposed, generic defect equation [19]:

$$4A_A^x + Ti_{Ti}^x \Rightarrow 4Bi_A^{\cdot} + V_{Ti}'''' \tag{4.1}$$

where A = A-site cation.

Since Bi^{3+} has a higher polarizability than Ca and Li/Nd, its substitution into the CTLNT matrix enhances the ionic polarizability of the CTLNT, thereby locally enhancing the relative permittivity of the matrix wherever the substitution has occurred (the light regions in the SEM images in section 4.4). As the bismuth substitutes into the matrix, the BBO becomes deficient in bismuth, leading to the formation of boron-rich liquid phase (the darker grey regions in the SEM images in section 4.4). It is a boron-rich liquid phase (glassy when cooled to room temperature) which now acts as the sintering aid, rather than the pure BBO. This explains the non-linear nature of the reduction of τ_f with increased BBO concentration. The B-rich phases and glasses are known to have large negative τ_f values [37]–[41], and this relatively small presence of residual amorphous, or crystalline, B-rich phases helps to compensate for the positive τ_f of the CTLNT matrix.

The precipitates themselves are too few in volume fraction to significantly affect MW properties. TiO_2 typically has a $\varepsilon_r \sim 100$, $\tau_f = +400\, ppm/°C$ and a $Qf_0 > 5000$ GHz [42]–[44], so, perhaps, the presence would not necessarily be significantly detrimental to the Qf_0 and ε_r but would in principal increase τ_f.

Figure 4. 45 schematically illustrates the proposed sintering mechanism of the CTLNT + $x$wt% BBO system, where, during sintering, the Bi substitutes into the CTLNT matrix, resulting in V_{Ti}'''', forcing the Ti to ex-solve into TiO_2 precipitates, leaving behind a B-rich BBO phase as the sintering aid surrounding the matrix. Note that the B-rich glassy/liquid phase is difficult to observed in TEM but abundant in the SEM images since its modulus is considerable lower than the matrix and preferentially thins during ion beam milling.

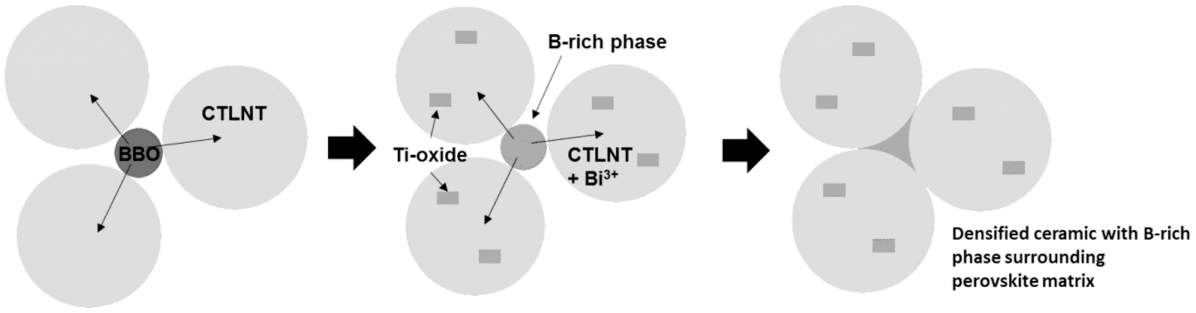

Figure 4. 45 Schematic of the proposed sintering mechanism, leading to enhanced MW properties as a result of BBO sintering aid additions [19].

4.8 Summary and Conclusion

The microwave and physical crystallographic properties of the material (1-x)CTLNT+xBBO have been investigated as a function of increased levels of BBO over a range of sintering temperatures to understand the causes and effects BBO has over the microwave properties of the CTLNT bulk material. BBO is used, primarily, as both a sintering aid to the CTLNT to reduce the sintering temperature and to reduce τ_f. In both respects, BBO is successful.

The sintering aid successfully reduces the optimal sintering temperature from approximately 1300°C down to between 1150-1200°C, whilst maintaining high density. As BBO concentration increased, a B-rich secondary glassy phase was routinely observed in the fracture surface and as darker contrast regions in the polished surface in the secondary electron images. EDS of the SEM samples revealed that the matrix contained larger proportions of bismuth with increased BBO content. An optimum composition of 4wt% BBO device yielded a balance of MW properties and reduction of sintering temperature down to 1200°C, with $\varepsilon_r = 125$, $Qf_0 = 2518$ and $\tau_f = 4\,ppm/°C$.

TEM analysis revealed similar findings to the SEM results, in that there were higher proportions of BBO within the CTLNT matrix as the BBO content increased. Very little evidence of liquid phase was present in the TEM samples, however this is likely due to preferential thinning of liquid-phase located at triple junctions during sample preparation. TEM diffraction patterns showed average diffraction patterns normally associated with perovskite diffraction patterns, with superstructure reflections and tilt systems consistent with those of the $CaTiO_3$ (CT) and $(Li_{0.5}Nd_{0.5})TiO_3$ (LNT) end members. There was also evidence of nano-chessboard ordering.

Most importantly, TEM bright field imaging and EDS revealed the presence of TiO_2 precipitates, ex-solved from the matrix in the higher BBO concentration samples. It was concluded that Bi substitutes into the CTLNT matrix, from the BBO liquid phase, creating V_{Ti}'''' regions within the matrix leaving a B-rich liquid phase behind. Bismuth is itself highly polarizable and its substitution into the CTLNT matrix creates a material with locally enhanced MW property regions to combat the negative influence of the presumably low ε_r liquid-phase, whilst the B-rich liquid-phase acts to reduce the sintering temperature and tune τ_f.

4.9 References

[1] I. M. Reaney and D. Iddles, “Microwave Dielectric Ceramics for Resonators and Filters in Mobile Phone Networks,” *J. Am. Ceram. Soc.*, vol. 89, no. 7, pp. 2063–2072, Apr. 2006.

[2] H. Takahashi, Y. Baba, K. Ezaki, Y. Okamoto, K. Shibata, K. Kuroki, and S. Nakano, “Dielectric Characteristics of $(A_{1/2}^{1+}\cdot A_{1/2}^{3+})TiO_3$ Ceramics at Microwave Frequencies,” *Jpn. J. Appl. Phys.*, vol. 30, no. Part 1, No. 9B, pp. 2339–2342, Sep. 1991.

[3] K. Ezaki, Y. Baba, H. Takahashi, K. Shibata, and S. Nakano, “Microwave Dielectric Properties of CaO-Li_2O-Ln_2O_3 -TiO_2 Ceramics,” *Jpn. J. Appl. Phys.*, vol. 32, no. Part 1, No. 9B, pp. 4319–4322, Sep. 1993.

[4] W. S. Kim, K. H. Yoon, and E. S. Kim, “Far-Infrared Reflectivity Spectra of $CaTiO_3$-$Li_{1/2}Sm_{1/2}TiO_3$ Microwave Dielectrics,” *Mater. Res. Bull.*, vol. 34, no. 14/15, pp. 2309–2317, 1999.

[5] D. A. Abdel Aziz, I. Sterianou, and I. M. Reaney, “$(1 - x)CaTiO_3$–$x(Li_{0.5}Nd_{0.5})TiO_3$ for ultra-small dielectrically loaded antennas,” *J. Mater. Sci.*, vol. 44, no. 23, pp. 6247–6250, 2009.

[6] X. Chen, W. Zhang, B. Zalinska, I. Sterianou, S. Bai, and I. M. Reaney, “Low Sintering Temperature Microwave Dielectric Ceramics and Composites Based on Bi_2O_3-B_2O_3,” *J. Am. Ceram. Soc.*, vol. 95, no. 10, pp. 3207–3213, Oct. 2012.

[7] V. N. Agafonov, V. A. Davydov, N. V. Porotnikov, and K. I. Petrov, “Vibrational Spectroscopic Study of the Structure of the Compounds Ln2Ti2O7 (Ln = La, Pr, and Nd) and the High-pressure Phase of $Sm_2Ti_2O_7$,” *Russ. J. Inorg. Chem*, vol. 28, p. 817, 1979.

[8] M. Yashima and R. Ali, “Structural phase transition and octahedral tilting in the calcium titanate perovskite CaTiO3,” *Solid State Ionics*, vol. 180, no. 2–3, pp. 120–126, 2009.

[9] A. G. Belous, G. N. Novitskaya, S. V Polyanetskaya, and Y. I. Gornikov, “The crystal-chemical and electrophysical characteristics of the complex oxides $Ln_{2/3-x}M_{3x}TiO_3$,” *Russ. J. Inorg. Chem*, vol. 32, pp. 156–157, 1987.

[10] A. D. Robertson, S. G. Martin, A. Coats, and A. R. West, “Phase diagrams and crystal chemistry in the Li+ ion conducting perovskites, $Li_{0.5-3x}RE_{0.5+x}TiO_3$: Re = La, Nd,” *J. Mater. Chem.*, vol. 5, no. 9, pp. 1405–1412, 1995.

[11] W. D. Kingery, H. K. Bowen, and D. R. Uhlmann, *Introduction to ceramics*, 2d ed. New York: Wiley, 1976.

[12] E. L. Colla, I. M. Reaney, and N. Setter, “Effect of structural changes in complex perovskites on the temperature coefficient of the relative permittivity,” *J. Appl. Phys.*, vol. 74, no. 5, p. 3414, 1993.

[13] L. Ingemarsson and M. Halvarsson, “SEM/EDX Analysis of Boron,” Gothenburgh, 2011.

[14] D. I. Woodward and I. M. Reaney, “Electron diffraction of tilted perovskites,” *Acta Crystallogr. Sect. B*, vol. 61, no. 4, pp. 387–399, 2005.

[15] A. Glazer, “Simple ways of determining perovskite structures,” *Acta Crystallogr. Sect. A*, vol. 31, no. 6, pp. 756–762, Nov. 1975.

[16] G. Burns and A. M. Glazer, *Space Groups for Solid State Scientists*, First Edit. New York, San Francisco, London: Academic Press, 1978.

[17] L. Farber, I. Levin, A. Borisevich, I. E. Grey, R. S. Roth, and P. K. Davies, “Structural study of $Li_{1+x-y}Nb_{1-x-3y}Ti_{x+4y}O_3$ solid solutions,” *J. Solid State Chem.*, vol. 166, no. 1, pp. 81–90, 2002.

[18] B. S. Guiton, W. Hui, and P. K. Davies, “Neutron powder diffraction of $(Nd_{7/12}Li_{1/4})TiO_3$ nano-checkerboard superlattices,” *Chem. Mater.*, vol. 20, no. 9, pp. 2860–2862, 2008.

[19] S. J. Nicholls, I. M. Reaney, and O. P. Leisten, “Enhancing Properties in Microwave Ceramics Using a Designer Sintering Aid,” *J. Am. Ceram. Soc.*, vol. 98, no. 12, pp. 3891–3896, Dec. 2015.

[20] B. S. Guiton and P. K. Davies, “Spontaneous compositional nanopatterning in Li-containing perovskite oxides,” *J. Am. Chem. Soc.*, vol. 130, no. 50, pp. 17168–17173, 2008.

[21] B. S. Guiton and P. K. Davies, “Nano-chessboard superlattices formed by spontaneous phase separation in oxides,” *Nat. Mater.*, vol. 6, no. 8, pp. 586–591, Aug. 2007.

[22] S. Yeo, Y. Horibe, S. Mori, C. M. Tseng, C. H. Chen, A. G. Khachaturyan, C. L. Zhang, and S.-W. Cheong, “Solid state self-assembly of nanocheckerboards,” *Appl. Phys. Lett.*, vol. 89, no. 23, p. 233120, 2006.

[23] “A checkerboard of materials,” *Nat. Mater.*, vol. 6, no. 2, pp. 87–87, Feb. 2007.

[24] H. J. Lee, H. M. Park, S. H. Oh, Y. K. Cho, J. O. Son, and S. Nahm, “Microstructures in Complex Perovskite $(Li_{1/2}Ln_{1/2})TiO_3$ (Ln = Pr, Nd, Sm),” *Jpn. J. Appl. Phys.*, vol. 43, no. 11A, pp. 7592–7595, Nov. 2004.

[25] M. Abe and K. Uchino, “X-ray study of the deficient perovskite,” *Mater. Res. Bull.*, vol. 9, no. 2, pp. 147–155, Feb. 1974.

[26] P. N. Iyer and A. J. Smith, “Double oxides containing niobium, tantalum, or protactinium. III. Systems involving the rare earths,” *Acta Crystallogr.*, vol. 23, no. 5, pp. 740–746, Nov. 1967.

[27] H. P. Rooksby, E. A. D. White, and S. A. Langston, “Perovskite-Type Rare-Earth Niobates and Tantalates,” *J. Am. Ceram. Soc.*, vol. 48, no. 9, pp. 447–449, Sep. 1965.

[28] J. A. Alonso, J. Sanz, J. Santamaría, C. León, A. Várez, and M. T. Fernández-Díaz, “On the Location of Li+ Cations in the Fast Li-Cation Conductor La0.5Li0.5TiO3 Perovskite,” *Angew. Chemie Int. Ed.*, vol. 39, no. 3, pp. 619–621, Feb. 2000.

[29] J. Sanz, J. A. Alonso, A. Varez, and M. T. Fernández-Díaz, “Octahedral tilting and ordering of vacancies in the fast ion conductor $Li_{0.12}La_{0.63}TiO_3$ perovskite: a neutron diffraction study,” *J. Chem. Soc. Dalt. Trans.*, no. 7, pp. 1406–1408, Mar. 2002.

[30] M. Sommariva and M. Catti, “Neutron Diffraction Study of Quenched $Li_{0.3}La_{0.567}TiO_3$ Lithium Ion Conducting Perovskite,” *Chem. Mater.*, vol. 18, no. 9, pp. 2411–2417, May 2006.

[31] M. Catti, “First-Principles Modeling of Lithium Ordering in the LLTO ($Li_xLa_{2/3 - x/3}TiO_3$) Superionic Conductor,” *Chem. Mater.*, vol. 19, no. 16, pp. 3963–3972, Aug. 2007.

[32] A. Feteira, D. Iddles, T. Price, D. Muir, and I. M. Reaney, “High-Permittivity and Low-Loss Microwave Dielectric Ceramics Based on $(x)RE(Zn_{1/2}Ti_{1/2})O_3$-$(1-x)CaTiO_3$ (RE=La and Nd),” *J. Am. Ceram. Soc.*, vol. 94, no. 3, pp. 817–821, Mar. 2011.

[33] E. V Chenskii, “Thermodynamic relations for the domain structure of ferroelectrics,” *Sov. Phys. Solid State*, vol. 14, pp. 1940–1944, 1973.

[34] W. Cao and C. A. Randall, “Grain size and domain size relations in bulk ceramic ferroelectric materials,” *J. Phys. Chem. Solids*, vol. 57, no. 10, pp. 1499–1505, Oct. 1996.

[35] G. Arlt, “The influence of microstructure on the properties of ferroelectric ceramics,” *Ferroelectrics*, vol. 104, no. 1, pp. 217–227, Apr. 1990.

[36] G. Arlt, “Twinning in ferroelectric and ferroelastic ceramics: stress relief,” *J. Mater. Sci.*, vol. 25, no. 6, pp. 2655–2666, Jun. 1990.

[37] N. Mori, Y. Sugimoto, J. Harada, and Y. Higuchi, “Dielectric properties of new glass-ceramics for LTCC applied to microwave or millimeter-wave frequencies,” *J. Eur. Ceram. Soc.*, vol. 26, no. 10–11, pp. 1925–1928, 2006.

[38] Z. N. Wing, B. Wang, and J. W. Halloran, “Permittivity of Porous Titanate Dielectrics,” *J. Am. Ceram. Soc.*, vol. 89, no. 12, pp. 3696–3700, 2006.

[39] C. L. Huang and K. H. Chiang, “Improved high-Q microwave dielectric material using B_2O_3-doped $MgNb_2O_6$ ceramics,” *Mater. Sci. Eng. A*, vol. 474, no. 1–2, pp. 243–246, 2008.

[40] H. X. Lin, Y. Zhang, X. Y. Zhao, W. Chen, and L. Luo, “Sintering and microwave dielectric properties of $La(Mg_{0.5}Ti_{0.5})O_3$ ceramics doped with La_2O_3-B_2O_3-TiO_2 glass,” *Jpn. J. Appl. Phys.*, vol. 47, no. 9, pp. 7243–7245, 2008.

[41] U. Došler, M. M. Kržmanc, and D. Suvorov, “The synthesis and microwave dielectric properties of $Mg_3B_2O_6$ and $Mg_2B_2O_5$ ceramics,” *J. Eur. Ceram. Soc.*, vol. 30, no. 2, pp. 413–418, 2010.

[42] R. C. Pullar, S. J. Penn, X. Wang, I. M. Reaney, and N. M. Alford, “Dielectric loss caused by oxygen vacancies in titania ceramics,” *J. Eur. Ceram. Soc.*, vol. 29, no. 3, pp. 419–424, 2009.

[43] S. Chao and F. Dogan, “Processing and Dielectric Properties of TiO_2 Thick Films for High-Energy Density Capacitor Applications,” *Int. J. Appl. Ceram. Technol.*, vol. 8, no. 6, pp. 1363–1373, 2011.

[44] S. Marinel, D. H. Choi, R. Heuguet, D. Agrawal, and M. Lanagan, “Broadband dielectric characterization of TiO_2 ceramics sintered through microwave and conventional processes,” *Ceram. Int.*, vol. 39, no. 1, pp. 299–306, 2013.

Chapter 5: Investigations into $0.2CaTiO_3$ – $0.8(Li_{0.5}Sm_{0.5})TiO_3$ (CTLST) with Additions of $Bi_4B_2O_9$ (BBO)

5.1 Introduction

The content of this chapter is a natural continuation from the previous chapter, driven by one simple question: is the substitution mechanism seen in the CTLNT+xBBO system repeatable for similar materials, or is it particular to CTLNT?

In this chapter, each experimental result obtained for the CTLNT+xBBO system is repeated, however the element neodymium is changed for samarium, to produce $0.2CaTiO_3$ - $0.8(Li_{0.5}Sm_{0.5})TiO_3$ (CTLST). Therefore, a parallel analysis will be conducted to compare both systems, including phase assemblage, density, microstructure observations under SEM and TEM, with EDS, as well as MW analysis.

Samarium was chosen as the rare-earth element replacement for Nd because it is a lanthanide element, with the same valence and similar (albeit slightly smaller) ionic radius, thus minimising the potential change to the perovskite tolerance factor, and overall MW properties. Takahashi *et al.* [1], [2] studied the change in overall MW properties between different CTL[RE]T systems (where RE = lanthanide) and found similar MW properties between the compounds, albeit with an overall reduction of ε_r and τ_f with decreased ionic radii of the RE element. As such, the CTLST system is expected to be an inferior MW dielectric product, compared with the CTLNT system.

However, CTLST has the advantage over the CTLNT system in that the RE element Sm is cheaper than its Nd counterpart [3]. Takahashi *et al.* [1], [2] also noted, however, that the RE element Sm is a more refractory, compared with Nd. As such, higher calcination and sintering temperatures are likely required to fabricate a CTLST antenna, potentially offsetting the saving of using Sm over Nd in raw material price.

5.2 Phase Assemblage

Initial fabrication routes followed that of the CTLNT system, with test reactions conducted to determine the correct calcination and sintering temperatures of the pure CTLST system. Since Sm has been reported as being a more refractory element [1], [2], [4], starting temperatures should be higher for the CTLST system. Powder X-Ray Diffraction was conducted on test samples of pure CTLST. Figure 5. 1 shows the presence of a secondary $Sm_2Ti_2O_7$ pyrochlore phase (ICDD: 04-005-7194 [5]), indicated by the triangles above the two main pyrochlore peaks.

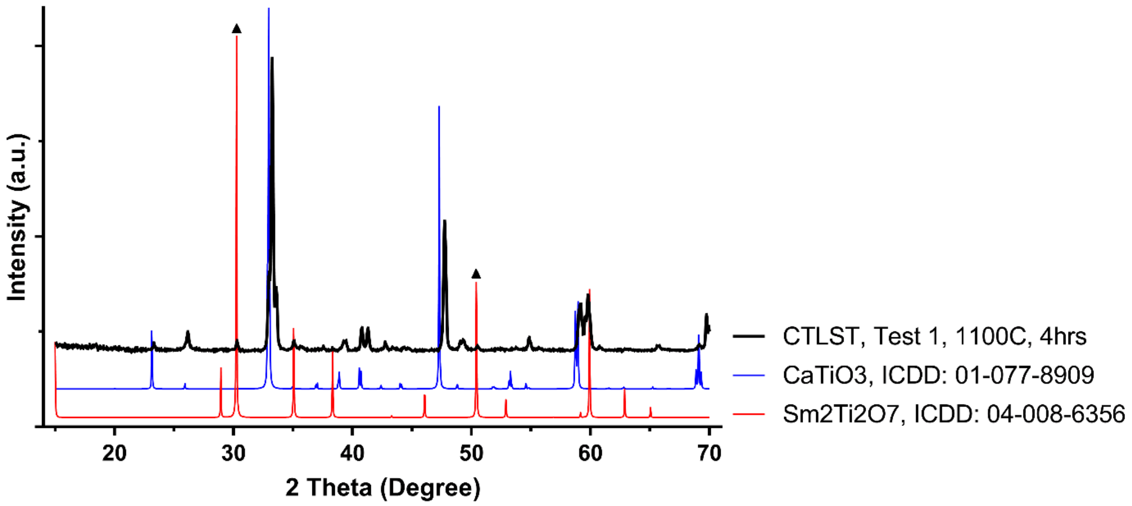

Figure 5. 1 XRD of the first CTLST test reaction compared with the XRD ICDD cards for CaTiO3 (ICDD: 01-077-8909 [6]) and Sm2Ti2O7 (ICDD: 04-008-6356 [5]), confirming that the secondary phase present is a $Sm_2Ti_2O_7$ pyrochlore structure, indicated by triangle symbols.

This is similar to the CTLNT test samples at 1100°C, indicating that the higher calcination temperatures are required. Figure 5. 2 showed that the calcination temperature for undoped CTLST was higher than that of the CTLNT, which has no secondary phases at 1150°C, rather than 1175°C for the CTLST. Increased calcination time at 1150°C also reduced the presence of the secondary phase, however increasing the temperature further proved to be the more effective option, as there were still traces of secondary phase after 16 hours of calcination at 1150°C.

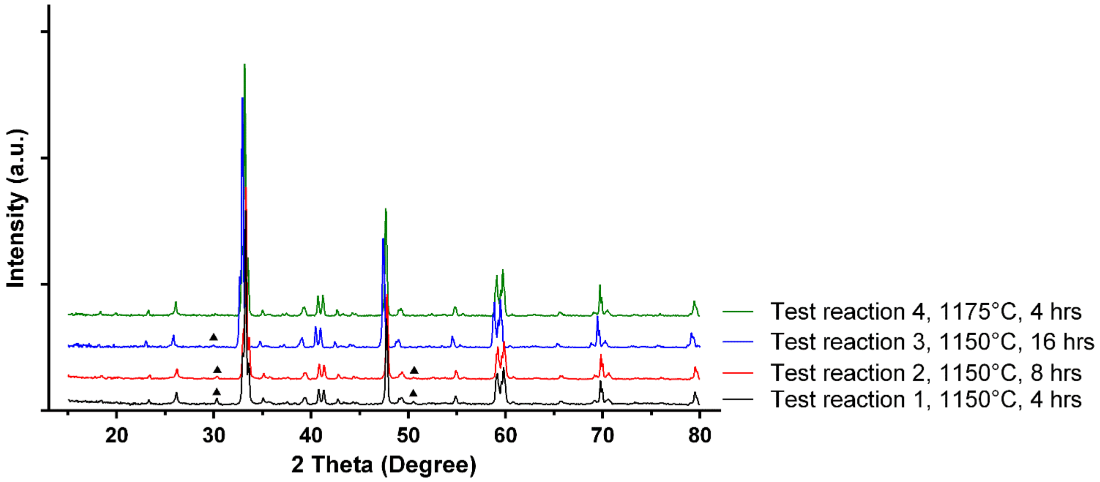

Figure 5. 2 XRD of 4 CTLST test reactions, showing the gradual elimination of the secondary, pyrochlore structure with increasing calcination times and, finally, calcination temperature.

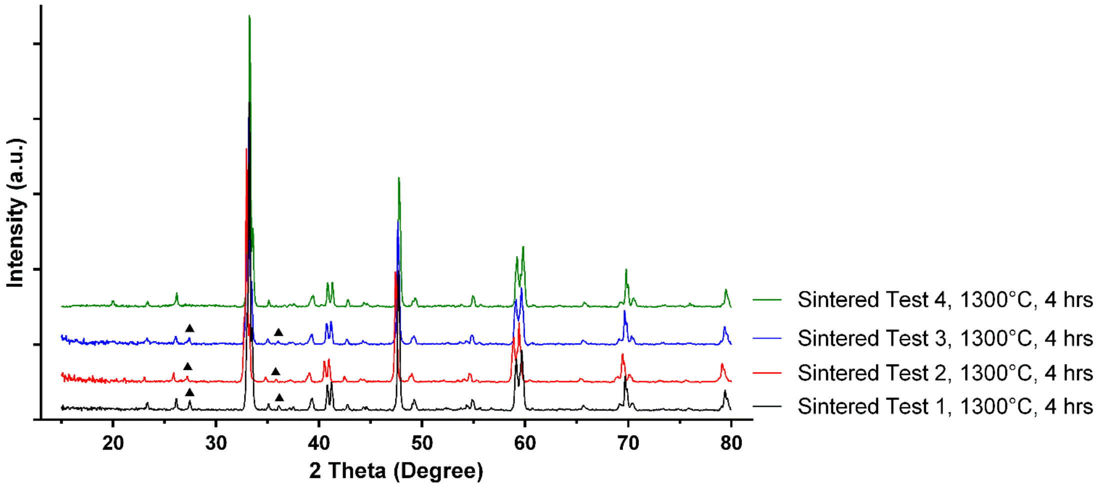

Figure 5. 3 XRD of 4 sintered test reactions, showing the elimination of secondary phases with the elimination of the pyrochlore structure from the calcination stage.

Upon sintering, if there is a pyrochlore phase is present after calcination, figure 5. 3, another residual secondary phase tends to be observed within the composite samples, irrespective of the intensity of the pyrochlore peaks (figure 5. 5). Only by removing the pyrochlore phase could secondary phase peaks in the sintered samples be removed. The XRD traces for CTLST were compared to both the $CaTiO_3$ (ICDD: 01-077-8909 [6]) and $(Li_{0.5}Sm_{0.5})TiO_3$ (ICDD: 04-006-1962 [7]) end-member ICDD cards, as seen in figure 5. 4. The same batch of BBO (figure 4. 4, p.74) used in the CTLNT compounds was also used in the CTLST compositions.

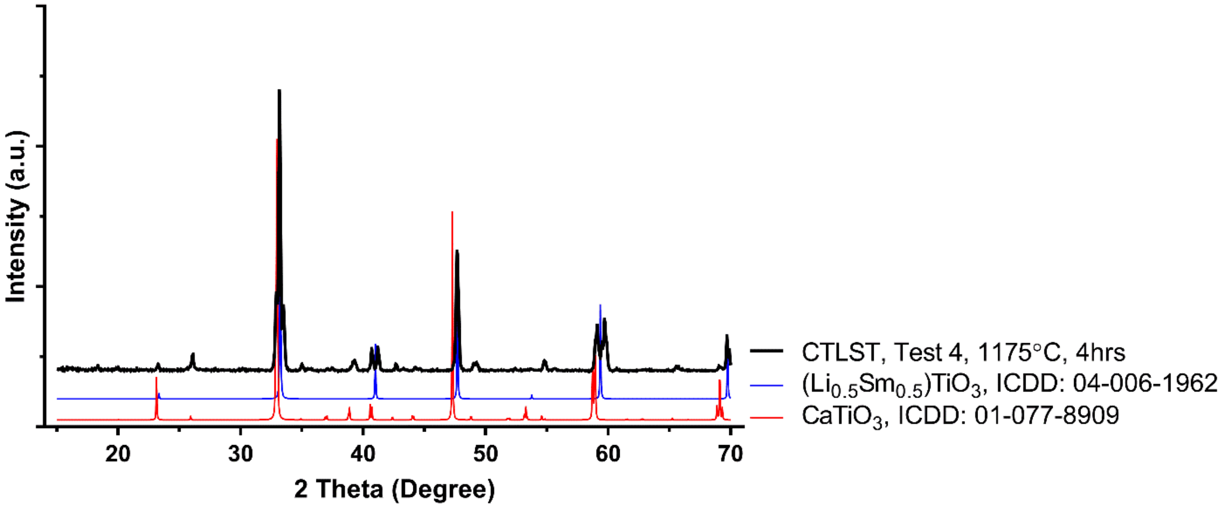

Figure 5. 4 XRD of CTLST Test 4, calcined at 1175°C, compared with the ICDD cards for CaTiO3 (ICDD: 01-077-8909 [6]) and (Li0.5Sm0.5)TiO3 (ICDD: 04-006-1962 [7]).

XRD patterns of crushed CTLST, for all fabricated compositions, are shown in figure 5. 5. Similar to the CTLNT system, no changes of phase assemblage, irrespective of sintering temperature and BBO concentration, was observed. There is, however, evidence of a secondary pyrochlore phase in all samples, regardless of sintering temperature and BBO content, indicated by a triangle at approximately 31 2θ°. This is perhaps remnant from the calcination step, due to lower sintering temperature, compared to the undoped composition.

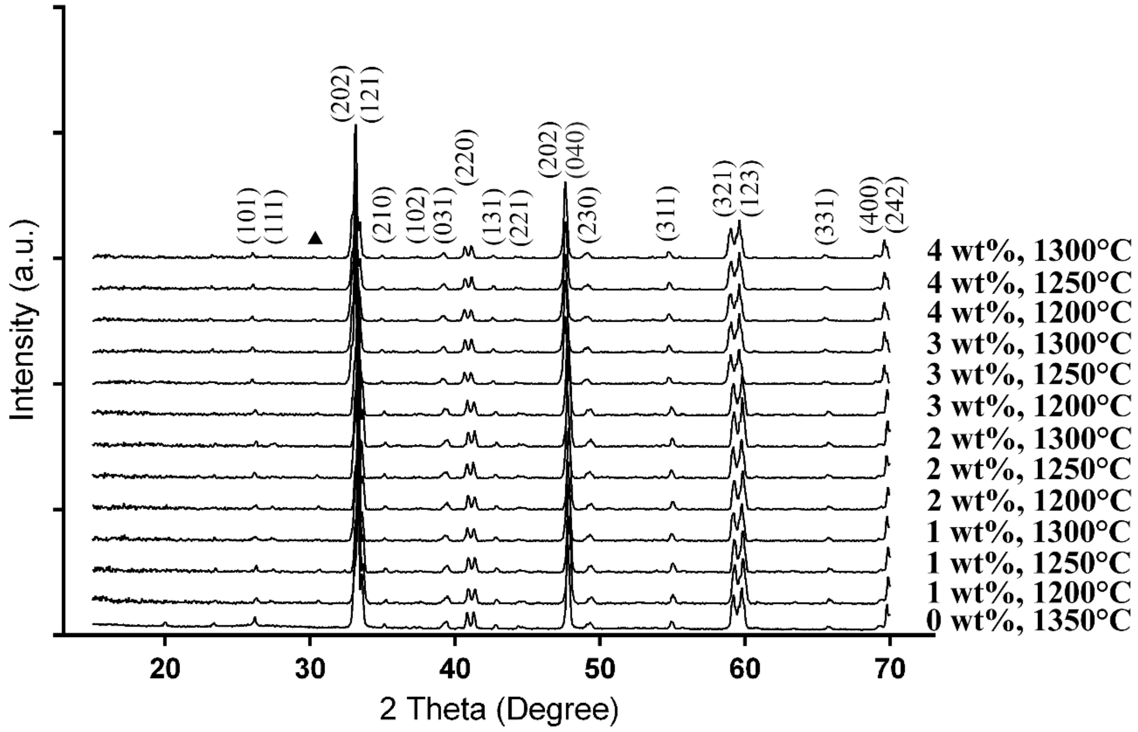

Figure 5. 5 X-Ray diffraction pattern of all CTLST + *x*wt% BBO compositions, sintered at 1350°C, for the pure CTLST sample, 1200°C, 1250°C and 1300°C. The triangle indicates the presence of a secondary, pyrochlore phase, present in all but the pure CTLST compositions.

5.3 Shrinkage and Density

Additions of BBO into the CTLNT system had a positive effect on the density and shrinkage, particularly at lower sintering temperatures. A similar trend was observed in the CTLNT system. Figure 5. 6 and table 5. 1 show the shrinkage and densification behaviour of each CTLST composition, plotted with respect to sintering temperature and composition.

At lower sintering temperatures, increasing the BBO content increases the density of the composite, with the 4wt% composition achieving a marginally denser sample than the pure CTLST material, at 1200°C. As the sintering temperature rises to 1250°C, the density of all compositions increase, with the largest rise in density appearing in the 1 and 2wt% BBO compositions, while the 3 and 4wt% compositions have a slight increase in density with the increase in sintering temperature. This is also synonymous with the CTLNT system, in which the largest rise in density occurs in the lower BBO compositions. However, at the highest sintering temperature investigated of 1300°C, all densities decreased from the maximum achieved at 1250°C.

Table 5. 1 List of densities and linear shrinkages of the (1-*x*)CTLST-*x*BBO compositions, including the pure end-members for comparison.

Sample Type	Sintering Temperature (°C)	Density (g/cm^3) (± 0.01)	% Theoretical Density (± 0.3)	Shrinkage (%) (± 0.1)
CTLST	1350	4.90	98.2	17.7
$Bi_4B_2O_9$	650	7.49	91.5	16.0
1wt%	1200	4.78	95.5	18.1
	1250	4.96	99.1	18.9
	1300	4.92	98.2	18.9
2wt%	1200	4.78	95.1	18.8
	1250	4.97	98.8	19.3
	1300	4.93	98.1	19.5
3wt%	1200	4.90	97.0	19.0
	1250	4.93	97.6	19.0
	1300	4.88	96.7	18.9
4wt%	1200	4.94	97.5	18.9
	1250	4.98	98.2	19.2
	1300	4.94	97.4	19.2

The linear shrinkage of the samples follows a similar trend with changes in density in the CTLST system. However, the linear shrinkage does not match with the increase in density as well as in the CTLNT system. In both cases, the 1wt% BBO system has the lowest linear shrinkage and density, and both cases have an initial rise in shrinkage, which reduces at higher temperatures. In the CTLST system, the initial rise in linear shrinkage happens between 1200-1250°C, and decreases at 1250-1300°C.

The addition of BBO into the CTLST systems appears to suggest that increased sintering, most likely as a result of liquid-phase sintering, is being promoted by the BBO. Especially as many of the density values appear to exceed the density of the pure CTLST, even at the lowest sintering temperature in the 4wt% system. The largest overall density observed was 4.98g/cm^3, in the 4wt% system, at a sintering temperature of 1250°C, and the lowest overall density observed was 4.78g/cm^3, in the 1wt% system, at 1200°C. All Values of density are reported with an error of ± 0.01 gcm^{-3}.

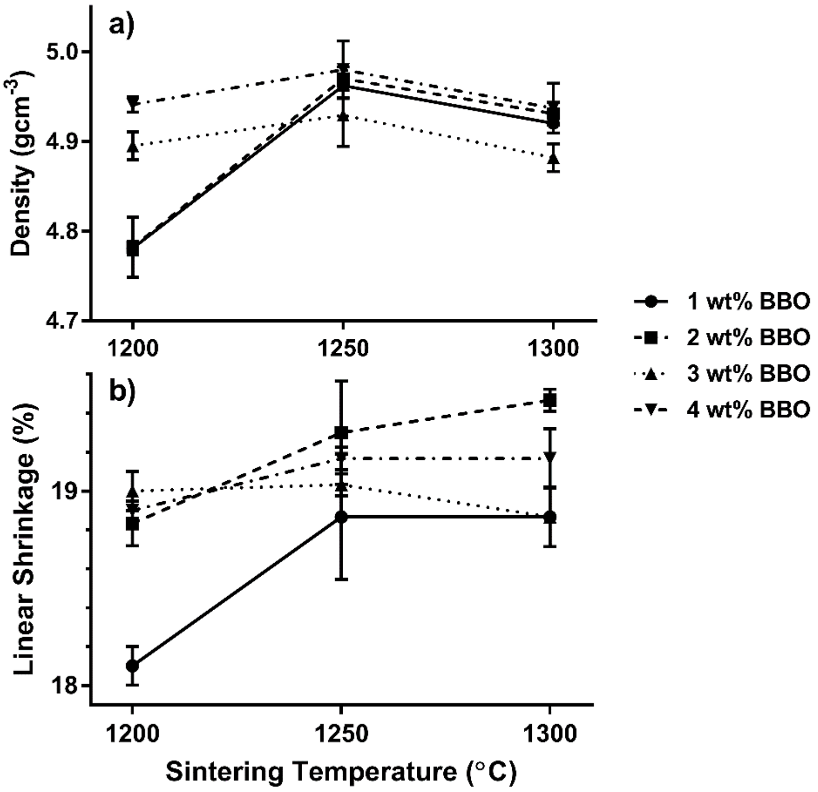

Figure 5. 6 Average relationships of sintering temperature and composition with that of a) density and b) linear shrinkage.

5.4 Microstructure Observations from Scanning Electron Microscopy (SEM)

Scanning electron microscopy (SEM) was conducted on composite samples to see differences in microstructure coincident with the changes in density and linear shrinkage. For each sample, secondary electron imaging (SEI) and backscatter electron (BE) imaging was conducted on polished surfaces, while only SEI was conducted on the fracture surfaces. Semi-quantitative energy-dispersive X-ray spectroscopy (EDS) was conducted on both the polished and fracture surface of each sample to see if different regions or structures are associated with different proportions of elements. Since the EDS is only semi-quantitative, rather than quantitative, exact numbers will not be accurate, however the spectra can still be used to give an idea of what elements are present within the samples. The lighter elements, such as boron, have low photon energies, which can lead to complications such as having large X-ray absorption [8].

CTLST + 1wt% BBO Compositions

The SEM images of the CTLST + 1wt% BBO samples, sintered at 1200°C, 1250°C and 1300°C, are pictured in figure 5. 7, figure 5. 8 and figure 5. 9, respectively. At a sintering temperature of 1200°C, grain sizes begin at an average of 3µm in figure 5. 7 c), although there is a large variation in grain size. Grain morphologies are regular (cuboid), more so than for the neodymium-based system, and there are some areas of amorphous phase present, while there was no visible amorphous phase in the neodymium system. The polished surface reveals a largely homogenous material, particularly when considering the BE image in figure 5. 7 b). The darker regions in the BE image correspond with larger pores seen in the SEI image, a). This may be due to pores being deep, thus restricting signal return or the presence of a liquid phase which is more likely to pool within the pores of the microstructure. In contrast to the CTLNT system, at 1wt% BBO, there are fewer pores in the CTLST system, although the density of CTLST at 1200°C is higher than the CTLNT at 1150°C, and more closely resembles the density of the equivalent CTLNT system sintered at 1250°C.

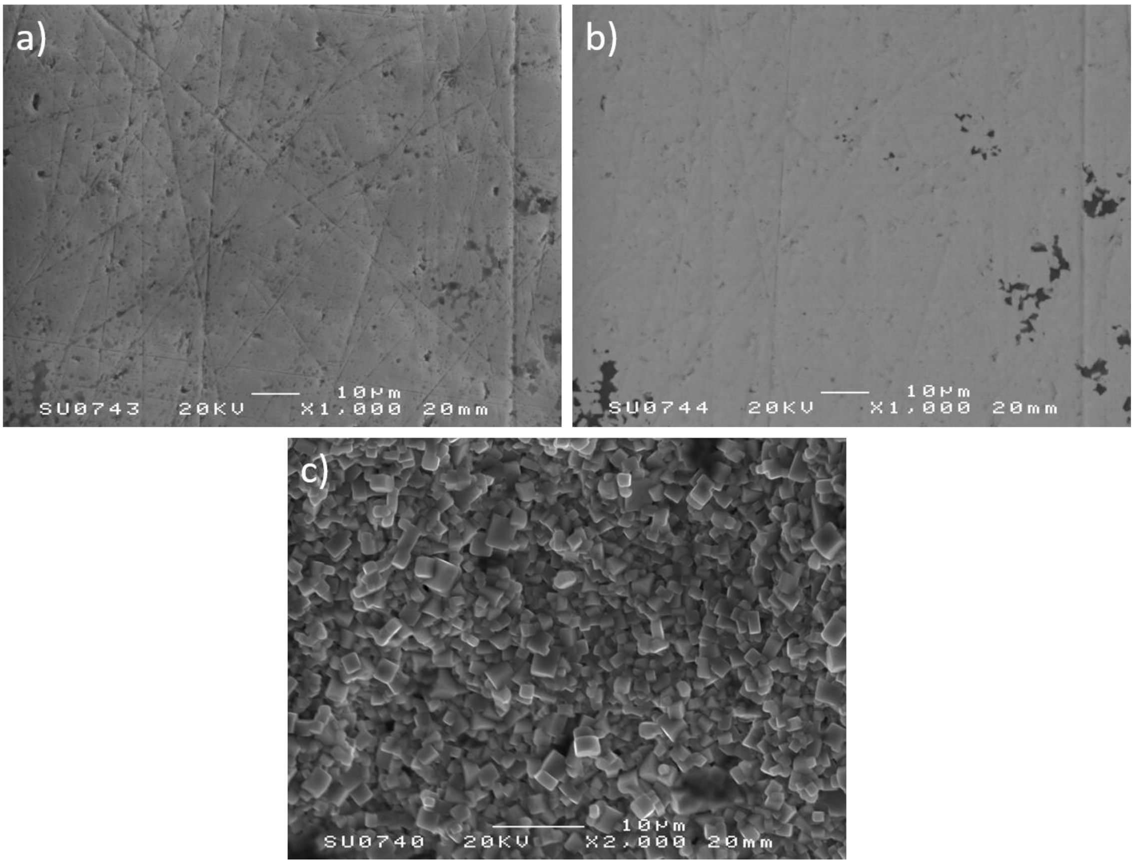

Figure 5. 7 SEM images of the CTLST + 1wt% BBO system, sintered at 1200°C for 4 hours, of the polished surface under a) SEI and b) BE, c) the fracture surface of the sample under SEI.

Upon raising the sintering temperature to 1250°C, the polished surface of the CTLST + 1wt% BBO system appears homogeneous, figure 5. 8 a) and b). Overall porosity in the SEI has reduced, due to a reduction in the presence of smaller pores, however there is evidence of sporadic, larger pores on the polished surface. This reduction in apparent porosity compares well with the increase in density observed in figure 5. 6 and table 5. 1. Grain size and morphology has further developed at the higher sintering temperature where the grain size has increased to an average of 4-5µm and the grains more defined. At 1250°C, some grains appear to have rounded edges even with small additions of BBO, reminiscent of the CTLNT system, presumably due to dissolution of the matrix into the liquid phase.

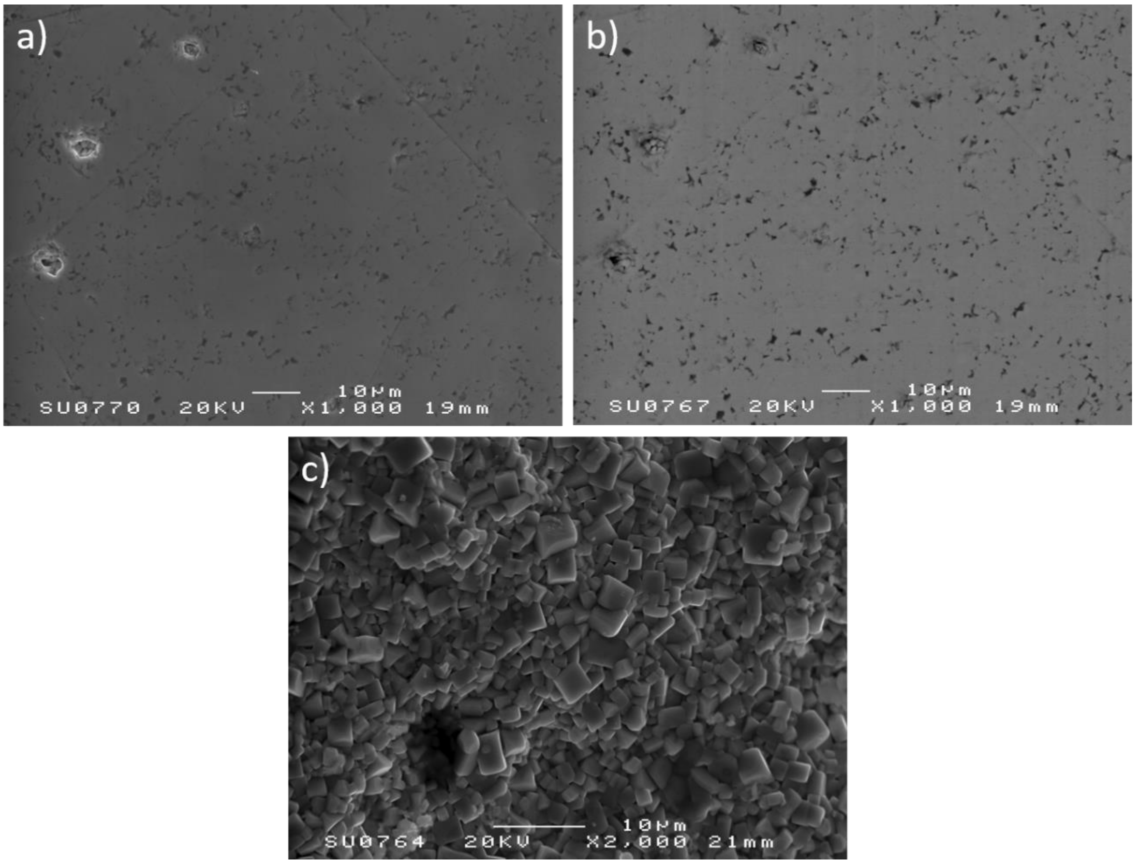

Figure 5. 8 SEM images of the CTLST + 1wt% BBO system, sintered at 1250°C for 4 hours, of the polished surface under a) SEI and b) BE, c) the fracture surface of the sample under SEI.

In figure 5. 9, a) SEI and the b) BE images of CTLST with 1wt% BBO suggest that the material is single phase, due to homogenous contrast in the image. The apparent density appears to be lower than the same system sintered at 1250°C, since there is a larger number of smaller and larger pores, as well as an increase in size of the largest pores. From the fracture surface images, a darker amorphous phase is observed amongst the crystal grains (figure 5. 9, d)). In addition, the grains themselves have increased in size, to an average of 5-7µm (figure 5. 9, c)).

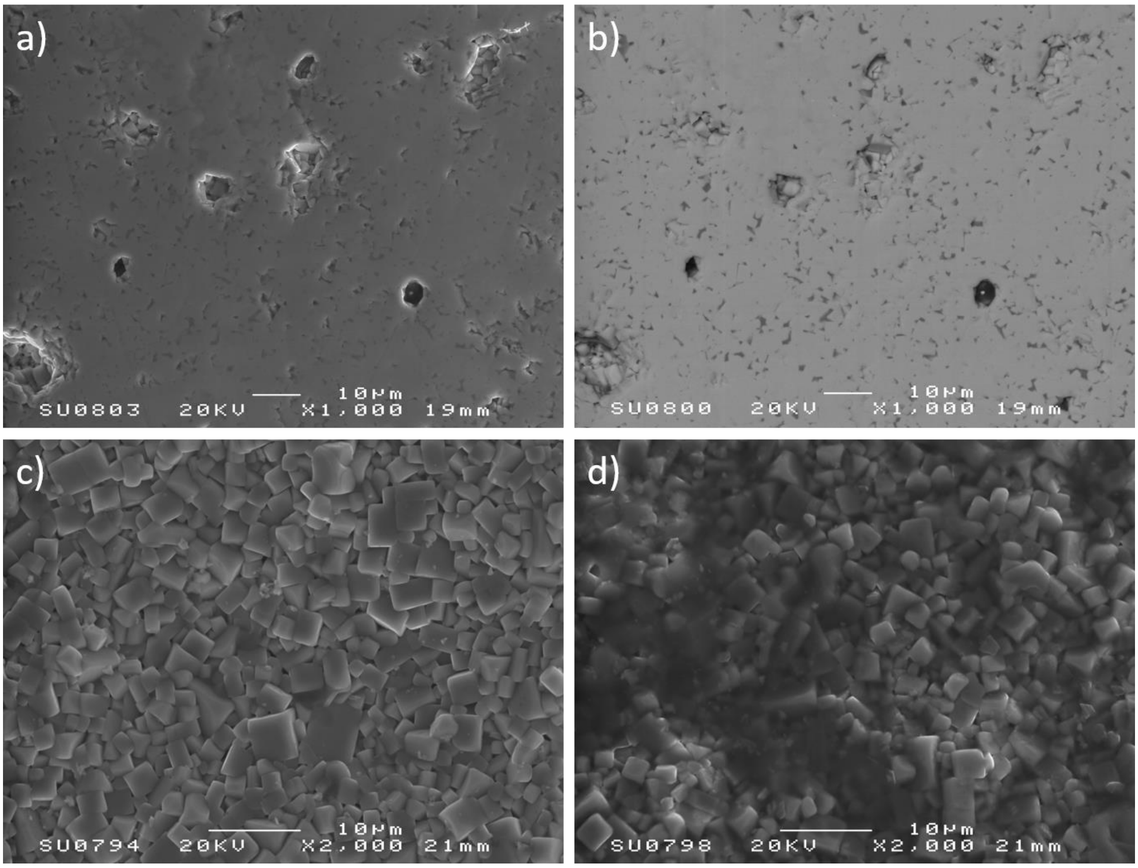

Figure 5. 9 SEM images of the CTLST + 1wt% BBO system, sintered at 1300°C for 4 hours, of the polished surface under a) SEI and b) BE, c) the fracture surface of the sample under SEI, and d) the fracture surface at a different location of crystal and amorphous morphologies under SEI.

Increasing the sintering temperature in the CTLST + 1wt% BBO system increases grain growth although overall low concentrations of BBO have little effect on the microstructure of the CTLST system over the 3 sintering temperatures. There is however, evidence of an amorphous phase in the sample sintered at 1300°C, rather than at lower sintering temperatures.

Figure 5. 10 and figure 5. 11 show the EDS analysis of the fracture and polished surface for the CTLST + 1wt% BBO composition, sintered at 1250°C, respectively. Within the fracture surface, spectra were taken of the brighter contrast grains and of the darker contrast, amorphous phase, visible surrounding some of the grains. The spectra of the fracture surface indicate that the brighter contrast of the grains have larger proportions of the heavier element, Sm, as well as Ca, consistent with the bright contrast. The darker region, by contrast, has a visibly larger Ti peak compared with the brighter contrast of the grains.

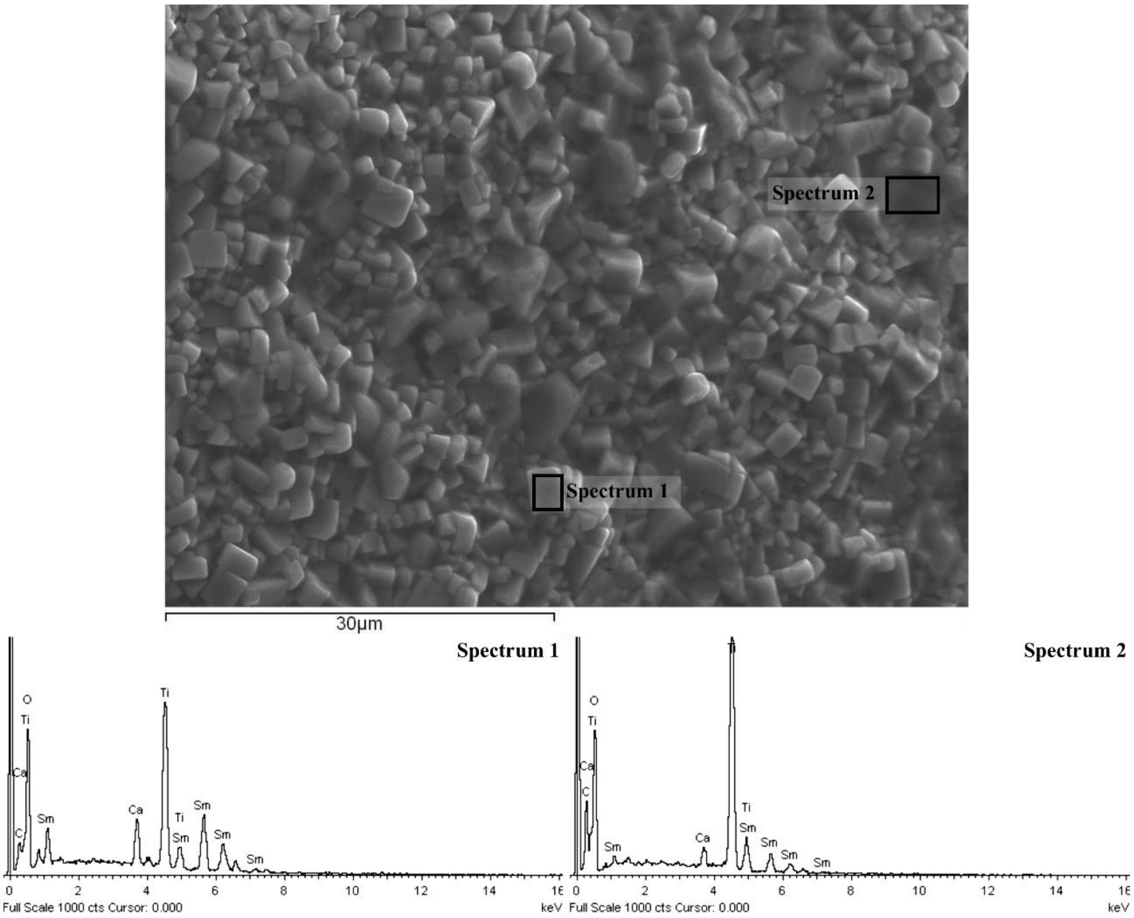

Figure 5. 10 EDS of the CTLST + 1wt% BBO composite fracture surface, sintered at 1250°C. Spectrum 1 is a typical representation of the grain, and spectrum 2 is of a darker region surrounding the grains. The SEI image indicates the locations of the EDS.

The EDS of the polished surface (figure 5. 11) is consistent with the EDS data obtained from the fracture surface, in that the average contrast of the matrix (brighter region scanned of the two indicated in the figure) has a larger Sm concentration. The darker regions, which are likely regions of B-rich liquid-phase, judging from similar results of the CTLNT system, appears to show lower proportions of Ca and Sm, with larger proportions of Ti. If the liquid-phase is the B-rich sintering aid, it would certainly explain why there would be less signal return for Ca and Sm, with little evidence of B due to the likelihood of X-ray absorption [8].

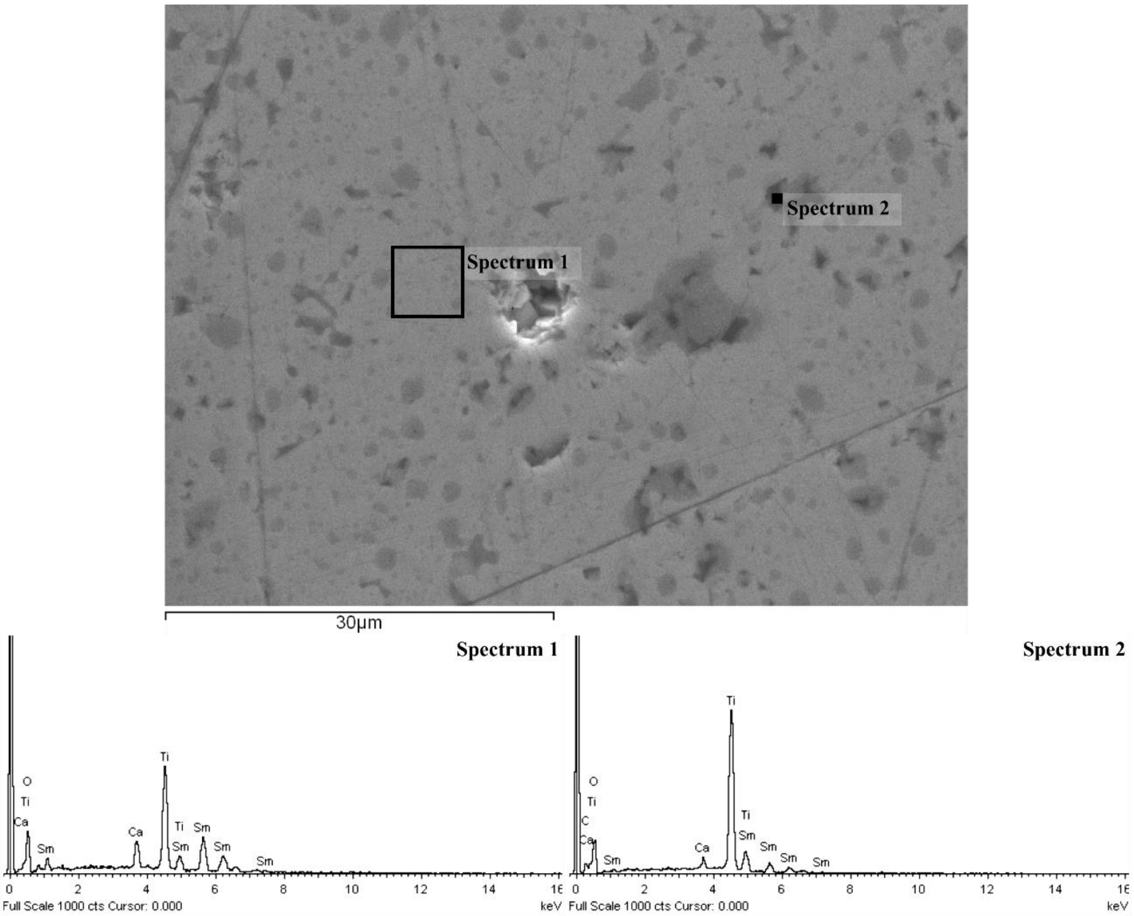

Figure 5. 11 EDS of the CTLST + 1wt% BBO composite polished surface, sintered at 1250°C. Spectrum 1 is a typical representation of the brighter contrast regions, and spectrum 2 is of the darker contrast regions. The SEI image indicates the locations of the EDS.

CTLST + 2wt% BBO Compositions

Figure 5. 12 show the polished surface of the CTLST + 2wt% BBO using SEI, a), and BEI, b). The CTLST + 2wt% BBO system is similar to the 1wt% composition at 1200°C, in terms of apparent density and homogeneity of the microstructure. SEI of the fracture surface of CTLST + 2wt% BBO can be seen in figure 5. 12 c) and d). The average grain size is 2-4µm and the grains are well defined. In both fracture surface images, but more prominently in figure 5. 12 d), there is already evidence of liquid phase surrounding the crystal grains.

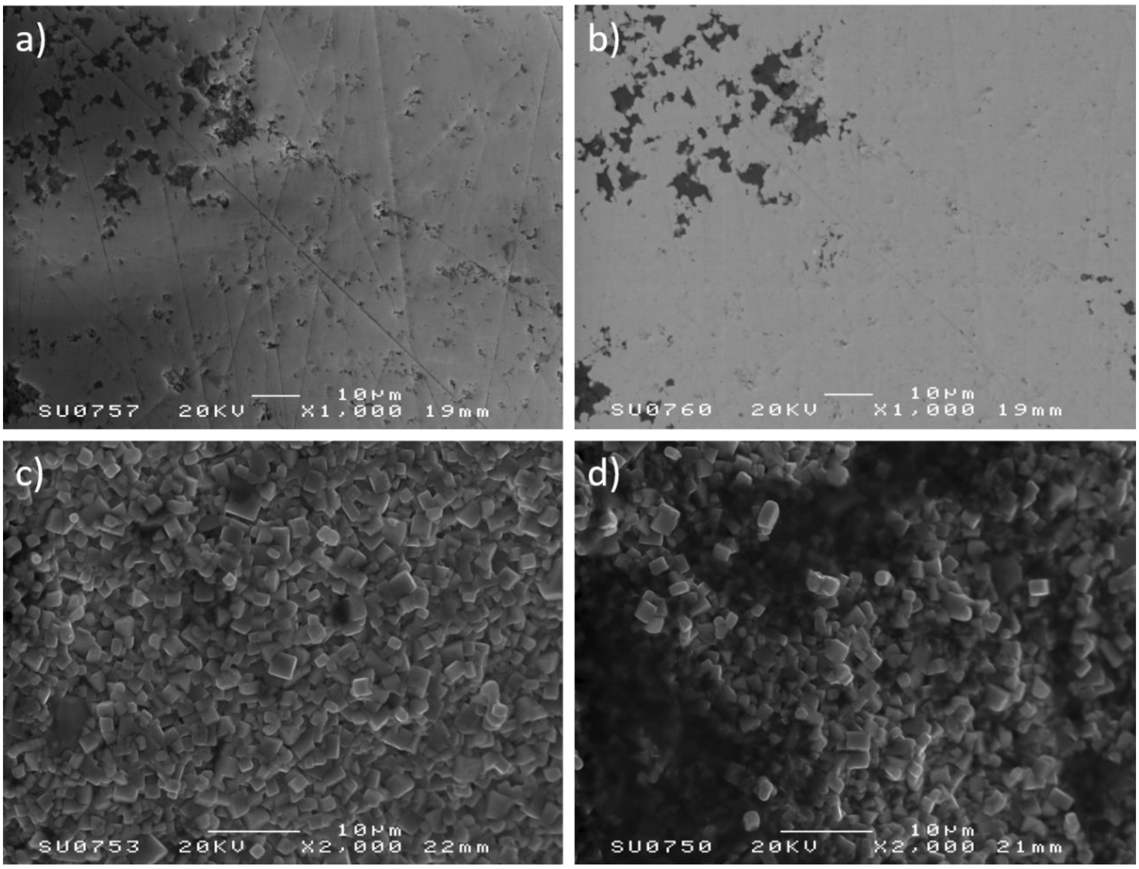

Figure 5. 12 SEM images of the CTLST + 2wt% BBO system, sintered at 1200°C for 4 hours, of the polished surface under a) SEI and b) BE, c) the fracture surface of the sample under SEI, and d) the fracture surface at a different location of crystal and amorphous morphologies under SEI.

Figure 5. 13 a) and b) are SEI and BE images of the polished surface of CTLST + 2wt% BBO sintered at 1250ºC with SEI images of the fracture surface in c) and d). The polished surface at 1250°C has higher density than the sample sintered at 1200°C, in agreement with the increased density observed in figure 5. 6. In addition, the sample has a homogenous distribution of elements, as evidenced by the single shade of grey in both figures. Any changes in gradient in the BE image are associated with porosity. Grain size has increased, with the increase in sintering temperature, to an average of 3-6µm, similar to that in CTLST + 1wt% BBO system. In figure 5. 13 d), the amorphous phase differs from figure 5. 12 d) since it contains Zr, present due to contamination from yttria-stabilised zirconia milling media (figure 5. 16).

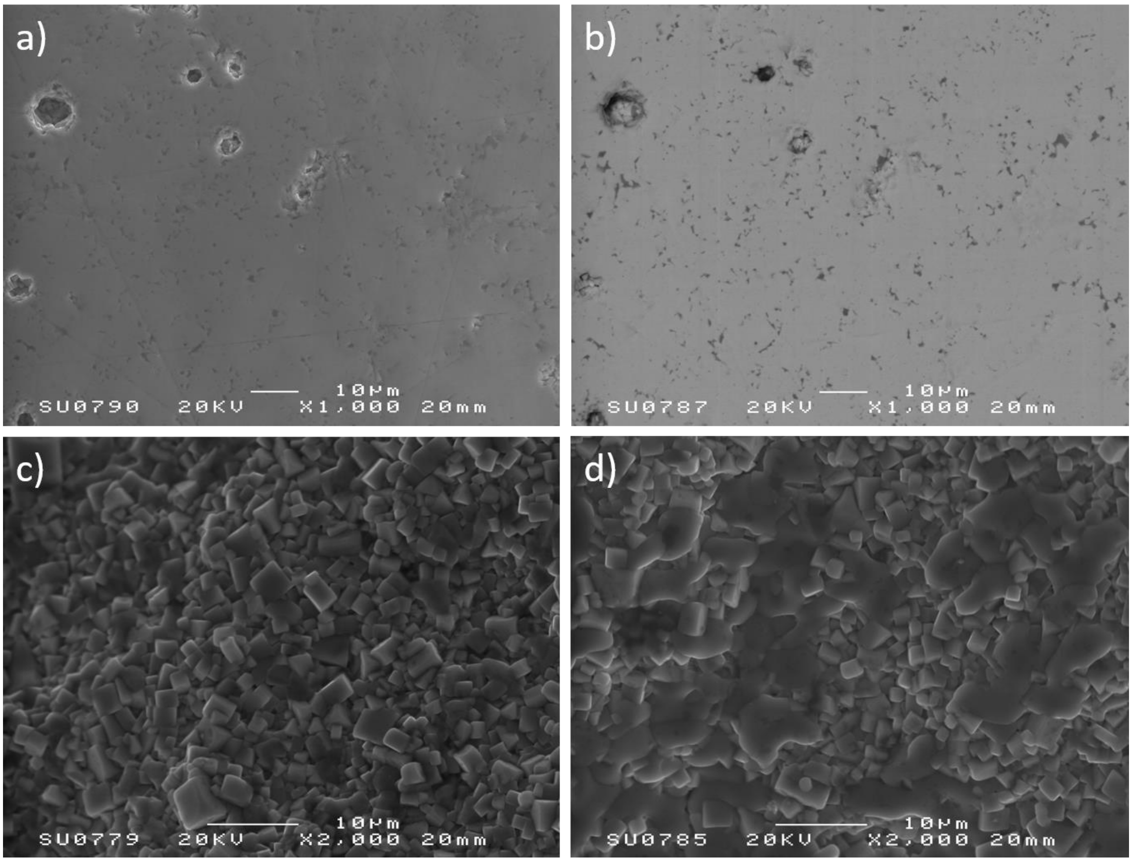

Figure 5. 13 SEM images of the CTLST + 2wt% BBO system, sintered at 1250°C for 4 hours, of the polished surface under a) SEI and b) BE, c) the fracture surface of the sample under SEI, and d) the fracture surface at a different location of two different phases under SEI.

The polished and fracture surface of the 2wt% BBO CTLST system sintered at 1300°C is represented in figure 5. 14, below, where a) and b) are SE and BE images, respectively, and c) and d) are fracture surface images taken at two different locations. The polished surface reveals greater porosity than the sample sintered at 1250°C and the even contrast suggest a homogenous distribution of constituent elements. However, upon closer inspection, figure 5. 15, there are some brighter specks present in the BE image, b), which are not easily discernible in the SEI image, a). A brighter contrast in a BE image represents a region of higher atomic number.

The fracture surface in both figure 5. 14 c) and d) shows an increase in grain size to an average of 5-8µm and more 'softening' of the grain edges and corners. There is also the presence of an amorphous phase, which is most likely the BBO sintering aid.

The larger grains, in combination with the rounding of the grain edges and corners would indicate a change in pore shape and size, and, rather than a decrease in porosity and increase the density, it relates to the decrease in density observed in figure 5. 6, in section 5.3. As described by Kingery (1976) [9], a change in pore/grain shape can lead to shrinkage during sintering, without necessarily leading to further densification. This may explain the discrepancy between the changes in density versus the changes in linear shrinkage observed in figure 5. 6.

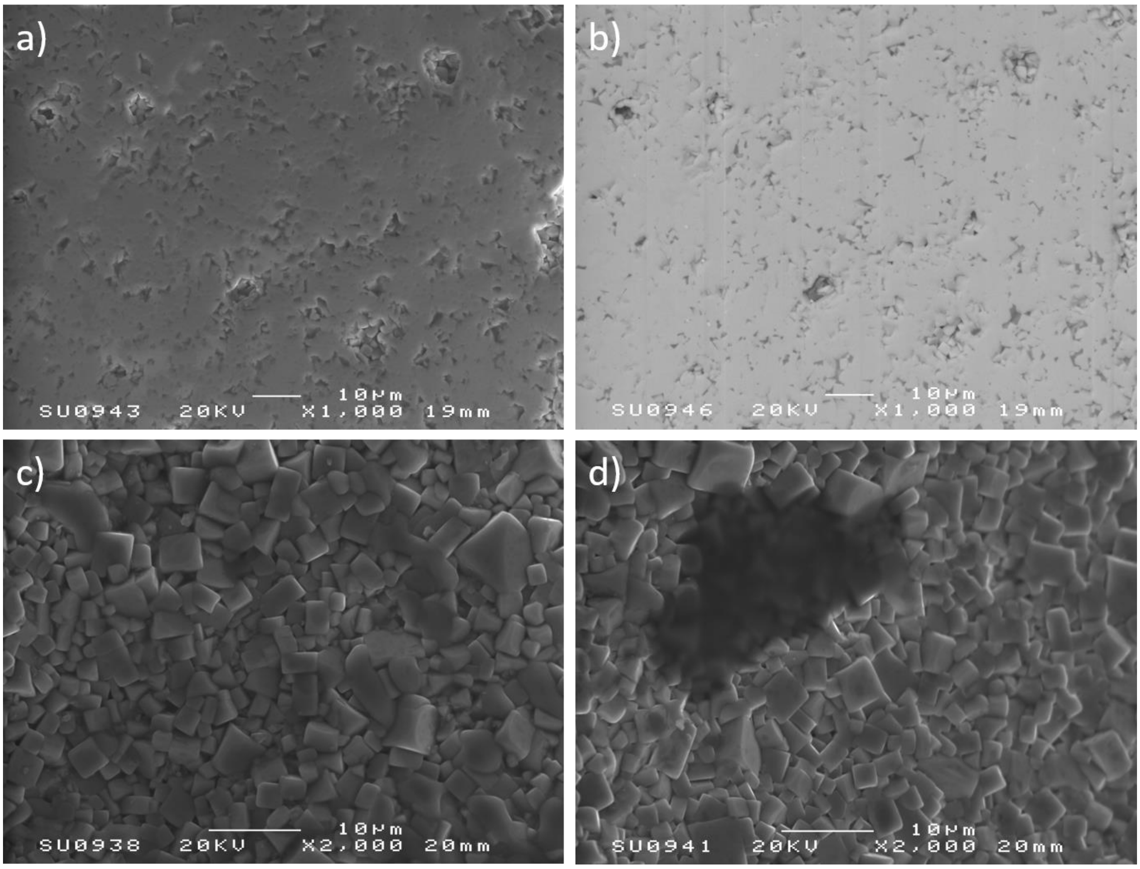

Figure 5. 14 SEM images of the CTLST + 2wt% BBO system, sintered at 1300°C for 4 hours, of the polished surface under a) SEI and b) BE, c) the fracture surface of the sample under SEI, and d) the fracture surface at a different location of crystal and amorphous morphologies under SEI.

The specks in figure 5. 15 may correspond to the secondary pyrochlore phase peaks seen in the XRD data for the sintered (1-x)CTLST+xBBO samples, in figure 5. 5. Since the pyrochlore phase would have a higher concentration of Sm compared with the average CTLST matrix, it is expected to appear brighter in a BE image.

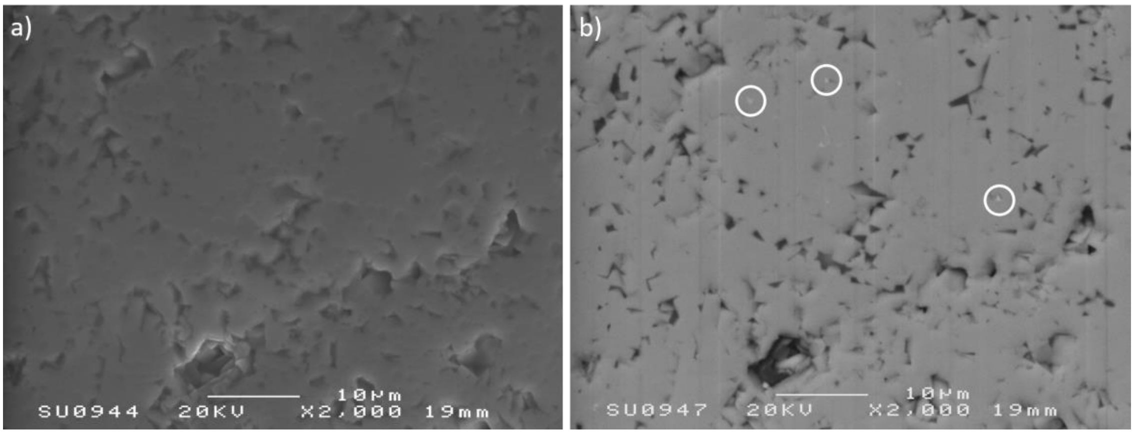

Figure 5. 15 A closer look at the two polished SEM images from figure 5. 14, above, where a) is the secondary electron image, and b) is the backscattered electron image, highlighting specks of lighter contrast in the BE image, circled.

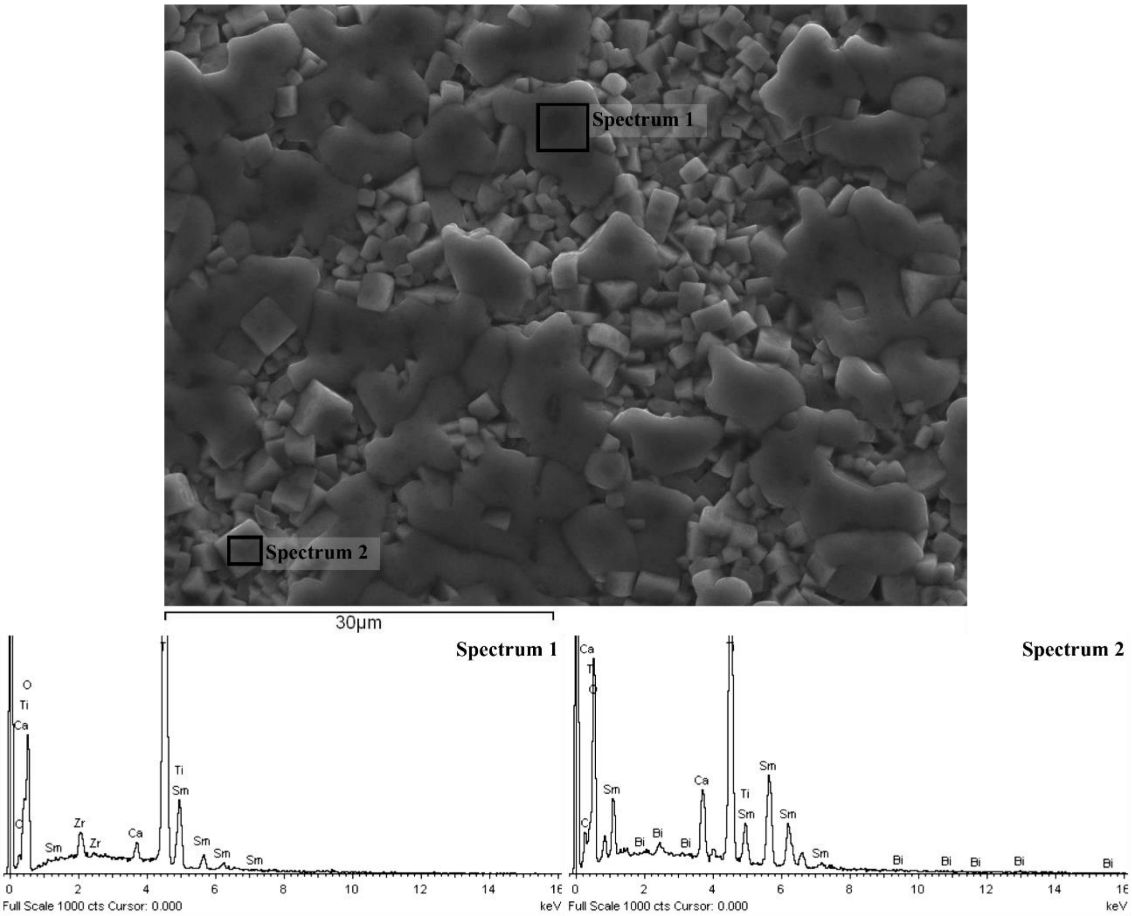

Figure 5. 16 EDS of the CTLST + 2wt% BBO composite fracture surface, sintered at 1250°C. Spectrum 1 is a typical representation of the darker, amorphous regions, and spectrum 2 is a typical representation of the grains. The SEI image indicates the locations of the EDS.

Figure 5. 16 and figure 5. 17 show the fracture and polished surface, respectively, of the CTLST + 2wt% BBO system, sintered at 1250°C, along with corresponding EDS locations. EDS of the fracture surface was conducted on the ‘glue-like’ phase (spectrum 1) and across the grains (typically represented by spectrum 2). This ‘glue-like’ phase was previously observed in figure 5. 13 and within the CLNT system (see figure 4. 16, figure 4. 18, and figure 4. 20, on p.88, 90 and 92, respectively). According to the EDS data, the ‘glue-like’ phase appears to be rich in Zr, thus it can be assumed that Zr contaminations appears to have similar effects for both systems. Spectrum 2, of the grains, reveals Ca, Ti and Sm, and the presence of Bi within the grains.

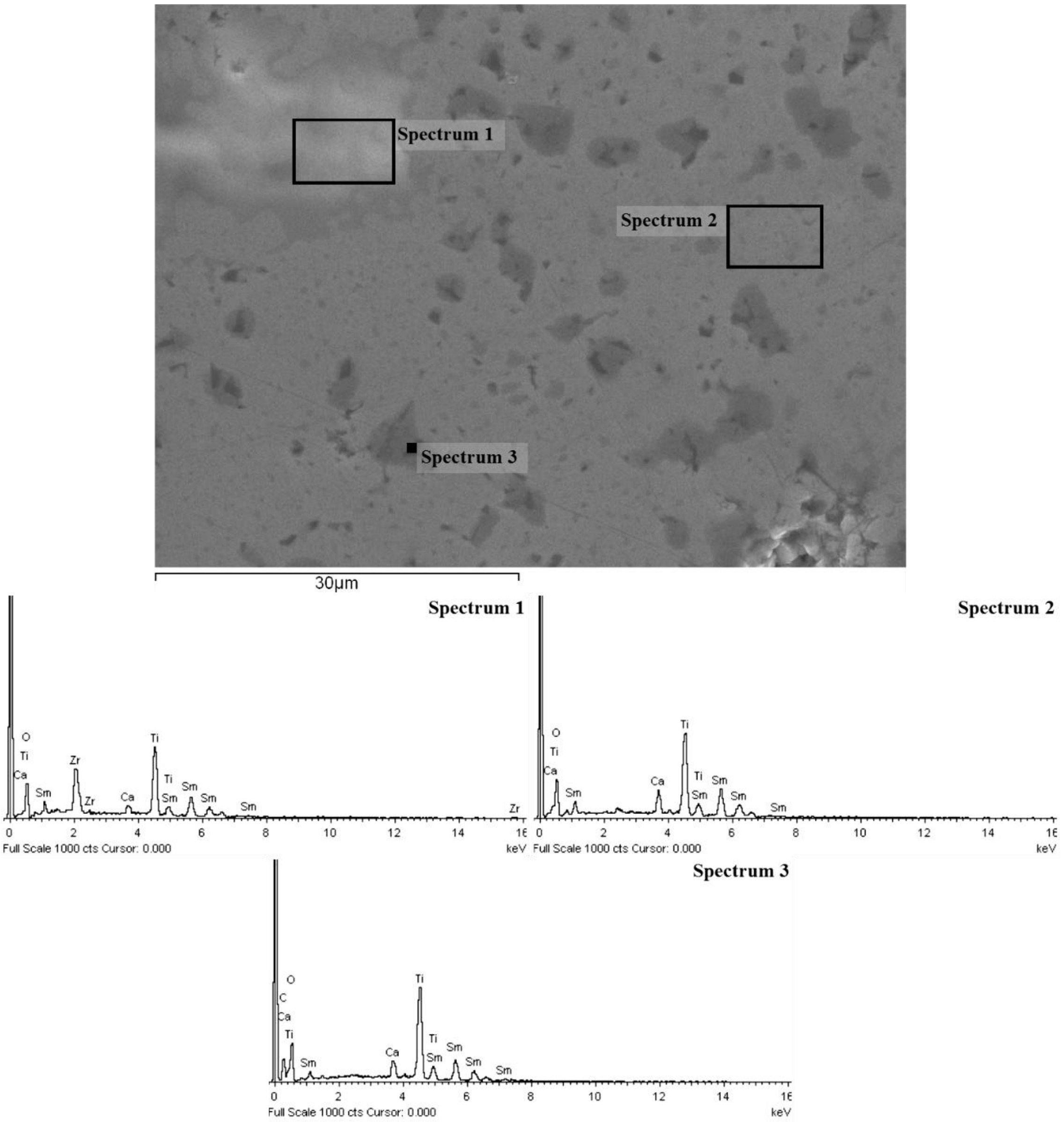

Figure 5. 17 EDS of the CTLST + 2wt% BBO composite polished surface, sintered at 1250°C. Spectrum 1 represents the brighter, amorphous region, spectrum 2 represents the average surface contrast, and spectrum 3 represents the darker contrast regions of the polished surface. The SEI image indicates the locations of the EDS.

Three EDS spectra are illustrated in figure 5. 17, from the polished surface. Spectrum 1 is of a non-uniform, overall brighter contrast region, of a phase which appears amorphous, spectrum 2 is from the medium grey contrast and spectrum 3 is of the darker contrast regions observed on the surface. The amorphous region of the spectrum 1 has a large proportion of Zr, compared with the other elements. If this is similar to the 'glue-like' phase of seen in the fracture surface, it should have a darker gradient. The fact that the gradation is not homogenous throughout the amorphous region could imply that there might be some charging effects present with this phase on the polished surface, since the fringes of this phase, in contact with the average matrix, have a darker contrast compared with the average matrix.

Between spectrums 2 and 3, the average matrix composition appears to have marginally larger proportions of Sm, compared with the darker region of spectrum 3. In addition, in spectrum 2, there is an unlabelled peak which most likely corresponds to Bi, at approximately 2.4 keV. The presence of Bi in spectrum 2 confirms that there are detectable levels of Bi with the grains of the CTLST matrix.

CTLST + 3wt% BBO Compositions

The 3wt% BBO composition continues the trends observed through the 1 and 2wt% compositions. Figure 5. 18 shows the polished and fracture surfaces of a 3wt% BBO compositions, sintered at 1200°C, where figure 5. 18 a) and b) are SE and BE images, respectively, from the polished surface and c) and d) are SEI of the fracture surface at two different locations. The polished surface exhibits fewer pores than the 2wt% composition at the same sintering temperature and the SEI reveals contrast variation across the surface, although the BE image appears to represent a largely homogenous material. This is the first observation of contrast variation within the CTLST system, aside from the possibility that contrast and brightness setting on the SEM instrument were not optimal when the images were taken of the 1 and 2wt% systems.

Grain size has also increased with the increase in BBO content to an average of 5-6µm, which can be seen in both figure 5. 18 c) and d), and there remains the presence of a darker, ‘glue-like’ phase which has been indicative of Zr contamination. Different grain morphologies area also observed, in figure 5. 18 d), which are longer, and more lath-like. These longer grains are much larger than the average, cuboid grains but appear to have the same contrast. Dissolution of the matrix resulted in rounding of the edges of the regular cuboidal grains.

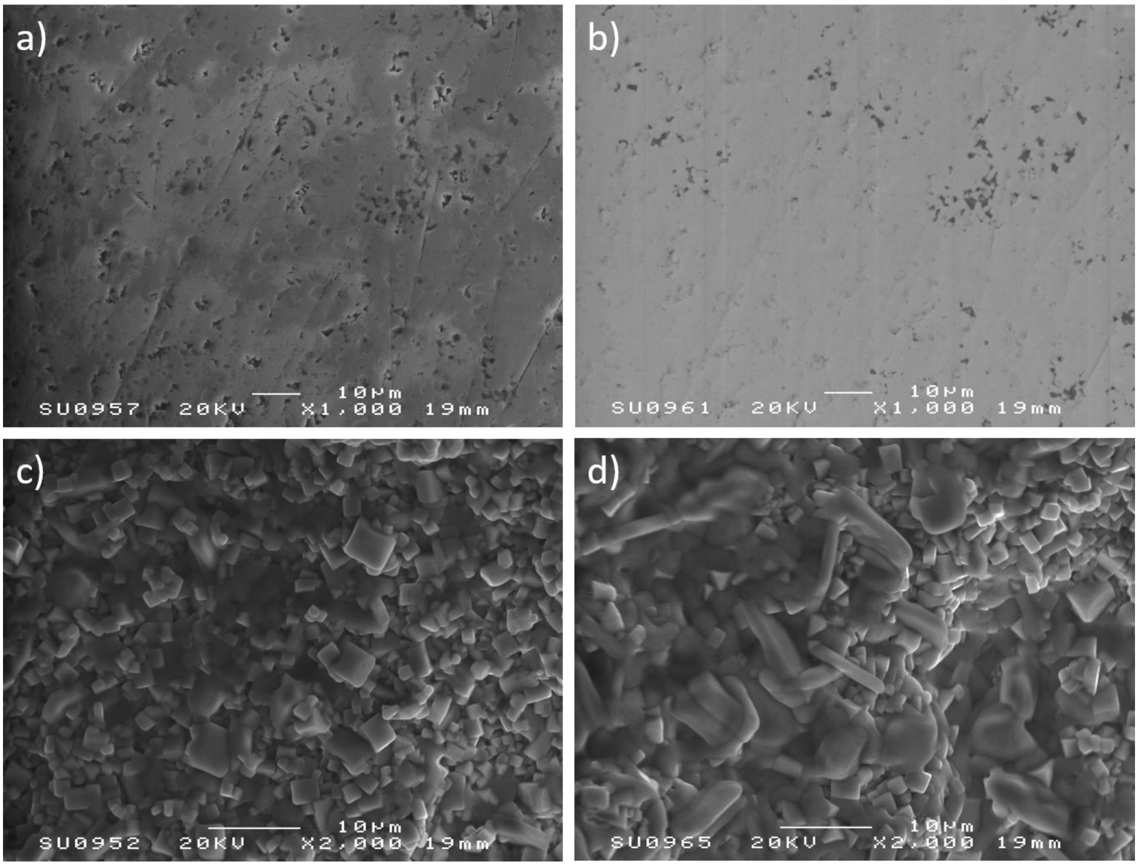

Figure 5. 18 SEM images of the CTLST + 3wt% BBO system, sintered at 1200°C for 4 hours, of the polished surface under a) SEI and b) BE, c) the fracture surface of the sample under SEI, and d) the fracture surface at a different location of different morphologies under SEI.

Figure 5. 19 shows the EDS analysis of the fracture surface seen in figure 5. 18 d), with spectrums 1 and 2 showing the typical spectra from the CTLST grains and the 'glue-like' phase, respectively, with spectrum 3 from the laths. The laths contain a high concentration of Zr along with Ca, Sm and Ti. This may be because the X-rays are also generated from the CTLST matrix below the laths. Although there was no evidence of Zr rich second phases in the XRD traces, it is possible that these are local regions which have reacted with contaminant particulates from the ZrO_2 milling media.

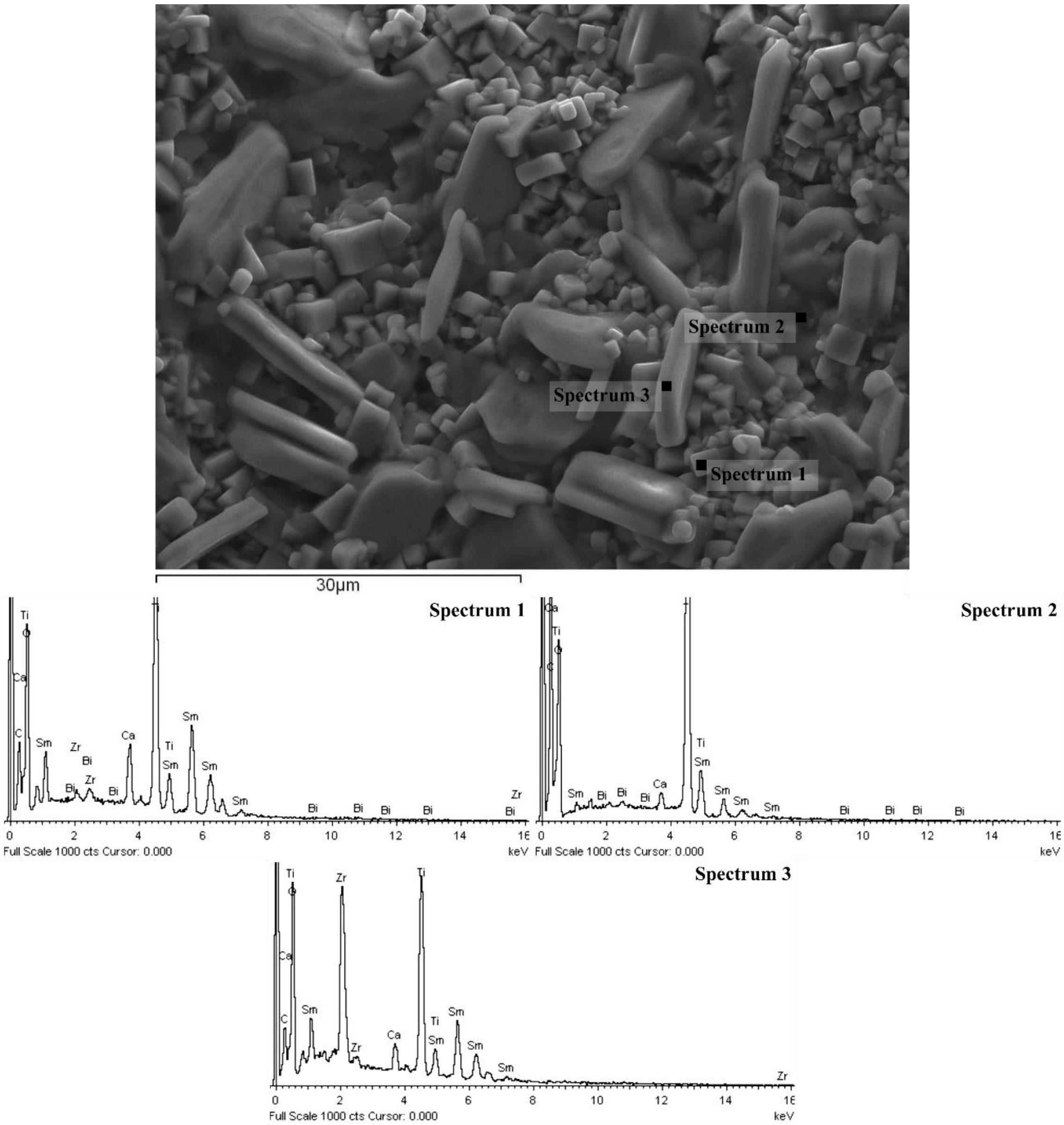

Figure 5. 19 EDS of the CTLST + 3wt% BBO composite fracture surface, sintered at 1200°C. Spectrums 1 and 2 show typical responses for the CTLST matrix and the 'glue-like' phase, and spectrum 3 shows strong Zr responses from the lath-like structures. The SEI image indicates the locations of the EDS.

The 3wt% BBO composition, sintered at 1250°C, is presented in figure 5. 20, where a) and b) are SE and BE images, respectively from the same polished surface and c) and d) are two different fracture surface locations. Both polished surface images reveal similar porosity to the 3wt% sample sintered at 1200°C, which implies a similar density, in agreement with the trends recorded in figure 5. 6. The BE image exhibits a homogenous contrast, although there are occasional brighter specks. These brighter specks are more readily visible in figure 5. 21. The SE image does show varying contrast over the surface of the sample but not to the same extent as in CTLST + 3wt% BBO composition sintered at 1200°C.

The fracture surface, figure 5. 20 c) and d), show regular, cuboid grains (5-6µm) similar to those seen at the lower sintering temperatures. Figure 5. 20 d) reveals what is likely the B-rich liquid phase surrounding the grains, which has darker contrast. Neither fracture surface images shows further evidence of longer lath-like grains found in figure 5. 18 d).

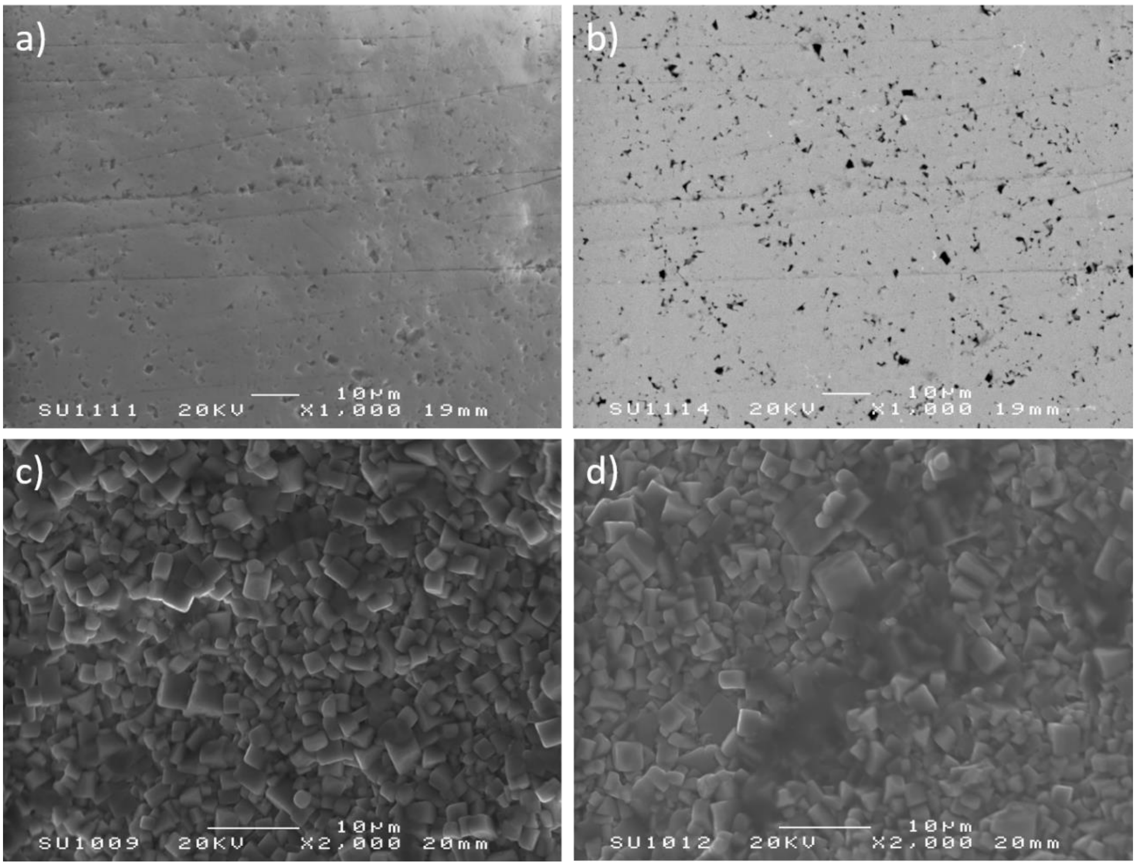

Figure 5. 20 SEM images of the CTLST + 3wt% BBO system, sintered at 1250°C for 4 hours, of the polished surface under a) SEI and b) BE, c) the fracture surface of the sample under SEI, and d) the fracture surface at a different location of crystal and amorphous morphologies under SEI.

Figure 5. 21 shows two BE images of the polished surface for the CTLST + 3wt% BBO system. Figure 5. 21 a) is a higher magnification view of the same location as in figure 5. 20 b), and figure 5. 21 b) is of a different location on the same sample. Small regions of brighter contrast were observed along with some laths of similar contrast, presumed to arise from a secondary phase of higher weight averaged atomic number, with $Sm_2Ti_2O_7$ pyrochlore a likely candidate.

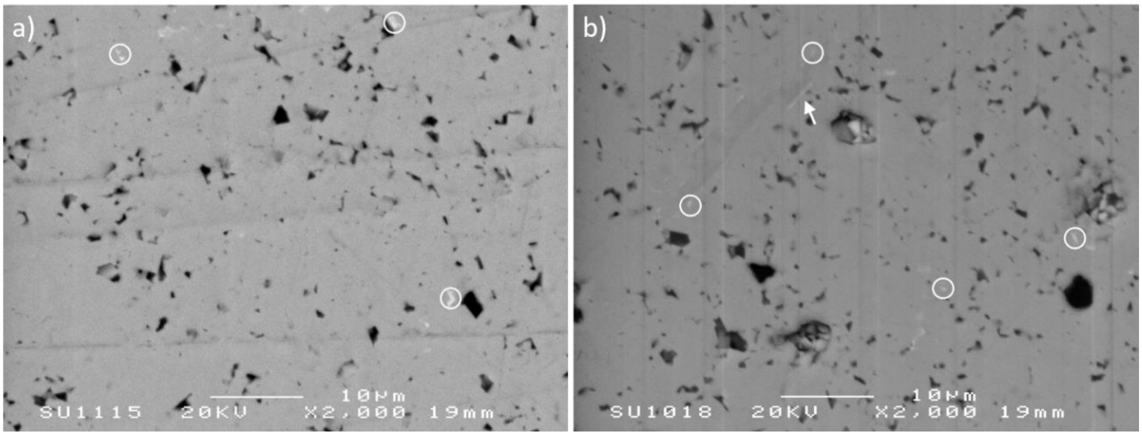

Figure 5. 21 A high magnification vew of the polished surface of the CTLST + 3wt% BBO system, sintered at 1250°C for 4 hours, where a) is a larger magnification of figure 5. 20 (b), above, and b) is a different location at the same magnification. Both images were taken under BE. Specks of secondary phase indicated by white circles and a lath of a secondary phase is arrowed.

Figure 5. 22 shows images of the polished and fracture surface of the CTLST + 3wt% BBO composition sintered at 1300°C, where a) and b) are SE and BE images, respectively, and c) and d) are fracture surface images taken under SEI at two different locations on the same sample. The polished surface reveals an essentially single-phase material as evidenced by the lack of contrast variation in both the SE and BE images. The sample appears to have lower density than the same composition sintered at lower temperatures, due to more numerous smaller pores and the presence of much larger single pores. This fits well with the lower densities measured for the CTLST + $x$wt% BBO system, shown in figure 5. 6 and listed in table 5. 1. The fracture surface reveals larger grains as a result of the increased sintering temperature, with an average size of 6-7µm, as well as more pronounced rounding of the corners and edges. The increased size and rounding of the grains may well contribute to the increase in porosity of the sample, leading to decreased density at the highest sintering temperatures. There is also confirmation of presence of the darker liquid-phase in the fracture surface of figure 5. 22 d).

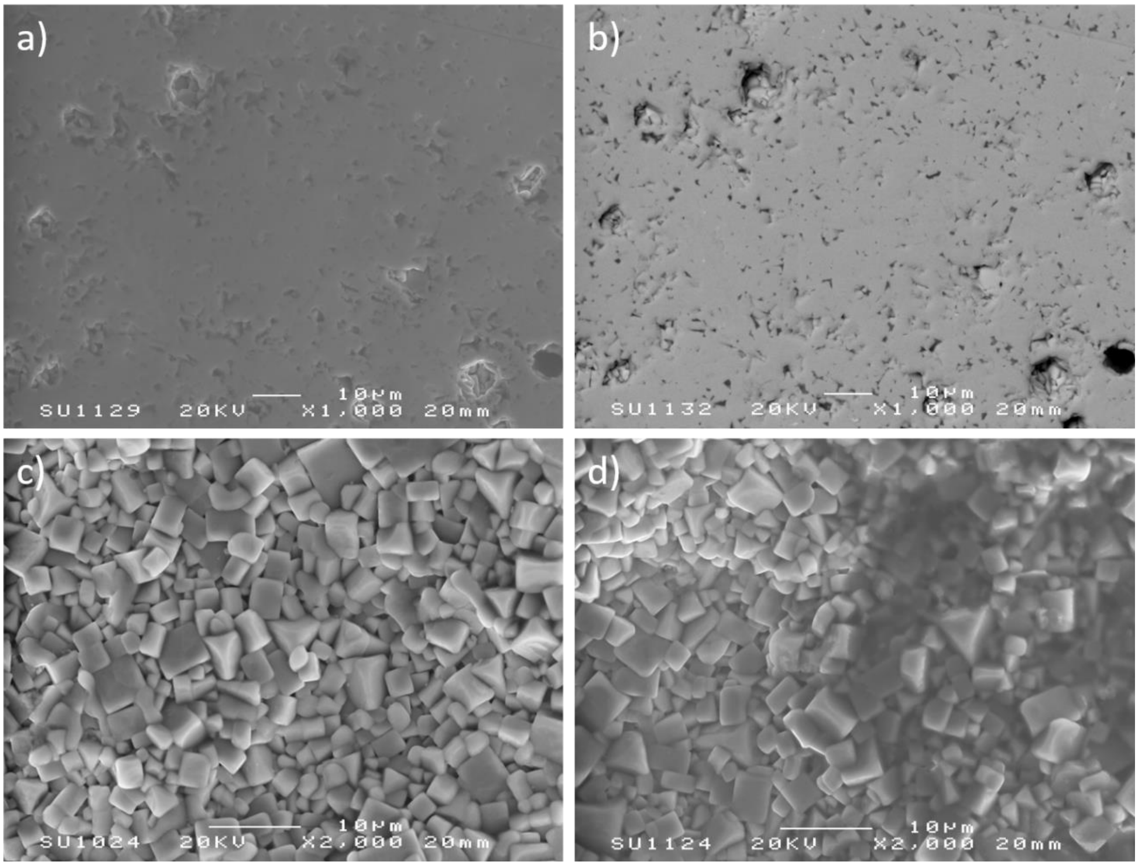

Figure 5. 22 SEM images of the CTLST + 3wt% BBO system, sintered at 1300°C for 4 hours, of the polished surface under a) SEI and b) BE, c) the fracture surface of the sample under SEI, and d) the fracture surface at a different location of crystal and darker, presumed amorphous phase in SEI mode.

EDS was conducted on both the fracture surface and polished surface of the CTLST + 3wt% BBO system, sintered at 1250°C, figure 5. 23 and figure 5. 24, respectively. Two spectra were taken on the fracture surface in figure 5. 23, spectrum 1 is of a darker region and spectrum 2 is a typical representation of the grains. The grains appear to contain larger proportions of the matrix elements, Ti and Sm, and detectable traces of Bi. The darker region shows reduced signal return for all elements, aside from the lighter elements such as Ca and C.

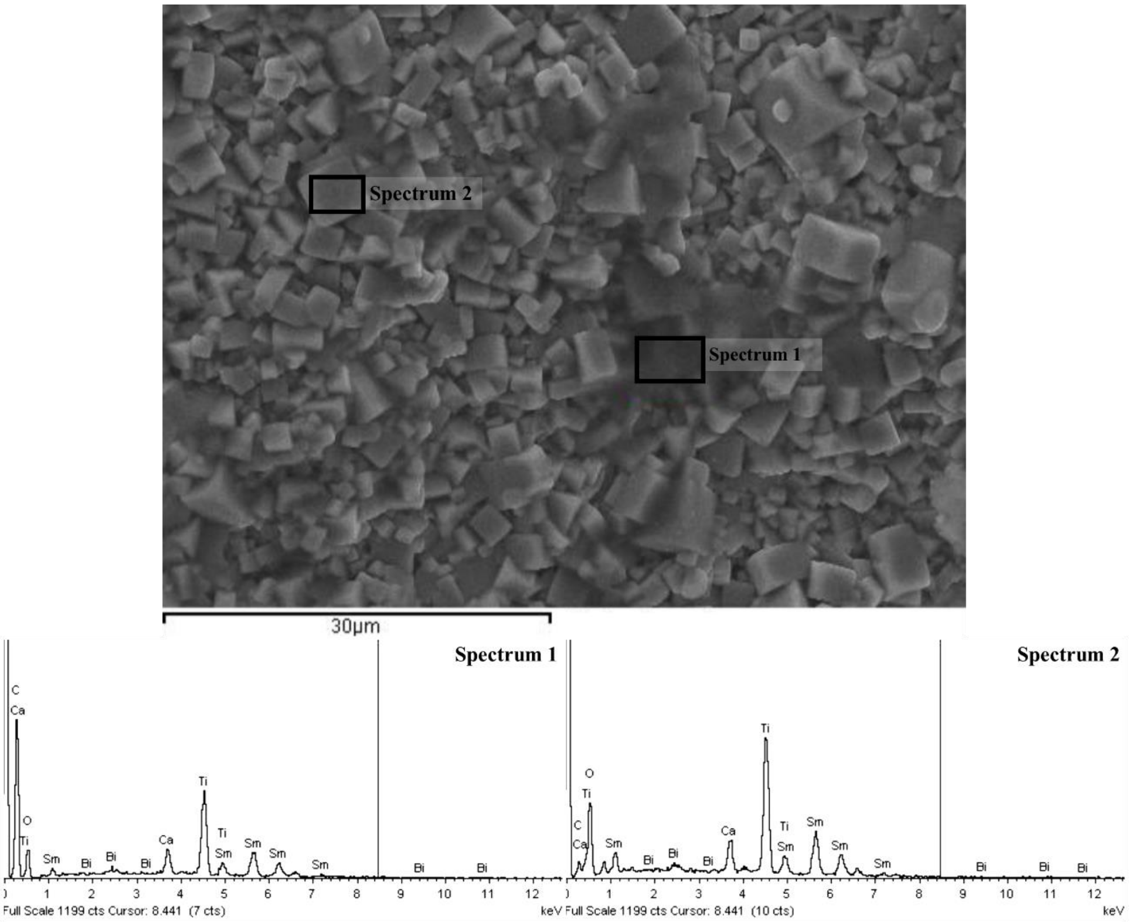

Figure 5. 23 EDS of the CTLST + 3wt% BBO composite fracture surface, sintered at 1250°C. Spectrum 1 is a typical representation of the darker contrast regions, and spectrum 2 represents the average grains. The SEI image indicates the locations of the EDS.

Figure 5. 24, similarly to figure 5. 23, shows two spectra of a brighter (spectrum 1) and darker contrast regions (spectrum 2). The brighter contrast region appears to have a higher concentration of Sm and Bi, inidicative of a phase with higher weight averaged atomic number. The darker contrast region has higher conentrations of the lighter elements.

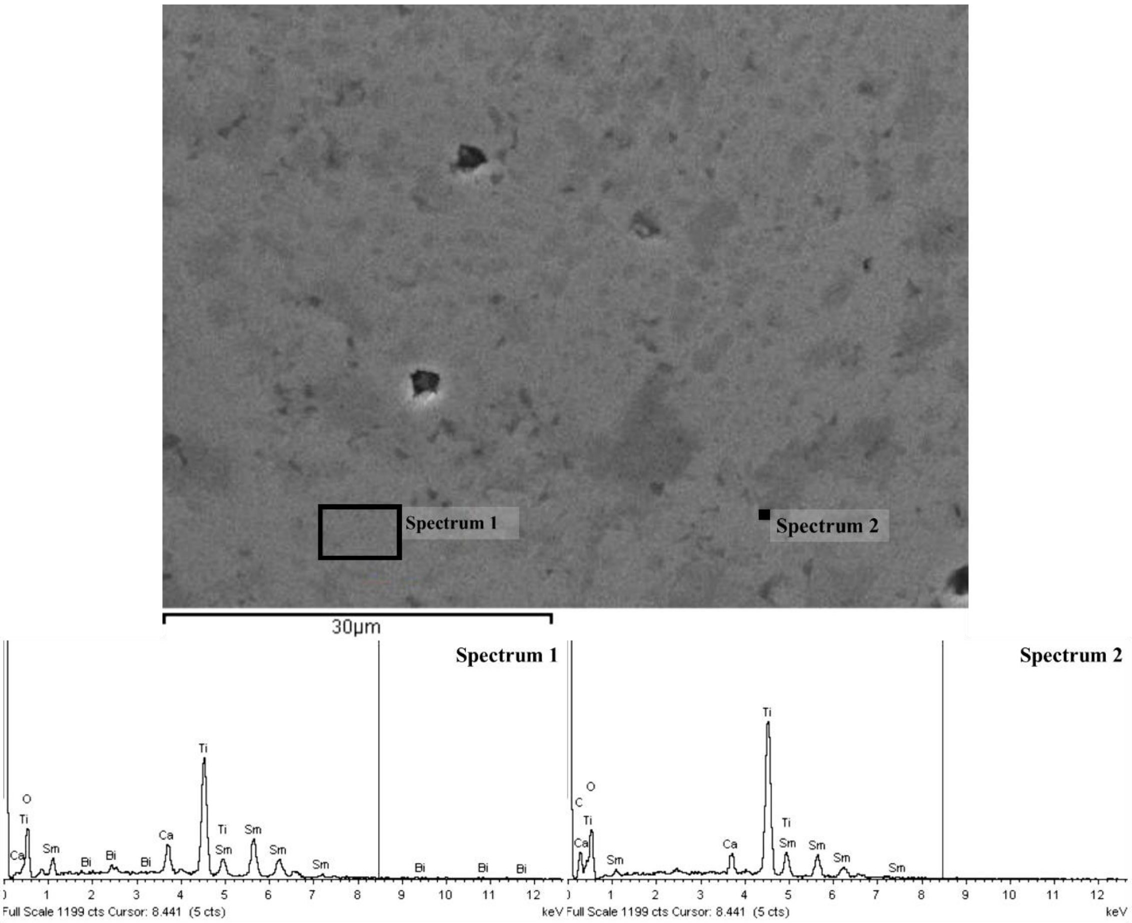

Figure 5. 24 EDS of the CTLST + 3wt% BBO composite polished surface, sintered at 1250°C. Spectrum 1 represents the average surface contrast, and spectrum 3 represents the darker contrast regions of the polished surface. The SEI image indicates the locations of the EDS.

CTLST + 4wt% BBO Compositions

SEM images of a CTLST + 4wt% BBO sample, sintered at 1200°C, are shown in figure 5. 25, where a) and b) are SE and BE images of the same area of polished surface, respectively, and c) and d) are SEI of the fracture surface, taken at two different locations of the same sample. The polished surface shows reduced porosity compared to a CTLST + 1wt% BBO sample sintered at 1200°C, due to the presence of smaller black specks in the BE image which are pores. The BE image in figure 5. 25 b) has a faint region of brighter contrast, which corresponds with a faintly brighter region in the SEI in figure 5. 25 a). These regions are circled in figure 5. 25. The grain morphology of the fracture surface is regular, with cuboidal grains, with a larger average grain size of 4-5 μm, compared with a CTLST + 1wt% BBO. As the BBO sintering aid concentration increases, the volume of dark (presumed liquid at the sintering temperature) phase surrounding the grains is greater. Both fracture surface images show that it is increasingly difficult to observe a region of the fracture surface devoid of any liquid-phase.

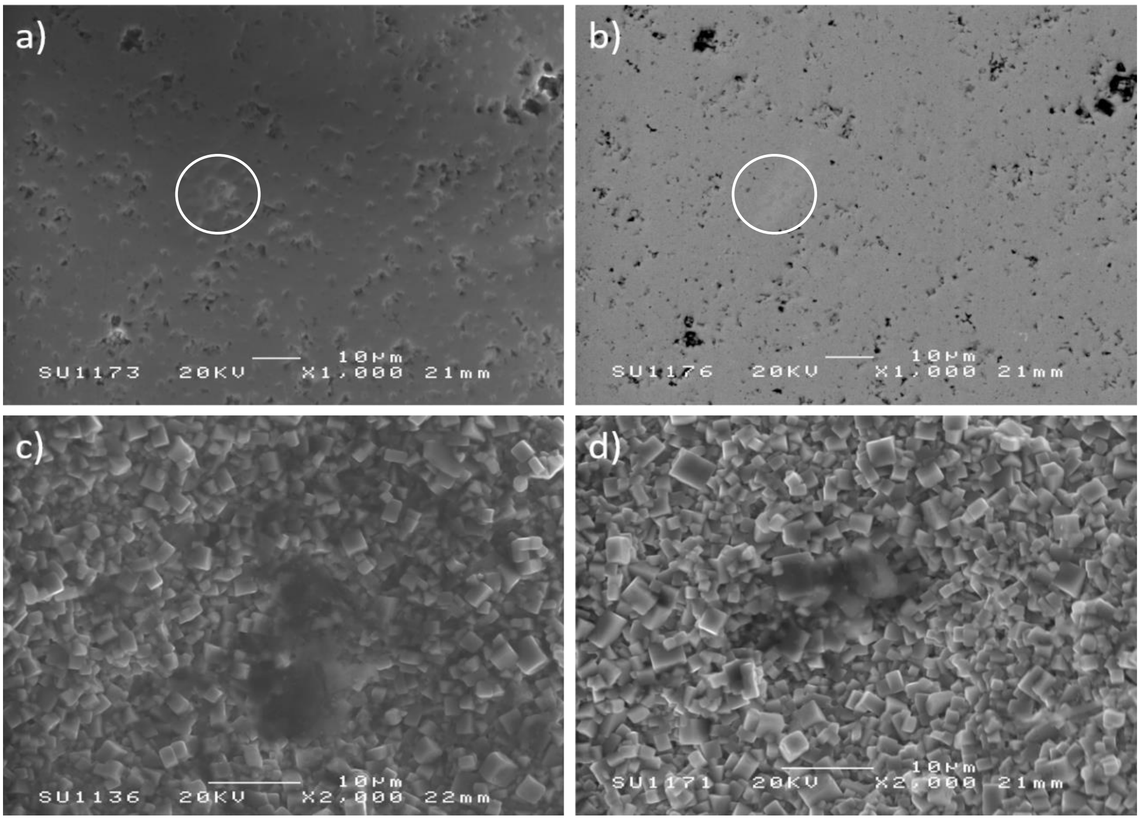

Figure 5. 25 SEM images of the CTLST + 4wt% BBO system, sintered at 1200°C for 4 hours, of the polished surface under a) SEI and b) BE, c) the fracture surface of the sample under SEI, and d) the fracture surface at a different under SEI. The circled regions highlight regions with slight contrast variation.

The polished and fracture surface of a 4wt% BBO composition, sintered at 1250°C, is shown in figure 5. 26, where a) and b) are SE and BE images of the same polished and c) and d) are SEI of the fracture surface, taken at two different locations of the same sample. Both images of the polished surface reveal a larger quantity of pores, including much larger pores, compared to the same composition, sintered at a lower sintering temperature. The shrinkage and density data (section 5.3, p.129) showed that CTLST + 4wt% BBO had a similar density across all sintering temperatures, however the samples sintered at 1250°C showed the largest error margin.

The SEI image of the polished surface, despite the presence of the pores, appeared otherwise to have a consistent contrast distribution across the surface of the sample. The BE image, on the other hand, of the same region, shows several specks of brighter contrast. These specks are more evident in figure 5. 27.

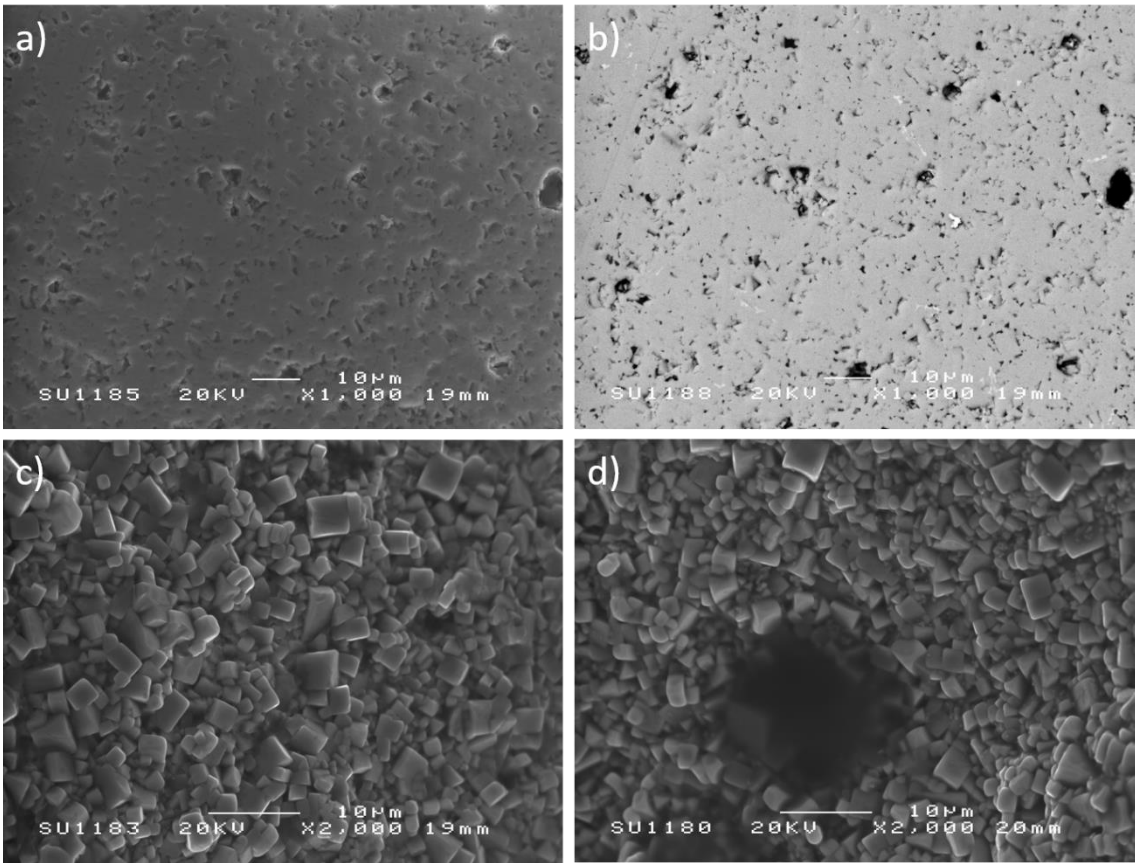

Figure 5. 26 SEM images of the CTLST + 4wt% BBO system, sintered at 1250°C for 4 hours, of the polished surface under a) SEI and b) BE, c) the fracture surface of the sample under SEI, and d) the fracture surface at a different location of crystal and amorphous morphologies under SEI.

The fracture surface in figure 5. 26 shows regular grains that are a larger average size (5-6 μm) compared with the CTLST + 4wt% BBO system sintered at a lower sintering temperature. The grains are also more rounded than the grains seen at a lower sintering temperature. The second fracture surface shows a pool of darker-contrast, liquid-phase, which is likely residual B-rich liquid-phase. Along with the rounder-edged grains, there is the presence of very small, bead-like structures on the surface of the grains, which are much more visible in figure 5. 26 d). These structures are ~500nm in size. These beads appear to be of the same approximate composition as the matrix phase since they have a similar contrast.

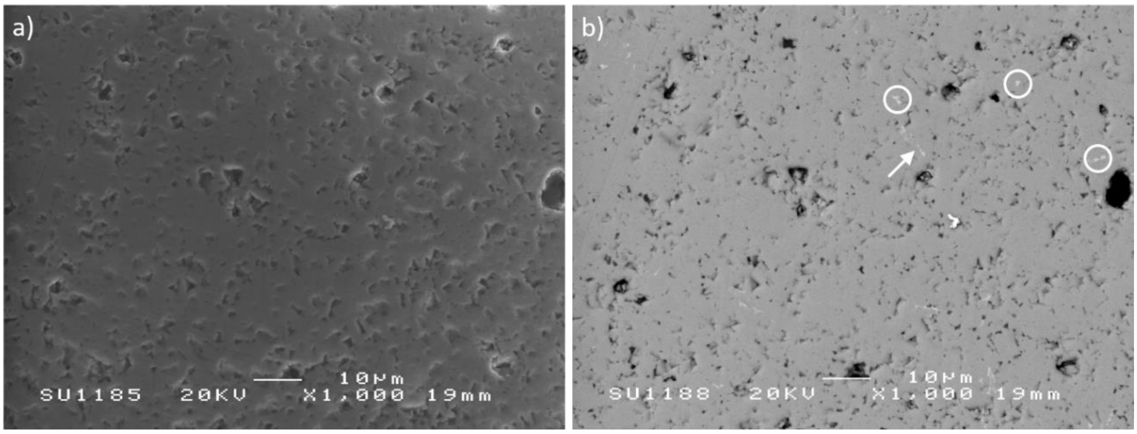

Figure 5. 27 A closer look at the two polished SEM images from figure 5. 26, above, where a) is the secondary electron image, and b) is the backscattered electron image, highlighting specks of lighter contrast in the BE image, circled, and a lath of brighter contrast, arrowed.

SEM images of the polished and fracture surfaces of a 4wt% BBO sample, sintered at 1300°C, are shown in figure 5. 28, where a) and b) are SE and BE images of the same polished surface, respectively, and c) and d) are SEI of the fracture surface, taken at two different locations of the same sample. The polished surface appears similar to the porosity of the same sample sintered at 1200°C, albeit with a larger, overall, pore size. The shrinkage and density data of Figure 5. 6 and Table 5. 1 do imply that the 4wt% BBO composition does have a slightly lower density, at a sintering temperature of 1300°C, than its counterpart sintered at 1200°C. The SEI appears to be homogenous, whereas the BE image reveals small, brighter contrast specks dotted across the surface. These are similar to those found in the sample sintered at 1250°C, in figure 5. 26 and a larger magnification image of these brighter specks can be seen in figure 5. 29.

The fracture surface shows an increase in grain size to 6-7µm, with some grains as large as 8µm, with increase in sintering temperature. The grains are more rounded, and appear to be fractured as illustrated in figure 5. 28 c). The larger, more rounded grains are contributing to the presence of larger pores and an overall reduction in porosity at higher sintering temperatures. Figure 5. 28 d) shows an example of large ‘pools’ of darker contrast, B-rich presumably liquid-phase at the sintering temperature surrounding the grains. Both fracture surface images reveal further evidence of the small ‘bead-like’ sediment on the surface of the grain, which are <500nm. This sediment is also present on the surface of, or within, the liquid-phase in figure 5. 28 d).

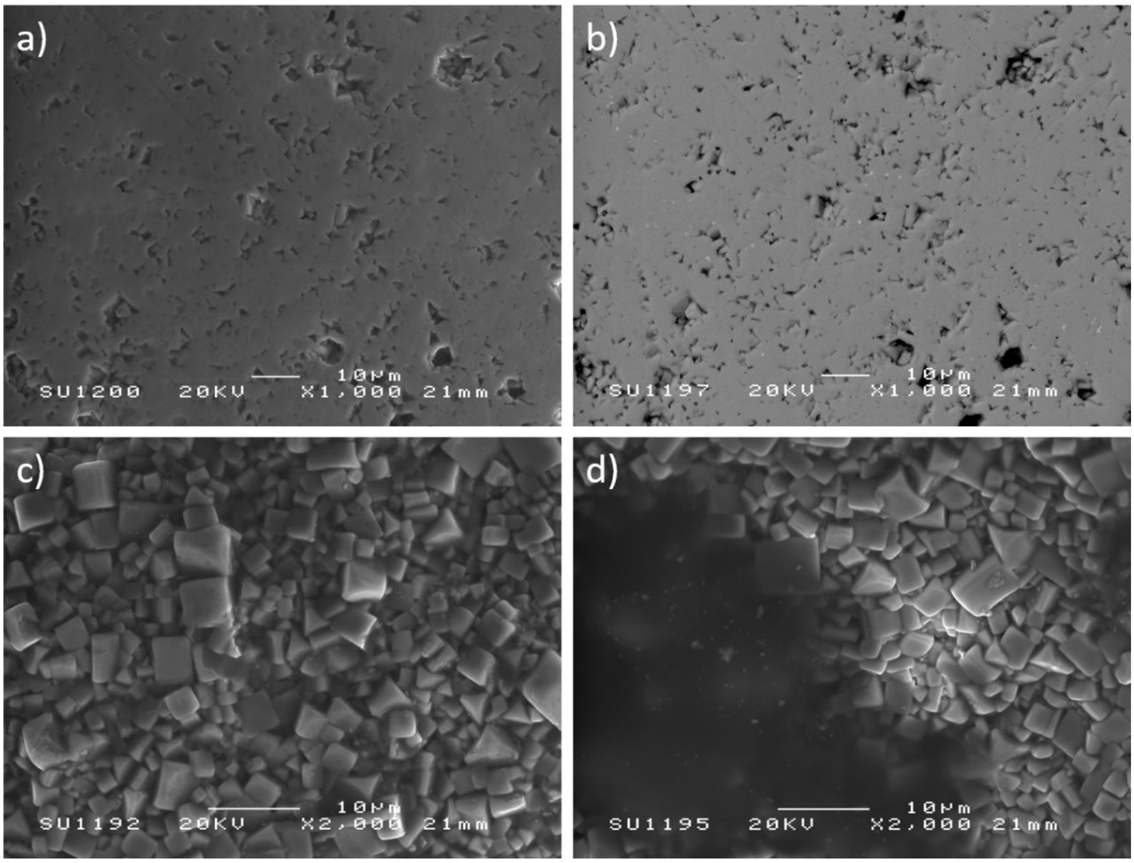

Figure 5. 28 SEM images of the CTLST + 4wt% BBO system, sintered at 1300°C for 4 hours, of the polished surface under a) SEI and b) BE, c) the fracture surface of the sample under SEI, and d) the fracture surface at a different location of crystal and amorphous morphologies under SEI.

The brighter specks observed in polished surface images are highlighted by white circles, in figure 5. 29, where a) is a SEI and b) is a BE image. The specks are visible in the BE image but the same areas in the SE image appear homogenous. This may be due to the different nature of the two signals, where backscatter electrons arise from deeper within the sample, compared with secondary electrons, which implies that these specks are below the polished surface. The brighter contrast indicates a region of heavier weight average atomic density, which implies a larger proportion of heavier elements. Since the XRD data indicates the presence of a secondary phase, these specks my well be evidence of a pyrochlore secondary phase, which consists of Ti, Sm and O. The pyrochlore would therefore have a larger concentration of heavier elements compared with the CTLST, which includes Ca and Li, and would have an overall lower atomic density, and a darker contrast, although, the presence of a Bi-rich second phase cannot be excluded. To confirm their composition, EDS analysis on the brighter regions is required.

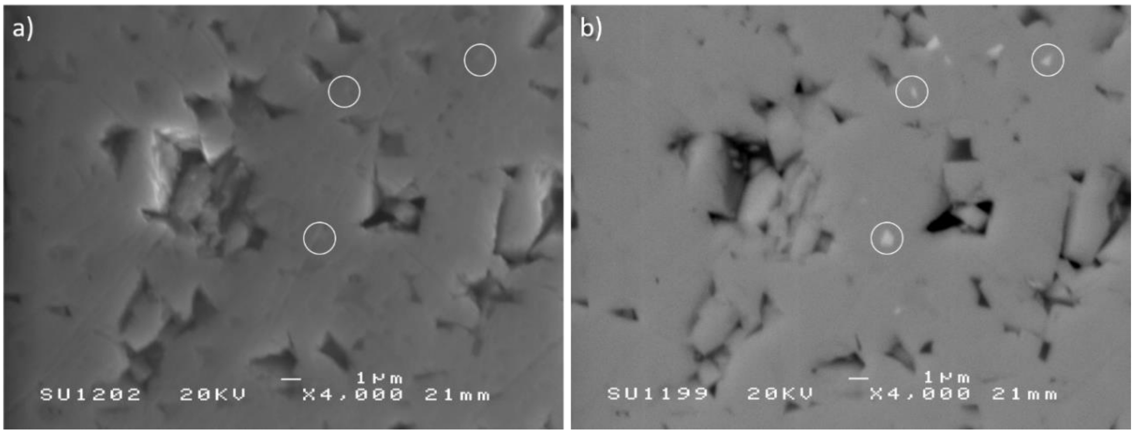

Figure 5. 29 SEM images of polished surfaces from figure 5. 28 where a) is the SE image, and b) is the BE image, highlighting specks of lighter contrast in the BE image and their positions in the SE image, circled.

EDS analysis of the fracture surface for the CTLST + 4wt% BBO composition, sintered at 1300°C, is shown in Figure 5. 30, where spectrum 1 is a typical representation of the grains and spectrum 2 of the darker contrast regions in the image. Spectrum 1 is similar to all other EDS spectra taken of the grains within a fracture surface, in that there is approximately the correct relative peak intensities for the matrix elements Ca, Ti and Sm. The CTLST + 4wt% BBO system does contain a larger relative Bi peak, compared with the other compositions in the CTLST series which implies that with increase in BBO concentration more Bi enters the CTLST matrix. The darker contrast region of the SEI have lower overall peak amplitudes, with qualitatively lower concentrations of Bi and Ti.

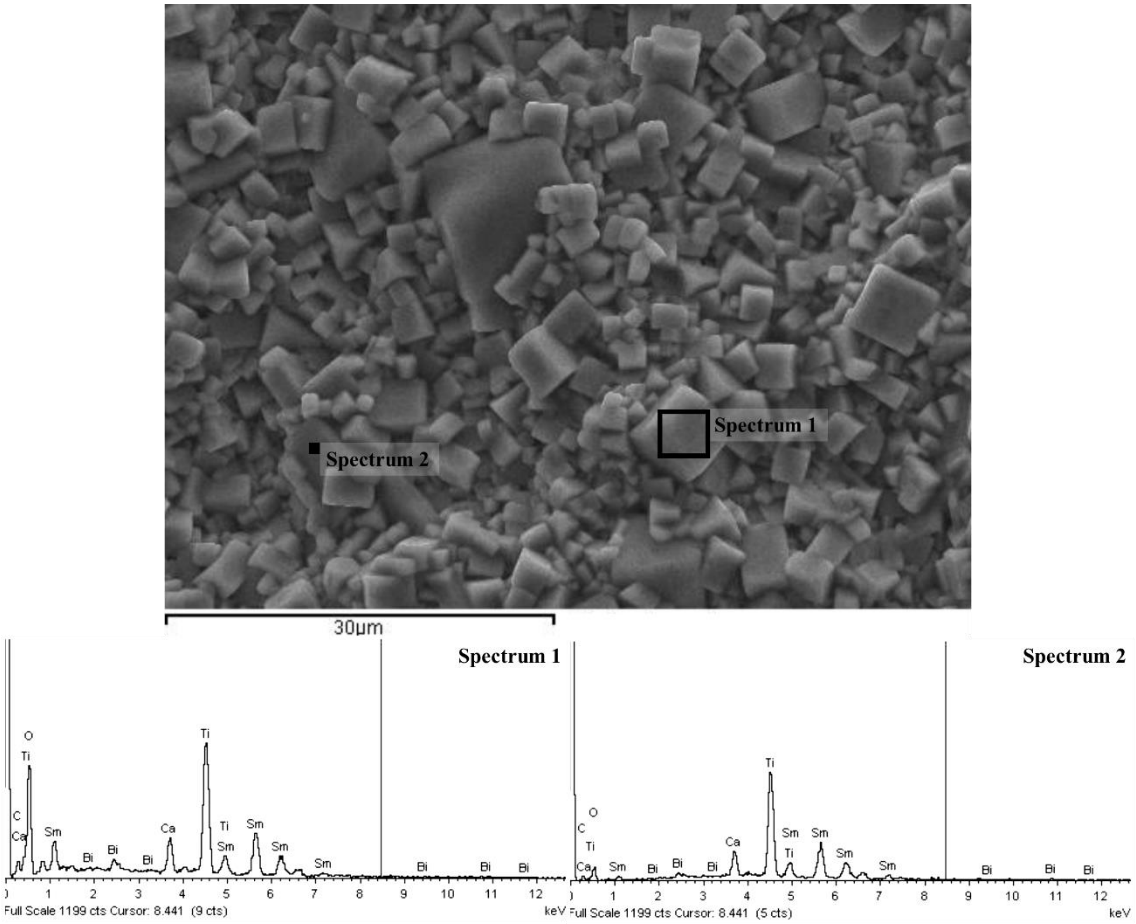

Figure 5. 30 EDS of the CTLST + 4wt% BBO composite fracture surface, sintered at 1250°C. Spectrum 1 represents the average grains and spectrum 2 represents a darker contrast region of the fracture surface. The SEI image indicates the locations of the EDS.

EDS analysis of the polished surface of the CTLST + 4wt% BBO composition is shown in figure 5. 31. Spectrum 1 represents the average contrast phase, spectrum 2 is of the brighter region on the polished surface, spectrum 3 is from liquid-phase occupying the volume of a pore and spectrum 4 is of a different region of the polished surface with similar contrast to spectrum 1. Spectrum 1 of the polished surface resembles that of the grains from the fracture surface and thus represents the matrix CTLST. Spectrum 2, with the exception of a relatively larger Ca peak, resembles spectrum 1 and thus the brighter region, which is located on the edge of a pore, is likely due to charging effects rather than any compositional differences.

Spectrum 3, from the liquid-phase, has reduced intensity of the Ti, O, Ca and Sm peaks but no evidence of Bi. There is, however a large peak at 0.2 keV associated with ‘Ca’ or ‘C’ which may be incorrectly labelled and could correspond to B (0.183 keV). In an EDS spectrum the lower keV region is densely populated with peaks and precise identification is difficult. Nonetheless, the lack of Bi in spectrum 3 suggests that the sintering aid reacts with the CTLST matrix and it is logical that a B-rich phase would be residual from the BBO, in a similar manner to that observed in the CTLNT system.

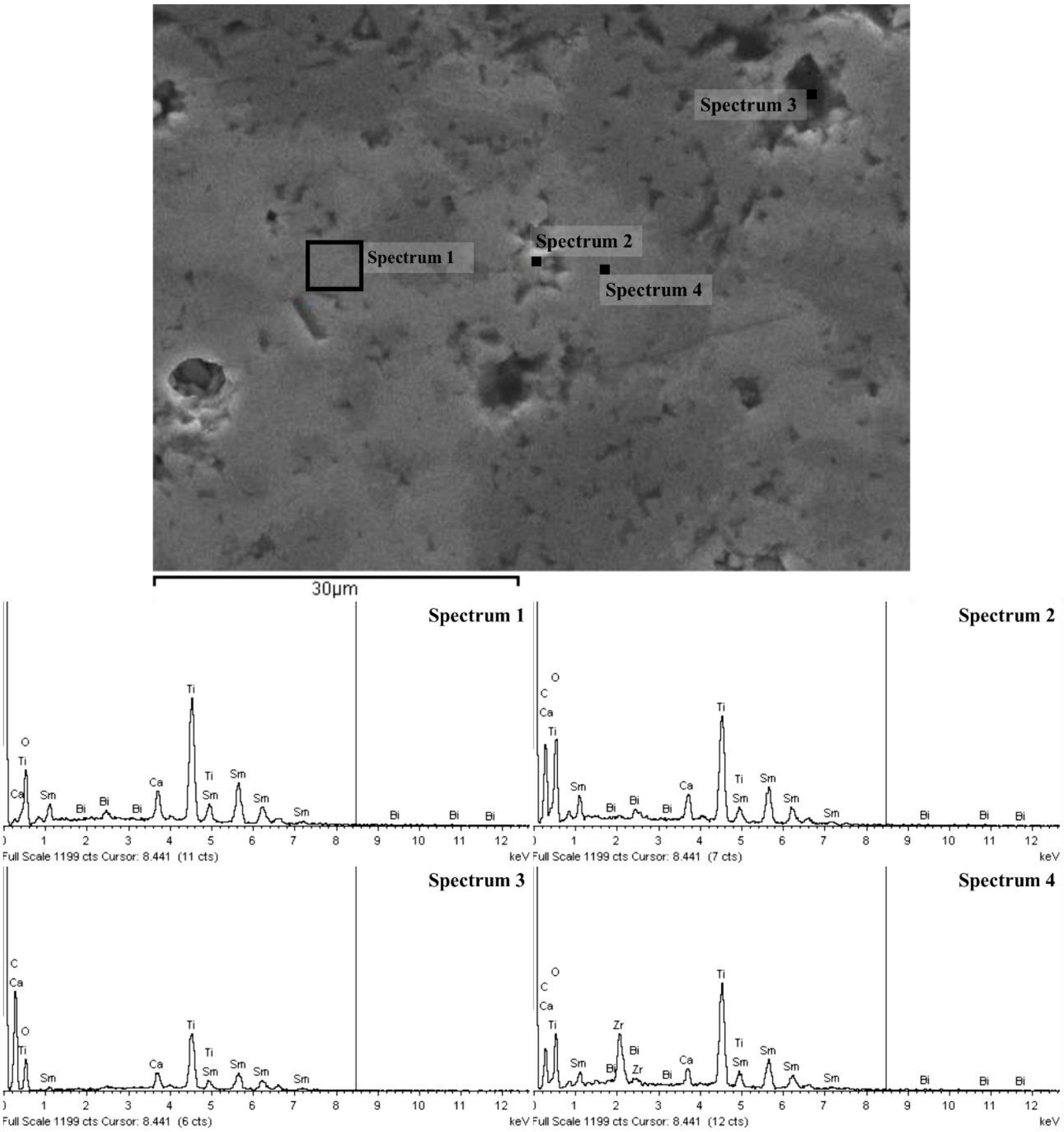

Figure 5. 31 EDS of the CTLST + 4wt% BBO composite polished surface, sintered at 1250°C. Spectrum 1 represents the average matrix contrast, spectrum 2 represents brighter contrast region, spectrum 3 represents the darker contrast regions of the polished surface, and spectrum 4 is a point-scan of the aparent average phase indicatin the presence of Zr. The SEI image indicates the locations of the EDS.

Finally, figure 5. 31 reveals that there is Zr, within the matrix phase in addition to Ca, Ti, Sm and Bi. Zr is observed in other spectra from the matrix phase, suggesting that it has arisen from localised that Zr contamination, presumably from the ball milling process. Zr is routinely observed in fracture surfaces.

5.5 Microwave Dielectric Properties

Table 5. 2 and figure 5. 32 show the relative permittivity (ε_r), quality factor (Qf_0) and the temperature coefficient of resonant frequency (τ_f) for all CTLST + $x$wt% BBO compositions, sintered at 1200°C, 1250°C and 1300°C for four hours. Table 5. 2 also shows the MW dielectric properties for a pure CTLST and BBO sample for comparison, sintered at 1350°C and 650°C for four hours, respectively.

Table 5. 2 Microwave dielectric results for the CTLST + $x$wt%BBO at each sintering temperature, including pure CTLST and BBO.

Sample Type	Sintering Temperature (°C)	Relative Permittivity (ε_r) (±0.5)	Quality Factor (Qf_0) (±60)	Temperature Coefficient of Resonant Frequency (τ_f) (±0.5)
Pure	1350	106	1599	12
$Bi_4B_2O_9$	650	40	2328	-178
1wt%	1200	100	1898	12
	1250	104	1884	3
	1300	100	2453	-9
2wt%	1200	99	2150	7
	1250	105	2476	1
	1300	99	3106	-15
3wt%	1200	104	2561	2
	1250	102	2245	-15
	1300	98	3009	-27
4wt%	1200	106	3295	-4
	1250	105	2806	-23
	1300	97	3392	-42

Unlike the CTLNT system, the CTLST system appears to have an overall reduction in ε_r as the sintering temperature increases across the compositions, in particular CTLST + 3 and 4wt% BBO compositions. The 1 and 2wt% BBO compositions increase in ε_r with sintering temperature until 1250°C. At the lowest sintering temperature of 1200°C, ε_r increases with increase in BBO concentration. At higher sintering temperatures, this trend does not continue and compositions with the highest BBO concentration exhibit the lowest ε_r.

Qf_0 values generally reflect the changes in ε_r. Qf_0 increases with increase in sintering temperature as the ε_r decreases. As the concentration of BBO increases, across all sintering temperatures, Qf_0 increases, most noticeably at 1200°C sintering temperature. Qf_0, unlike the ε_r, does not have a strong trough where there is a peak in the ε_r data, at the 1250°C sintering temperature. As BBO concentration increases, the most prominent dip in Qf_0 occurs at 1250°C. Only CTLST + 2wt% BBO composition shows a monotonous increase in $Qf_0$with sintering temperature.

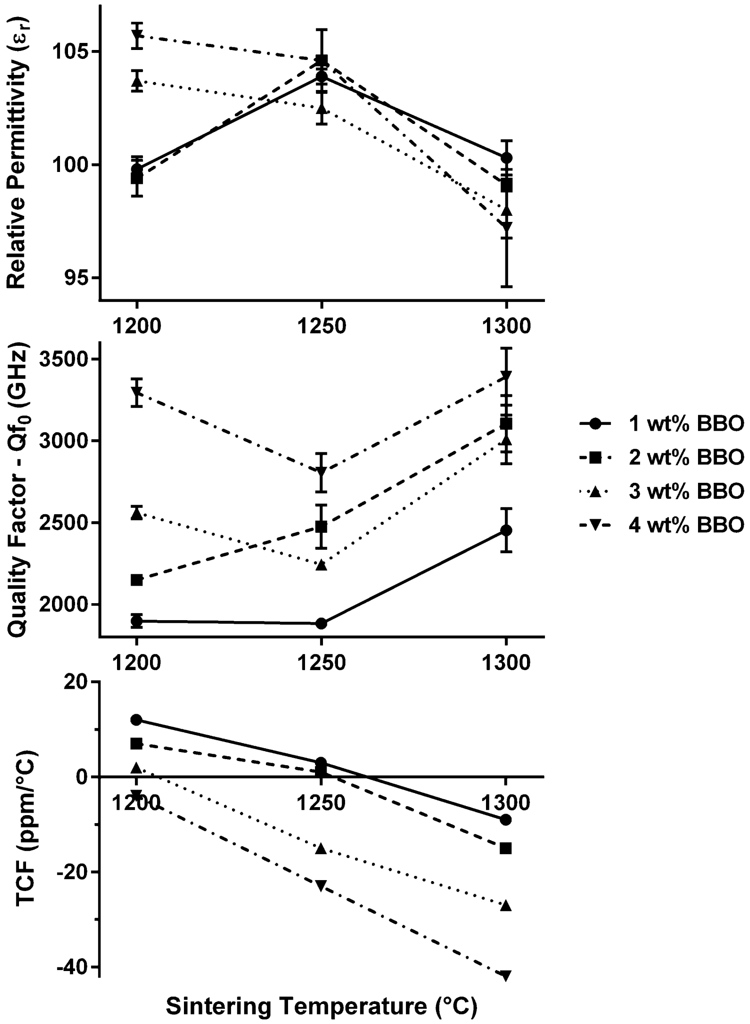

Figure 5. 32 Microwave dielectric results of each CTLST + $x$wt% BBO with increasing sintering temperature.

CTLNT and CTLST systems also demonstrate different trends for τ_f with respect to composition and sintering temperature, figure 5. 32. For the CTLNT, the change in τ_f with increased BBO concentration and sintering temperature was non-linear. In contrast, for CTLST, τ_f becomes more negative with increase in sintering temperature and BBO concentration. CTLST + 3wt% BBO sample sintered at 1200°C, and the 2wt% BBO sample sintered at 1250°C have τ_f values close to zero, of 2 and 1 ppm/°C, respectively. However, the composition with the most promising properties is CTLST + 4wt% BBO, sintered at 1200°C, with ε_r = 106, Qf_0 = 3295 GHz and τ_f = -4 ppm/°C.

The change in MW behaviour with changes of BBO content, with respect to the CTLNT system, suggests that a different interaction between the two materials is taking place. The dip in ε_r coincides with the dip in density observed in figure 5. 6 at higher sintering temperatures, as does the rise in Qf_0 at higher sintering temperatures. It may therefore be concluded that the changes in ε_r and Qf_0 are due to changes in density, rather than from a specific chemical reaction between the two materials. However, while it seems that the BBO sintering aid is inducing earlier sintering at lower sintering temperatures and creating denser samples, perhaps at sintering temperatures above 1250°C the effect of dissolution of the CTLST phase into the liquid phase is very strong. This causes strong rounding of the grain edges and increases the size of the pores, and decreases density, as observed at higher sintering temperatures in the SEM images in the previous section. The effect BBO has on τ_f is much more linear, and in-line with predictions of simply mixing two different +ve and -ve τ_f materials, suggesting no reaction between the CTLST and BBO materials, contrasting with the CTLNT results.

With regards to the CTLNT system, the rate of change of the overall values for ε_r slows down between 1200-1250°C, like the CTLST system. Likewise, the Qf_0 values fall to a trough at 1250°C, with similar values for the 1wt% BBO compositions. This may be, in part, down to morphological changes, due dissolution at higher sintering temperatures, and the implications this has on density. Aside from the density-MW property correlations, there is no clear indication that Zr contamination or secondary phases contribute significantly to the MW properties.

5.6 Transmission Electron Microscopy Observations

Transmission electron microscopy (TEM) and EDS was conducted on CTLST + 4wt% BBO samples to compare with the CTLNT system. Bright field (BF) TEM images and electron diffraction patterns from a CTLST + 4wt% BBO sample, sintered at 1300°C, are shown in figure 5. 33. The fundamental reflections <101>, <110> and $[111]$ zone axes are indexed according to a pseudocubic perovskite cell with superstructure reflections at half-integer positions. As with the CTLNT system, the superstructure reflections result from an $a^-a^-c^+$ Glazer tilt system [10] with $\frac{1}{2}\{ooo\}$ and $\frac{1}{2}\{ooe\}$ arising from anti-phase and in-phase tilting, denoted by ‘a’ and ‘i’ respectively in figure 5. 33. These results are consistent with the CTLNT system, and the CTLNT end-members $CaTiO_3$ (CT) and $(Li_{0.5}Nd_{0.5})TiO_3$ (LNT).

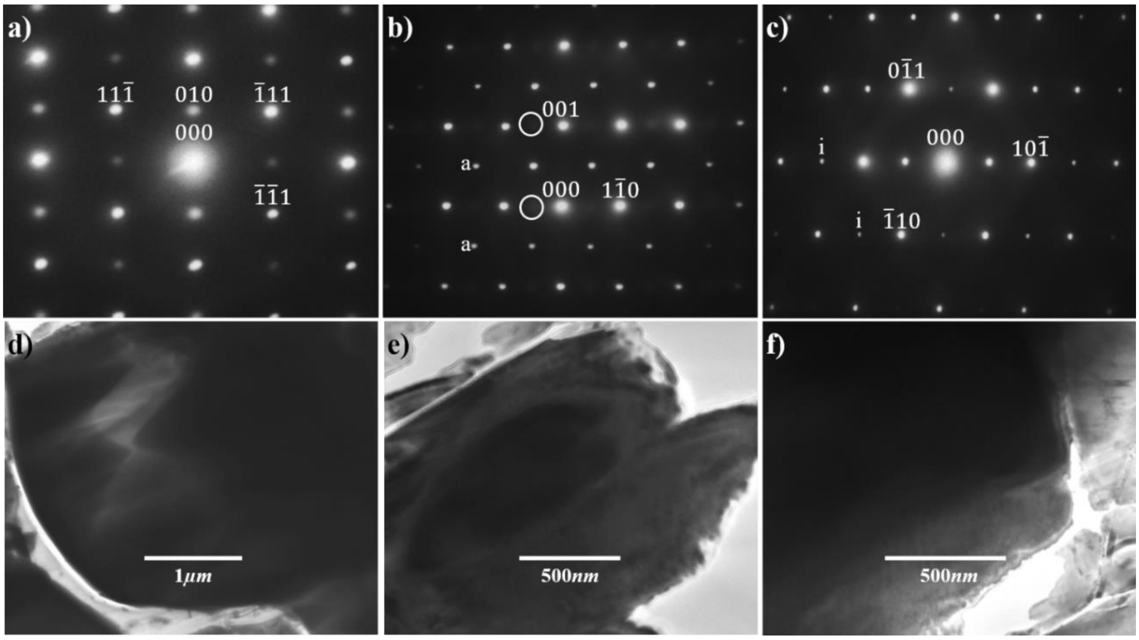

Figure 5. 33 Electron diffraction patterns obtained from a sample of CTLST + 4wt% BBO, sintered at 1300°C for 4h. These are arbitrarily indexed with zone axes a) [101], b) [110] and c) [111], with respective diffraction pattern locations d), e) and f) below. Superstructure reflexions are labelled with: a = anti-phase tilting, i = in-phase tilting. The ringed region in b) shows evidence of some diffuse scatter.

There is also evidence of some diffuse scatter in figure 5. 33 b), indicated by the circled regions. In the CTLNT system, this diffuse scatter was attributed to the formation of a short range version of "nano-checkerboard", or "nano-chessboard", structures within the matrix as a result of the end-member compound, $Li_{1/2}RE_{1/2}TiO_3$ (LRT) [11]–[13]. This may be true for CTLST system also, although the diffuse scatter is much weaker compared with CTLNT system.

figure 5. 34 shows two BF images of different grains from a sample of CTLST + 4wt% BBO, sintered at 1300°C. Figure 5. 34 a) shows larger grains (>2μm) with evidence of a ferroelastic domain wall in the upper left part of the image. The observation of a single ferroelastic domain is not truly representative of the whole sample and very few were observed. The absence of ferroelastic domains is similar to the CTLNT system, suggesting that the spontaneous strain in the CTLST ceramics may be lower than in the $CaTiO_3$ end-member.

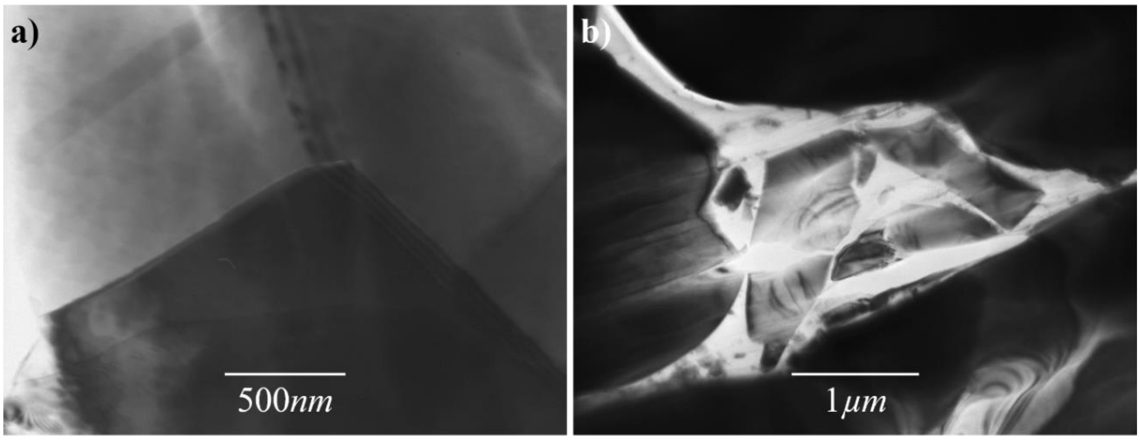

Figure 5. 34 TEM bright field image of a CTLST + 4wt% BBO sample, sintered at 1300°C, showing evidence of a) a ferroelastic domain within the grain and strain along the grain boundaries, and b) a lot of strain within smaller grains.

5.7 Mechanisms of Densification and Enhancement of Properties

The previous chapter, of the CTLNT system, showed that BBO, in addition to being a highly successful sintering aid for CTLNT composition, reacted so that Bi substituted into the CTLNT matrix and ex-solved Ti precipitates into the grains, all of which was found to contribute positively to the overall MW properties of the material.

BBO is evidently a successful sintering aid for CTLST in a similar way as in CTLNT, resulting in increased densification and grain growth whilst reducing sintering temperature by 150°C, and maintaining good MW properties. Similar to the CTLNT system, a darker contrast, glassy-phase was observed on fracture surfaces, as well as brighter contrast, Bi-rich regions on the polished surface. Due to the similarities observed between the CTLNT and CTLST compositions, it is assumed that there is a reaction between the CTLST and BBO sintering aid. However, the observed differences in the MW behaviour between the two compositions implies that there is potentially a different reaction taking place.

Figure 5. 35 shows a BF image, and the corresponding EDS analysis of a CTLST grain. From figure 5. 35, EDS revealed that the grains contained similar proportions of Ca, Ti, and Sm to that observed in the SEM, in addition to trace amounts of Bi. Cu is present due to transference of ions from the Cu mounting ring during ion beam thinning.

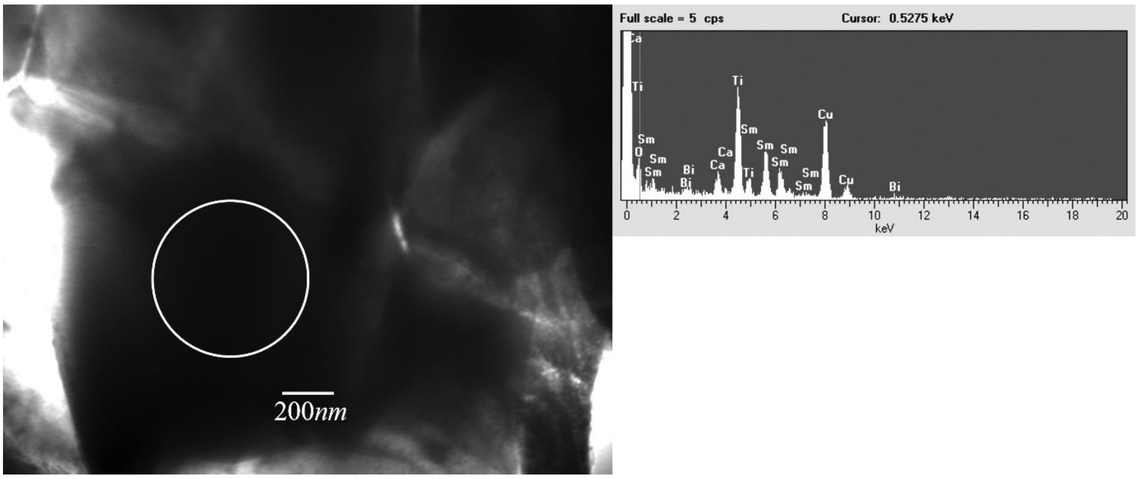

Figure 5. 35 TEM bright field image of a CTLST + 4wt% BBO sample, sintered at 1300°C, with corresponding EDS analysis of the average grain composition, circled.

Figure 5. 36 is a further BF TEM image along with the accompanying EDS analysis of the matrix and from a triple junction between the grains containing trace amounts of liquid-phase (broken circle to the lower right of the image). EDS of the matrix revealed similar proportions of elements to those in figure 5. 35, including trace amounts of Bi. The EDS of the much brighter, thinner, liquid-phase is inconclusive due to the lack of signal returned to the EDS sensor. As discussed in the previous chapter, the modulus of the liquid phase is considerably lower than the ceramic matrix and is, thus, preferentially thinned during ion beam milling. As such, observing liquid-phase under TEM is very unlikely and any observation will be too thin to return an EDS signal of sufficient quality.

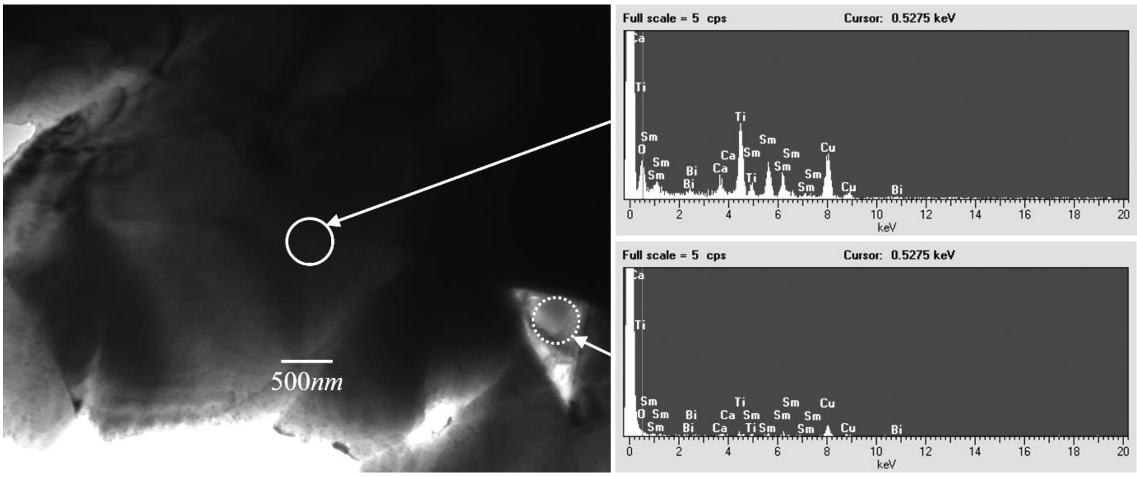

Figure 5. 36 TEM bright field image of a CTLST + 4wt% BBO sample, sintered at 1300°C, showing EDS analysis comparisons of the grain, in the centre of the BF image, and a liquid-phase in a triple junction, to the right of the BF image.

Figure 5. 37 shows a TEM BF image, with corresponding EDS analysis, of a significantly darker region located within a grain and the average matrix adjacent to the dark region. The dark regions are exceptionally rich in Bi, more so than any other element, while there are reduced levels of Sm and Ti, and a lack of Ca. The adjacent matrix EDS is typical for the CTLST + 4wt% BBO system, when compared to figure 5. 35 and figure 5. 36.

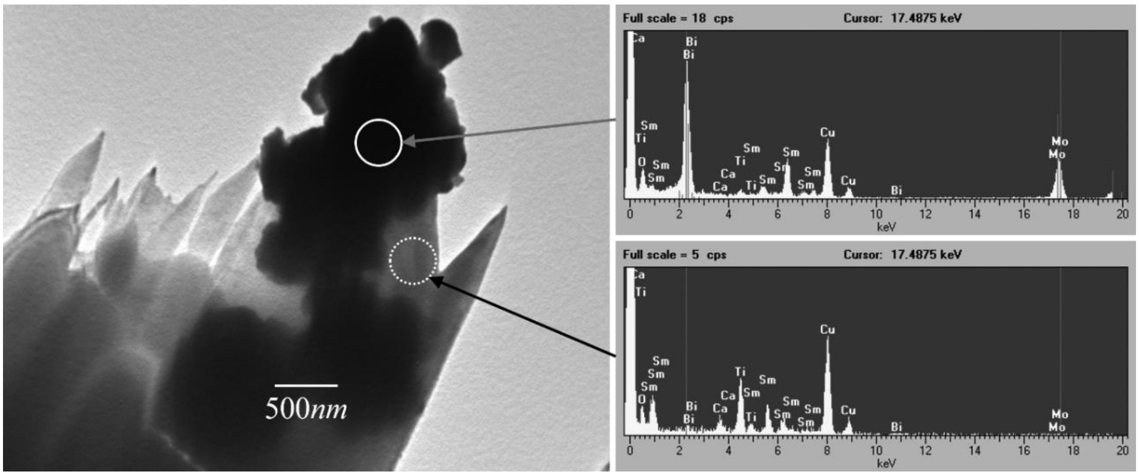

Figure 5. 37 TEM bright field image of a CTLST + 4wt% BBO sample, sintered at 1300°C, of a distinctly darker region within a grain, with corresponding EDS analysis of the darker region and lighter region immediately adjacent.

Despite evidence of Bi substituting into the CTLST matrix, no ex-solved Ti precipitates were observed which suggest that that defect chemistry in CTLST is different to that in CTLNT. To achieve a greater understanding, however, of the defect chemistry and substitution mechanism of Bi into the CTLST matrix, further investigation is required.

5.8 Summary and Conclusions

The previous chapter, of the CTLNT system, showed that BBO, in addition to being a highly successful sintering aid for CTLNT composition, reacted with the CTLNT in such a way that Bi substituted into the CTLNT matrix and ex-solved Ti precipitates, all of which was found to contribute positively to the overall MW properties of the material.

There are many parallels between the two CTLNT and CTLST systems. Initially, the sintering aid successfully reduced the optimal sintering temperature of the CTLST system from approximately 1350°C down to between 1200-1250°C, whilst maintaining high density. Like the CTLNT system, as the BBO content was increased, a B-rich secondary phase was routinely observed in the fracture surfaces of the samples, and as darker contrast regions in the polished surface of the SEM images of the samples. EDS of the SEM samples confirmed that the matrix contained larger proportions of Bi as the BBO content increased. An optimum composition of CTLST + 4wt% BBO, sintered at 1200°C, yielded a balance of MW properties and larger reduction in sintering temperature, compared to the CTLNT system, of 150°C, down to 1200°C, with $\varepsilon_r = 105.7$, $Qf_0 = 3295\ GHz$ and $\tau_f = -4\ ppm/℃$.

TEM analysis showed further similarities to the CTLNT system, in terms of diffraction patterns, including superstructure reflections and tilt systems, grain morphologies, stress within the grains and evidence of Bi within the grains from the EDS analysis. Very little evidence of liquid-phase was present in the TEM samples, likely due to preferential thinning of the liquid-phase located at triple junctions during ion beam milling of the samples. Electron diffraction patterns were typical of a perovskite crystal system, with superstructure reflections and tilt systems consistent with those reported for the $CaTiO_3$ and $(Li_{0.5}Nd_{0.5})TiO_3$ (LNT) end-members. While there was no direct evidence of a nano-chessboard structure from TEM BF imaging, the diffuse scatter present in the electron diffraction pattern was suggestive of their presence.

No TiO_2 precipitates, however, were observed within the grains of the CTLST system despite evidence of Bi in the matrix grains. Overall, the data suggests a similar reaction takes place between the CTLST and the BBO sintering aid, where the Bi substitutions creates locally enhanced MW properties and a leaving behind a B-rich liquid phase to tune the τ_f but the local defect chemistry maybe subtly different to that in CTLNT.

As well as notable similarities, differences were also observed between the CTLST and CTLNT systems. XRD results showed the presence of a secondary phase in the CTLST + $x$wt% BBO compositions, which were not present in the CTLNT system, however the amount of secondary phase did not vary with varying additions of BBO. This suggests that the sintering aid did not contribute to the secondary phase, and that it was endemic of the CTLST system with respect to calcination or sintering temperatures.

SEM analysis of the fracture surface revealed grains which were rich in Zr. This suggested that the CTLST system had larger quantities of Zr contamination from the milling process. If Zr is being incorporated into CTLST, then the excess of B-site (Zr) may well be compensated by the injection of Bi into the A-site, negating the need to ex-solve TiO_2 from the matrix during reaction. Without further data however, this mechanism is only speculative and further work is required.

The SEM also revealed greater rounding of grains, in addition to larger overall grain size and pores, as sintering temperature and BBO content increased. This suggests that CTLST is more soluble in the liquid phase than CTLNT, consistent with greater densification at lower temperatures.

Overall, the results show that the use of BBO as a sintering aid for the CTLST system is successful in reducing the sintering temperature, while maintaining very good MW properties. As such, the CTLST + 4wt% BBO composition, sintered at 1200°C, could be a cheaper, substitute candidate for commercialisation than pure CTLST.

5.9 References

[1] H. Takahashi, Y. Baba, K. Ezaki, and K. Shibata, “Microwave Dielectric Properties and Crystal Structure of CaO–Li_2O–(1- x)Sm_2O_3 – xLn_2O_3 – TiO_2 (Ln: lanthanide) Ceramics System,” *Jpn. J. Appl. Phys.*, vol. 35, no. Part 1, No. 9B, pp. 5069–5073, Sep. 1996.

[2] K. Ezaki, Y. Baba, H. Takahashi, K. Shibata, and S. Nakano, “Microwave Dielectric Properties of CaO-Li_2O-Ln_2O_3 -TiO_2 Ceramics,” *Jpn. J. Appl. Phys.*, vol. 32, no. Part 1, No. 9B, pp. 4319–4322, Sep. 1993.

[3] A. Walters, P. Lusty, and A. Hill, “Rare Earth Elements,” Nottingham, 2011.

[4] H. Takahashi, Y. Baba, K. Ezaki, Y. Okamoto, K. Shibata, K. Kuroki, and S. Nakano, “Dielectric Characteristics of $(A_{1/2}^{1+}\cdot A_{1/2}^{3+})TiO_3$ Ceramics at Microwave Frequencies,” *Jpn. J. Appl. Phys.*, vol. 30, no. Part 1, No. 9B, pp. 2339–2342, Sep. 1991.

[5] Y. Tabira, R. L. Withers, L. Minervini, and R. W. Grimes, “Systematic Structural Change in Selected Rare Earth Oxide Pyrochlores as Determined by Wide-Angle CBED and a Comparison with the Results of Atomistic Computer Simulation,” *J. Solid State Chem.*, vol. 153, no. 1, pp. 16–25, 2000.

[6] M. Yashima and R. Ali, “Structural phase transition and octahedral tilting in the calcium titanate perovskite $CaTiO_3$,” *Solid State Ionics*, vol. 180, no. 2–3, pp. 120–126, 2009.

[7] S. M. Emel’yanov and G. Geguzina, “Preparation and investigation of new oxides $A'_{0.5}A''_{0.5}BO_3$ with perovskite-type structure,” *Izv. Akad. Nauk SSSR, Neorg. Mater.*, vol. 20, no. 12, pp. 2005–2008, 1984.

[8] L. Ingemarsson and M. Halvarsson, “SEM/EDX Analysis of Boron,” Gothenburgh, 2011.

[9] W. D. Kingery, H. K. Bowen, and D. R. Uhlmann, *Introduction to ceramics*, 2d ed. New York: Wiley, 1976.

[10] D. I. Woodward and I. M. Reaney, “Electron diffraction of tilted perovskites,” *Acta Crystallogr. Sect. B*, vol. 61, no. 4, pp. 387–399, 2005.

[11] B. S. Guiton, W. Hui, and P. K. Davies, “Neutron powder diffraction of $(Nd_{7/12}Li_{1/4})TiO_3$ nano-checkerboard superlattices,” *Chem. Mater.*, vol. 20, no. 9, pp. 2860–2862, 2008.

[12] B. S. Guiton and P. K. Davies, “Spontaneous compositional nanopatterning in Li-containing perovskite oxides,” *J. Am. Chem. Soc.*, vol. 130, no. 50, pp. 17168–17173, 2008.

[13] B. S. Guiton and P. K. Davies, “Nano-chessboard superlattices formed by spontaneous phase separation in oxides,” *Nat. Mater.*, vol. 6, no. 8, pp. 586–591, Aug. 2007.

Chapter 6: Investigations into using CTLNT as a Class 1, C0G (NP0), Multilayer Ceramic Capacitor (MLCC)

6.1 Introduction and Brief Literature Review

Capacitors make use of dielectric materials to enhance their ability to store charge. As previously stated in chapter 2.2.1, most dielectric materials are defined by their performance as an electrical insulator within a parallel plate capacitor, over a known distance between the plates [1], through the relationship given by eq. 2.1. The conducting plates hold equal but opposite charge on their facing surfaces and the dielectric develops an electric field [2], [3]. A charge (Q) is then stored between the parallel plates upon the application of a potential difference (V), relating to both the capacitance (C) and V of the system, as illustrated by eq. 2.2.

A capacitance of 1 Farad (F) means that 1 coulomb of charge is held under an applied voltage (or potential difference, V) of 1V across the device. Increasing both the permittivity of the material between the plates and the area of the plates, as well as decreasing the distance between the plates, increases the capacitance of the capacitor, as well as the charge stored. An ideal capacitor is characterised by a constant capacitance, which is defined by the ratio of ±Q on each conductor and the voltage between them, as shown by expression [1]–[3]:

$$C = \frac{Q}{V} \tag{6. 1}$$

Capacitors have become one the most important electrical components in the modern era, predominantly because of their use in laptops, smartphones and tablets, with hundreds of individual capacitor components used in each device. Capacitors with ceramic dielectrics offer the greatest potential for miniaturisation, because of their large ε_r. In addition to using large ε_r materials, design of the capacitor plays a large role in its 'volumetric efficiency' and the most successful capacitor design on the market is that of the multilayer ceramic capacitor (MLCC) design, with high capacitance, small physical size, high reliability and excellent high-frequency characteristics [4]. Over the last 20 years, the volumetric efficiency (the capacitance per volume) of the MLCC has risen at a rate exceeding that of Moore's Law, where the maximum available capacitance, for a given physical size of capacitor, is doubling every 13-14 months, compared with every 18 months for Moore's Law [5].

In 2008, the ceramic capacitor occupied approximately 90% of the overall capacitor market in volume, and 40% in market price [6]. In 2009, ~1.5 trillion individual capacitors were manufactured, between 26 global manufacturers, worth about 12.7 billion USD ($) [6], [7], with an annual growth of 13-15% [4], [6], [8], [9].

Ceramic capacitors are not wholly limited to MLCC's, however; other, more specialist, designs and dielectric material compositions do exist and fill the gaps not covered by MLCC's. Examples include high-temperature capacitors, capable of performing at temperatures of up to several hundred degrees Celsius, and single-element capacitors able to withstanding very large potential differences of 50-100 kV [7].

6.1.1 Multilayer Ceramic Capacitors (MLCCs)

MLCC's are mainly used within resonant circuits and filters, as well as power supply and decoupling. Resonant circuits and filters require capacitors with high stability, low dielectric losses (high Q) and a linear temperature coefficient of capacitance (TCC or τ_C), while power supply and decoupling capacitors require high capacitance, while tolerating moderate dielectric losses, τ_C and voltage dependence of capacitance.

Fabricating MLCC's

The typical design for an MLCC was first conceived in the 1960's and took another 20 years to gain global commercialisation. It is essentially many ceramic plate capacitors stacked above one another, and connected in parallel, figure 6. 1. The combination of a large surface area, thin dielectric layers and high ε_r material results in a device with a large capacitance for its physical volume, i.e.: a large volumetric efficiency.

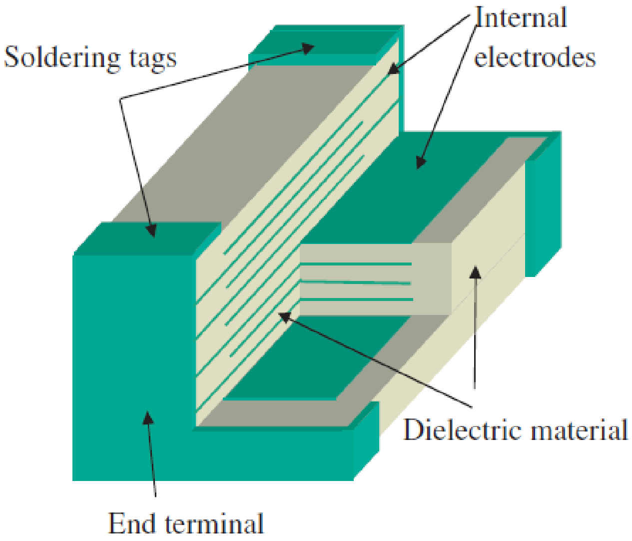

Figure 6. 1 Cutaway schematic of a typical MLCC [4].

The capacitance (C) of an MLCC is given by the following expression, which is a variation of the basic capacitance equations given in section 2.2.1 [4]:

$$C = \frac{\varepsilon_r \varepsilon_0 (n-1) s}{t}$$

(6. 2)

where:

C = the capacitance of the MLCC;

ε_r = the relative permittivity/dielectric constant of the dielectric material;

ε_0 = the permittivity of free space (8.854x10^{-12} Fm^{-1});

n = the number of internal layers;

s = the overlap area of the internal electrodes;

t = the thickness of the dielectric layers between the electrodes.

This relationship states that for a large C in MLCC's, a high ε_r dielectric material is required, along with a large number of stacked layers, a large overlapping area and thin dielectric layers.

The process by which a MLCC is made follows several different steps, illustrated by figure 6. 2. The powder of the green, un-sintered dielectric material is mixed with solvents, a dispersant, a binder and plasticiser to form a homogenous, suspended slurry. This slurry is then cast into a thin film sheet using a 'doctor blade', of set thickness, allowed to dry to form a flexible tape via the evaporation of the solvents, and then cut into many individual sheets. An electrode paste, made of very fine powder of the internal electrode material, suspended in its own solvents, is then applied to the surface of the dielectric tape through screen printing. The screen-printed tapes are then precisely stacked and laminated together through the application of pressure and/or heat. These stacks are then cut or diced into individual, green capacitors and sintered under a carefully controlled heating route to consolidate the layers, form a dense body and allow the burnout of binders from the devices. Metallisation is applied to the end-terminals of the sintered devices, to provide a connection to the internal electrodes, which is then fired.

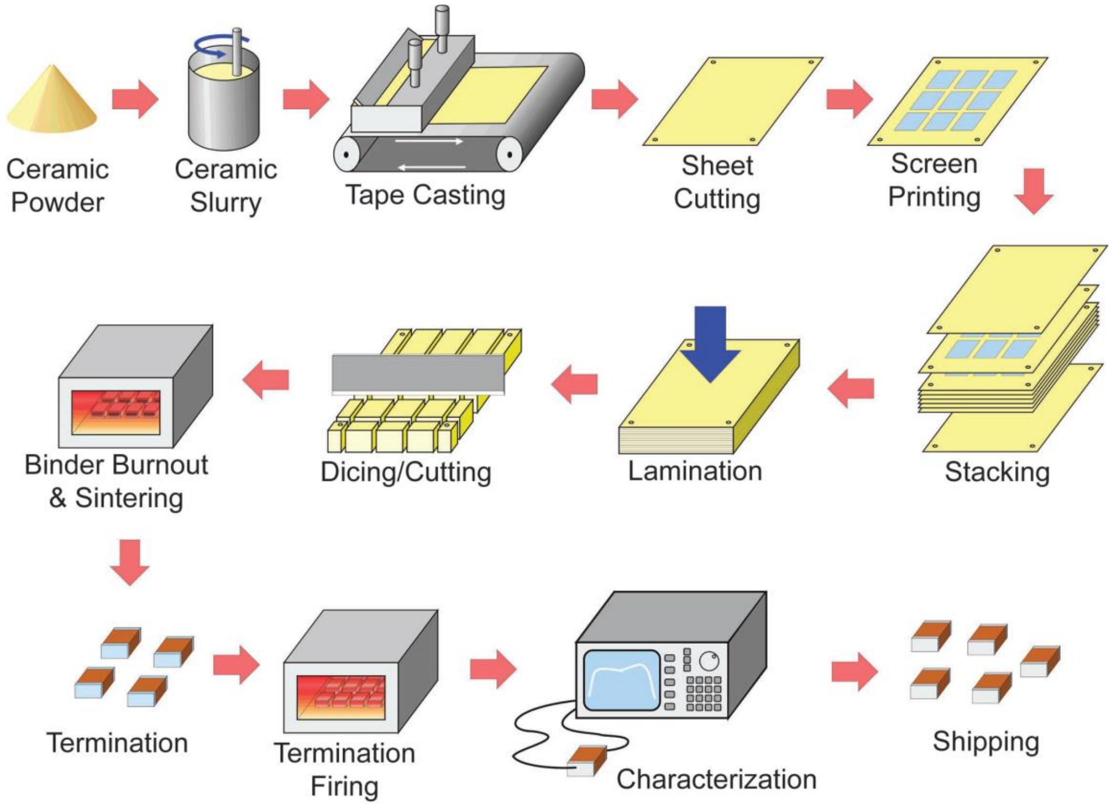

Figure 6. 2 A schematic of a typical MLCC fabrication route [7].

This multi-stage, multi-material/component processing route does not come without challenges, which is why there was a 20-year gap between its conception and its use in industry. One such challenge is the mismatch between the sintering temperatures of the ceramic dielectric and the melting temperature of most metals used as internal electrodes. Solutions to this challenge include using liquid-phase sintering aids to reduce the sintering temperature of the dielectric, or the use of smaller powder particle sizes. Problems associated with internal electrodes include oxidation of the metal at high processing temperatures or diffusion into, or reaction with, the ceramic material, which would fundamentally change the properties of the device. Residual stresses may be introduced into the layers as a result of different shrinkage rates, upon sintering, of the various different materials used, which increases the chances of warping, cracking or delamination of layers. If burnout of the plasticiser and binders is too rapid, large pores or delamination of layers may occur, all of which have a negative impact on the properties of the MLCC device. Thus, the fabrication of an MLCC is a compromise between the best possible properties and the relationship between the constituent materials which make up the MLCC device.

Development of the Internal Electrodes and Dielectric Materials

In the initial development of MLCCs, it was considered that the high temperatures involved required the used of noble metal internal electrodes. The most suitable noble metals for MLCC’s include Au, Pt, Pd and Ag. Au and Pt were considered too expensive and consequently early

MLCC's were based on internal electrodes formed from Ag-Pd alloys of different composition depending on the firing temperature. These alloys however, presented 3 main challenges to overcome [10]–[12]. Firstly, Pd is used as a catalyst in many different reactions and, in the case of MLCC's, catalyses the exothermic binder burnout reaction taking place during firing. If this is not carefully managed, the Pd may cause a runaway burnout reaction inducing elevated temperatures within the device and damage in the form of delamination [10]. Secondly, Pd experiences a 68% volumetric change as it oxidises and reduces between the temperatures of ~500°C and 800°C, which can impart mechanical stress on the device during firing and, at worst, causes cracking and delamination [11]. Thirdly, depending on the precise Ag-Pd mixture, MLCC devices may only be fired at relatively low temperatures due to the melting points of the two metals (~900-1100°C) [12]. This forces the use of glassy sintering aids to reduce the densification temperature of the dielectric ceramic which have detrimental effects to the overall properties of the MLCC. [13]–[15].

During the 1990's, the use of Pd as an internal electrode material became unfeasible due mainly to the increase in global demand of Pd for other applications, driving the price of Pd up by nearly an order of magnitude, from ~$120/oz., in 1996, to ~$1085/oz. in 2001 [16]. Additionally, devices became smaller, the dielectric thickness consequently thinner, thereby increasing the volume fraction of the electrode (figure 6. 3).

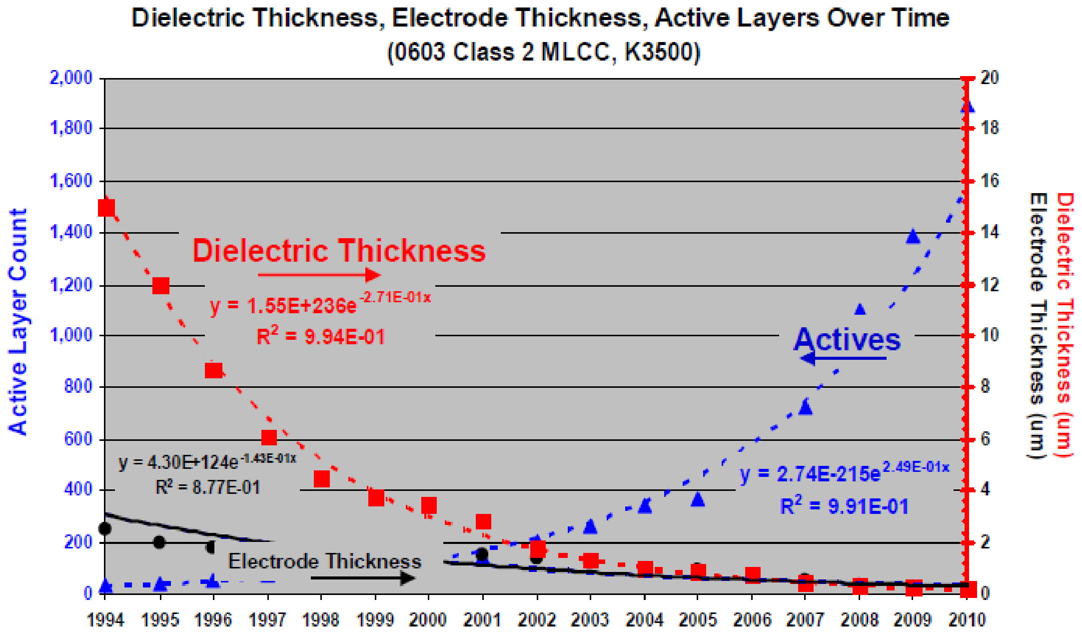

Figure 6. 3 The change of dielectric and electrode thicknesses, and the number of active layers, over time within a specific device: 0603 Class II MLCC, K3500 [5].

As a result, global interest shifted to finding an alternative, cheaper base-metal electrode which could withstand elevated firing temperatures. Nickel (Ni) was found to be the most promising and, after significant investment, became the most popular base-metal archetype for MLCC internal electrodes.

Ni is cheap in comparison to Ag and Pd, and has a very high melting temperature (1455°C), however its major drawback is that it readily oxidises. Consequently, MLCCs are fabricated in a controlled, reducing atmosphere, designed to avoid the oxidation of Ni as well as that of the dielectric ceramic.

To aid in the prevention of reduction for the dielectric ceramic used, acceptor dopants are usually added, such as MnO, Cr_2O_3 and CaO, particularly for the most successful MLCC dielectric ceramic, $BaTiO_3$ [17]–[20]. This acceptor dopant strategy was initially used in an attempt to commercialise Ni-based MLCC's in the 1980's, however these acceptors shortened the lifetime of devices at high operating temperatures and high yields, compared with their Ag-Pd MLCC counterparts [4], [21]–[23].

In the 1990's, a series of new dopants led to a breakthrough for the popularity of Ni-based internal electrode MLCC's: the discovery of the so-called 'magic dopants', Y_2O_3 and rare-earth oxides Dy_2O_3, Ho_2O_3 and Er_2O [21], [22], [24], [25]. The 'magic dopants' had similar ionic radii to both the A-site, Ba^{2+}, and the B-site, Ti^{4+}, of the perovskite, with corresponding coordination numbers 12 and 6, respectively, and were thus able to occupy both sites as an electron donor and acceptor. This significantly decreased the oxygen vacancy concentration in the dielectric, which led to a rise in MLCC lifetime [26]–[31].

6.1.2 MLCC Device Classifications and Specifications

As a result of the large variation in ε_r and temperature stability in $BaTiO_3$ based ceramic dielectrics, devices with different specifications and performances have been grouped together into different classes, each with their own classification codes. Devices with completely different compositions may therefore have the same performance classification code, if they have the same properties, differentiated only by cost and environmental impact of the materials used.

There are three main classes of MLCC's, Class 1, 2 and 3. Class 1 capacitors use ceramics with low ε_r, from 5 to a few hundred, low dielectric losses (<<0.01, high Q >>100) and usually have a linear τ_{ε_r} from zero to a few thousand ppm/°C. Class 2 devices are those which utilise ceramics with large ε_r (between 1000-20,000) and are typically based on ferroelectrics with dielectric losses between 0.01 and 0.03. The important feature of Class 2 capacitors is that they have moderate to high τ_{ε_r} [7]. Class 3 capacitors utilise a 'core-shell' microstructure of the dielectric for ‘barrier layer capacitors’, resulting in very large capacitance values at relatively small applied voltages (< 25V) [1]. As such, the class 3 capacitors operate very differently to conventional MLCC devices.

Class I Dielectrics

Most early dielectric materials belong to the class 1 group, and include traditional materials not necessarily associated with electronic components, such as porcelain and talc, but also TiO_2 and modified (Ca,Sr)(Zr,Ti)O_3 perovskites. Polycrystalline TiO_2 devices have $\varepsilon_r \approx 100$, τ_C between -750 and +400 ppm/°C [32]–[34] and may be mixed with other class 1 dielectrics to create ‘tailored’ dielectric properties and performance [32]–[34].

One drawback of the TiO_2-based perovskite dielectrics is that oxygen vacancies can be introduced which have a negative impact on the dielectric losses and can also cause rapid degradation. However, this is normally countered through the addition of donor-dopants, such as Nb_2O_5 [35], [36].

As a result of the large potential variation of properties for class 1 capacitors, as well as the need for devices with different specifications to fill different functions in industry, the Electronic Components Industry Association (EIA) and the International Electrotechnical Commission (IEC) set out to produce standards with which to classify the capacitors. The standards classify the devices in terms of the magnitudes and tolerances of the τ_C of the capacitors. The EIA classification takes the form of a 3-digit code, composed of a letter, a number and a final letter (“EIA Standard RS-198”), and the IEC was simply a letter (normally N, P or NP) followed by a number (“IEC/EN 60384-8/21” standard).

The first letter of the EIA standard represents the significant figure of τ_C, in ppm/°C, the second digit applies a multiplier to the significant digit, and the final letter gives the maximum tolerance of τ_C, in ppm/°C (table 6. 1) [37]. The IEC codification of τ_C simply uses a letter (N = negative, P = positive and NP = negative/positive) and a number representing the magnitude of τ_C, in ppm/°C, however there is no appreciation for the tolerances for the τ_C values in the IEC classification system. There is overlap between the two systems and devices often state their specifications using both. For example, an MLCC device with τ_C of 150 ppm/°C, with a drift tolerance of 250 ppm/°C, can be labelled both as P7K (EIA) or P150 (IEC), and a device with $\tau_C = 0$ ppm/°C, with very little drift is labelled as C0G or NP0.

Table 6. 1 EIA Codes for Class 1 Ceramic Capacitors, under EIA Standards RS-198 [7], [37].

First Character		Second Character		Third Character	
Symbol	**Significant Figure ($\tau_C\ ppm/℃$)**	**Symbol**	**Multiplier**	**Symbol**	**τ_C Tolerance ($ppm/℃$)**
C	0.0	0	-1	G	±30
B	0.3	1	-10	H	±60
L	0.8	2	-100	J	±120
A	0.9	3	-1000	K	±250
M	1.0	5	+1	L	±500
P	1.5	6	+10	M	±1000
R	2.2	7	+100	N	±2500
S	3.3	8	+1000		
T	4.7				
V	5.6				
U	7.5				

Class 1 dielectrics are predominantly used in resonant circuits to sustain a high tolerance on the frequency, and typically operate between 100MHz to 30GHz [38], [39]. This resonance is influenced by the combined interaction of the capacitor and the inductor properties, and a controlled temperature coefficient of capacitance and permittivity is required to match that of the inductor. Additionally, the resonance peak can be made sharper through the use of materials with lower dielectric losses (higher Q factor), less than 0.001 (Q > 1000) [40], [41].

Class II Dielectrics

Class 2 dielectrics belong to those with very large ε_r values (from 1000 to greater than 20,000), and often have diffuse or broad phase transitions. In general, class 2 dielectrics exhibit a very high volumetric efficiency as a result of the large ε_r values, and have, on average, lower sintering temperatures. In addition, a larger temperature coefficient of capacitance is tolerated because of the high ε_r values.

Similar to class 1, class 2 devices have a large variety of materials with similar and different properties. Class 2 dielectric devices have also been classified by the EIA, with a similar 3-digit code under the same standard “EIA Standard RS-198” (table 6. 2), and the IEC, which utilises its own 3-digit code under standard “IEC/EN 60384-9/22” (table 6. 3). The first two characters of the EIA code gives the low- and high-end operating temperatures, respectively, and the third character gives the allowed change of capacitance within that temperature range. The IEC code, instead, represents the change in capacitance with the first two characters, followed by a single character code for the temperature range.

Table 6. 2 EIA code for Class 2 Dielectric Ceramic Capacitors, under EIA Standards RS-198 [7].

First Character		Second Character		Thirst Character	
Symbol	Low-End Temperature Limit (°C)	Symbol	High-End Temperature Limit (°C)	Symbol	Maximum Capacitance Change (%)
Z	+10	4	+65	A	±1.0
Y	-30	5	+85	B	±1.5
X	-55	6	+105	C	±2.2
		7	+125	D	±3.3
		8	+150	E	±4.7
				F	±7.5
				P	±10.0
				R	±15.0
				S	±22.0
				T	+22/-33
				U	+22/-56
				V	+22/-82

Table 6. 3 IEC Code for Class 2 Dielectric Ceramic Capacitors, under IEC Standard: IEC/EN 60384-9/22.

Capacitance Change Code	Maximum Capacitance Change (%) $(\frac{\Delta C}{C_0}$ at $U = 0)$	Maximum Capacitance Change (%) $(\frac{\Delta C}{C_0}$ at $U = U_N)$	Temperature Range Character	Temperature Range (°C)
2B	±10	+10/-15	1	-55 to +125
2C	±20	+20/-30	2	-55 to +85
2D	+20/-30	+20/-40	3	-40 to +85
2E	+22/-56	+22/-70	4	-25 to +85
2F	+30/-80	+30/-90	5	-10 to +70
2R	±15	-	6	+10 to +85
2X	±15	+15/-25	-	-

$BaTiO_3$-based dielectrics are the most populace class 2 dielectric ceramic material on the market. $BaTiO_3$ is a ferroelectric material with a high ε_r (> 10,000), and was initially discovered, simultaneously by different groups, during the second world war, where its potential was very quickly understood. Since then, more than 60 years of research has been conducted on this dielectric material [36]. $BaTiO_3$ is a perovskite material, with 3 phase transitions upon cooling from high to low temperatures, from cubic to tetragonal at approximately 120°C, tetragonal to orthorhombic at ~0°C and, finally, orthorhombic to rhombohedral at ~-90°C [1].

Each of these transitions has an associated dielectric peak, which is not ideal in terms of device usage if the peaks are particularly large. However, it is possible to manipulate the phase transition, and thus the dielectric peaks by forming a solid solution with other perovskites, such as $SrTiO_3$ which shifts and broadens the peaks, or by adding dopants, such as Ca, Zr, Sn and other rare-earth elements, which can also shift or suppress these peaks [1].

The properties of $BaTiO_3$ can also be influenced by the introduction of a core-shell grain structure through the addition of small amounts of dopants [1], [42], [43]. The core-shell structure is typically characterised by grains, where the centre (or 'core') of the grains are composed of pure $BaTiO_3$ and the regions of the grain at the grain boundaries (the 'shell') are composed of a diffuse phase transition. The diffusion of the dopants into the grains to create this structure is controlled with the sintering temperature. Benefits of a core-shell grain structure include a reduced τ_C, which can be beneficial in producing a class 2 capacitor with tighter tolerances of capacitance changes with temperature. The structure itself creates a lattice mismatch between the core and the shell, introducing a mechanical stress which stabilises the tetragonal phase of the core. Finally, the dopant-rich grain boundaries, the shells, also have the benefit of restricting ion migration through the grains, resulting in both low conductivity and dielectrics with higher reliability [42], [43].

Between the Pb- and $BaTiO_3$-based class 2 dielectric ceramic compositions, there is clearly great scope in class 2 dielectrics to be tailor-made for various applications, especially in the case of $BaTiO_3$. Kishi *et al.* [4] created a table which summarises, at least for $BaTiO_3$-based materials, the potential properties which can be attained from different mixtures of materials, along with their respective classes and classifications (table 6. 4).

Table 6. 4 A summary of different Class 1 and 2 MLCC's, under EIA specifications, with respective materials [4].

EIA Classification	Class	Temperature Range (°C)	Capacitance Change (%)	Maximum ε_r	$BaTiO_3$ Content	Other Dopants	Grain Size (μm)
C0G (NP0)	1	-55 to +125	±30 ppm	100	10-50	TiO_2, $CaTiO_3$, $Nd_2Ti_2O_7$	1
X7R	2	-55 to +125	±15	4000	90-98	MgO, MnO, Nd_2O_5, CoO, Rare-Earth	<1.5
Z5U	2	+10 to +85	+22/-56	14000	80-90	$CaZrO_3$, $BaZrO_3$	3-10
Y5V	2	-30 to +85	+22/-82	18000	80-90	$CaZrO_3$, $BaZrO_3$	3-10

As there is a drive for smaller devices and larger volumetric efficiencies, through the reduction of layer thicknesses in MLCC's, this has had 2 profound effects on $BaTiO_3$-based devices especially, with similar effects on similar materials. Firstly, thinner dielectric layers require smaller and smaller grains, much smaller than 1μm in size. However, the dielectric properties of $BaTiO_3$ is highly dependent on grain size [1], [36]. As a result, this has implications on the further viability of $BaTiO_3$ as grain size reduction demands increase over time. Secondly, as the layers become thinner, the electric field created within the dielectric material becomes sufficiently high such that the voltage dependence of the dielectric properties becomes worrying [44], [45].

A Brief Mention on Capacitor Case Sizes Nomenclature

Since there are many different devices, for a large variety of applications, including the ever-present need for miniaturisation or improved performance, it is only natural that there would be great variety in capacitor shapes and sizes, including the MLCC archetype.

For MLCC devices, both the EIA and IEC have very similar nomenclatures for categorising the 'case sizes' of the devices, where the difference is that the EIA standardised the nomenclature using imperial inches, and the IEC used metric millimetres. Both codes use an even-numbered code of either 4-digits or 6-digits, where the first half represents the 'length' dimension of a device and the second half represents the 'width' dimension of the device (table 6. 5). The height is normally not represented, as it is generally smaller than the width of the device. As there is overlap between both standards, one must be aware of which standard is being used, however the updated and modern metric version has become more popular.

Table 6. 5 A table of dimension codes for the EIA Imperial Format and the IEC Metric Format, for MLCC archetypes.

EIA Inch Code	Dimensions in Inches (L x W)	IEC/EN Metric Code	Dimensions in Millimeters (L x W)
01005	0.016 × 0.0079	0402	0.4 × 0.2
015015	0.016 × 0.016	0404	0.4 × 0.4
0201	0.024 × 0.012	0603	0.6 × 0.3
0202	0.02 × 0.02	0505	0.5 × 0.5
0302	0.03 × 0.02	0805	0.8 × 0.5
0303	0.3 × 0.03	0808	0.8 × 0.8
0504	0.05 × 0.04	1310	1.3 × 1.0
0402	0.039 × 0.020	1005	1.0 × 0.5
0603	0.063 × 0.031	1608	1.6 × 0.8
0805	0.079 × 0.049	2012	2.0 × 1.25
1008	0.098 × 0.079	2520	2.5 × 2.0
1111	0.11 × 0.11	2828	2.8 × 2.8
1206	0.126 × 0.063	3216	3.2 × 1.6
1210	0.126 × 0.10	3225	3.2 × 2.5
1410	0.14 × 0.10	3625	3.6 × 2.5
1515	0.15 × 0.15	3838	3.81 × 3.81
1806	0.18 × 0.063	4516	4.5 × 1.6
1808	0.18 × 0.079	4520	4.5 × 2.0
1812	0.18 × 0.13	4532	4.5 × 3.2
1825	0.18 × 0.25	4564	4.5 × 6.4
2010	0.20 × 0.098	5025	5.0 × 2.5
2020	0.20 × 0.20	5050	5.08 × 5.08
2220	0.225 × 0.197	5750	5.7 × 5.0
2225	0.225 × 0.25	5664/5764	5.7 × 6.4

2512	0.25 × 0.13	6432	6.4 × 3.2
2520	0.25 × 0.197	6450	6.4 × 5.0
2920	0.29 × 0.197	7450	7.4 × 5.0
3333	0.33 × 0.33	8484	8.38 × 8.38
3640	0.36 × 0.40	9210	9.2 × 10.16
4040	0.4 × 0.4	100100	10.2 × 10.2
5550	0.55 × 0.5	140127	14.0 × 12.7
8060	0.8 × 0.6	203153	20.3 × 15.3

6.2 Fabrication of Pt-electrode, CTLNT, MLCC Devices

The microwave study on the CTLNT + $x$wt% BBO, supplementing previous work by other groups [46]–[49], shows that this system has temperature stability and dielectric constant properties which could be promising as a C0G/NP0, Class 1 multi-layer ceramic capacitor (MLCC). As such, a brief study on the fabrication and electrical characterisation of the CTLNT + 4wt% BBO composition as a MLCC was conducted.

The initial processing route followed that of the procedure summarised and outlined by Pan and Randall [7], using platinum internal electrodes which offer the lowest reactivity in air at high temperatures and the highest melting point. Four 3-Layer devices were fabricated successfully, after stacking under 200 kg of uniaxial pressing for 10 minutes, 5 minutes of further pressing at ~200 MPa, using the cold isostatic press (CIP), and firing at 1200°C on platinum foil for approximately 57 hours, allowing for burnout time. The 3-layer samples were dense and there was little evidence of warping, showing similar shrinkage rates to pellets in the MW study. Figure 6. 4 shows a typical green (a) and sintered (b) MLCC, demonstrating darkening of the colour, as the sample has densified, and with ~30% shrinkage.

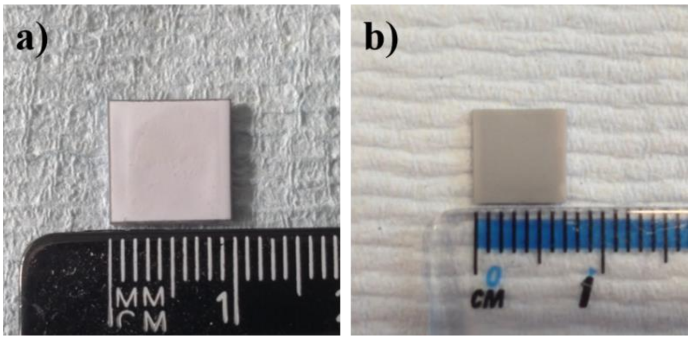

Figure 6. 4 A typical MLCC sample a) pre-sintering as a green sample and b) post-sintering at 1200°C.

There were, however, several problems in the fabrication of samples with larger layer numbers than 3, which required the appropriate modification to the processing. The issues which arose are categorised as those relating to the pressing of the stacks and devices, and those relating to the firing process.

6.2.1 Pressing Problems

The 4 and 5-layer MLCC devices, upon firing and sintering, showed visible signs of delamination, figure 6. 5. Further attempts to laminate and press the green 4 and 5-layer samples resulted in individual, tightly packed layers, as opposed to a single, merged cross-section. Although the numbers of layers were increased, the applied pressure could not be increased, as the CIP was already operating at maximum pressure. The pressure per layer therefore decreased, resulting in reduced compactness. As a result, the layers were less likely to fuse or stick together during sintering and shrinkage.

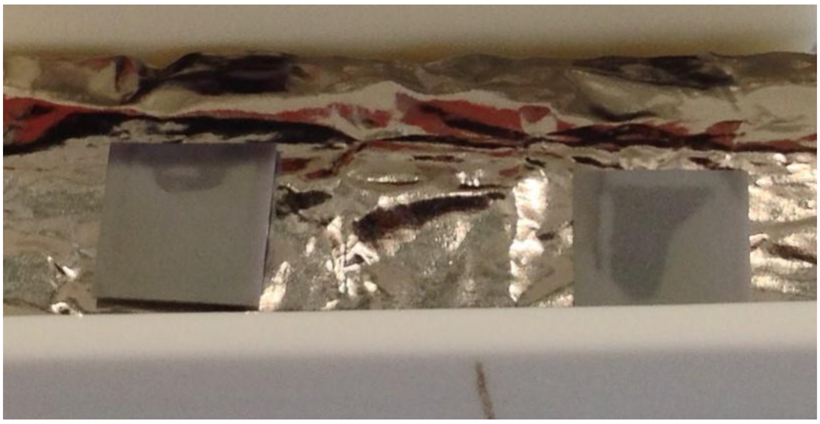

Figure 6. 5 Two sintered 4-Layer MLCC devices, sintered in an alumina boat on platinum foil at 1200°C, showing clear signs of delamination of the outer layers.

One solution was to apply heat during the uniaxial pressing stage to soften, or partially melt, the plasticiser within the tape, allowing the tape to better press together and more successfully laminate the layers. However, the softening from the heat resulted in deforming and stretching the stacks, which had two further effects. Firstly, the following dicing stage became inaccurate, as the stack was stretched to larger proportions than the jig, and, secondly, as the plasticiser relaxed upon re-softening during firing, delamination continued to occur as a result of this movement.

A further solution was to wet the surface of each layer during the stacking stage with the solvent used earlier in the fabrication process, and applying even pressure upon stacking each layer with the steel plates of the stacking jig. The solvent partially dissolved the plasticiser within the tape, causing it to fuse with the other layer. This method resulted in one single layer upon inspection of the cross section of the diced, green samples and, along with refining some other firing and sintering issues, was used to successfully fabricate 4 and 5-layer MLCC devices with no visible delamination. In addition, this solution streamlined the fabrication process by eliminating both the uniaxial press and CIP processes.

6.2.2 Sintering/Firing Issues

In addition to processing issues which arose as a result of pressing, there were a number of additional challenges to overcome which occurred during the firing and sintering stages of the fabrication route.

Layer Number and Sintering Time

As the number of layers increased, the volume of material increased, resulting in greater difficulty for the egress of gasses during binder burnout. As a result, the firing and sintering route outlined in section 3.1.5, gave rise to pockets of gas, creating large pores, cracks between layers and delamination, figure 6. 6. Consequently, as the layer number increased, the binder burn-out temperature/time was modified from 16 to 20 hours at 350°C, and 1 hour to 4 hours at 550°C, respectively. This increased the sintering time from ~57 hours to ~67 hours.

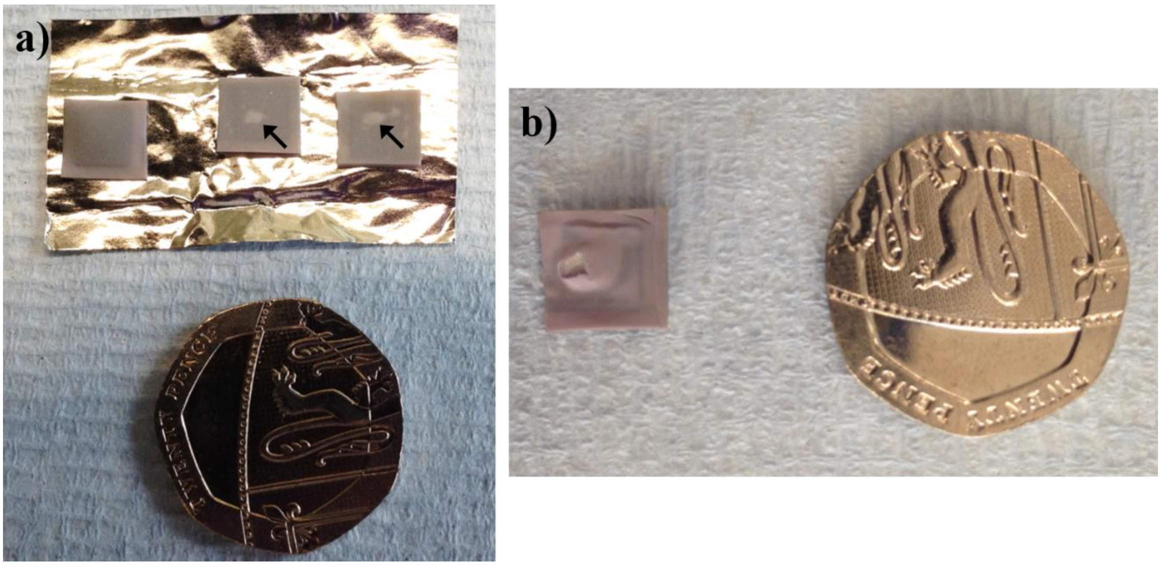

Figure 6. 6 Evidence of trapped gas creating bubbles beneath the surface of the layers, a) causing visible bubbles, arrowed, in the centre and right sample, and bulging in the left sample, indicative of bubbles in the centre layers, and b) escaping more violently at elevated temperatures. A twenty pence (20p) sterling coin is used as a reference of scale.

Platinum Foil Surface

Increase in sintering times resulted in samples ‘sticking’ and reacting with the platinum foil on which the samples were fired upon. As a consequence, the side of the device in contact with the platinum deformed onto the surface, resulting in delamination and exposing the internal electrode.

Figure 6. 7 shows the extent to which prolonged exposure the platinum has on the CTLNT + 4wt% BBO MLCC devices. The overhead view shows splitting of the surface, due to shrinkage while the surface stuck to the platinum is held in place. The area of the sample which is unable to shrink, bulges beneath the surface as the remaining sample continues to shrink, figure 6. 7 b).

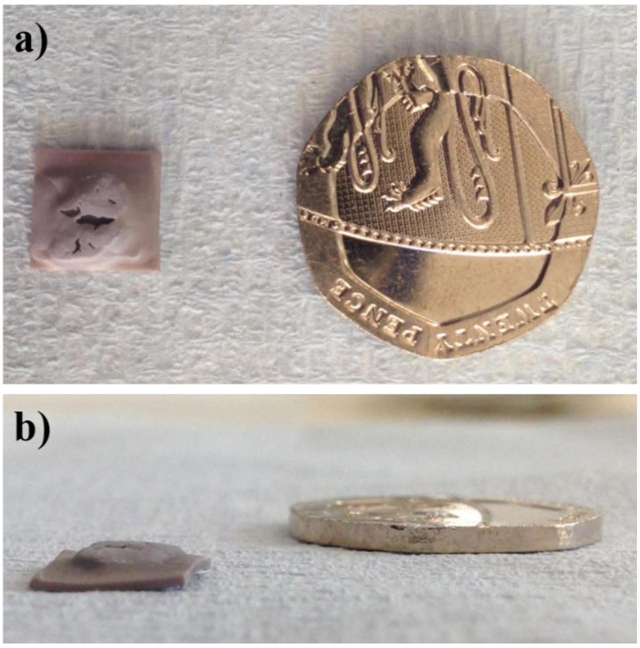

Figure 6. 7 An example of prolonged exposure to the platinum foil on which the samples were sintered on, for a 5-layer sample. A) and b) are different angles of the same sample, where a) shows the overhead, fractured view of the sample, and b) shows the bulge of the sample onto the platinum foil. A twenty pence (20p) sterling coin is used as a reference of scale.

Alumina Powder Surface

Figure 6. 8 illustrates the improvement using Al_2O_3 powder has on the sintering process. Samples sintered on calcined alumina, and stacked using the solvent wetting method, appeared to be uniformly dense, with little warping, cracking or delamination of the samples. Sintering on a bed of calcined alumina powder left behind traces of the powder embedded in the outer surface of the samples, as can be seen in figure 6. 8 b) and c). However, this is not an active layer within the design of the MLCC. 3, 4 and 5-layer MLCC devices were therefore successfully produced, with an imperial EIA case size of ‘2928’, or a metric IEC case size of ‘7472’.

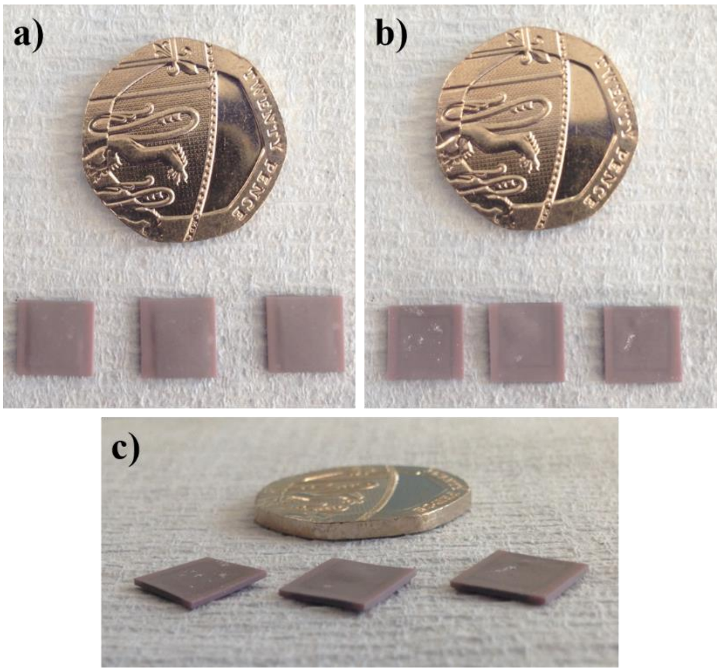

Figure 6. 8 The surfaces of sintered samples, using a bed of calcined alumina powder, showing a) the top surface, b) the bottom surface in contact with the powder and c) a shallowed angle of the bottom surface. A twenty pence (20p) sterling coin is used as a reference of scale.

6.2.3 SEM Analysis of the MLCC Cross-Section

Cross sections of the devices were examined under SEM, using SEI, BE and EDS to determine whether there is good layer adhesion, observe any causes of any delamination and whether there was evidence of reaction between the electrodes and the dielectric.

3-Layers MLCC

The cross-section of a 3-layer MLCC is displayed in figure 6. 9, where a) shows all 3 overlapping electrodes, b) shows one side of the overlapping edges, c) is from the end-terminals of the device, where the external Au terminal is in contact with the internal Pt electrode and d) shows a larger magnification of the interaction between the dielectric material and the internal electrode. Figure 6. 9 reveals large amounts of porosity within the dielectric, with an average pore sizes of a ~5μm in diameter. There are also examples of brighter-contrast regions, indicated by a broken circle in figure 6. 9 b), which are present throughout the sample.

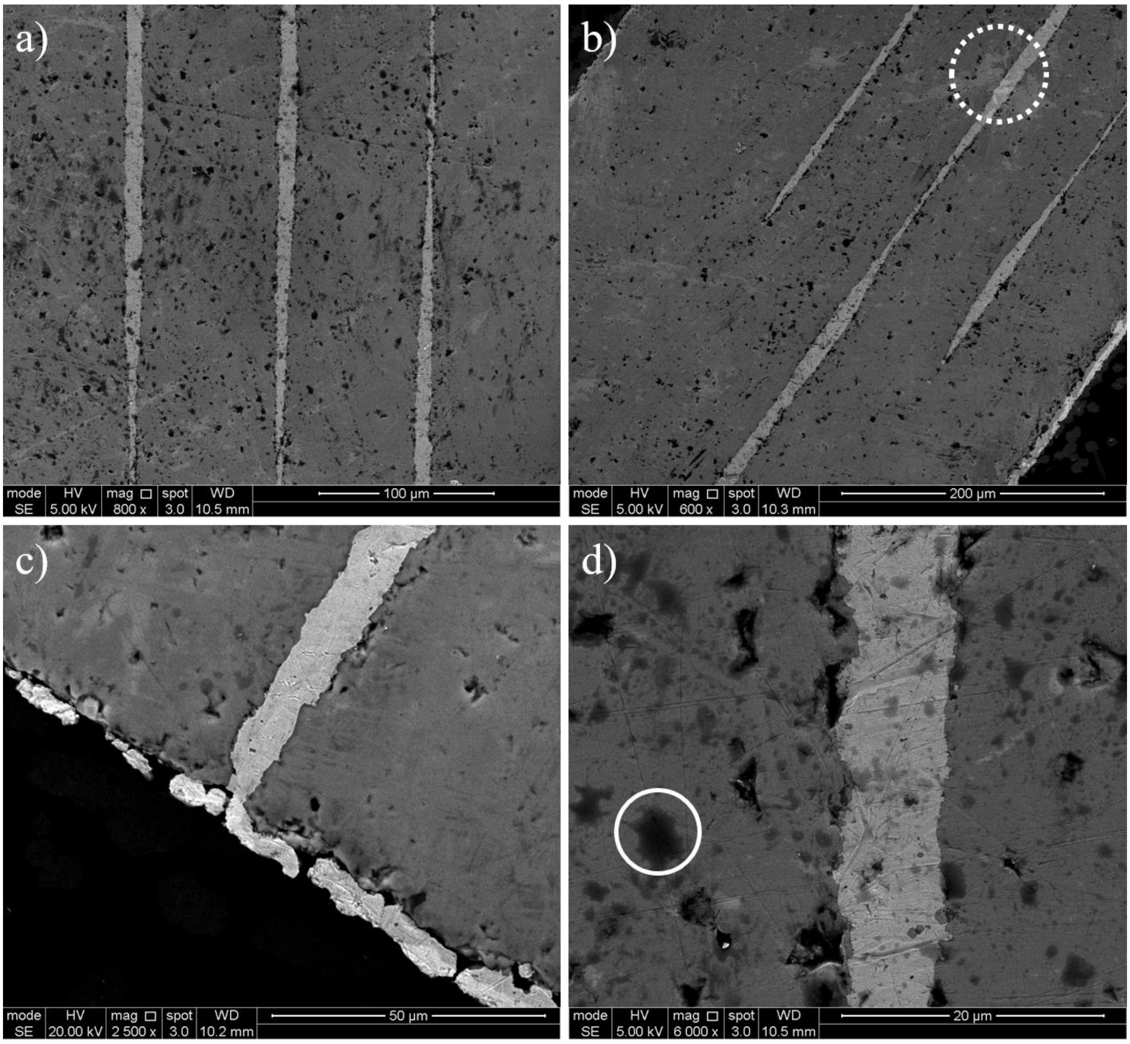

Figure 6. 9 SEM analysis of the cross-section of a 3-layer CTLNT + 4wt% BBO device, where a) is taken of the middle of the device, where all 3 layers are fully overlapping, b) shows the overlapping edge and brighter contrast regions (broken circle), c) is taken at one of the end-terminals, where the Au external terminal connects with the internal Pt electrodes and d) is a closer view of the boundary between the internal Pt electrode and the dielectric, showing small pores and liquid-phase (circled).

The phase contrast of the SEM images is similar to that of the ceramic pellets (Chapter 4) but the number of pores present are larger in number within the MLCC sample. This is likely an artefact of the binder burnout where gasses have formed pockets which were, then, not fully sealed upon sintering. Figure 6. 9 c) confirms that there is sufficient contact between the Au external conductive terminal and the Pt internal electrode. Finally, figure 6. 9 d) shows evidence of darker regions, similar to the 'pools' of liquid-phase found in chapter 4, presumably the same B-rich liquid-phase. Figure 6. 9 d) also shows excellent adhesion and contact between the dielectric and electrode, despite the presence of pores along some of the boundary. In addition, there appears to be no reaction, or transference of material between the two components. Figure 6. 9, however, presents a non-uniform thickness of the internal electrode throughout the sample. This is likely due to issues with the screen-printing process, rather than the firing and sintering.

EDS was then conducted on the surface of the cross section of the 3-layer MLCC to confirm the presence of the expected elements. Figure 6. 10 shows a BE image of the area from which the corresponding EDS analysis was conducted. The EDS data confirms the presence of only B, Ca, O, Ti, Nd, Bi and Pt.

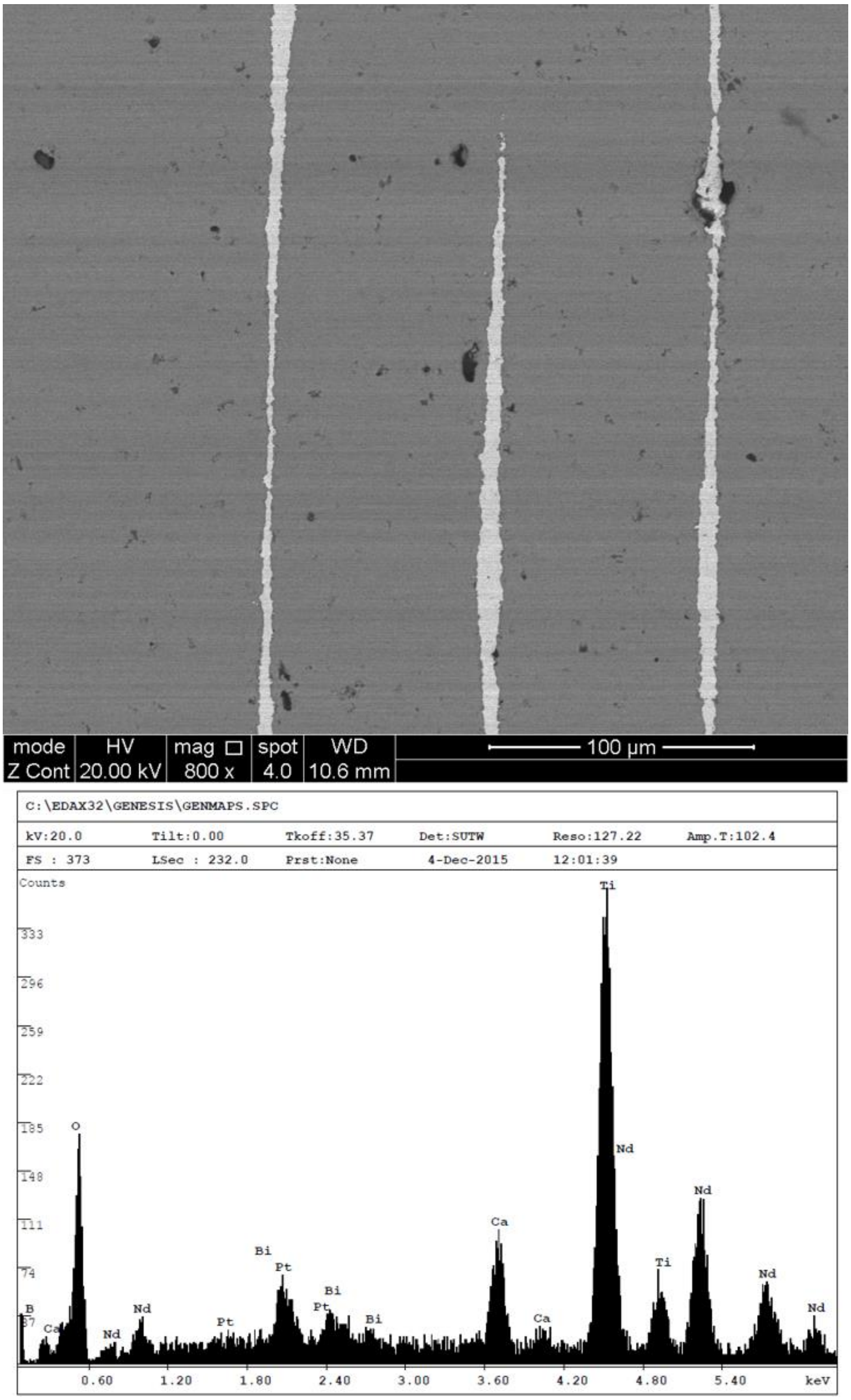

mode	HV	mag ☐	spot	WD
Z Cont	20.00 kV	800 x	4.0	10.6 mm

```
C:\EDAX32\GENESIS\GENMAPS.SPC
kV:20.0        Tilt:0.00        Tkoff:35.37      Det:SUTW         Reso:127.22      Amp.T:102.4
FS : 373       LSec : 232.0     Prst:None          4-Dec-2015     12:01:39
```

Figure 6. 10 SEM BE image of a region of a 3-layer cross section (above), with corresponding EDS analysis of the same region (below).

To prove that no reaction, or exchange of materials, took place during sintering, an EDS line scan analysis was conducted across the cross-section (figure 6. 11), as well as EDS mapping to show the overall distribution of elements (figure 6. 12). The line scan in figure 6. 11 showed troughs in the presence of O, Ca, Ti and Nd in the exact locations of Pt electrodes and Au contact, suggesting only limited reaction if any.

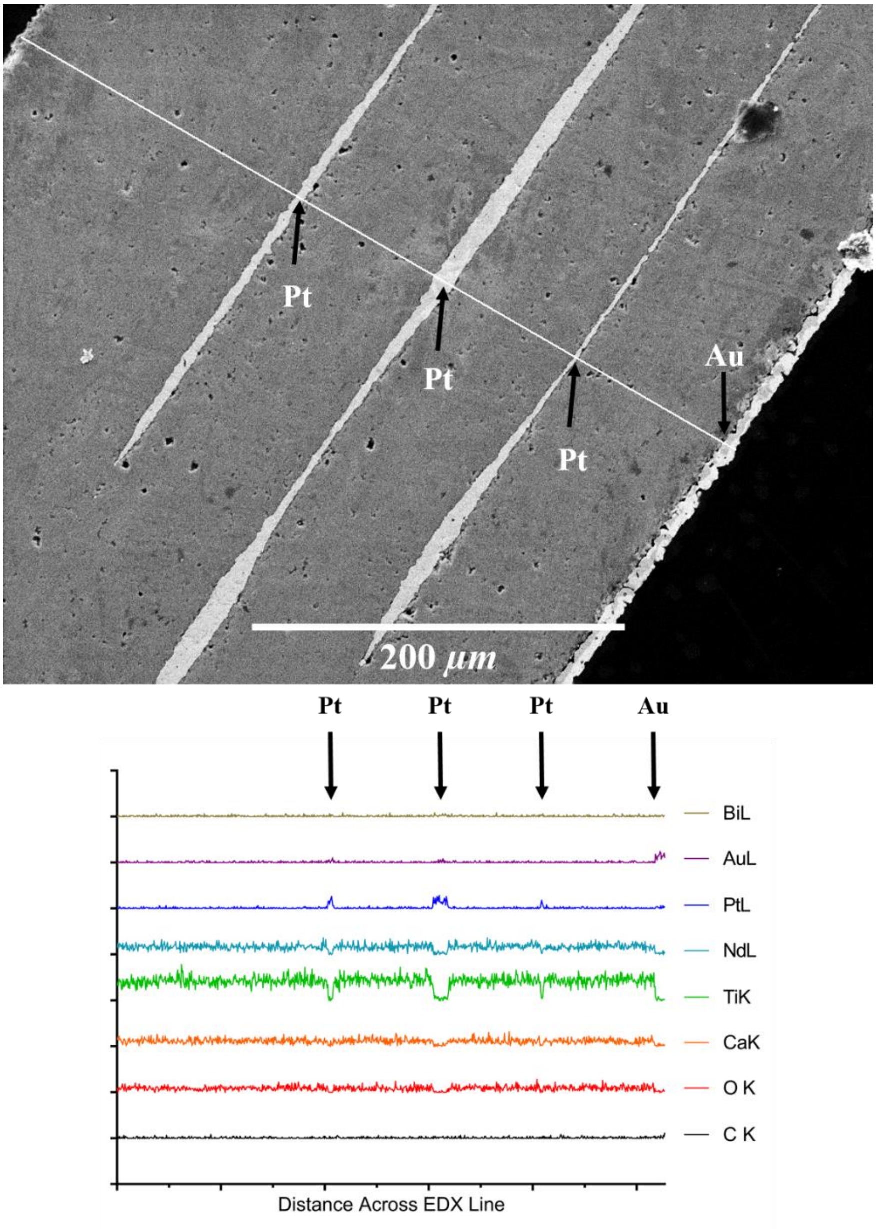

Figure 6. 11 SEM image (top) containing a line EDS analysis (bottom) across the cross-section of a 3-layer MLCC device. EDS analysis confirms dips in dielectric elements where there are peaks in electrode and external terminal elements (arrowed).

Similar findings were obtained by EDS mapping, as shown in figure 6. 12. The location of the mapping is shown by the BE image in the upper left corner of figure 6. 12. Pt is confined to the electrode layers with other elements homogenously distributed throughout the remainder of the sample.

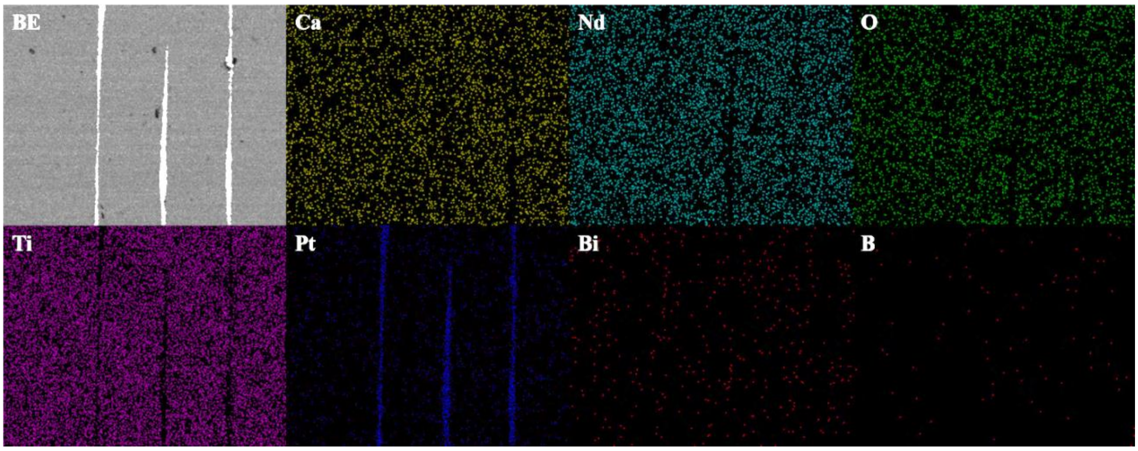

Figure 6. 12 EDS mapping of elements, acquired over 15 minutes, at the same location of figure 6. 10, showing distinct regional differences and no apparent mixing between the dielectric material and the internal electrode. The top left image is a BE image of the mapping location. The other images show the location of each element, indicated by the elemental name in the top left corners of each image, represented by individual 'dots'.

4-Layer MLCC

The cross-sections of two 4-layer MLCC samples were imaged under SEM SEI and BE imaging. Figure 6. 13 was taken of a 4-layer sample with no apparent delamination, which underwent the 64-hour firing and sintering process, while the figure 6. 14 was taken of a 4-layer sample which was sintered following the original firing and sintering route of 54 hours.

The 4 images in figure 6. 13 are from two locations, each taken under SEI and BE imaging, where a) and b) are SEI and BE images, respectively, of the centre of the 4-layer sample, showing full overlapping of the internal electrodes as well as uneven electrode thickness. Figure 6. 13 c) and d) are SEI and BE images, respectively, of a magnified view of the electrode/dielectric interaction. In comparison with the 3-layer sample, there are far fewer pores as a result of the longer burnout time applied to this sample, allowing more gas to escape the sample before the sample is densified.

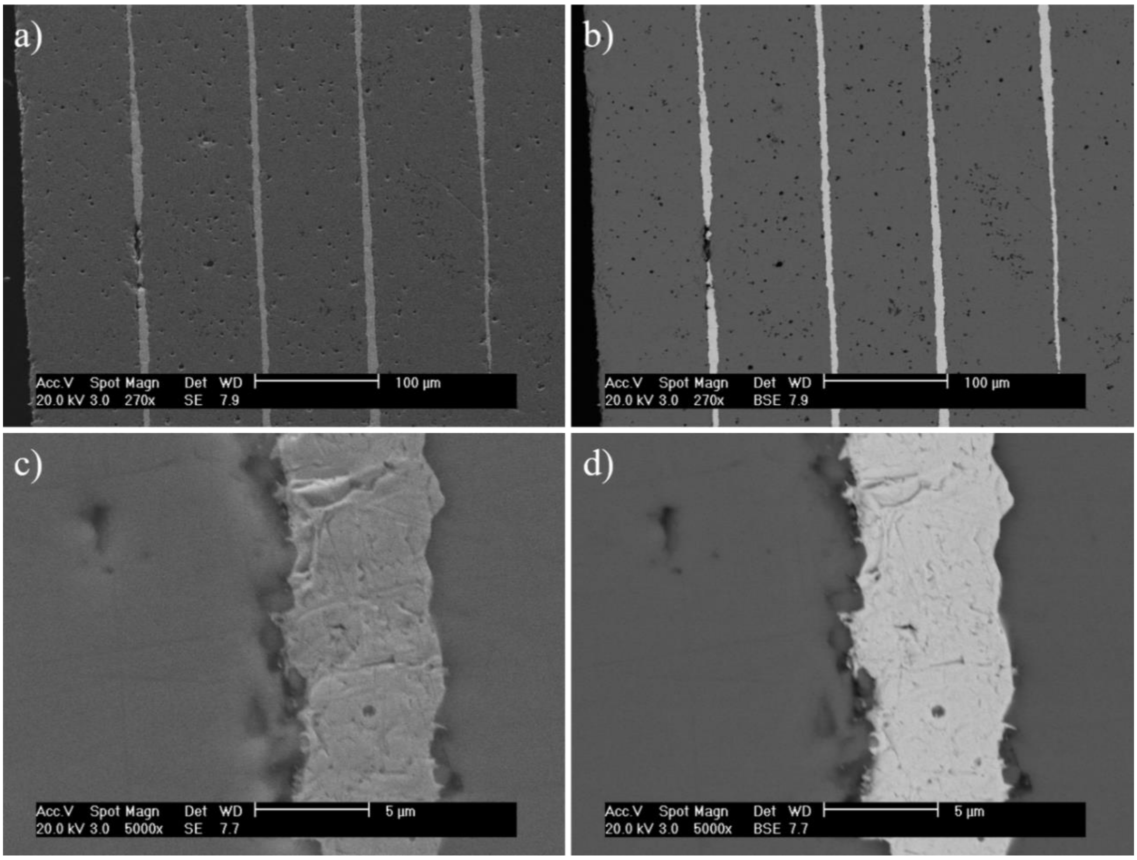

Figure 6. 13 SEM images of the cross-section of a 4-layer MLCC device of a) the middle of the sample under SEI, with b) corresponding BE image, and c) a closer view of the boundary between electrode and dielectric under SEI, with d) corresponding BE image. Both BE images show distinct differences between materials, with no mixing.

The contact between the dielectric and the electrodes has improved, with respect to the 3-layer sample, since fewer pores are observed at the dielectric/Pt interface. Figure 6. 13 c) and d) both show strong integration and large surface contact between the CTLNT and electrodes, as well as no evidence of reaction.

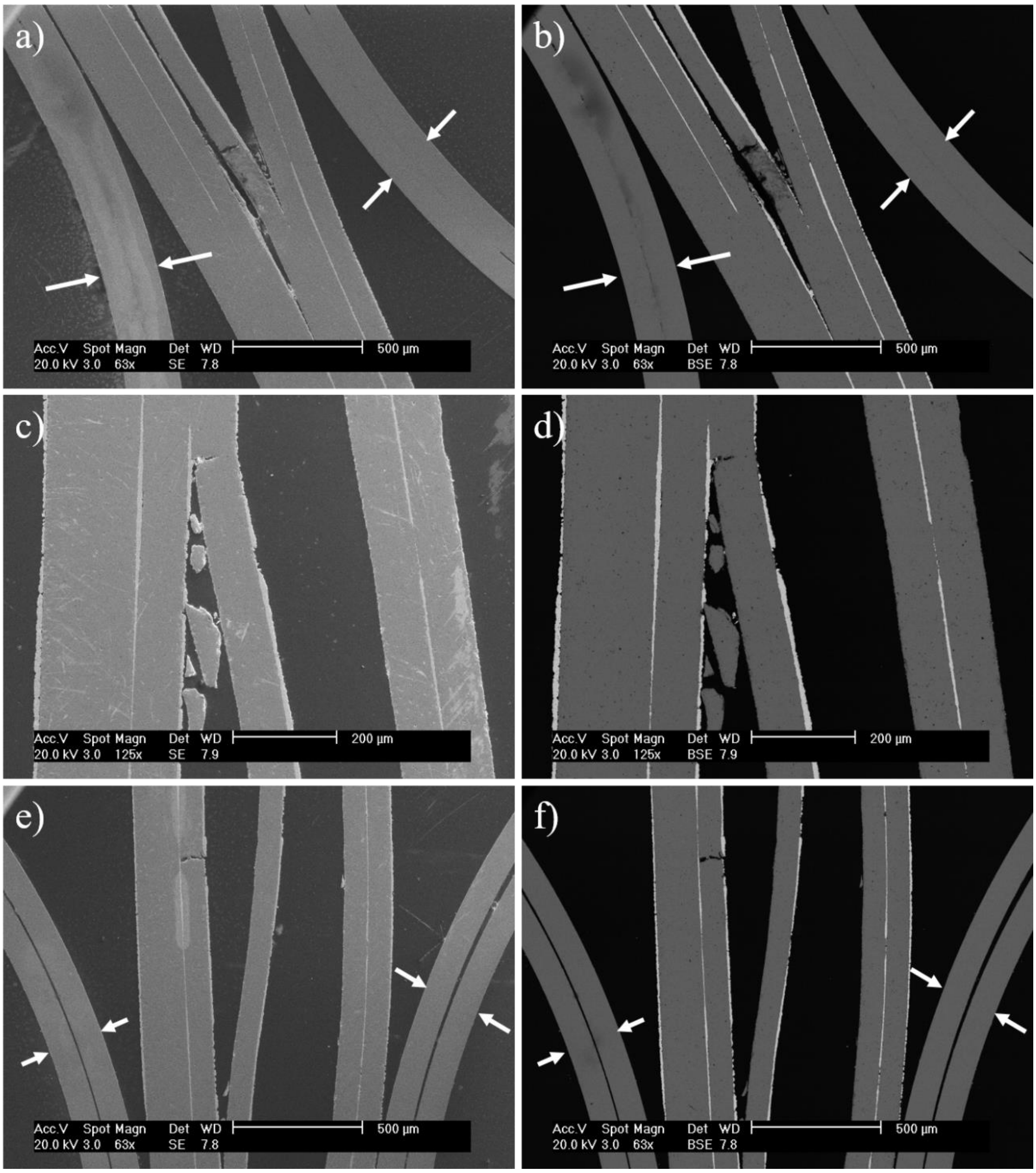

Figure 6. 14 SEM cross-section images of a 4-layer MLCC which has been sintered following the original, shorter sintering route, resulting in substantial delamination, due to gas expansion during heating, within the central layers. A) and b) are SEI and BE images, respectively, of the overlapping edge of the electrodes, c) and d) are SEI and BE images, respectively, of the other opposite overlapping edge, and e) and f) are SEI and BE images, respectively, of the middle of the sample. The structures between the arrows are stainless steel coils used to mount the MLCC samples vertically for SEM imaging.

Figure 6. 14 shows SE and BE images of a 4-layer MLCC sample which underwent the shorter, 54 hour firing and sintering process, taken at 3 different locations along the cross-section. Figure 6. 14 a) and b) were taken at the edge of the electrode overlap, showing initial delamination, c) and d) were taken over the other electrode overlap edge, and e) and f) were taken across the centre of cross-section. The curved structures located between the arrows indicated within figure 6. 14 are stainless steel coils which were used to mount the MLCC samples vertically. From figure 6. 14, the delamination has occurred in the centre of sample, between the centre-most electrode

layers, suggesting that, as the number of Pt layers increased, not enough time was allowed during binder burnout for gas to escape. Examples of cracking can be seen in figure 6. 14 a), b), e) and f). As layers delaminate, the internal Pt electrode tends to remain on one layer, suggesting greater adhesion between the layer upon which the electrode was screen-printed in comparison with the subsequent layer.

Figure 6. 15 confirms that there is good contact between the external Au terminals and the internal Pt electrodes. Figure 6. 15 a) and b) shows excellent adhesion between the dielectric and the internal electrode, as well as the presence of B-rich liquid phase occupying two different pores, arrowed. There is also evidence, circled, of some brighter particles in the SEI in a) which exhibit dark contrast in the BE image b). However, since they are also present away from the sample in c) and have the same contrast as the SEM mounting resin in the BE image of d), they are likely residual resin particles from the polishing process.

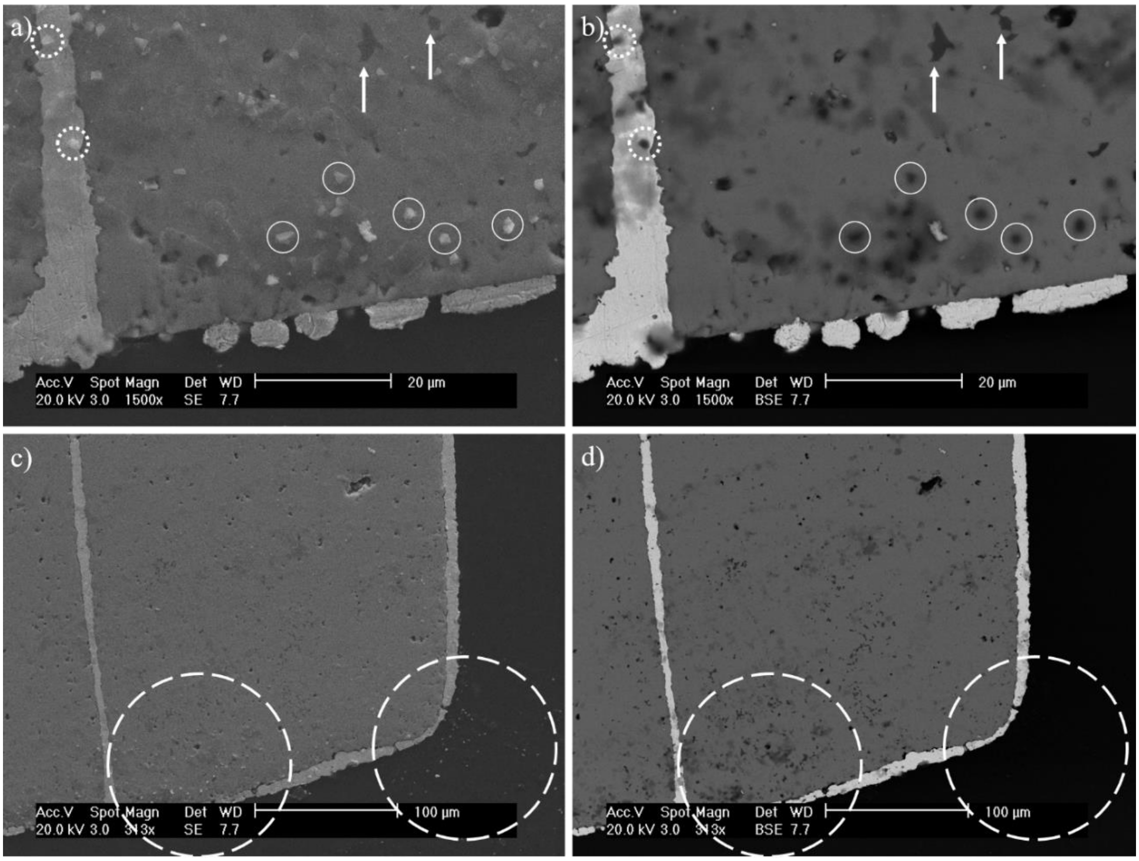

Figure 6. 15 SEM images of a 4-layer MLCC a) end-terminal, showing contact between the external Au terminal and the internal Pt electrode, taken under SEI and b) BE modes, and the same region taken at 313x magnification under SEI and d) BE imaging modes. The circled particles in a) and b) are likely particles of the resin used to mount the samples, present through probably inadequate cleaning during polishing, as they are present outside of the MLCC sample in c) and have the same contrast as the resin surrounding the sample in the d) BE image. Arrowed in a) and b) are regions of likely B-rich liquid-phase occupying pores within the sample.

5-Layer MLCC

The cross-section of a 5-layer MLCC sample, which underwent the 64-hour firing and sintering route, as well as the solvent wetting technique, is shown in figure 6. 16, where a) and b) are SE and BE images, respectively, of 5 electrode layers fully overlapping, and c) and d) are BE and SE images of the electrode/dielectric interface. The volume fraction of pores is similar to the 4-layer and less than that observed in the 3-layer sample. Clusters of pores, circled in figure 6. 16 a) and b), may contain liquid-phase since they exhibit a lighter contrast than observed for empty pores, which appear dark grey in the BE image. The arrows in figure 6. 16 a) and b) point to a series of pores on the right-hand side of the central internal electrode, suggesting that these areas may be precursors to delamination. This implies that the extended burnout time used for the 4-layer samples was too short for the 5-layer samples. Similar to the 3- and 4-layer samples, there is good contact between the CTLNT and the Pt electrode, with no evidence of reaction, figure 6. 16 c) and d).

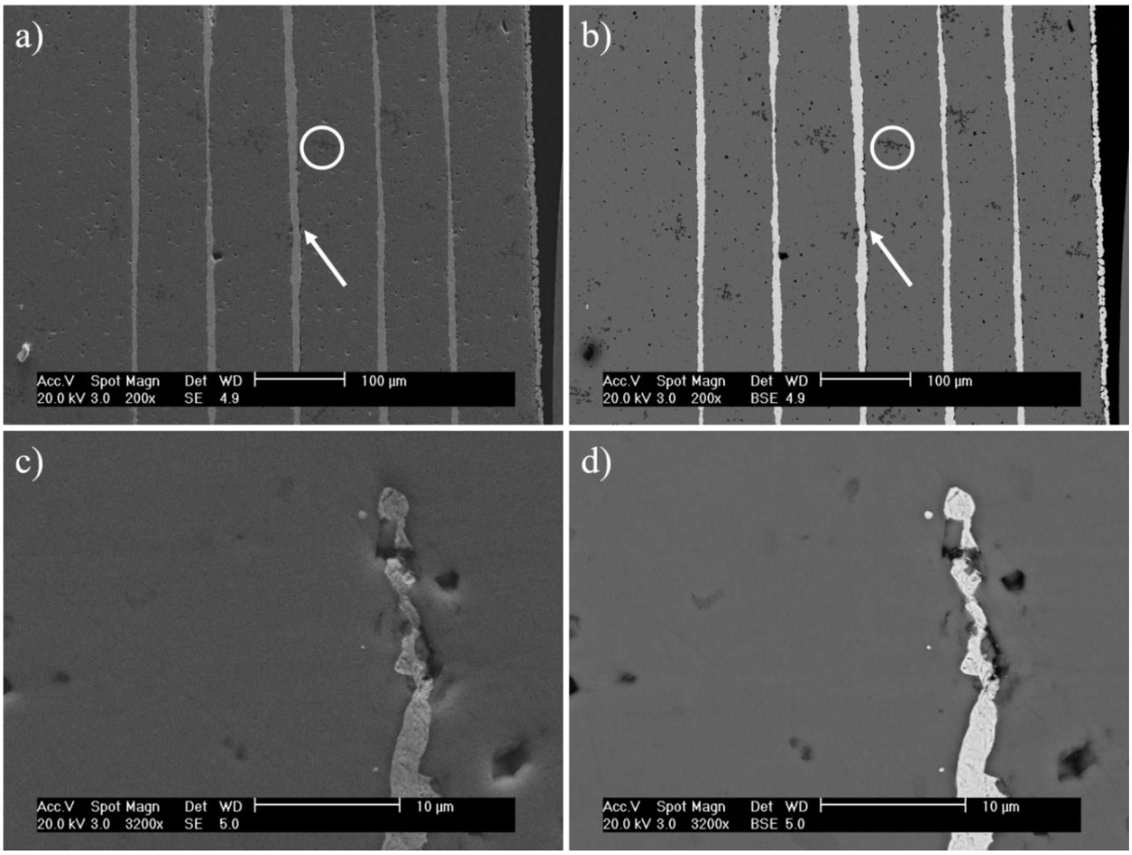

Figure 6. 16 SEM images of the cross-section of a 5-layer MLCC device of a) the middle of the sample under SEI, with b) corresponding BE image, showing the overlapping of all 5 layers and the presence of B-rich liquid phase within some pores (circled), and c) a closer view of the boundary between electrode and dielectric under SEI, with d) corresponding BE image. Both BE images show distinct differences between materials, with no mixing. There is marginal evidence of delamination of the third, middle, electrode due to a long line of pores located on the immediate right side of the electrode (arrowed).

SE and BE images of the end-terminals for the 5-layer MLCC sample are shown in figure 6. 17 a) and b), respectively, as well as c) SE and d) BE images of the edge of the electrode overlap. The end-terminals show only a small area of contact with the external Au terminal but since the image is a 2D section, it is very likely that there is a better quality of contact above, or below, the plane of the image. Figure 6. 17 c) and d) shows more evidence of pores which are occupied by a B-rich liquid phase in the BE image (circled), and empty pores which are black in the BE image (arrowed).

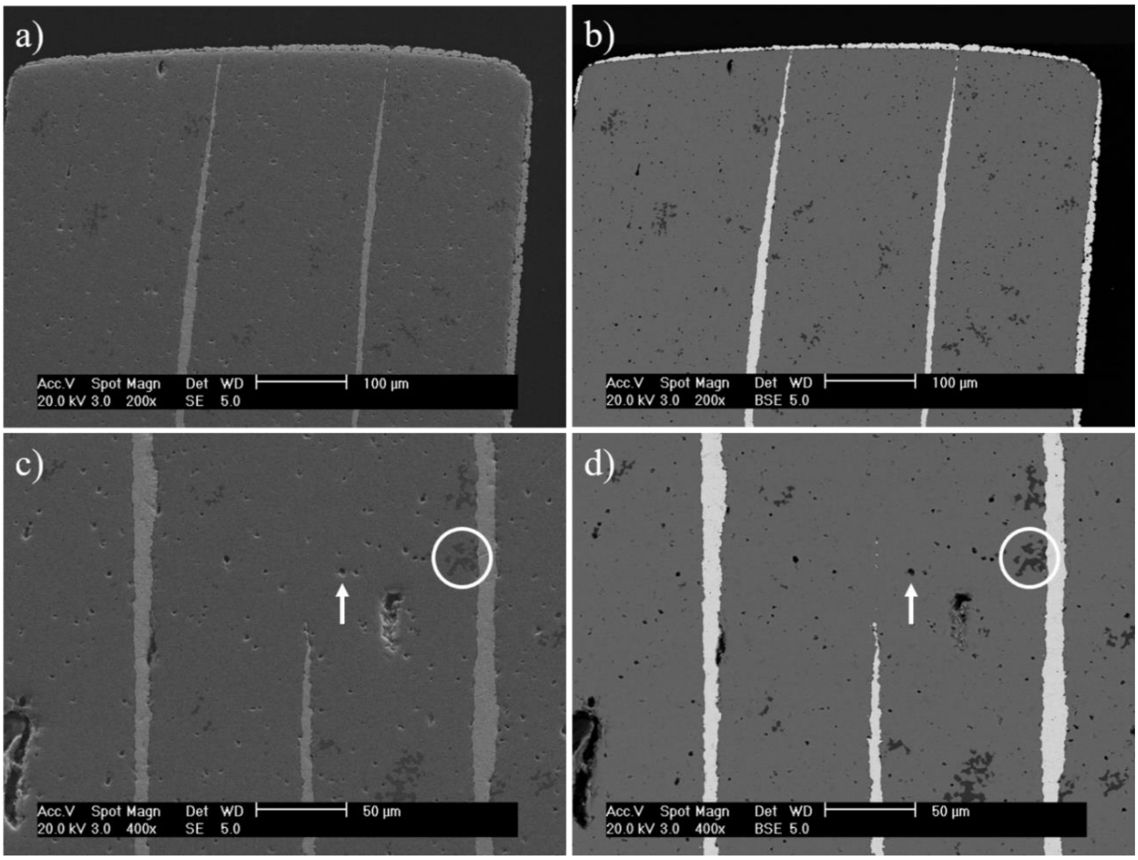

Figure 6. 17 SEM of the cross-section of a 5-layer MLCC of a) on of the two end-terminals under SEI, with b) corresponding BE image, and a closer view of the overlapping edge under a) SEI and d) BE imaging, showing the presence of a darker liquid phase (circled) filling-in some pores and how this differs from 'empty' pores (arrowed).

A sample of a 5-layer device which underwent the original 54-hour firing and sintering route, showing catastrophic delamination is displayed within figure 6. 18. Figure 6. 18 a) and b) are SEI and BE images of the same area, taken across the centre of the sample, respectively, and c) and d) are SE and BE images, respectively, of a different location on the sample. The delamination and cracking observed in the 5-layer sample is similar to that observed in the 4-layer sample but overall more severe. The catastrophic delamination in the 5-layer is due to the greater volume of binder and plasticiser to burn out. As a result, deformation due to delamination is more pronounced, producing elevated levels of cracking between layers. Within figure 6. 18, large sections of debris can be seen to have fallen between the layers.

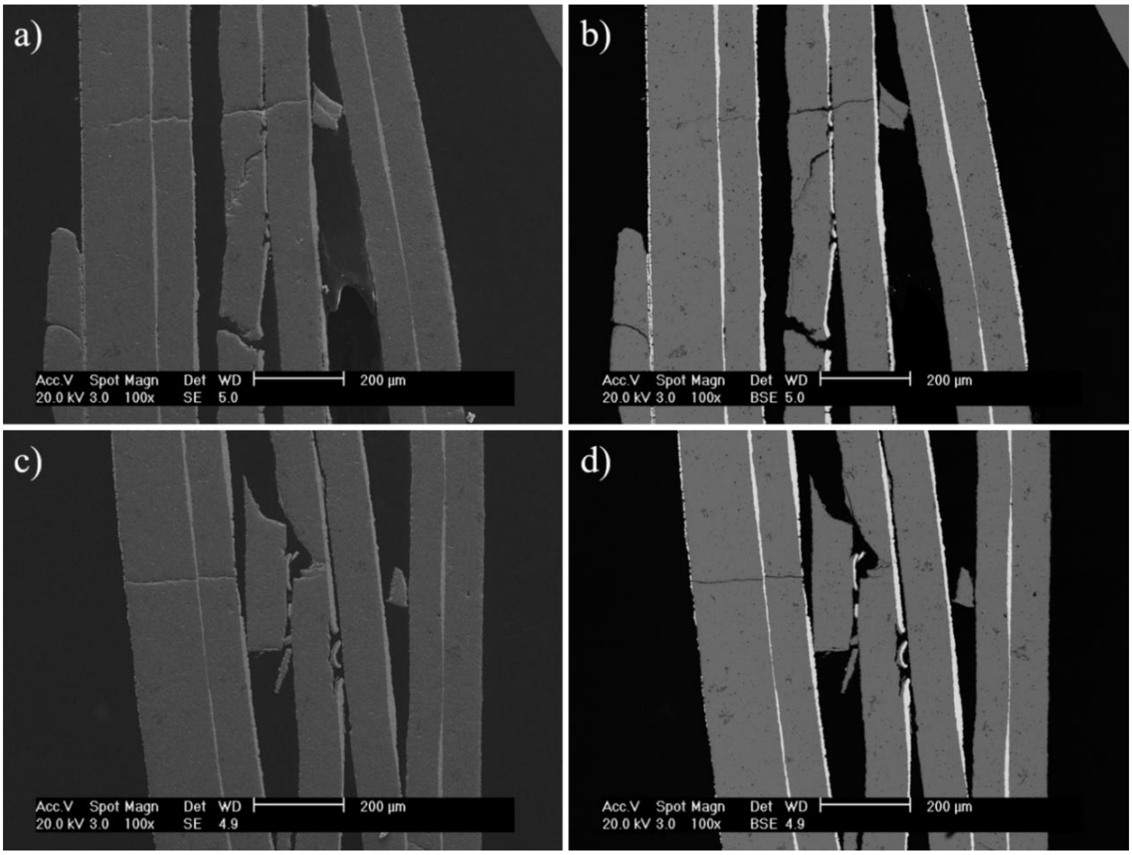

Figure 6. 18 SEM images of the cross-section of a 5-layer MLCC sample, showing substantial delamination and fracture within the centre of the sample, between the deepest layers. A) and c) are SEI of two different locations along the same sample, and b) and d) are the corresponding BE images, respectively.

As with the delamination of other samples, the internal electrode remains attached to only one side of each of the layers, suggesting there is greater adhesion between the two materials when the Pt electrode is screen-printed onto the surface. Further evidence for this phenomena may be observed in figure 6. 16 a) and b), where there is a line of pores on only the right-side of the middle electrode. Figure 6. 19 a) and b) are SE and BE images which illustrates that a small section of warped electrode is still attached to the dielectric only on one side.

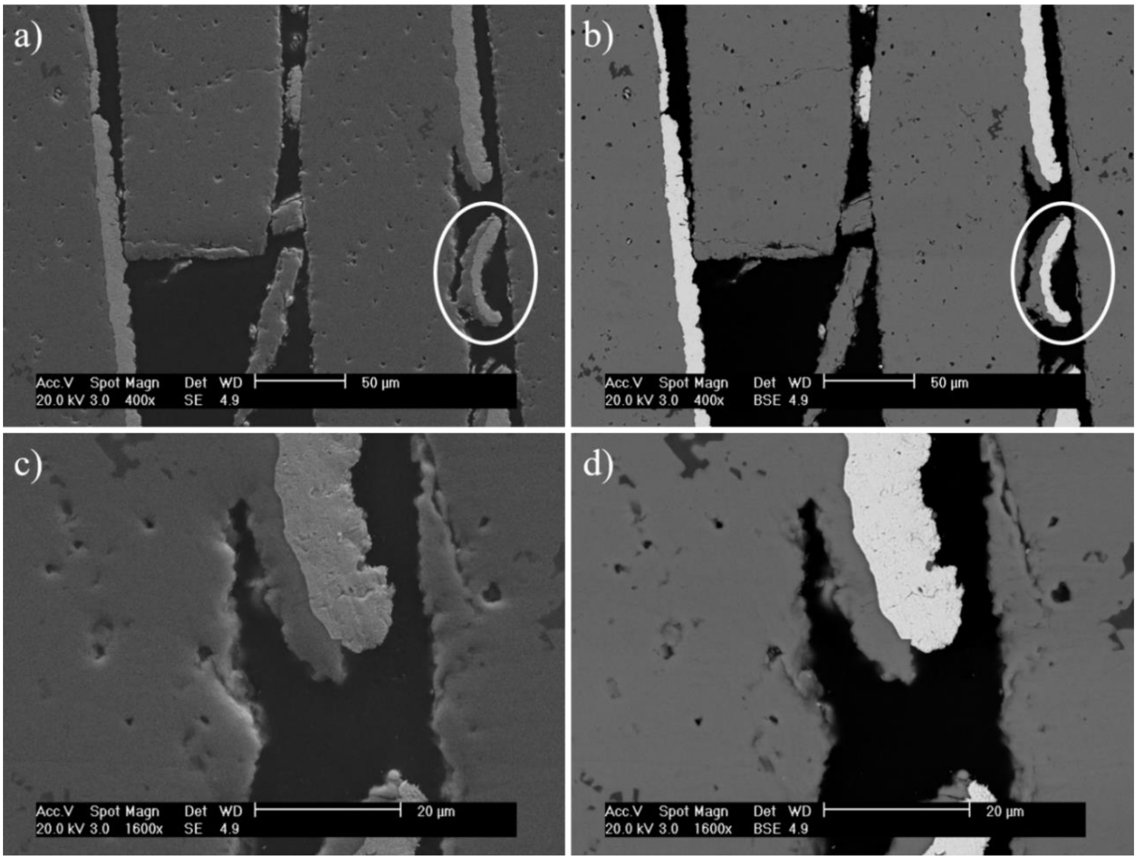

Figure 6. 19 A closer view of a portion of figure 6. 18 c) and d), of a 5-layer MLCC, under SEI and BE imaging. Pictured in a) and b), under SEI and BE respectively, is a warped section of electrode, with dielectric still attached to one side (circled), and c) is a closer view of the upper part of the circled region, with d) corresponding BE image. Adhesion between electrode and dielectric appears particularly strong with the layer the electrode was screen-printed upon, rather than the layer stacked onto it.

Through analysis of the cross-section of the 3, 4 and 5-layer MLCC samples, it can be seen that resolving the issues listed in section 6.2.1 and 6.2.2 has yielded acceptable quality MLCC devices for the CTLNT system. The results presented in this section confirm that, as layer numbers are increased within the samples, more time is required to burn-off the plasticiser to avoid delamination. Additionally, wetting of each layer with a solvent has positive effects in reducing delamination over simply pressing the layers together.

The apparent ‘weakness’ in adhesion on one side of the layers may be a contributing factor to some of the delamination observed in the samples. It is implied that this preference is a result of the application, and drying, of the Pt electrodes as a paste (which is suspended as a fluid in a solvent), which then dries and fuses more strongly with the substrate layer.

6.3 Electrical Characterisation Results

To characterise the electrical properties of the fabricated MLCC devices, LCR measurements were performed to acquire changes in ε_r, capacitance and dielectric losses with respect to temperature, at 5 different frequencies followed by impedance spectroscopy, which measures inductance, capacitance and resistance over a sweep of frequencies. Both tests were conducted with an applied voltage of 100 mV.

From equation 6.2 (p. 170), and using dimensions of the internal electrode of a sintered sample, which were exposed (figure 6. 20), it is possible to produce an estimate of the ideal capacitance of the CTLNT MLCC devices. This value is considered ideal as the equation assumes a 100% dense sample, with no pores of any kind, perfectly flat and 100% contact between the dielectric and electrode. Furthermore, the equation assumes that each sample has sintered equally, into the same dimensions, and that the same area of overlap is present in all samples. As such, the quality of the MLCC device can be considered to be higher, if its values more closely resemble the 'ideal' value.

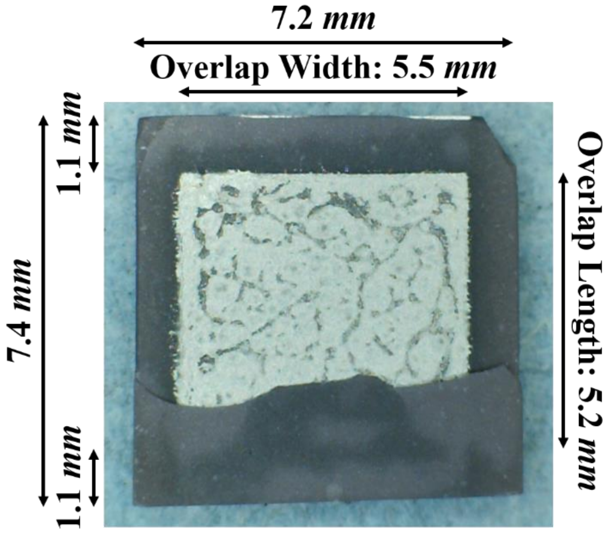

Figure 6. 20 Apparent dimensions of a sintered 4-layer MLCC device, where the top layer of dielectric delaminated and fractured, exposing the internal Pt electrode, from which dimensions of the area of overlap could be measured.

6.3.1 LCR Measurements

3-Layer

LCR results for a 3-layer MLCC sample are shown in figure 6. 21 which reveals the temperature dependence of ε_r (top left), capacitance (top right) and dielectric loss, tanδ, (bottom), taken at 5 different frequencies from 1 kHz to 1 MHz. The LCR results shows a clear tendency for increased temperature stability with increased frequency, with 1 MHz being the most stable. This is, perhaps, unsurprising as the base material, CTLNT, was originally designed to be a microwave resonator, operating in the GHz frequency range. Nonetheless, there is promising temperature stability of ε_r and capacitance from as early as 100 kHz, although the τ_C of the 1 MHz frequency, the most stable capacitance, is +988ppm/°C between 23-110°C, and +746ppm/°C between 23-60°C. The frequency exhibiting acceptable levels of dielectric loss is the 1 MHz frequency, where tanδ is below 0.1 over the temperature range.

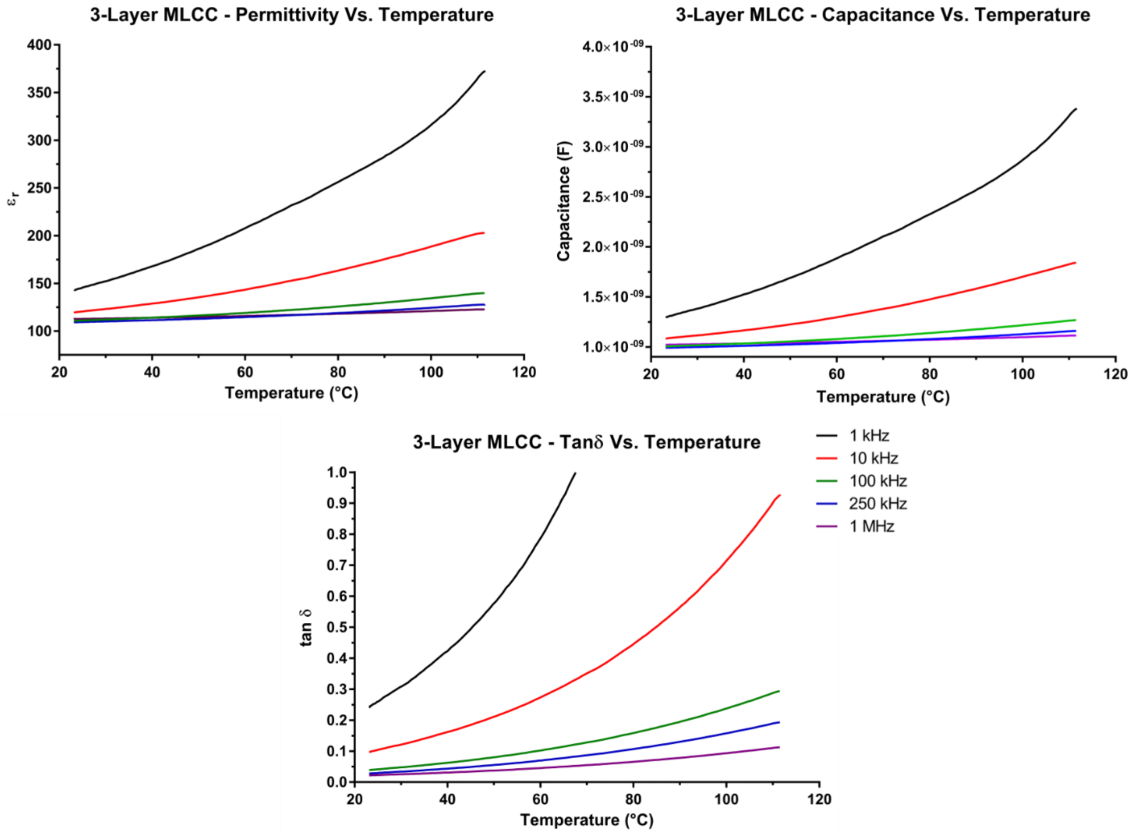

Figure 6. 21 LCR temperature sweep measurements of a 3-layer MLCC, at 5 different frequencies from 1 kHz to 1 MHz, showing results for the temperature dependence of ε_r (top left), capacitance (top right) and tanδ (bottom), at different frequencies.

4-Layer

The LCR results for a 4-layer MLCC sample are displayed in figure 6. 22, which shows the temperature variation of ε_r (top left), capacitance (top right) and tanδ (bottom), at 5 different frequencies, from 1 kHz to 1 MHz. The electrical properties become more stable as the operating frequency is increased but only 1 MHz gives tanδ < 0.1. Between the 3 and 4-layer samples, the 3-layer sample had overall larger ε_r values, while the overall capacitance of the 4-layer sample was greater. However, the τ_C at 1 MHz is +993ppm/°C between 23-100°C, and +761ppm/°C between 23-60°C is larger than the 3-layer sample.

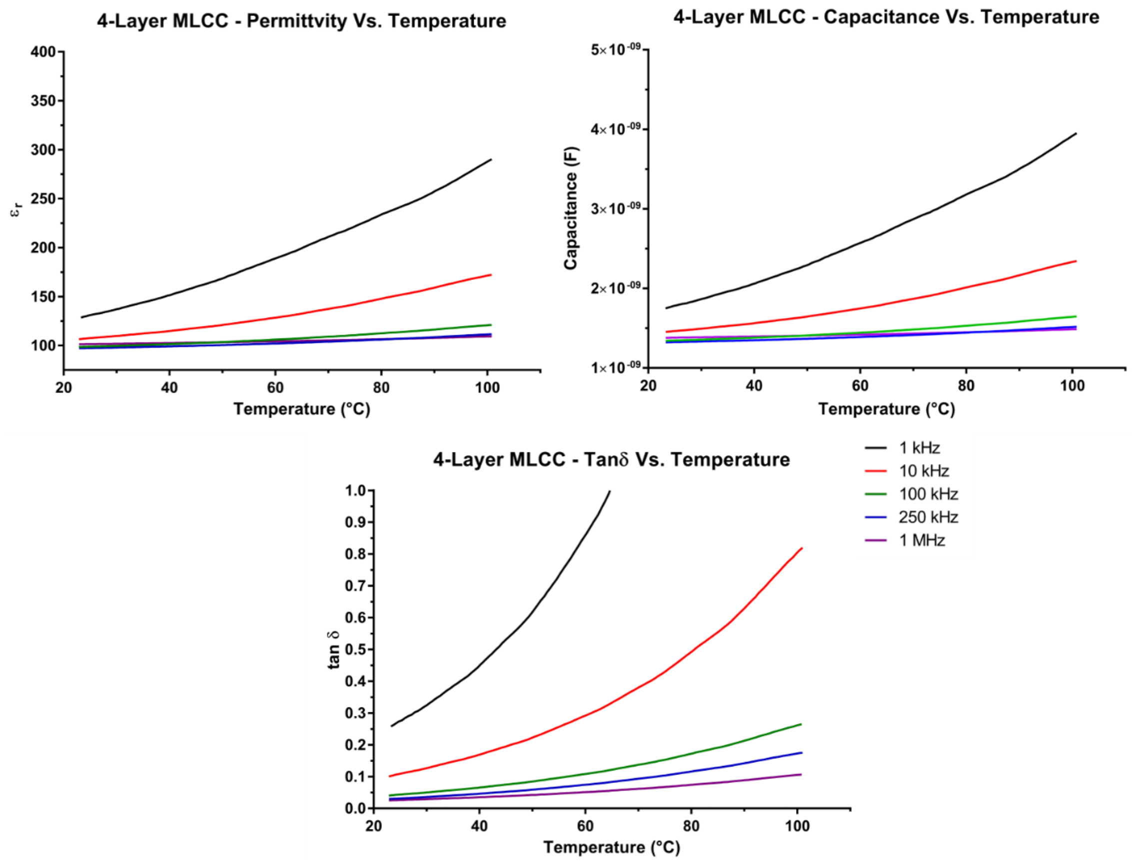

Figure 6. 22 LCR temperature sweep measurements of a 4-layer MLCC, at 5 different frequencies from 1 kHz to 1 MHz, showing results for the temperature dependence of ε_r (top left), capacitance (top right) and tanδ (bottom), at different frequencies.

5-Layer

The LCR results of a 5-layer MLCC sample are displayed in figure 6. 23, showing the temperature dependence of ε_r (top left), capacitance (top right) and tanδ (bottom), at 5 different frequencies, from 1 kHz to 1 MHz. Again, as the frequency was increased, the temperature variation of each electrical property reduced. The overall ε_r of the 5-layer sample was lower than the 3 and 4-layer MLCC samples, while the capacitance of the sample, regardless of frequency, was greater than for the 3-layer sample, but lower than the 4-layer sample. From the SEM images of the cross-section of the samples in section 6.2.3, it was suggested that the 5-layer sample was experiencing some minor delamination, despite the longer firing time and the use of the new stacking method, which could be having an impact on the overall properties of the 5-layer sample in figure 6. 23. This is reflected in the dielectric losses of the 5-layer sample, which were greater across all frequencies. Irrespective, the 5-layer sample has greater temperature stability of ε_r down to 10 kHz. While ε_r appears more stable, the τ_C of the 5-layer sample is +1946ppm/°C between 28-148°C, and +1089ppm/°C between 28-60°C, the largest of the 3 different devices.

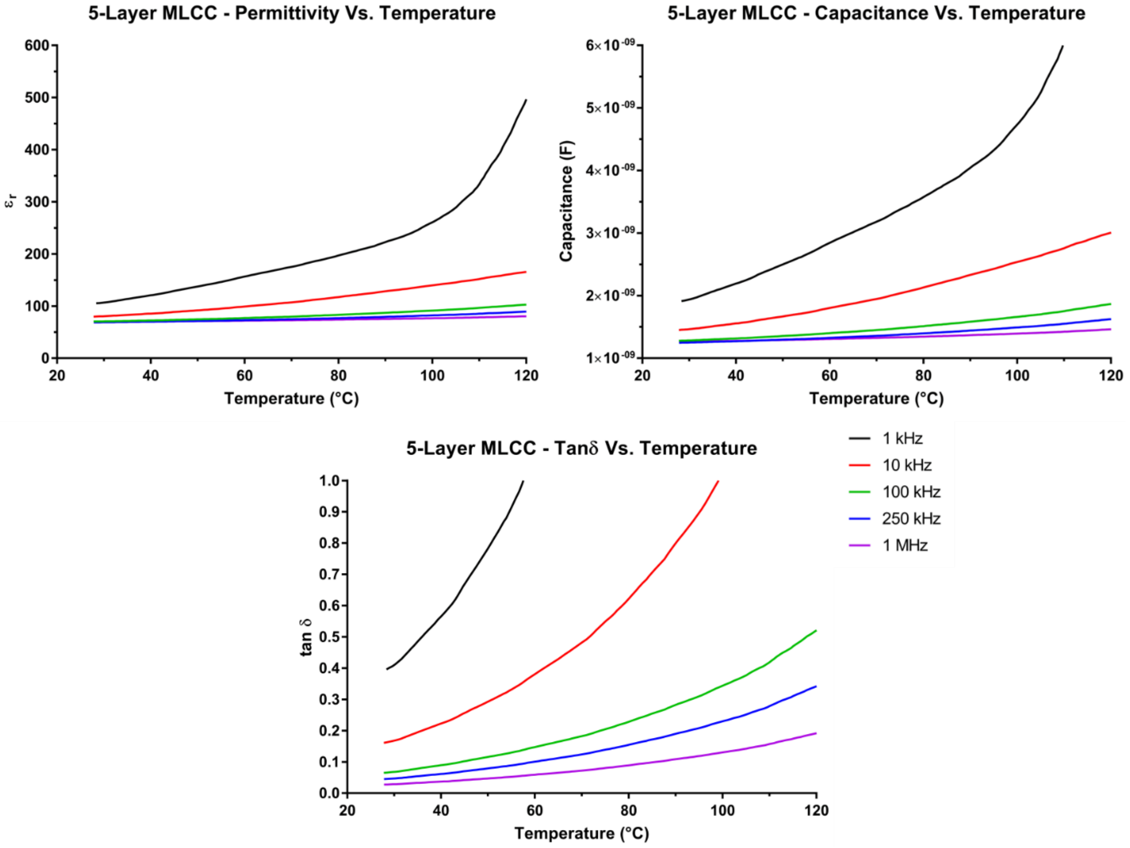

Figure 6. 23 LCR temperature sweep measurements of a 5-layer MLCC, at 5 different frequencies from 1 kHz to 1 MHz, showing results for the temperature dependence of ε_r (top left), capacitance (top right) and tanδ (bottom), at different frequencies.

The LCR results of a delaminated 5-layer MLCC sample are displayed in figure 6. 24, to illustrate the impact of delamination, where the temperature dependence of ε_r (top left), capacitance (top right) and tanδ (bottom), at the 5 different frequencies, from 1 kHz to 1 MHz, are presented. The rate of change of each parameter is very similar to the laminated 5-layer sample in figure 6. 23 but there is a marked difference between ε_r and capacitance between the two samples. ε_r for the delaminated sample is lower than the laminated sample, and as much as half the level of the 3-layer MLCC sample. Consequently, capacitance has likewise reduced, compared to its laminated counterpart.

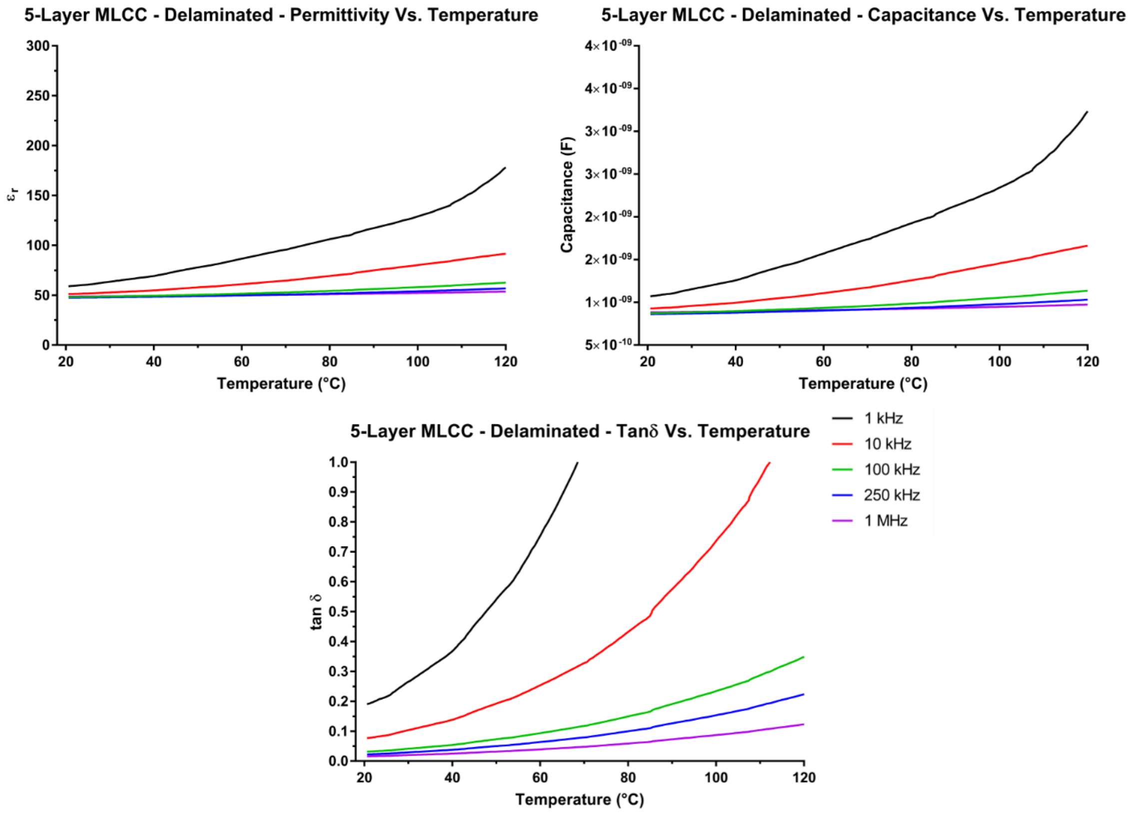

Figure 6. 24 LCR temperature sweep measurements of a delaminated 5-layer MLCC, at 5 different frequencies from 1 kHz to 1 MHz, showing results for the temperature dependence of ε_r (top left), capacitance (top right) and tanδ (bottom), at different frequencies.

Figure 6. 25 shows a direct comparison between the 1 MHz frequency data of each sample tested, including a single-layer CTLNT + 4wt% BBO pellet sample, with Au external electrodes where the temperature variation of ε_r, capacitance and tanδ are displayed in the top left, top right and bottom of the figure, respectively. Theoretically, the ε_r values should remain constant, regardless of the number of layers present, since the dielectric used has not changed, however, as can be seen in figure 6. 25, ε_r decreases as the layer number increases. This is likely due to porosity and acuteness of delamination present within the samples. Since the pellet and 3-4-layer samples have similar ε_r values, figure 6. 25 lends further credence to small levels of delamination being present within the 'laminated' 5-layer sample.

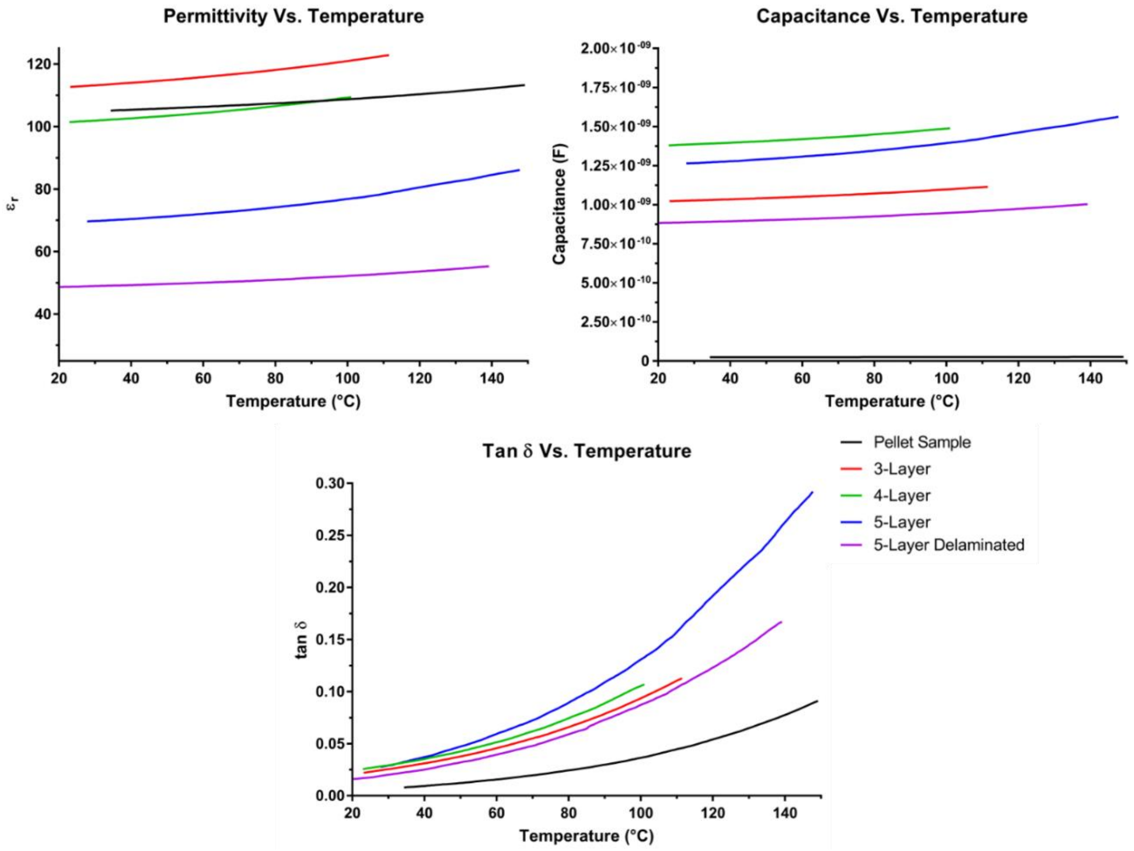

Figure 6. 25 LCR temperature sweep measurements, comparing the 1 MHz frequency data of all samples, including measurements taken of a single-layer CTLNT + 4wt% BBO pellet sample, showing results for the temperature dependence of ε_r (top left), capacitance (top right) and tanδ (bottom), between room temperature and 150°C.

Despite the reduction in ε_r, increasing the number of layers within a sample appears to have the desired effect of increasing the capacitance of the MLCC devices. The severely delaminated 5-layer sample has a lower capacitance than the 3-layer sample. The capacitance of the single-layer pellet sample is much lower than the MLCC samples, however this is likely due to the dimensions of the sample, where the thickness of the dielectric is much larger than the MLCC samples, compared with the surface area of the electrodes. As for C, this appears to grow with increasing layer number and increasing temperature, however a larger sample size may be required, including samples with much larger layer numbers so that the data is more comparable to existing devices within industry.

As it stands the fabricated devices studied in this chapter have properties of class 1 MLCC devices labelled as "M8J", in the EIA classification standard, or "P1000" in the EIC classification standard. It should be noted, however, that the typical operating frequencies of class 1 MLCC devices are much higher than the available testing conditions, thus these results are promising as they show increased stability with increasing frequency. Finally, as the layers increase in number, so too does the dielectric loss. This is most likely due to greater number/volume of interfacial regions, a major cause of loss at low frequencies.

6.4 Conclusions

Following investigations into the use of CTLNT + $x$wt% BBO as a new, high-end, temperature stable microwave resonator, CTLNT + 4wt% BBO was used and fabricated into a multilayer ceramic capacitor, using platinum internal electrodes, to illustrate its potential as a temperature stable, class 1 C0G/NP0 MLCC device. In this chapter, a preliminary study into MLCC devices consisting of 3, 4 and 5 internal electrode layers were fabricated and tested.

Initially, the fabrication of the MLCC devices followed the conventional method outlined by Pan and Randall [7]. Problems arose in the form of layer delamination in the 4 and 5-layer devices, and material sticking to the Pt foil used to fire and sinter the samples upon. A mixture of altering the stacking process with inter-layer solvent wetting, increased burnout times and swapping the sintering contact surface from Pt to calcined alumina resulted in uniform MLCC devices, with case sizes: EIA ‘2928’, IEC ‘7472’. This was confirmed through the analysis of the cross-section of the MLCC devices which saw a marked improvement in densification and reduced delamination. The 5-layer device however, still showed evidence of partial delamination, suggesting an even longer burnout time was required for the 5-layer sample.

SEM analysis of the cross section revealed that, while there was sticking to the Pt foil used during sintering, no significant chemical reaction was observed between the CTLNT + 4wt% BBO dielectric and the Pt internal electrode. There was, overall, very good contact adhesion between the two materials, creating a large contact area. However, analysis of the cross-section revealed two further, potential issues with the devices. Firstly, if there are trapped gasses unable to escape during the firing process, these gases tend to accumulate on the surface of the electrode, causing a concentration of pores around the electrodes and, thus, reduced contact between the dielectric and the electrode. If left in large enough quantities, thermal expansion due to raising the temperatures up to sintering temperatures will increase the size of the pores or lead to delamination. Secondly, the adhesion strength appeared to be stronger with the layer the electrode was screen-printed onto, increasing the risk of delamination from mechanical stresses as a result of sintering.

Electrical characterisation results revealed that the capacitance of the devices do tend to increase as layer number increases, as expected. They also corroborate with the SEM results showing lower performance in the 5-layer samples compared with the 3 and 4-layer samples, due to mild delamination within the samples. LCR results showed increased temperature stability of all electrical properties as frequency increased. At larger layer numbers, temperature stability of ε_r

and τ_C appeared to improve at lower frequencies. However, increased dielectric losses were observed for samples with more layers and at lower frequencies due to a high volume of interfacial material.

Between the 3, 4 and 5-layer MLCC devices, the results suggest that increasing the number of layers in the devices would decrease temperature stability of capacitance (τ_C), despite the increase in the capacitance and volumetric efficiency of the devices. With regards to the temperature stability of capacitance of the devices at 1 MHz, the LCR results indicate a change of +988ppm/°C between 23-110°C, and +746ppm/°C between 23-60°C for the 3-layer device, +993ppm/°C between 23-100°C, and +761ppm/°C between 23-60°C for the 4-layer device and +1946ppm/°C between 28-148°C, and +1089ppm/°C between 28-60°C for the 5-layer device. This would give the fabricated CTLNT + $x$wt% BBO based MLCC devices an EIA class 1 classification of "M8J" and an IEC class 1 rating of "P1000". Note that delamination contributes to the decrease in the temperature stability of capacitance, and that an upper test frequency of 1 MHz may be too low for the material, since the operating frequency for class 1 devices is between 100 MHz and 30 GHz. These frequencies are, after all, the frequencies the CTLNT + 4wt% BBO material was originally designed for use as a MW resonator (about 4 GHz).

In conclusion, the CTLNT + $x$wt% BBO based MLCC devices may be a suitable class 1, C0G/NP0 capacitor candidate. However, more research will need to be conducted to fabricate larger layer number samples, to make more comparable devices with those existing on the market. Further development of 5+ layer devices to eliminate delamination, as well as creating devices with equal adhesion to both sides of the electrode with the dielectric is required. Critically, LCR measurements into much larger frequencies are required in order make more accurate determination of the CTLNT + 4wt% BBO MLCC properties and classifications.

6.5 References

[1] A. J. Moulson and J. M. Herbert, *Electroceramics: Materials, Properties, Applications*. New York: Chapman & Hall, 1990.

[2] P. Hammond, “Chapter 2 – Electric Charges at Rest—I,” in *Electromagnetism for Engineers*, 1986, pp. 8–26.

[3] P. Hammond, “Chapter 3 – Electric Charges at Rest—II,” in *Electromagnetism for Engineers*, 1986, pp. 27–53.

[4] H. Kishi, Y. Mizuno, and H. Chazono, “Base-Metal Electrode-Multilayer Ceramic Capacitors: Past, Present and Future Perspectives,” *Jpn. J. Appl. Phys.*, vol. 42, no. Part 1, No. 1, pp. 1–15, Jan. 2003.

[5] M. Randall, D. Skamser, T. Kinard, J. Qazi, A. Tajuddin, S. Trolier-Mckinstry, C. Randall, S. W. Ko, and T. Dechakupt, “Thin film MLCC,” 2007, pp. 372–384.

[6] Yano Research Institute, “Capacitor Market in Japan: Key Research Findings 2009,” Tokyo, 2009.

[7] M.-J. Pan and C. A. Randall, “A brief introduction to ceramic capacitors,” *IEEE Electr. Insul. Mag.*, vol. 26, no. 3, pp. 44–50, May 2010.

[8] Yano Research Institute, “High-Capacity Capacitors Market in Japan: Key Research Findings 2013,” Tokyo, 2013.

[9] Yano Research Institute, “High-Capacity Capacitor Market in Japan: Key Research Findings 2015,” Tokyo, 2015.

[10] S. F. Wang, J. P. Dougherty, W. Huebner, and J. G. Pepin, “Silver-Palladium Thick-Film Conductors,” *J. Am. Ceram. Soc.*, vol. 77, no. 12, pp. 3051–3072, Dec. 1994.

[11] J. G. Pepin, W. Borland, P. O’Callaghan, and R. J. S. Young, “Electrode-Based Causes of Delaminations in Multilayer Ceramic Capacitors,” *J. Am. Ceram. Soc.*, vol. 72, no. 12, pp. 2287–2291, Dec. 1989.

[12] T. Garino and M. Rodriguez, “Behavior of Silver and Palladium Mixtures during Heating,” *J. Am. Ceram. Soc.*, vol. 83, no. 11, pp. 2709–2714, Dec. 2000.

[13] I. Burn, “Flux-sintered $BaTiO_3$ dielectrics,” *J. Mater. Sci.*, vol. 17, no. 5, pp. 1398–1408, May 1982.

[14] N. Yamaoka, M. Fukui, and H. Nakamura, “Low Temperature Sintered BaTiO 3 Ceramics with $Bi_4Ti_3O_{12}$ Added,” *Jpn. J. Appl. Phys.*, vol. 20, no. S4, p. 139, Jan. 1981.

[15] J. M. Haussonne, G. Desgardin, P. Bajolet, and B. Raveau, “Barium Titanate Perovskite Sintered with Lithium Fluoride,” *J. Am. Ceram. Soc.*, vol. 66, no. 11, pp. 801–807, Nov. 1983.

[16] Apmex Incorporated, “Palladium Prices,” 2016. [Online]. Available: http://www.apmex.com/spotprices/palladium-price. [Accessed: 07-Jul-2016].

[17] H.-J. Hagemann and H. Ihrig, “Valence change and phase stability of 3d-doped $BaTiO_3$ annealed in oxygen and hydrogen,” *Phys. Rev. B*, vol. 20, no. 9, pp. 3871–3878, Nov. 1979.

[18] I. Burn and G. H. Maher, “High resistivity BaTiO3 ceramics sintered in CO-CO_2 atmospheres,” *J. Mater. Sci.*, vol. 10, no. 4, pp. 633–640, Apr. 1975.

[19] Y. H. Han, J. B. Appleby, and D. M. Smyth, “Calcium as an Acceptor Impurity in $BaTiO_3$,” *J. Am. Ceram. Soc.*, vol. 70, no. 2, pp. 96–100, Feb. 1987.

[20] D. F. K. Hennings and H. Schreinemacher, “Ca-acceptors in dielectric ceramics sintered in reducive atmospheres,” *J. Eur. Ceram. Soc.*, vol. 15, no. 8, pp. 795–800, Jan. 1995.

[21] H. Saito, H. Chazono, H. Kishi, and N. Yamaoka, “X7R Multilayer Ceramic Capacitors with Nickel Electrodes,” *Jpn. J. Appl. Phys.*, vol. 30, no. Part 1, No. 9B, pp. 2307–2310, Sep. 1991.

[22] H. Shizuno, S. Kusumi, H. Saito, and H. Kishi, “Properties of Y5V Multilayer Ceramic Capacitors with Nickel Electrodes,” *Jpn. J. Appl. Phys.*, vol. 32, no. Part 1, No. 9B, pp. 4380–4383, Sep. 1993.

[23] S. Sumita, M. Ikeda, Y. Nakano, K. Nishiyama, and T. Nomura, “Degradation of Multilayer Ceramic Capacitors with Nickel Electrodes,” *J. Am. Ceram. Soc.*, vol. 74, no. 11, pp. 2739–2746, Nov. 1991.

[24] H. Kishi and N. Yamaoka, *Science of ceramic interfaces II*, vol. 81. Amsterdam: Newnes, 1995.

[25] Y. Okino, H. Shizuno, S. Kusumi, and H. Kishi, “Dielectric Properties of Rare-Earth-Oxide-Doped $BaTiO_3$ Ceramics Fired in Reducing Atmosphere,” *Jpn. J. Appl. Phys.*, vol. 33, no. Part 1, No. 9B, pp. 5393–5396, Sep. 1994.

[26] K. Takada, E. Chang, and D. M. Smyth, “Advances in Ceramics, Volume 19,” in *Multilayer Ceramic Devices*, J. B. Blum and R. W. Cannon, Eds. Westerville, OH, United States: American Ceramic Society, 1985, p. 147.

[27] G. V. Lewis and C. R. A. Catlow, “Computer modelling of barium titanate,” *Radiat. Eff.*, vol. 73, no. 1–4, pp. 307–314, Jan. 1983.

[28] G. . Lewis and C. R. . Catlow, “Defect studies of doped and undoped barium titanate using computer simulation techniques,” *J. Phys. Chem. Solids*, vol. 47, no. 1, pp. 89–97, Jan. 1986.

[29] R. D. Shannon, “Revised effective ionic radii and systematic studies of interatomic distances in halides and chalcogenides,” *Acta Crystallogr. Sect. A*, vol. 32, no. 5, pp. 751–767, Sep. 1976.

[30] A. Sato, A. Hitomi, Y. Nakano, and T. Nomura, “Study on the reduction-resistant BaTiO3-based dielectric materials,” *Funtai Oyobi Fummatsu Yakin/Journal Japan Soc. Powder Powder Metall.*, vol. 40, no. 5, pp. 545–549, 1993.

[31] A. Hitomi, A. Sato, Y. Nakano, and T. Nomura, “Effects of the Dopants on the Electrical Properties of the Ni-electrode Ceramic Capacitors.,” *J. Japan Soc. Powder Powder Metall.*, vol. 40, no. 4, pp. 455–460, Aug. 1993.

[32] R. C. Pullar, S. J. Penn, X. Wang, I. M. Reaney, and N. M. Alford, “Dielectric loss caused by oxygen vacancies in titania ceramics,” *J. Eur. Ceram. Soc.*, vol. 29, no. 3, pp. 419–424, 2009.

[33] S. Chao and F. Dogan, “Processing and Dielectric Properties of TiO_2 Thick Films for High-Energy Density Capacitor Applications,” *Int. J. Appl. Ceram. Technol.*, vol. 8, no. 6, pp. 1363–1373, 2011.

[34] S. Marinel, D. H. Choi, R. Heuguet, D. Agrawal, and M. Lanagan, “Broadband dielectric characterization of TiO_2 ceramics sintered through microwave and conventional processes,” *Ceram. Int.*, vol. 39, no. 1, pp. 299–306, 2013.

[35] A. R. West, *Solid State Chemistry and Its Applications*. Wiley India Pvt. Limited, 2007.

[36] R. C. Buchanan, *Ceramic materials for electronics*, 3rd ed., vol. 1. New York: Marcel Dekker, Inc, 2004.

[37] Electronic Components Industry Association (EIA), “EIA-198-1F Ceramic Dielectric Capacitors, Classes I, II, III, IV - part 1: Characterization and requirements,” 2002.

[38] C. J. Rawn, D. P. Birnie, M. A. Bruck, J. H. Enemark, and R. S. Roth, “Structural investigation of $Ba_{6-3x}Ln_{8+2x}Ti_{18}O_{54}$ (x = 0.27, Ln = Sm) by single crystal x-ray diffraction in space group Pnma (No. 62),” *J. Mater. Res.*, vol. 13, no. 01, pp. 187–196, Jan. 1998.

[39] M. S. Randall, P. Blais, J. Prymak, M. Prevallet, D. Skamser, A. Gurav, P. Pinceloup, X. Xu, A. Tajuddin, P. Lessner, and T. Ashburn, “Capacitor considerations for power management,” 2006, pp. 79–93.

[40] I. M. Reaney and D. Iddles, “Microwave Dielectric Ceramics for Resonators and Filters in Mobile Phone Networks,” *J. Am. Ceram. Soc.*, vol. 89, no. 7, pp. 2063–2072, Apr. 2006.

[41] H. Ohsato, “Research and Development of Microwave Dielectric Ceramics for Wireless Communications,” *J. Ceram. Soc. Japan*, vol. 113, no. 1323, pp. 703–711, 2005.

[42] T. R. Armstrong, L. E. Morgens, A. K. Maurice, and R. C. Buchanan, “Effects of Zirconia on Microstructure and Dielectric Properties of Barium Titanate Ceramics,” *J. Am. Ceram. Soc.*, vol. 72, no. 4, pp. 605–611, Apr. 1989.

[43] C.-H. Kim, K.-J. Park, Y.-J. Yoon, M.-H. Hong, J.-O. Hong, and K.-H. Hur, “Role of yttrium and magnesium in the formation of core-shell structure of $BaTiO_3$ grains in MLCC,” *J. Eur. Ceram. Soc.*, vol. 28, no. 6, pp. 1213–1219, Jan. 2008.

[44] Z. Tian, X. Wang, Y. Zhang, J. Fang, T.-H. Song, K. H. Hur, S. Lee, and L. Li, “Formation of Core-Shell Structure in Ultrafine-Grained $BaTiO_3$ -Based Ceramics Through Nanodopant Method,” *J. Am. Ceram. Soc.*, vol. 93, no. 1, pp. 171–175, Jan. 2010.

[45] T. Tsurumi, H. Adachi, H. Kakemoto, S. Wada, Y. Mizuno, H. Chazono, and H. Kishi, “Dielectric Properties of $BaTiO_3$ -Based Ceramics under High Electric Field,” *Jpn. J. Appl. Phys.*, vol. 41, no. Part 1, No. 11B, pp. 6929–6933, Nov. 2002.

[46] X. Chen, W. Zhang, B. Zalinska, I. Sterianou, S. Bai, and I. M. Reaney, “Low Sintering Temperature Microwave Dielectric Ceramics and Composites Based on Bi_2O_3-B_2O_3,” *J. Am. Ceram. Soc.*, vol. 95, no. 10, pp. 3207–3213, Oct. 2012.

[47] H. Takahashi, Y. Baba, K. Ezaki, and K. Shibata, “Microwave Dielectric Properties and Crystal Structure of $CaO - Li_2O - (1\text{-}x)Sm_2O_3 - xLn_2O_3 - TiO_2$ (Ln: lanthanide) Ceramics System,” *Jpn. J. Appl. Phys.*, vol. 35, no. Part 1, No. 9B, pp. 5069–5073, Sep. 1996.

[48] K. Ezaki, Y. Baba, H. Takahashi, K. Shibata, and S. Nakano, “Microwave Dielectric Properties of CaO-Li_2O-Ln_2O_3-TiO_2 Ceramics,” *Jpn. J. Appl. Phys.*, vol. 32, no. Part 1, No. 9B, pp. 4319–4322, Sep. 1993.

[49] H. Takahashi, Y. Baba, K. Ezaki, Y. Okamoto, K. Shibata, K. Kuroki, and S. Nakano, “Dielectric Characteristics of $(A_{1/2}^{1+}\cdot A_{1/2}^{3+})TiO_3$ Ceramics at Microwave Frequencies,” *Jpn. J. Appl. Phys.*, vol. 30, no. Part 1, No. 9B, pp. 2339–2342, Sep. 1991.

Chapter 7: General Discussion

In this thesis, the interaction between the CTLNT MW dielectric materials and the BBO sintering aid have been investigated to ascertain the mechanism behind maintaining excellent MW properties at reduced sintering temperatures. The CTLNT + 4wt% BBO composition was reported to have excellent MW results, even at sintering temperatures of 1200°C, by Chen *et al.* in 2012 [1], with little understanding as to how this was achieved. Investigations using a variety of techniques, including SEM, TEM and EDS, eventually revealed a likely mechanism. Thereafter, the experiments were repeated on a similar material, the CTLST system, in order to see whether the sintering aid produces the same sintering mechanism as the CTLNT system, in terms of reducing the sintering temperature, while maintaining the MW properties.

Upon completion of the CTLST study, the thesis was extended to investigate the properties of the CTLNT + 4wt% BBO material as a Class 1 MLCC.

7.1 Interaction of BBO with CTLNT

CTLNT + xBBO samples were fabricated after Chen *et al.* [1] to repeat and confirm the findings stated in their work, with 1, 3, 4 and 5wt% BBO samples created. 7.5 and 10wt% BBO samples were not recreated as the original focus was on the composition resulting in a near-zero τ_f.

XRD of the samples did not show any secondary phases within the CTLNT samples, regardless of BBO additions. This was likely due to the nature of the BBO sintering aid being an amorphous phase within the samples, and therefore unlikely to return any peaks. In addition, the quantities of the BBO additions involved were below the minimum detectable threshold of the XRD equipment used. It was noted by Chen *et al.* [1] that any secondary phases produced by the BBO additions were reported to only be detected by compositions with greater than 5wt% additions of BBO.

Density of the samples tended to increase as the BBO concentration increased, and the increase in density was greater than for a simple rule of mixtures between two materials of different densities. As such, along with SEM images of the samples, it was concluded that the BBO sintering aid was inducing liquid-phase sintering at lower sintering temperatures, increasing crystal grain growth at lower sintering temperatures, as well increasing density. As the BBO concentration increased, so too did the rate of sintering and density at lower sintering temperatures. As BBO concentration and sintering temperature reached the upper margins of analysis, rounding of crystal grain corners were observed, which suggested that elevated levels of BBO at higher sintering temperatures was causing dissolution of the matrix phase into the liquid-phase. The rounding of crystal edges was linked to changes in density and degradation of MW properties observed for those samples.

SEM analysis revealed the presence of B-rich 'pools' of amorphous phase within the fracture surface, which was observed with increasing frequency and quantity as BBO content was increased. Note that boron could not be directly detected by EDS but the dark contrast was assumed to arise from a low density phase. The absence of B in EDS spectra was likely due to high X-ray reabsorption rates due to low photon energies from B, especially within amorphous, glassy phases [2]. Samples with larger quantities BBO also showed regions of lighter and darker contrast on the polished surface of the samples in SEM. These regions, under EDS analysis, corresponded with a heavier and lighter average atomic weight, respectively, including larger proportions of Bi within the brighter regions. This suggested that a reaction between the two materials was occurring and that the Bi was entering the CTLNT matrix, and went some way to explain the absence of Bi within the liquid-phases. SEI was more likely to reveal contrast variations than the BE images, which suggested that these regions were relatively thin or shallow, resulting in a BE response more reflective of the bulk material below these regions.

The MW results showed an increase in ε_r and a decrease in Qf_0 as the BBO content was increased, with marked improvement of MW properties as BBO content increased at the lower sintering temperatures. Contrary to expectations, the change of τ_f with BBO was non-linear. The largest change of MW properties with sintering temperature was the 1wt% BBO composition, as the sample was almost pure CTLNT and would show an increase in MW properties as the sintering temperature approached the optimal sintering temperature of pure CTLNT. Samples with more BBO sintering aid maintained better MW properties at lower sintering temperatures. Generally, increases in ε_r matched well with increases in density, as a result of increased BBO content. The non-linearity of the τ_f with increased BBO content suggested, along with the contrast variations observed in the SEM images, that a reaction was occurring between the BBO and the CTLNT, which was becoming more pronounced as BBO content increased. Optimum MW properties were produced by the 4wt% BBO samples, sintered at 1200°C, with $\varepsilon_r = 125$, $Qf_0 = 2518$ and $\tau_f = 4\ ppm/°C$.

Initial TEM diffraction patterns showed no anomalous features as a result of the BBO. When compared to $CaTiO_3$ (CT) and $(Li_{0.5}Nd_{0.5})TiO_3$ (LNT) end-members, the diffraction patterns showed typical diffraction patterns normally associated with a $CaTiO_3$ perovskite material, with superstructure reflections consistent with an $a^-a^-c^+$ Glazer tilt system [3]. Any diffuse scattering and anomalous reflections observed were from a nano-chessboard structure, associated with the LNT end-member [4]–[9], and not the BBO sintering aid. Evidence of this nano-chessboard structure was observed in subsequent BF images. The nano-chessboard structure was likely a result of local inhomogeneous mixing of the CTLNT matrix, causing the prerequisite 1:1 ordering of Nd ions, Li ions and vacancies to form on the nano-metre scale, which were periodically arranged as a superlattice of nano-domains [10]–[17].

TEM EDS confirmed that Bi was entering the matrix of the CTLNT. Subsequent BF images along with EDS analysis revealed the presence of Ti-rich cuboid precipitates *inside* the grains. As Bi^{3+} enters the CTLNT lattice the formation of the TiO_2 precipitates suggested that substitution of Bi^{3+} onto the A-site was not isovalent for Nd^{3+}. Instead, Ti^{4+} ex-solves from the perovskite matrix, which implied the formation of titanium vacancies (V_{Ti}'''') within the CTLNT. Most likely, the Bi substitutes for either the Ca site or the combined Li/Nd site, and the generic defect equation:

$$4A_A^x + Ti_{Ti}^x \Rightarrow 4Bi_A^{\cdot} + V_{Ti}''''$$

was proposed, where A = A-site. The highly polarisable Bi^{3+} ion, therefore, along with the MW properties of TiO_2 precipitates, is likely locally enhancing the MW properties in the brighter contrast regions of the SEM images, leaving behind a B-rich liquid-phase as the sintering aid with large negative τ_f values [18]–[22]. This contribution has therefore, resulted in an understanding of the sintering mechanism between the CTLNT microwave dielectric material and the BBO liquid-phase sintering aid.

7.2 Interaction of BBO with CTLST

CTLST + $x$wt% BBO was investigated to see whether this could be repeated for a similar material, and 1, 2, 3 and 4wt% BBO compositions were fabricated. The XRD between the two materials followed similar trends with no apparent changes of phases with respect to BBO concentration. XRD results revealed a secondary phase in all of the CTLST + $x$wt% BBO compositions, not present in the CTLNT system, regardless of the composition, which was likely a pyrochlore secondary phase. The pyrochlore phase was therefore endemic of the CTLST system. SEM images of the polished surface containing small, brighter specks were attributed to the secondary phase which were likely a pyrochlore and, therefore, would be slightly brighter in the SEM images due to a higher weight average atomic number than the CTLST matrix.

The sintering aid successfully lowered the sintering temperature of the CTLST system from approximately 1350°C to between 1200-1250°C, whilst maintaining high density. Unlike the CTLNT system, the results showed that density fell at sintering temperatures greater than 1250°C. Although, the CTLNT system was not sintered, with BBO, higher than 1250°C, there is no evidence to suggest that the behaviour of CTLST, at 1300°C, is different to the CTLNT system. SEM was then also used to see physical differences between the CTLNT and CTLST systems, which would result in this degradation of density, despite the initial increase in density.

SEM analysis of the fracture surface revealed grains which were rich in Zr, in addition to a Zr-rich glue-like phase. The CTLST system either had larger quantities of Zr contamination from the milling process, or was more susceptible to reacting with the Zr in some way to produce grains.

Aside from the presence of Zr contamination within the samples, Bi was routinely observed in the EDS of the matrix, and little data could be collected from the darker contrast liquid-phase, which was similar to the CTLNT system. This suggested that, in some capacity, Bi was entering the CTLST matrix, as in CTLNT, leaving behind a B-rich liquid-phase.

SEM analysis also revealed more dissolution of the grains, and larger overall grains and pores, as sintering temperature and BBO content increased, than the CTLNT system. This was likely the result of two different effects. Firstly, the BBO sintering aid was successful in causing sintering to occur at lower temperatures, which produced larger grains at higher sintering temperatures. Secondly, this was causing elevated levels of material dissolution from the matrix into the liquid-phase, causing rounding of the grain edges and larger pores, which would be detrimental to the density and overall MW properties and densities of the material.

There were large differences between the MW results between the two ceramic systems. Some of this was explained by the physical, morphological differences observed in the SEM, discussed above, where the deterioration of grain morphologies, porosity and density were contributing to the ε_r and Qf_0 values. However, the linear τ_f trend suggested that a different reaction occurred, compared with the CTLNT system, and was much more in keeping with the mixing of two materials of positive and negative τ_f.

Despite this, an optimum composition of 4wt% BBO, sintered at 1200°C, yielded a balance of MW properties and larger reduction in sintering temperature, compared to the CTLNT system, of 150°C, down to 1200°C, with $\varepsilon_r = 105.7$, $Qf_0 = 3295\ GHz$ and $\tau_f = -4\ ppm/℃$.

TEM did not reveal the presence of TiO_2 precipitates within the grains of the CTLST system, however this is not proof that they do not exist. However, with the presence of Zr contamination changing the defect chemistry within CTLST, the need to ex-solve TiO_2 may well be negated by the substitution of Bi onto the A-site to compensate for excess Zr on the B-site of the perovskite structure. Although, further investigation into this is required.

Overall, with all factors considered, it is possible to infer that a similar reaction between the CTLST and BBO sintering aid is occurring, however due to various possible effects, in this particular study, this reaction may not have been as pronounced as for the CTLNT system. Regardless, overall results show that the use of BBO as a sintering aid for the CTLST system was successful in reducing the sintering temperature, while maintaining very good MW properties. As such, the CTLST + 4wt% BBO composition, sintered at 1200°C, could be a decent, cheaper, substitute candidate for a wider market.

7.3 The use of CTLNT + 4wt% BBO as a MLCC

Since the CTLNT + 4wt% BBO material has a large ε_r and near-zero τ_f value, it was postulated that the material may be a suitable candidate for testing as a Class 1, C0G/NP0 MLCC device. In this study, and for the purposes of simplifying the fabrication of the MLCC device, platinum internal electrodes were used, as it has a high melting point and is inert at the sintering temperatures required. A preliminary study was conducted into the fabrication and testing of 3, 4 and 5 internal electrode layer MLCC devices, following a conventional fabrication procedure.

Initially, the fabrication of the MLCC devices followed the conventional method outlined by Pan and Randall [23], however the 4 and 5-layer devices delaminated during the firing and sintering stage, as well as the material 'sticking' to the Pt foil used to fire and sinter the samples upon.

Delamination was attributed to two different processes involving the stacking and laminating of the layers, and the firing and sintering steps. The first effect was identified by the way the layers remained as individual, distinguishable layers, rather than a single fused layer, after stacking and pressing, upon examination of the cross-section of the green samples. This was the result of insufficient pressure being applied to the stacks, as the layer numbers were increased. Instead, each layer was wetted using a solvent, and pressed together manually. The resulting stack, upon inspection of the diced samples, appeared to be a single fused layer.

The second effect was identified by the way the samples would bulge, deform, present bubbles within the layers, and by sticking to the platinum foil used to fire the samples upon. The sticking to the platinum foil was likely due to the surface tension of the liquid-phase sintering aid used in the samples, deforming the sample as the rest of the sample continued to shrink during sintering. Firing the samples on calcined alumina powder resolved this issue. The bubbling and bulging delamination effect was a result of a firing time which was too short for the amount of additional gas produced as the amount of material and layer numbers increased. Any gas which did not burn out at the lower temperatures would expand as the temperature increased to the sintering temperature, causing increased porosity or delamination. This could be observed when comparing the cross-section of the 4 and 5-layer samples sintered using the shorter (57 hours) and longer (67 hours) burnout times under SEM. Examination of the 5-layer sample along the cross-section suggested that the longer firing time was still not long enough, due to a line of pores along the central internal electrode.

SEM SEI, BE and EDS mapping analysis of the cross section revealed that no chemical reaction, exchange or diffusion of material occurred between the CTLNT + 4wt% BBO dielectric and the platinum internal electrode. SEI showed a similar presence of brighter contrast regions of dielectric, as well as pores filled with B-rich liquid-phase, compared with the samples produced in the CTLNT study of the same composition. There was good contact adhesion between the two materials, creating a large contact area. The adhesion strength appeared to be stronger with the layer the electrode was screen-printed onto, increasing the risk of delamination from mechanical stresses as a result of sintering.

Electrical characterisation results revealed that the capacitance of the devices increased as the number of layers increased. They also correlated well with the SEM results, showing lower performance in the 5-layer samples compared with the 3- and 4-layer samples, due to mild delamination. LCR results showed increased temperature stability of all electrical properties as frequency increased. At larger layer numbers, temperature stability of ε_r and τ_C improved at lower frequencies. However, increased dielectric losses were observed for samples with more layers and at lower frequencies, which was likely a result of the increased number of interfacial regions.

LCR results indicated a change in temperature stability of +988ppm/°C between 23-110°C, and +746ppm/°C between 23-60°C for the 3-layer device, +993ppm/°C between 23-100°C, and +761ppm/°C between 23-60°C for the 4-layer device and +1946ppm/°C between 28-148°C, and +1089ppm/°C between 28-60°C for the 5-layer device. This would define the CTLNT + $x$wt% BBO based MLCC devices with an EIA class 1 classification of “M8J” and an IEC class 1 rating of “P1000”. Since the operating frequency for class 1 devices is between 100 MHz and 30 GHz, the upper frequency of 1 MHz tested here were likely yielding results which were not typical of the material. The frequencies the CTLNT + 4wt% BBO material was originally designed for the 1-3 GHz range. CTLNT + 4wt% BBO based MLCC devices may therefore be a suitable class 1, C0G/NP0 capacitor candidate. More research will need to be conducted in terms of fabricating samples with more layers to make more comparable devices commercial MLCCs. More work is also needed to fabricate 5+ layer devices without delamination, and creating devices with equal adhesion to both sides of the electrode with the dielectric.

7.4 References

[1] X. Chen, W. Zhang, B. Zalinska, I. Sterianou, S. Bai, and I. M. Reaney, “Low Sintering Temperature Microwave Dielectric Ceramics and Composites Based on Bi_2O_3-B_2O_3,” *J. Am. Ceram. Soc.*, vol. 95, no. 10, pp. 3207–3213, Oct. 2012.

[2] L. Ingemarsson and M. Halvarsson, “SEM/EDX Analysis of Boron,” Gothenburgh, 2011.

[3] D. I. Woodward and I. M. Reaney, “Electron diffraction of tilted perovskites,” *Acta Crystallogr. Sect. B*, vol. 61, no. 4, pp. 387–399, 2005.

[4] L. Farber, I. Levin, A. Borisevich, I. E. Grey, R. S. Roth, and P. K. Davies, “Structural study of $Li_{1+x-y}Nb_{1-x-3y}Ti_{x+4y}O_3$ solid solutions,” *J. Solid State Chem.*, vol. 166, no. 1, pp. 81–90, 2002.

[5] B. S. Guiton, W. Hui, and P. K. Davies, “Neutron powder diffraction of $(Nd_{7/12}Li_{1/4})TiO_3$ nano-checkerboard superlattices,” *Chem. Mater.*, vol. 20, no. 9, pp. 2860–2862, 2008.

[6] B. S. Guiton and P. K. Davies, “Spontaneous compositional nanopatterning in Li-containing perovskite oxides,” *J. Am. Chem. Soc.*, vol. 130, no. 50, pp. 17168–17173, 2008.

[7] B. S. Guiton and P. K. Davies, “Nano-chessboard superlattices formed by spontaneous phase separation in oxides,” *Nat. Mater.*, vol. 6, no. 8, pp. 586–591, Aug. 2007.

[8] S. Yeo, Y. Horibe, S. Mori, C. M. Tseng, C. H. Chen, A. G. Khachaturyan, C. L. Zhang, and S.-W. Cheong, “Solid state self-assembly of nanocheckerboards,” *Appl. Phys. Lett.*, vol. 89, no. 23, p. 233120, 2006.

[9] “A checkerboard of materials,” *Nat. Mater.*, vol. 6, no. 2, pp. 87–87, Feb. 2007.

[10] H. J. Lee, H. M. Park, S. H. Oh, Y. K. Cho, J. O. Son, and S. Nahm, “Microstructures in Complex Perovskite $(Li_{1/2}Ln_{1/2})TiO_3$ (Ln = Pr, Nd, Sm),” *Jpn. J. Appl. Phys.*, vol. 43, no. 11A, pp. 7592–7595, Nov. 2004.

[11] M. Abe and K. Uchino, “X-ray study of the deficient perovskite,” *Mater. Res. Bull.*, vol. 9, no. 2, pp. 147–155, Feb. 1974.

[12] P. N. Iyer and A. J. Smith, “Double oxides containing niobium, tantalum, or protactinium. III. Systems involving the rare earths,” *Acta Crystallogr.*, vol. 23, no. 5, pp. 740–746, Nov. 1967.

[13] H. P. Rooksby, E. A. D. White, and S. A. Langston, “Perovskite-Type Rare-Earth Niobates and Tantalates,” *J. Am. Ceram. Soc.*, vol. 48, no. 9, pp. 447–449, Sep. 1965.

[14] J. A. Alonso, J. Sanz, J. Santamaría, C. León, A. Várez, and M. T. Fernández-Díaz, “On the Location of Li+ Cations in the Fast Li-Cation Conductor $La_{0.5}Li_{0.5}TiO_3$ Perovskite,” *Angew. Chemie Int. Ed.*, vol. 39, no. 3, pp. 619–621, Feb. 2000.

[15] J. Sanz, J. A. Alonso, A. Varez, and M. T. Fernández-Díaz, “Octahedral tilting and ordering of vacancies in the fast ion conductor $Li_{0.12}La_{0.63}TiO_3$ perovskite: a neutron diffraction study,” *J. Chem. Soc. Dalt. Trans.*, no. 7, pp. 1406–1408, Mar. 2002.

[16] M. Sommariva and M. Catti, “Neutron Diffraction Study of Quenched $Li_{0.3}La_{0.567}TiO_3$ Lithium Ion Conducting Perovskite,” *Chem. Mater.*, vol. 18, no. 9, pp. 2411–2417, May 2006.

[17] M. Catti, “First-Principles Modeling of Lithium Ordering in the LLTO ($Li_xLa_{2/3-x/3}TiO_3$) Superionic Conductor,” *Chem. Mater.*, vol. 19, no. 16, pp. 3963–3972, Aug. 2007.

[18] N. Mori, Y. Sugimoto, J. Harada, and Y. Higuchi, “Dielectric properties of new glass-ceramics for LTCC applied to microwave or millimeter-wave frequencies,” *J. Eur. Ceram. Soc.*, vol. 26, no. 10–11, pp. 1925–1928, 2006.

[19] Z. N. Wing, B. Wang, and J. W. Halloran, “Permittivity of Porous Titanate Dielectrics,” *J. Am. Ceram. Soc.*, vol. 89, no. 12, pp. 3696–3700, 2006.

[20] C. L. Huang and K. H. Chiang, “Improved high-Q microwave dielectric material using B_2O_3-doped $MgNb_2O_6$ ceramics,” *Mater. Sci. Eng. A*, vol. 474, no. 1–2, pp. 243–246, 2008.

[21] H. X. Lin, Y. Zhang, X. Y. Zhao, W. Chen, and L. Luo, “Sintering and microwave dielectric properties of $La(Mg_{0.5}Ti_{0.5})O_3$ ceramics doped with La_2O_3-B_2O_3-TiO_2 glass,” *Jpn. J. Appl. Phys.*, vol. 47, no. 9, pp. 7243–7245, 2008.

[22] U. Došler, M. M. Kržmanc, and D. Suvorov, “The synthesis and microwave dielectric properties of $Mg_3B_2O_6$ and $Mg_2B_2O_5$ ceramics,” *J. Eur. Ceram. Soc.*, vol. 30, no. 2, pp. 413–418, 2010.

[23] M.-J. Pan and C. A. Randall, “A brief introduction to ceramic capacitors,” *IEEE Electr. Insul. Mag.*, vol. 26, no. 3, pp. 44–50, May 2010.

Chapter 8: Final Conclusions

The development of dielectrically loaded antennas is driven by miniaturisation, which require materials with ever increasing ε_r. However, materials with the highest levels of ε_r tend to have relatively high sintering temperatures, resulting in expensive devices for the mass market, as well as large positive τ_f values. Sintering aids are normally mixed into the compositions to reduce the sintering temperature, however tend to be detrimental to the MW properties.

The work conducted in this contribution focussed on:

1: Investigating the sintering mechanism behind the CTLNT + $x$wt% BBO system;
2: Using the same sintering aid in a slightly different material and conducting the same experiments in the CTLST + $x$wt% BBO system;
3: The viability of the CTLNT + 4wt% BBO system as a Class 1 C0G/NP0 MLCC device.

Overall, it was shown that the BBO reacts with the CTLNT system in such a way as to produce local enhancements to the MW properties, maintaining average MW properties and increasing density at lower sintering temperatures. The CTLST system showed similarities as well as differences with the CTLNT system, but also showed improved MW properties at lower sintering temperatures. Finally, despite limitations with the electrical testing equipment, promising trends in the electrical properties were shown for the CTLNT MLCC devices. The main bullet points of the findings in this contribution are listed below.

8.1 CTLNT + $x$wt% BBO System

- 1, 3, 4 and 5wt% BBO compositions were fabricated at 1150, 1200 and 1250°C, and tested successfully;
- Optimum composition was: 4wt% BBO, sintered at 1200°C, with $\varepsilon_r = 125$, $Qf_0 = 2518$ and $\tau_f = 4\ ppm/°C$;
- Density of samples increased as BBO content increased, at a greater rate than simple rule of mixtures;
- XRD unable to detect secondary phases, and suggests a single-phase CTLNT material, regardless of BBO content;
- SEM of the fracture surface revealed the following:
  i) Increased crystal grain size as BBO content increased;
  ii) Dissolution of CTLNT matrix at larger BBO contents and higher sintering temperature;
  iii) Presence of a B-rich liquid-phase, with increased prevalence with increased BBO content.
- SEM of the polished surface showed:

    i) Decreased overall porosity with increased BBO, however pores increased in size;
    ii) Regions of differing contrast, suggesting the occurrence of a reaction;
    iii) EDS confirms greater presence of Bi in the matrix as BBO content increased.
- MW results reflect density trends, with increasing ε_r as BBO content and sintering temperature increases;
- τ_f results were non-linear with additions of BBO, suggesting a reaction between CTLNT and BBO;
- TEM EDS data shows Bi within the CTLNT grains, and BF images reveal the presence of ex-solved TiO_2 precipitates within the grains;
- CTLNT + BBO sintering mechanism observed: Bi substitutes into the A-site of the perovskite structure, creating Ti vacancies, leaving behind a B-rich liquid-phase as the sintering aid;
- Generic defect equation for the observed interactions postulated: $4A_A^x + Ti_{Ti}^x \Rightarrow ABi_A^{\cdot} + V_{Ti}''''$.

8.2 CTLST + $x$wt% BBO System

- 1, 2, 3 and 4wt% BBO compositions were fabricated at 1200, 1250 and 1300°C, and tested successfully;
- Optimum composition was: 4wt% BBO, sintered at 1200°C, with $\varepsilon_r = 105.7$, $Qf_0 = 3295\ GHz$ and $\tau_f = -4\ ppm/$°C;
- XRD showed no change in phase, regardless of BBO content, however similar pyrochlore observed in all compositions, regardless of BBO content;
- Density increased with BBO content, up to 1250°C, and decreased again at 1300°C;
- SEM revealed increased crystal grain definition and size as BBO content increased, however also showed increased matrix dissolution which related to decrease in density at 1300°C;
- SEM EDS showed increased Bi present within matrix as BBO content increased, as well as increased B-rich liquid-phase;
- MW results reflect density trends, ε_r increases to a maximum at 1200°C, and decreases again at 1300°C, ε_r and Qf_0 increase with increased BBO content at lowest sintering temperatures;
- τ_f values remarkably linear, compared with CTLTN system
- TEM EDS data revealed Bi within the grains, although no TiO_2 precipitates;
- Presence of Bi within the CTLST grains suggestive of Bi substitution, although to a lesser extent compared with CTLNT;
- Local defect chemistry in the CTLST + xBBO system likely subtly different;
- Excess Zr contamination onto the B-site may be compensated by Bi substitution onto the A-site, negating the need to ex-solve TiO_2 precipitates.

8.3 CTLNT + 4wt% BBO Composition as MLCC Dielectric

- 3, 4 and 5-layer MLCC successfully fabricated using CTLNT + 4wt% BBO as dielectric, using platinum as internal electrode, with average case size of EIA ‘2928’, IEC ‘7472’;
- Fabrication process altered due to issues with conventional method leading to delamination;
- Capacitance of devices increases as layer numbers increase;
- Temperature stability of electrical properties increases at increased frequencies;
- At maximum test frequency of 1 MHz, samples would be classified as EIA “M8J” and IEC “P1000”;
- Maximum test frequency much lower than average operating frequency for Class 1 devices, of 100 MHz - 30 GHz, CTLNT system designed for use in 1-5 GHz range;
- Increased stability trends up to 1 MHz suggestive of good potential in CTLNT + 4wt% BBO material as EIA “C0G” and IEC “NP0” device if tested between 100 MHz – 30 GHz.

Chapter 9: Future Work

The work conducted within this project has given a thorough account of the key issues and discoveries. However, over the course of the study, there have been several avenues of research which could not be pursued, either due to time constraints or limitations with the equipment available. With the luxury of more time and funding, the following presents thoughts of further research to pursue.

9.1 CTLNT

1) The discovery of TiO_2 precipitates were only observed within the TEM samples of the 5wt% BBO composition, sintered at the highest sintering temperature, and observing them were highly unlikely. Additionally, previous work hinted at visible secondary phases in XRD analysis of compositions of greater than 5wt% BBO. As such, there is interest in recreating the 7.5 and 10wt% BBO compositions, to observe the secondary phases within XRD and conduct TEM analysis on the samples with the knowledge that increasing the BBO content would increase the likelihood of observing precipitates under TEM. It would be interesting to confirm whether the TiO_2 precipitates are the secondary phase observed within the XRD.

2) Later work into the CTLST system showed a reversal in density and MW properties at 1300°C, due to increased dissolution of the matrix into the liquid-phase. It would be pertinent to observe if the CTLNT would follow a similar path upon increasing the sintering temperature further to 1300°C as well.

9.2 CTLST

1) In a similar vein to increasing the sintering temperature for the CTLNT system, decreasing the sintering temperature of the CTLST system to 1150°C would be just as valuable, as it would allow for a complete comparison between the two systems.

2) Since no TiO_2 precipitates were observed within the CTLST system under TEM, it is suggested that the compositional range should be increased to include 5, 7.5 and 10wt% BBO compositions to the study, to allow more Bi to enter the CTLST matrix and increase the chance of observing precipitates.

3) Increasing the calcination temperature further for the CTLST is also recommended, to guarantee no secondary phases post calcination and sintering of the CTLST with additions of BBO, to make better comparisons between the two materials. As it stands, the secondary phases observed in the CTLST may be influencing the behaviours of the CTLST and BBO materials.

9.3 Suggestions Relevant for Both CTLNT and CTLST Systems

1) Both the CTLNT and CTLST systems have Zr contamination within them, which may be influencing the ways both materials behave. This contamination is likely entering the materials as a result of attrition milling, which uses yttria-stabilized zirconia milling media. Reducing Zr contamination, especially for the CTLST system would likely provide higher quality samples and data, and also reduce excess Zr onto the B-site and encouraging more TiO_2 precipitates to ex-solve. This could be achieved by using less-abrasive, yet more time consuming methods, such as ball-milling, instead.

2) The sintering temperature intervals used for both systems is relatively large. Sintering at 10-25°C intervals would provide a higher resolution of data in terms of observable trends as the sintering temperature increases. This would consume more time to research, and is therefore recommended to be done where changes in behaviour is observed. For example, in the CTLST system, sintering at 10°C intervals would provide more insight as to exactly when, and how rapidly the decrease in density and MW properties occurs between 1250°C and 1300°C.

9.4 MLCC

1) Since the 5-layer MLCC samples still had some delamination present, it would be wise to repeat and re-fabricate the 5-layer MLCC samples, and increasing the burnout-time for these samples again. This would hopefully show an improvement of properties and temperature stability as the layer numbers increase, as it did between the 3 and 4-layer samples, and confirm that more layers would prove advantageous.

2) As the average operating frequency of Class 1 MLCC devices is between 100 MHz and 30 GHz, any further work in the use of CTLNT as the dielectric material for multilayer capacitors should include electrical testing within this range. As such, it may be worthwhile investing in equipment capable of testing between these frequencies, or seeking collaboration with other institutions with the available equipment.

3) SEM analysis of the cross sections of the devices revealed that there is a higher quality of contact between the internal electrode and dielectric layer the electrode was screen-printed onto. Research should therefore be considered to modify the fabrication process to ensure equal contact adhesion on both sides of the internal electrode. An initial thought would be looking at the possibility of stacking the layers together, before drying the electrode after screen-printing. This may provide issues in terms of electrode ‘smearing’ if there is any movement of layers during stacking, and if the layers are diced through the electrodes. If one is careful when using the

stacking jig, then layer movement can be minimised, and dicing can be conducted without cutting through the internal electrodes, which can be exposed through polishing after sintering.